
¹

Single-cell time-series analysis of metabolic rhythms in yeast

²

Arin Wongprommoon

³



⁴

Doctor of Philosophy

⁵

THE UNIVERSITY OF EDINBURGH

⁶

2023

7

To my family,

8

Dad and Mum, my brother Arun, and aunt Pinnapa.

Abstract

11 The yeast metabolic cycle (YMC) is a biological rhythm in budding yeast (*Sac-*
12 *charomyces cerevisiae*). It entails oscillations in the concentrations and redox
13 states of intracellular metabolites, oscillations in transcript levels, temporal par-
14 titioning of biosynthesis, and, in chemostats, oscillations in oxygen consumption.
15 Most studies on the YMC have been based on chemostat experiments, and it
16 is unclear whether YMCs arise from interactions between cells or are generated
17 independently by each cell. This thesis aims at characterising the YMC in single
18 cells and its response to nutrient and genetic perturbations. Specifically, I use
19 microfluidics to trap and separate yeast cells, then record the time-dependent
20 intensity of flavin autofluorescence, a component of the YMC.

which is

21 Single-cell microfluidics produces a large amount of time series data. Noisy and
22 short time series produced from biological experiments restrict the computational
23 tools that are useful for analysis. I developed a method to filter time series,
24 ~~develop~~ a machine learning model to classify whether time series are oscillatory,
25 and ~~develop~~ ^{on} an autocorrelation method to examine the periodicity of time series
26 data.

27 My experimental results show that yeast cells show oscillations in the fluorescence
28 of flavins. Specifically, I show that in high glucose conditions, cells generate
29 flavin oscillations asynchronously within a population, and these flavin oscillations
30 couple with the cell division cycle. I show that cells can individually reset the

31 phase of their flavin oscillations in response to abrupt nutrient changes, independ-
32 ently of the cell division cycle. I also show that deletion strains generate flavin
33 oscillations that exhibit different behaviour from dissolved oxygen oscillations
34 from chemostat conditions.

35 Finally, I use flux balance analysis to address whether proteomic constraints in
36 cellular metabolism mean that temporal partitioning of biosynthesis is advant-
37 ageous for the yeast cell, and whether such partitioning explains the timing of
38 the metabolic cycle. My results show that ~~a~~ *under* proteomic constraint means ~~that~~ it is
39 advantageous for the cell to sequentially synthesise biomass components because
40 doing so shortens the timescale of biomass synthesis. However, the degree of
41 advantage of sequential over parallel biosynthesis is lower when both carbon and
42 nitrogen sources are limiting.

43 This thesis thus confirms autonomous generation of flavin oscillations, and sug-
44 gests a model in which the YMC responds to nutrient conditions and subsequently
45 entrains the cell division cycle. It also emphasises the possibility that subpopula-
46 tions in the culture explain chemostat-based observations of the YMC. Further-
47 more, this thesis paves the way for using computational methods to analyse large
48 datasets of oscillatory time series, which is useful for many ~~and~~ *various* fields of study beyond
49 the YMC.

Lay Summary

52 Living things have biological clocks that make sure that their processes happen
 53 in a sequence. An example is the circadian rhythm, which makes sure that our
 54 body's processes happen at the correct times in a day. For example, the circadian
 55 rhythm makes sure we sleep at night and are awake during daytime.

56 Baker's yeast has a biological clock called the yeast metabolic cycle (YMC). Be-
 57 cause of this cycle, as the yeast cell grows, its metabolism and the concentrations
 58 of chemicals in the yeast cell changes over time. Most ~~scientists who have studied~~
 59 the YMC have ~~studied them in~~ ^{focused on} large cultures. So, we do not know whether the
 60 cells need to talk to each other to generate the YMC, or whether each cell can
 61 generate the YMC on its own. To study the YMC, I use ~~an experimental apparatus~~
 62 ^{that} ~~called~~ a microfluidics platform, ~~which~~ can separate yeast cells. This allows me to
 63 monitor a glowing chemical that changes intensity during the metabolic cycle by
 64 taking a series of photographs of each cell, like a movie.

65 My experiments showed that when the yeast cells grow in conditions ~~when they~~
 66 ~~are happy~~, each cell generates its metabolic cycle in sync with cell division, but
 67 out-of-sync with other cells. But, when I took away the cells' nutrients, these
 68 cells started generating their metabolic cycles in sync. Additionally, I showed
 69 that individual cells behave differently from cells in large cultures.

bit too
long.
Sounds AI

a large amount of temporal

70 Because my experiments produce a lot of time-dependent data, I explored ways
71 to use the computer to help analyse this data. I was able to teach a machine
72 learning algorithm, a common type of computer algorithm, to tell apart signals
73 that repeated in cycles from signals that did not. (And, I was also able to use a
74 mathematical formula to tell how often those cycles repeated.)

75 I then asked the question of: does it make sense for the yeast cell to make its
76 building blocks in sequence while it grows, or does it make more sense for it to
77 make all its building blocks in parallel? ~~So~~ I found a large list of equations that
78 describes all the chemical reactions that happen in yeast. Then, I solved those
79 equations to tell which of these reactions happen the most when the cell has
80 limited resources. These equations tell me that if the yeast cell makes its building
81 blocks in sequence, it saves time, but not when it has few nutrients to grow on.

too long

82 To summarise, my thesis shows that each yeast cell generates its YMC on its
83 own and how it does so depends on which nutrients they grow on. My results
84 were different from studies based on large cultures. So, to explain both kinds of
85 results, I think there are groups of cells in the large culture that behave differently.

too long

86 Furthermore, my thesis shows how people can use algorithms to help analyse large
87 amounts of time-dependent data. These algorithms will be useful for studying
88 things other than baker's yeast.

Abstract (Thai)

Nice

วัฏจักรเมtabolism ในยีสต์ (ภาษาอังกฤษ: "yeast metabolic cycle" หรือตัวย่อ YMC) เป็นวัฏจักรทางชีวภาพในยีสต์ ทำขั้นปั่ง (*Saccharomyces cerevisiae*) ในวัฏจักรนี้ ความเข้มข้นกับสถานะเริ่ดออกซ์ของเมtabolite และระดับกรดไฮบินิวคีอิกภายในเซลล์มีจังหวะซึ่งลง มีการแบ่งปั่งเวลาในการสังเคราะห์สารในเซลล์ และการใช้ออกซิเจนเมจังหวะซึ่งลงที่สังเกตได้จากอุปกรณ์เคมีสแตท (chemostat)

โดยส่วนมาก การศึกษาวัฏจักรเมtabolism ในยีสต์ใช้เคมีสแตทเป็นเครื่องมือ จึงไม่เป็นที่ชัดเจนว่าวัฏจักรเมtabolism ในยีสต์เกิดจากปฏิกิริยาพันธุ์ระหว่างเซลล์หรือถูกสร้างอย่างเป็นอิสระในแต่ละเซลล์ วิทยานิพนธ์นี้จึงมุ่งแสดงคุณลักษณะของวัฏจักรเมtabolism ในยีสต์ในเซลล์เดียวและมุ่งศึกษาผลตอบสนองของวัฏจักรนี้ต่อการเปลี่ยนแปลงของสารอาหารและสารพันธุกรรม โดยเฉพาะ ข้าพเจ้าใช้เครื่องมือไมโครฟลูอิดิกส์ (microfluidics) เพื่อดักและแยกเซลล์ยีสต์ และวัดความเรืองแสงของฟลาวิน (flavin) ตามกาลเวลา เป็นการผ่านสังเกตวัฏจักรเมtabolism ในยีสต์

ไมโครฟลูอิดิกส์เซลล์เดียวสร้างข้อมูลอนุกรมเวลาเป็นจำนวนมาก เนื่องจากอนุกรมเวลาที่สร้างโดยการทดลองเชิงชีววิทยา มีลักษณะสั้นและมีสัญญาณรบกวน เครื่องมือทางคอมพิวเตอร์ที่สามารถใช้ในการวิเคราะห์จุดที่สำคัญจากการทดลอง ดังนั้นข้าพเจ้าพัฒนาวิธีกรองอนุกรมเวลา พัฒนามาโดยใช้ปัญญาประดิษฐ์เพื่อแยกและอนุกรมเวลาที่มีจังหวะช้า และพัฒนาวิธีสัมพันธ์เชิงอนุกรมเพื่อประเมินความถี่ของจังหวะในข้อมูลอนุกรมเวลา

ผลการทดลองของข้าพเจ้าแสดงให้เห็นว่าเซลล์ยีสต์แสดงความเรืองแสงของฟลาวินเป็นจังหวะ คู่ขนานกับวัฏจักรการแบ่งตัวของเซลล์ โดยในสภาพกลุ่มสูงประชากรเซลล์สร้างจังหวะนี้อย่างไม่พร้อมกัน ข้าพเจ้าแสดงให้เห็นว่าเซลล์สามารถตั้งเฟสของวัฏจักรเมtabolism ในแหล่งมีสารอาหารเปลี่ยนแปลงอย่างกะทันหัน และอย่างเป็นอิสระจากวัฏจักรการแบ่งตัวของเซลล์ นอกจากนี้ข้าพเจ้าแสดงให้เห็นว่าพันธุ์เซลล์ที่เกิดจากการตัดยืนมีจังหวะการเรืองแสงของฟลาวินที่มีพฤติกรรมที่แตกต่างจากจังหวะของความเข้มข้นของออกซิเจนในเคมีสแตท

ข้าพเจ้าใช้ flux balance analysis เพื่อตอบคำถามว่าข้อจำกัดในโปรติโอมนำไปสู่ความได้เปรียบของการแยกเวลาการสังเคราะห์สารในเซลล์หรือไม่ และตอบคำถามว่าการแยกเวลาการสังเคราะห์สารนี้สามารถอิบายระยะเวลาของวัฏจักรเมtabolism ได้หรือไม่ ผลการศึกษาของข้าพเจ้าแสดงให้เห็นว่าข้อจำกัดในโปรติโอมนำไปสู่การแยกเวลาการสังเคราะห์สารในเซลล์เนื่องจากการแยกเวลาซึ่งยั่งระยะเวลาการสังเคราะห์สารในเซลล์โดยรวม แต่ทว่าความได้เปรียบนี้ลดต่ำลงหากแหล่งพลังงานมีปริมาณต่ำ

กล่าวโดยสรุป วิทยานิพนธ์นี้ยืนยันว่าจังหวะการเรืองแสงของฟลาวินถูกสร้างโดยอิสระในเซลล์ และเสนอว่าวัฏจักรเมtabolism ในยีสต์ตอบสนองต่อสภาพสารอาหารแล้วกำหนดเวลาการแบ่งตัวของเซลล์ วิทยานิพนธ์นี้เน้นว่ากลุ่มเซลล์ย่อยในการเพาะเลี้ยงเซลล์อาจอิบายผลการสังเกตวัฏจักรเมtabolism ในยีสต์ในเคมีสแตท นอกจากนี้วิทยานิพนธ์นี้ปูทางสำหรับการใช้วิธีทางคณิตศาสตร์ในการวิเคราะห์ข้อมูลอนุกรมเวลาขนาดใหญ่ ซึ่งมีประโยชน์กับสาขาวิชาอื่นนอกจากวัฏจักรเมtabolism ในยีสต์

Acknowledgements

95 This work would not have been possible without the support of many people and
96 organisations.

97 I would like to thank the financial support provided by School of Biological
98 Sciences, University of Edinburgh, and the Edinburgh Global Scholarship.

99 I would like to express my deepest gratitude towards my supervisors Dr Diego
100 Oyarzún and Prof Peter Swain for the unique opportunity of joining two research
101 teams, and for creating such a great environment for me to learn and work in
102 Edinburgh. I am also very grateful your advice, patience, and mental support –
103 especially in the very isolating days of the COVID-19 pandemic.

104 I am most grateful for Dr Kevin Correia for his mentorship in the early parts of
105 my PhD: especially teaching me how to ask questions, bringing in laboratory
106 best practices from his experience, and even philosophical insights in science and
107 life.

108 I am very grateful for the main software developers of the Swain lab: Dr Julian
109 Piesch, Dr Ivan Clark, Dr Diane Adjavon, and Dr Alán Muñoz Gonzalez. I would
110 like to thank Julian in particular for his patience as I grasped the ropes of the
111 old software pipeline. Thank you, Diane and Alán, for including me in your
112 very ambitious project to re-write the pipeline – this was an immense learning
113 experience for me. Alán – we've been through thick and thin, and I'm most
114 grateful to have you as a partner in crime (?), and for doom emacs too.

115 I am very grateful for Dr Ivan Clark and Iseabail Farquhar for imparting their
116 wet-lab expertise and their patience during my experiments. Ish, I'd like to thank
117 you for your patience and perseverance training me CRISPR during the chaotic
118 times of the COVID-19 lockdown.

119 I would also like to thank my other colleagues at the Swain Lab: Dr François
120 El-Daher, Dr Julien Hurbain, Dr Nahuel Manzanaro Moreno, Dr Yu Huo, and
121 Sofía Esteban Serna.

122 I would like to thank my colleagues at the Biomolecular Control Group for
123 creating a fantastic social environment and continuously sparking ideas. I am
124 grateful for Dr Vanessa Smer-Barreto and Dr Babita Verma for their mentorship
125 and feedback on my research. I would like to thank Dr Mona Tonn and Denise
126 Thiel for our weekly movie nights and continued moral support. And I would like
127 to thank Evangelos Marios-Nikolados for a great collaboration opportunity, and
128 (too) regular pub nights. Let's drink to health!

129 I would like to thank my friends from university – Christos Nicolaou, Esther Ng,
130 Patawee Jintana, among others – for their moral support. I would like to extend
131 special thanks to my best friends Jessica Wang and Maetavee Asavabhokhin for
132 their unwavering emotional and moral support during all ups and downs. And I
133 would also like to thank my high school friends, scattered across the globe, Attawit
134 Chaiyaroj, Paloch Vasudhara, and Dr Pravarit Athiprayoon for their support too.

135 Last but not least, I would like to thank my family. I express my deepest gratitude
136 for my parents who have taught me the wonder of science, the importance of
137 education, and the value of working hard. None of this would have been possible
138 without you. Aunt Pinnapa, I now have a PhD! And lastly, I thank my brother
139 Arun Wongprommoon and cousin Pornsom Ruengpirasiri for their continuous
140 support in this long journey.

Declaration

143 I declare that this thesis was composed by myself, that the work contained herein
144 is my own except where explicitly stated otherwise in the text, and that this work
145 has not been submitted for any other degree or professional qualification except
146 as specified.

148 **Arin Wongprommoon**

Contents

¹⁵²	Abstract	iii
¹⁵³	Lay Summary	v
¹⁵⁴	Abstract (Thai)	vii
¹⁵⁵	Acknowledgements	viii
¹⁵⁶	Declaration	x
¹⁵⁷	Figures and Tables	xvi
¹⁵⁸	1 Introduction	1
¹⁵⁹	1.1 Biological rhythms	2
¹⁶⁰	1.1.1 Biological basis of biological rhythms	2
¹⁶¹	1.1.2 Mathematical basis of biological rhythms	7
¹⁶²	1.2 Yeast metabolic cycle	10
¹⁶³	1.2.1 Definition and description of the yeast metabolic cycle . . .	10
¹⁶⁴	1.2.2 Yeast metabolic cycles under perturbations	17
¹⁶⁵	1.2.3 Modelling the yeast metabolic cycle	22
¹⁶⁶	1.2.4 Big picture/Hypothesis	25
¹⁶⁷	1.2.5 Disputes and unresolved questions	26
¹⁶⁸	1.2.6 Implications of the metabolic cycle	32
¹⁶⁹	1.3 Flavins and flavoproteins	36
¹⁷⁰	1.3.1 Introduction to cellular autofluorescence	36

CONTENTS

xii

171	1.3.2 Biochemical basis of flavins and flavoproteins	36
172	1.3.3 Flavins and flavoproteins in the yeast metabolic cycle . . .	42
173	2 Methods	45
174	2.1 Laboratory methods	45
175	2.1.1 Strains and media	45
176	2.1.2 Single-cell microfluidics	47
177	2.2 Image analysis methods	49
178	2.3 Computational methods	50
179	2.3.1 Classical periodogram	50
180	2.3.2 Autoregressive model	51
181	2.3.3 Precision and recall	53
182	2.3.4 Cross-correlation function	54
183	2.3.5 Synthetic oscillations	55
184	2.3.6 Signal-to-noise ratio	57
185	3 Microfluidics and fluorescence microscopy for cellular metabolic cycles	59
186	3.1 Coupled oscillations in permissive conditions	61
187	3.2 Decoupling between the metabolic and cell division cycles	67
188	3.3 Metabolic cycles in different genetic backgrounds	71
189	3.4 Metabolic cycles in different carbon sources	74
190	3.5 Metabolic cycles persist in potassium-deficient media	79
191	3.6 Metabolic cycles in deletion strains	84
192	3.7 Discussion	88
193	3.7.1 Interpretation of results	88
194	3.7.2 Study caveats and future directions	91
195	4 Analysis of oscillatory time series in the yeast metabolic cycle	94
196	4.1 Analysing time series in a biological context	95

197	4.2 Data cleaning: filtering out long-term trends	97
198	4.3 Visualising groups in the dataset	99
199	4.3.1 UMAP	100
200	4.3.2 Graph-based clustering	101
201	4.4 Detection of rhythmicity	107
202	4.4.1 Rhythmicity detection using spectral methods	107
203	4.4.2 Rhythmicity detection using model fitting	110
204	4.4.3 Rhythmicity detection using machine learning	112
205	4.5 Period estimation using the autocorrelation function	116
206	4.5.1 Effect of noise parameters on the autocorrelation function of synthetic sinusoids	116
207	4.5.2 FitzHugh-Nagumo oscillator: effect of oscillation shape .	121
208	4.5.3 Real data <i>from XXX</i>	122
209	4.6 Detection of synchrony	124
210	4.6.1 Synthetic data	124
211	4.6.2 Real data <i>from XXX</i>	124
212	4.7 Discussion	127
213	 	
214	5 Modelling yeast biosynthesis strategies under constraints	130
215	5.1 Introduction to flux balance analysis	131
216	5.2 Modelling temporal scheduling of biosynthesis	133
217	5.3 The Yeast8 and ecYeast8 models and their formalisms	135
218	5.3.1 GECKO	137
219	5.3.2 Computing molecular weights of pseudometabolites	141
220	5.4 Ablating pseudometabolites from the biomass reaction	142
221	5.4.1 Definition of ablation	142
222	5.4.2 Effect of ablation on allocation of proteome to enzymes .	144
223	5.5 Estimating timescale of biosynthesis	148

224	5.6 Effect of restricting the enzyme pool	153
225	5.7 Effect of carbon and nitrogen sources	153
226	5.7.1 Saturation of exchange reactions	155
227	5.7.2 Effect of carbon and nitrogen sources on biomass synthesis strategies	157
229	5.7.3 Relationship between proteome allocation and resource al- location strategy	163
231	5.8 Discussion	169
232	6 Conclusions	173
233	6.1 Microfluidics and fluorescence microscopy for cellular metabolic cycles	174
235	6.2 Analysis of oscillatory time series in the yeast metabolic cycle .	175
236	6.3 Modelling yeast biosynthesis strategies under constraints	177
237	6.4 Summary and broader context of thesis	178
238	Appendices	
239	A Time series	180
240	A.1 catch22 features	180
241	A.2 UMAP hyperparameters	180
242	A.3 Classification pipeline	182
243	A.4 Gillespie algorithm for stochastic chemical systems	183
244	B Flux balance analysis	186
245	B.1 Modifications of chemical reactions in GECKO for non-simple cases	186
246	B.2 Computing molecular weights of pseudometabolites in ecYeast8 .	187
247	B.2.1 Carbohydrate, DNA, RNA, cofactor, and ion pseudometa- bolites	189

CONTENTS**xv**

249	B.2.2 Protein pseudometabolite	189
250	B.2.3 Lipid pseudometabolite	191
251	B.3 Mathematical explanation of the effect of restricting the enzyme	
252	pool	193

Figures and Tables

255 Figures

256 1.1	Overview of the cell division cycle	3
257 1.2	Glycolytic cycles	6
258 1.3	Phases of the yeast metabolic cycle	11
259 1.4	The yeast metabolic cycle has been described as spontaneous respi- atory cycles	11
260		
261 1.5	The yeast metabolic cycle is characterised by transcript cycling . . .	12
262 1.6	The yeast metabolic cycle seen as coordinated cycling of metabolites in the cell	12
263		
264 1.7	The yeast metabolic cycle seen as sequential scheduling of cellular processes into phases	13
265		
266 1.8	Effects of genetic perturbations on the yeast metabolic cycle	20
267 1.9	The relationship between the yeast metabolic cycle and the cell divi- sion cycle can be seen as a system of coupled oscillators	24
268		
269 1.10	Model for how sub-populations of cells may account for oscillations of dissolved oxygen observed in the chemostat	28
270		
271 1.11	Chemical structure of FMN and FAD	37
272 1.12	Simplified schematic of biosynthesis of flavins	38
273 1.13	Reference pathway for biosynthesis of riboflavin and derivatives . . .	38
274 1.14	Fluorescence spectrum of riboflavin	39
275 1.15	Flavoproteins shown by abundance	41

276	2.1	Overview of single-cell microfluidics set-up using the ALCATRAS sys- tem	48
277	2.2	Illustration of signal-to-noise ratio.	57
279	3.1	Flavin fluorescence and histone 2B levels in a single, representative FY4 HTB2::mCherry cell grown in 20 g L ⁻¹ glucose.	61
281	3.2	Engineering a fluorescent protein cassette fused to <i>HTB2</i> allows the identification of phases of the cell division cycle through monitoring changes in fluorescence of the fluorescent protein.	62
284	3.3	Mean Fourier spectrum of flavin fluorescence time series across cells. Median autocorrelation functions of flavin fluorescence and histone 2B levels time series, along with the periods of each oscillator across cells. Data are from FY4 HTB2::mCherry cells under 20 g L ⁻¹ glucose.	63
288	3.4	Heatmap showing the flavin fluorescence and budding events of each cell over time. Median flavin fluorescence signal across cells, aligned to first budding event. Median cross-correlation function between flavin and histone 2B signals. Data are from FY4 HTB2::mCherry cells in 20 g L ⁻¹ glucose.	65
293	3.5	Flavin fluorescence and histone 2B levels in a single, representative FY4 HTB2::mCherry cell. Heatmap showing the flavin fluorescence and budding events of each cell. Data are from FY4 and HTB2::mCherry cells, subject to glucose starvation.	66
297	3.6	Mean growth rate, derived from changes in the sum of estimated parent cell and bud volumes and mean cumulative number of budding events per cell of FY4 and HTB2::mCherry strains over time during the glucose-starvation experiment.	67
301	3.7	Flavin fluorescence and histone 2B levels in two sample FY4 HTB2::mCherry cells in the glucose starvation experiment.	69

303	3.8 Distributions of flavin and mCherry fluorescence over time, for the 304 glucose-starvation experiment.	70
305	3.9 Mean Fourier spectrum of flavin fluorescence time series across cells. 306 Median autocorrelation function of flavin fluorescence time series, along 307 with the periods across cells. Heatmap showing the flavin fluorescence 308 and budding events of each cell. Median flavin fluorescence signal 309 across cells, aligned to first budding event. Data are from BY4741 310 cells in 10 g L ⁻¹ glucose.	72
311	3.10 Mean Fourier spectrum of flavin fluorescence across cells. Median auto- 312 correlation function of flavin fluorescence time series, along with the 313 periods across cells. Median flavin fluorescence signal across cells, 314 aligned to first budding event. Data are from CEN.PK113-7D cells 315 in 10 g L ⁻¹ glucose.	73
316	3.11 Flavin fluorescence and histone 2B levels in a single, representative 317 FY4 HTB2::mCherry cell grown in 20 g L ⁻¹ pyruvate. Median auto- 318 correlation functions of flavin fluorescence and histone 2B levels time 319 series, along with the periods of each oscillator across cells. Median 320 cross-correlation function between flavin and histone 2B signals. Data 321 are from FY4 HTB2::mCherry cells in 20 g L ⁻¹ pyruvate.	75
322	3.12 Flavin fluorescence and histone 2B levels in a single, representative 323 FY4 HTB2::mCherry cell grown in 0.010 g L ⁻¹ glucose. Median auto- 324 correlation functions of flavin fluorescence and histone 2B levels time 325 series, along with the periods of each oscillator across cells. Data are 326 from FY4 HTB2::mCherry cells in 0.010 g L ⁻¹ glucose.	77

327	3.13 Mean growth rate, derived from changes in the sum of estimated parent	
328	cell and bud volumes of FY4 and HTB2::mCherry strains over time	
329	during the glucose-starvation experiment, for the glucose-limiting con-	
330	dition and the high glucose condition. Similarly, the mean cumulative	
331	number of budding events per cell.	78
332	3.14 Distributions of signal-to-noise ratios of flavin signals from cells in	
333	(yellow) 0.010 g L^{-1} glucose, (blue) 20 g L^{-1} pyruvate, and (orange)	
334	20 g L^{-1} glucose. Vertical axis shows probability density, computed by	
335	dividing the number of cells in each bin by the total number of cells	
336	and then by the bin width.	79
337	3.15 Decreasing extracellular potassium (K^+) concentration shortens, then	
338	under 1 mmol dm^{-3} , destroys metabolic oscillations in the chemostat.	
339	Adapted from O' Neill et al. (2020).	80
340	3.16 Flavin fluorescence and histone 2B levels in a single, representative	
341	FY4 HTB2::mCherry cell. Median autocorrelation functions of flavin	
342	fluorescence and histone 2B levels time series, along with the periods	
343	of each oscillator across cells. Data are from FY4 and HTB2::mCherry	
344	cells; autocorrelation functions only used time points from the potassium-	
345	deficient condition.	81
346	3.17 Distributions of signal-to-noise ratios of flavin signals from cells before,	
347	during, and after potassium-deficiency.	82
348	3.18 Mean growth rate, derived from changes in the sum of estimated	
349	parent cell and bud volumes and mean cumulative number of budding	
350	events per cell of FY4 and HTB2::mCherry strains over time during	
351	the potassium-deficient experiment.	82
352	3.19 Distributions of flavin and mCherry fluorescence over time, for the	
353	potassium-deficient experiment.	83

354	3.20 Flavin fluorescence levels in a single, representative <i>zwf1Δ</i> cell. Mean 355 Fourier spectrum of flavin fluorescence across cells. Median autocor- 356 relation function of flavin fluorescence time series, along with the 357 periods across cells. Median flavin fluorescence signal across cells, 358 aligned to first budding event. Distribution of signal-to-noise ratios 359 of flavin signals from cells. Data are from <i>zwf1Δ</i> (BY4741) cells in 360 10 g L ⁻¹ glucose.	85
361	3.21 Flavin fluorescence levels in a single, representative <i>tsa1Δ tsa2Δ</i> cell. 362 Overlaid Fourier spectra of flavin fluorescence across cells. Median 363 autocorrelation function of flavin fluorescence time series, along with 364 the periods across cells. Median flavin fluorescence signal across cells, 365 aligned to first budding event. Distribution of signal-to-noise ratios of 366 flavin signals from cells. Data are from <i>tsa1Δ tsa2Δ</i> (BY4742) cells in 367 10 g L ⁻¹ glucose.	86
368	4.1 Time series and Fourier spectra corresponding to a sample raw time 369 series of flavin autofluorescence, the time series processed by a high- 370 pass Butterworth filter, and the time series detrended using a moving 371 average.	98
372	4.2 UMAP embedding of a dataset of time series featurised using <i>catch22</i> . 100	
373	4.3 Grid search of UMAP hyperparameters.	102
374	4.4 Process of preparing a dataset of time series for modularity clustering. 104	
375	4.5 Pruned graph of BY4741 and <i>zwf1Δ</i> time series from the same exper- 376 iment.	105
377	4.6 Sample time series from BY4741 and <i>zwf1Δ</i> cells.	106
378	4.7 Best five time series in the <i>zwf1Δ</i> dataset and their periodograms, 379 ranked by the quality of oscillation based on the maximum power in 380 the periodogram (Glynn et al., 2006)	108

381	4.8	Worst five time series in the <i>zwf1Δ</i> dataset and their periodograms, ranked by the quality of oscillation based on the maximum power in the periodogram (Glynn et al., 2006)	109
382	4.9	ROC curve of classifier based on Glynn et al. (2006).	109
383	4.10	Sample time series, with a fitted autoregressive model computed ac- cording to Jia and Grima (2020).	111
384	4.11	Power spectra analytically derived from fitting an autoregressive model to time series can be divided into four types.	111
385	4.12	Precision and recall from five-fold cross-validation of support vector classifiers trained using different featurisation methods.	113
386	4.13	Histogram of probabilities of whether a time series in the test data set is classified as oscillatory by the SVC, and as a control, with labels randomly re-assorted to time series.	114
387	4.14	Sample time series arranged by probability that each is oscillatory, as predicted by the support vector classifier.	115
388	4.15	Sample sinusoids without noise, with Gaussian noise, and with Gillespie noise, along with their autocorrelation functions.	117
389	4.16	Illustration of the birth-death process.	118
390	4.17	Effect of death rate of Gillespie noise on the autocorrelation function.	119
391	4.18	Effect of birth rate of Gillespie noise on the autocorrelation function.	120
392	4.19	Sample FitzHugh-Nagumo oscillators with Gillespie noise, and its auto- correlation function.	121
393	4.20	Sample time series of flavin autofluorescence, its autocorrelation func- tion, and fitting exponential decay functions.	122
394	4.21	Sample time series of histone 2B abundance, its autocorrelation func- tion, and fitting exponential decay functions.	123

407	4.22 Sample sinusoid and FitzHugh-Nagumo oscillators without noise and with Gillespie noise, along with their cross-correlation functions.	125
408		
409	4.23 Sample time series of flavin autofluorescence and histone 2B abund- ance, along with the cross-correlation function.	126
410		
411	5.1 Modifications to the stoichiometric matrix of a genome-scale model that GECKO imposes	138
412		
413	5.2 Growth rates from the original model and from the ablated versions of the model	143
414		
415	5.3 $\log_2(\text{FC})$ of enzyme usage reaction flux in rounds of ablation	146
416		
417	5.4 Estimated synthesis times of biomass components, from ablation and from scaling doubling time by mass fraction.	149
418		
419	5.5 Estimated synthesis times of biomass components, for BY4741, $zwf\Delta$, and $tsa2\Delta$	152
420		
421	5.6 Effect of the size of the proteome pool available for enzymes	154
422		
423	5.7 Effect of exchange reactions on growth rate	156
424		
425	5.8 Effect of glucose and ammonium exchange rates	158
426		
427	5.9 Effect of pyruvate and ammonium exchange rates	162
428		
429	5.10 Changes in enzyme usage reaction flux and Kendall's τ -b rank cor- relation coefficient for each pair, $R_{\text{glc}} = 1.69 \text{ mmol g}_{\text{DW}}^{-1} \text{ h}^{-1}$, $R_{\text{amm}} =$	164
430		
431	5.11 Changes in enzyme usage reaction flux and Kendall's τ -b rank correl- ation coefficient for each pair, $R_{\text{glc}} = 16.89 \text{ mmol g}_{\text{DW}}^{-1} \text{ h}^{-1}$	165
432		
433	5.12 Changes in enzyme usage reaction flux and Kendall's τ -b rank cor- relation coefficient for each pair, $R_{\text{pyr}} = 3.73 \text{ mmol g}_{\text{DW}}^{-1} \text{ h}^{-1}$, $R_{\text{amm}} =$	167
434		
435	5.13 Changes in enzyme usage reaction flux and Kendall's τ -b rank correl- ation coefficient for each pair, $R_{\text{pyr}} = 8.89 \text{ mmol g}_{\text{DW}}^{-1} \text{ h}^{-1}$	168
436		

434	5.14 Measures of similarity between enzyme usage fluxes in different nutrient conditions	170
435		
436		

437 Tables

438	1.1 Roles of the most abundant flavoproteins.	40
439	2.1 Strains used in this thesis.	46
440	2.2 Composition of base minimal medium	46
441	2.3 Composition of trace metal mix	46
442	2.4 Composition of vitamin mix	47
443	2.5 Supplements to minimal media for auxotrophic strains	47
444	2.6 Confusion matrix	53
445	4.1 Confusion matrix to evaluate the performance of using the autoregressive model (Jia and Grima, 2020) to detect rhythmicity.	112
446		
447	5.1 Computed molecular weights of bulk metabolites in ecYeast8, compared to experimentally recorded biomass composition	141
448		
449	A.1 <i>catch22</i> features	181
450	B.1 Straightforward cases of computing pseudometabolite molecular weights	
451	from pseudoreactions in ecYeast8	190
452	B.2 ecYeast8 reactions that generate the fatty acid backbone metabolite	192
453	B.3 f_i values for each biomass component.	193

Chapter 1

Introduction

456 This thesis aims to understand how an organism adapts its metabolism and
457 cellular processes in response to external conditions, in the context of a biological
458 rhythm. Specifically, I use the yeast metabolic cycle (YMC) as a framework for
459 biological rhythms. My reasons are twofold: (a) biological rhythms are important
460 for coordination of responses and are present across kingdoms, (b) there are un-
461 answered questions about the mechanistic basis of the YMC and about reconciling
462 evidence from two types of experimental studies.

463 This thesis is divided into six chapters:

- 464 1. Chapter 1 discusses the background behind the yeast metabolic cycle and
465 using flavin autofluorescence as a way to monitor the yeast metabolic cycle.
- 466 2. Chapter 2 discusses the methods: single-cell microfluidics of yeast strains,
467 an automated image analysis pipeline, and time series analysis methods.
- 468 3. Chapter 3 presents results from single-cell microfluidics and fluorescence
469 microscopy to detect flavin-based metabolic cycles in yeast cells. I show that
470 the metabolic cycle and cell division cycle are autonomous and synchronise
471 in permissive conditions, while perturbations affect the relationship between
472 these two biological oscillators.

-
- 473 4. Chapter 4 discusses the analysis of oscillatory time series. Given and the
474 challenges of analysing noisy low-resolution time series, this deserves dis-
475 cussion in its own right. This chapter explores processes to visualise groups
476 in the dataset, detecting rhythmicity, period estimation, and detecting syn-
477 chrony.
- 478 5. Chapter 5 discusses using flux balance analysis to address whether pro-
479 teome constraints explain sequential scheduling of biosynthesis in the yeast
480 metabolic cycle.
- 481 6. Finally, Chapter 6 presents a conclusion based on the previous three results
482 chapters and suggests further avenues of study.

483 1.1 Biological rhythms

484 1.1.1 Biological basis of biological rhythms

485 Biological rhythms are repeating physiological or cellular processes. Biological
486 rhythms include the circadian rhythm, the cell division cycle, the glycolytic
487 cycle, and the yeast metabolic cycle. Genetic oscillators, biochemical oscillators,
488 and metabolic oscillators, all linked to a cellular redox cycle, govern biological
489 rhythms (Mellor, 2016). Biological rhythms can occur at different time scales,
490 from seconds, to ultradian cycles (more frequent than 24 hours), to circadian
491 rhythms (24 hours). Biological rhythms are important in temporally separating
492 physiological processes. This separation is instrumental in responding to external
493 conditions, including nutrient conditions, growth requirements, or the day-night
494 cycle.

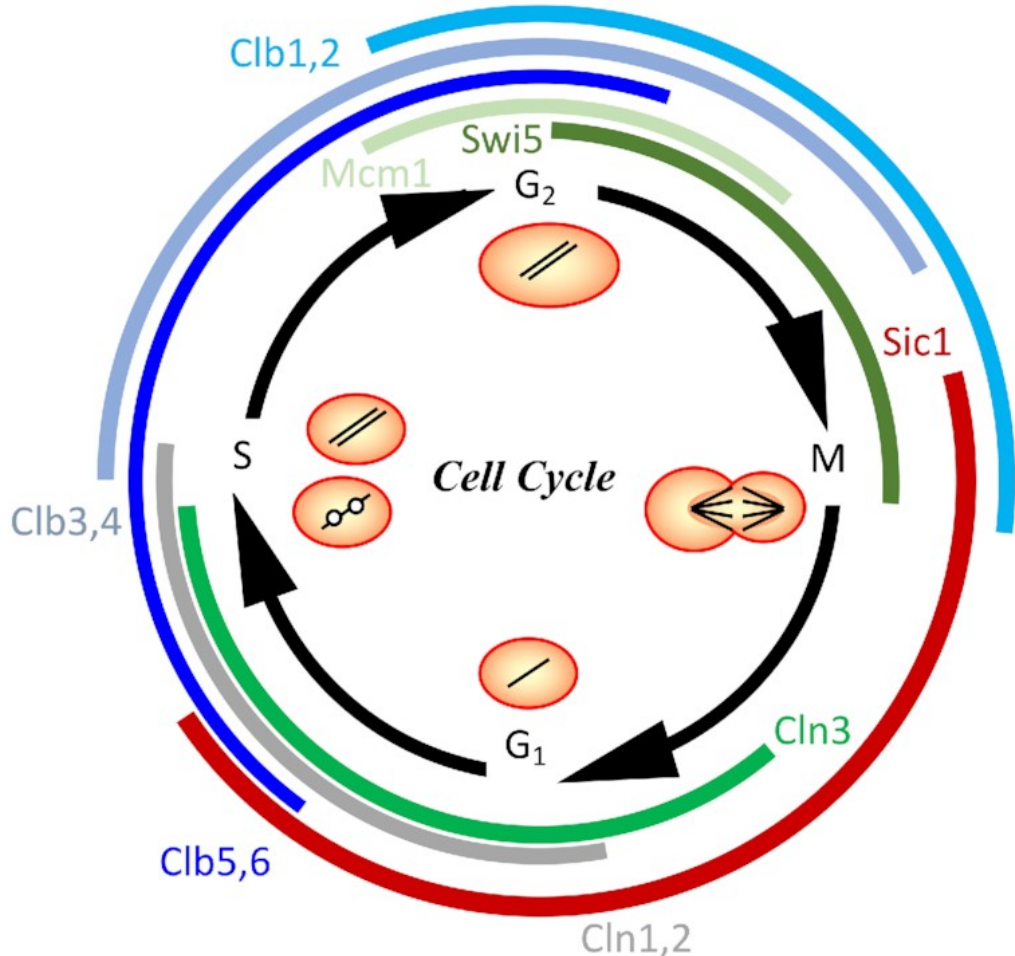


Figure 1.1: Overview of the cell division cycle in budding yeast. The cell division cycle consists of G₁, S, G₂, and M phases (black arrows). The cell expresses different cyclins (coloured curves), cell division cycle regulators, as it transitions through different phases of the cell division cycle. Adapted from Adler et al. (2022).

495 To demonstrate the definition of biological rhythm, I discuss the cell division
496 cycle, which is well-characterised, and the glycolytic cycle, which is less well-
497 characterised.

498 Cell division cycle

499 The cell division cycle is a series of cellular events that ensure that a parent cell
500 divides into two progeny cells. These events include cell growth and accumulation
501 of biomass, replication of genetic material with proofreading, and dividing the cell
502 into two compartments. In eukaryotes, the latter event consists of karyokinesis
503 (division of the nucleus) and cytokinesis (division of the cell). In budding yeast
504 (*Saccharomyces cerevisiae*), the cell division cycle is divided into the G₁, S, G₂,
505 and M phases (Fig. 1.1). In the gap phases (G₁ and G₂), the cell primarily grows
506 and accumulates biomass. The cell replicates DNA in the S phase and in the
507 M phase it conducts mitosis, in which chromosomes are segregated between the
508 progeny cells.

509 The cell division cycle is important in unicellular organisms such as budding
510 yeast because it is the mechanism by which the organism reproduces. Regulation
511 of the cell division cycle is thus important (a) because the cell must only divide
512 when necessary, (b) because the cell must have resources available for division
513 before it divides, (c) because the cell must ensure faithful replication of DNA
514 to prevent deleterious mutations in progeny cells, and (d) because the cell must
515 ensure that its components are divided equally between the two progeny cells so
516 that its progeny cells can function normally. The cell division cycle in budding
517 yeast has checkpoints between phases to ensure that biological events from the
518 previous phases are completed before the cell proceeds to the next phase. The
519 most important checkpoint is START in late G₁ phase. Upon START, the cell
520 checks whether it has the resources needed to replicate, and if requirements are
521 met, it irreversibly commits to cell division. The cell division cycle in budding
522 yeast is also governed by a series of gene regulatory networks that interact in a
523 feedback loop, resulting in oscillatory expression of cyclin-CDK complexes that

524 regulate cellular events in a temporal manner (Adler et al., 2022; Orlando et al.,
525 2008; A. W. Murray, 2004). Specifically, cyclins are proteins that sequentially
526 accumulate and are destroyed as the cell transitions through phases of the cell
527 division cycle. In budding yeast, these cyclins bind to and activate the cyclin-
528 dependent kinase (CDK) Cdc28, which is constitutively expressed. The different
529 cyclin-CDK combinations in each phase thus determines the events in the cell
530 (Adler et al., 2022):

- 531 1. In early G₁, Cln3-Cdc28 phosphorylates Whi5, leading to activation of genes
532 that regulate budding and DNA replication.
- 533 2. In late G₁, Cln1-Cdc28 and Cln2-Cdc28 hyperphosphorylates Sic1, leading
534 to activation of DNA replication which marks S phase.
- 535 3. In late S phase, Clb1-Cdc28 and Clb2-Cdc28 phosphorylates Ndd1, leading
536 to a feedback loop that activates entry into mitosis.
- 537 4. To exit mitosis, the cell activates a system to target Clb1 and Clb2 for
538 degradation.

539 To coordinate cell division and metabolism with nutrient availability, budding
540 yeast also has a system of cross-talk between nutrient signalling, growth, and the
541 cell division cycle (Ewald, 2018). The cell integrates information from nutrient-
542 sensing systems at START. In response to carbon deprivation, Cip1 delays START,
543 while Msa1/2 responds to nutrient depletion and blocks START. In addition,
544 Rim15 integrates information from the TOR and PKA pathways, which respond
545 to nutrient depletion and other stresses, and induces cell division cycle arrest.
546 Rim15 also responds to nutrient-poor conditions like non-fermentable carbon
547 sources by inducing an earlier entry into START.

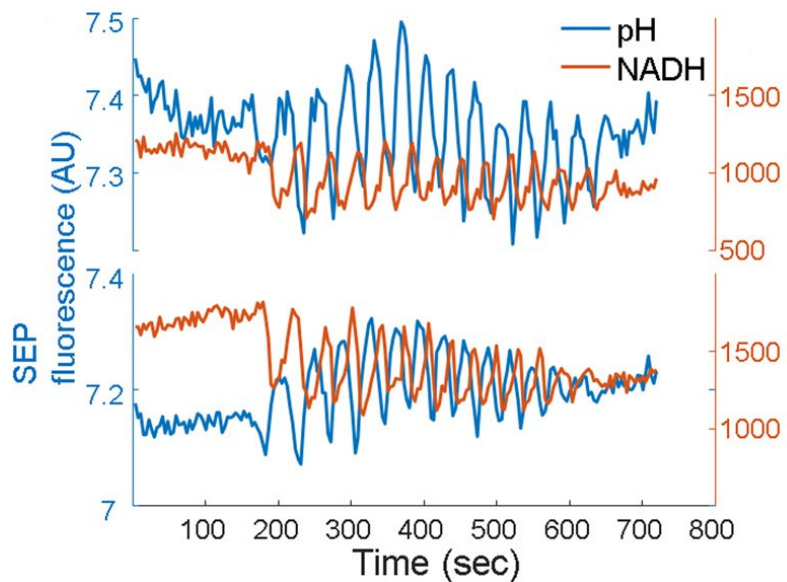


Figure 1.2: Glycolytic cycles are characterised by oscillations in NADH (orange) and pH (blue) at a period of approximately 40–50 s, and are usually highly damped. Adapted from B. J. T. Dodd and Kralj (2017).

548 Furthermore, there is also evidence that sudden starvation at other phases affects
549 cell division cycle progression, for example, through the S-phase inhibitor Sic1.
550 The cell also coordinates internal nutrient stores with the cell division cycle.
551 During S/G₂/M, Cdc28 activates the trehalase Nth1 so that the storage carbo-
552 hydrate trehalose can be liquidised to provide glucose for glycolysis (Ewald et al.,
553 2016). Additionally, during G₁/S, Cdc28 activates the lipase Tgl4 to break down
554 storage lipids (Kurat et al., 2009). There is also evidence for an additional cyclin-
555 dependent kinase, Pho85 (Huang et al., 2007), which inhibits the expression of
556 genes involved in the phosphate starvation response in high levels of environ-
557 mental phosphate (E. M. O'Neill et al., 1996), and also has roles in inhibiting
558 glycogen synthase (Wilson et al., 1999).

559 Glycolytic cycle

560 The glycolytic oscillation is a biochemical oscillator in budding yeast, character-
561 ised by damped oscillations in the levels of glycolytic intermediates at a period of
562 40–50 seconds (Ghosh and Chance, 1964). These oscillations have been observed
563 as a response to high-glucose conditions and in anaerobic conditions. Later studies
564 show that levels of NADH (Lloyd, 2019; Olsen and Lundsgaard, 2021), pH, and
565 mitochondrial membrane potential (B. J. T. Dodd and Kralj, 2017) also oscillate
566 at the same frequency (Fig. 1.2).

567 Many hypotheses have been proposed to explain the existence of glycolytic os-
568 cillations, but there is no consensus (Lloyd, 2019), though Thoke et al. (2018)
569 proposed that these oscillations are the result of cells attempting to maintain a
570 constant low-entropy state while remaining metabolically active. Evidence shows
571 that glycolytic oscillations are regulated through solely biochemical means. Spe-
572 cifically, a high ADP/ATP ratio and the presence of fructose-1,6-bisphosphate
573 activate the activity of phosphofructokinase, which then controls the flux through
574 glycolysis, forming a negative feedback loop that causes oscillations (Ghosh and
575 Chance, 1964; Higgins, 1964). Such a biochemical mechanism would explain how
576 oscillations are sustained at a short timescale.

577 1.1.2 Mathematical basis of biological rhythms

578 The mathematical modelling of biological rhythms originated in included simple
579 systems of ordinary differential equations to describe negative feedback control
580 circuits (Goodwin, 1965; Griffith, 1968). Experimental observations have then
581 informed the development of models with finer detail. Furthermore, subsequent
582 studies have modelled and synthesised artificial genetic circuits (Elowitz and
583 Leibler, 2000).

584 The well-characterised cell division cycle has inspired models with a variety of ap-
585 proaches. Early models are based on a negative feedback loop of key components
586 as identified by experimental studies. For example, Goldbeter (1991) assumed a
587 minimal model of one cyclin, one kinase, and one protease to construct a negative
588 feedback loop with a delay, giving rise to stable oscillations. Such a strategy forms
589 the basis of later models that incorporate more detail, including additional control
590 points of the cell division cycle (Chen et al., 2004), responses to perturbations such
591 as osmotic stress (Adrover et al., 2011), and relationship with other oscillators like
592 the circadian rhythm (Gérard and Goldbeter, 2012; Charvin et al., 2009; Droin
593 et al., 2019). More recent, comprehensive models include Adler et al. (2022) which
594 is based on a system of ordinary differential equations adapted for the modelling
595 to pheromone and osmotic shock responses, and Novak and Tyson (2022), which
596 models the cell division cycle as a series of switches between two stable steady
597 states whose behaviour is regulated by the CDK oscillator.

598 Models of glycolytic oscillations have less precision because the oscillation is less
599 well-characterised. Most models focus on few intermediates of glycolysis that
600 would explain the observed oscillations. Ghosh and Chance (1964) proposed a
601 simple biochemical mechanism governed by the action of phosphofructokinase,
602 dependent on the concentration of fructose-1,6-bisphosphate. Higgins (1964) then
603 tested this mechanism, by describing differential equations that model six chem-
604 ical reactions. Later, Termonia and Ross (1981) incorporated pyruvate kinase
605 kinetics and levels of AMP, ADP, and ATP as part of their kinetic model based on
606 Michaelis-Menten kinetics. Other studies focus on non-linear dynamics. Goldbeter
607 and Lefever (1972) models the product-activated phosphofructokinase reaction,
608 taking into account the allosteric nature of the enzyme. This model contains a
609 single positive feedback loop as a instability-generating mechanism in a bistability
610 model that explains oscillations. In Morán and Goldbeter (1984), the model

611 was modified to incorporate a reaction of product recycling into substrate to
612 explain birhythmicity, namely, the potential for oscillations of different am-
613plitudes. Another development of the model includes a three-variable model that
614 represents two coupled reactions each under a positive feedback loop, explaining
615 more complex oscillatory phenomena that could arise from pulsing of substrates
616 (Decroly and Goldbeter, 1982). In contrast to work that models the cell division
617 cycle, gene expression dynamics and the effects of perturbations have not been
618 incorporated in the modelling of the glycolytic cycle.

619 As biological rhythms are often coupled with each other, forced and coupled
620 oscillators have been modelled. If an oscillator is forced, it has a natural oscillation
621 frequency, but is forced from it due to an external force applied at a regular
622 interval. An example is the circadian clock, which is entrained to the light-
623 dark cycle (Goldbeter and Yan, 2022). Yeast glycolytic oscillations can also be
624 entrained via a periodic input of substrate.

625 Forced oscillators are closely linked to coupled oscillators, in which two oscillators
626 are coupled to each other by certain activation or deactivation events. Two
627 coupled oscillators tend to oscillate at a compromise frequency if the natural
628 frequencies of each are close enough to each other. Otherwise, complex oscillations
629 can occur: the oscillators lock to a rational ratio of frequencies — i.e. one oscillator
630 goes through p periods while the other goes through q periods. In this case, the
631 exact ratio depends on the ratio of the natural frequencies. Furthermore, in certain
632 cases, chaos can occur. There is a mathematical basis in Arnold tongues (Heltberg
633 et al., 2021). Experimental observations support this. For example, Charvin et
634 al. (2009) showed that externally forcing cell division cycles via glucose pulsing
635 leads to phase-locking of the cell division cycle oscillator only within a range of
636 extrinsic periods.

637 1.2 Yeast metabolic cycle

638 1.2.1 Definition and description of the yeast metabolic cycle

639 The yeast metabolic cycle is an ultradian biological rhythm which has been
640 described to entail oscillations in oxygen consumption, metabolite concentrations,
641 transcript levels, and cellular events, at the population level. This yeast metabolic
642 cycle is linked to the cell division cycle, but operates autonomously.

643 The yeast metabolic cycle is classed as a type of biological rhythm because it has
644 the properties that define a biological rhythm. Namely, it has gene-expression
645 oscillators as evidenced by transcript cycling in its phases, it has biochemical
646 oscillators as evidenced by changes in dissolved oxygen in the chemostat, and it
647 has metabolite oscillations as evidenced by changes in the levels of compounds
648 that undergo redox reactions like NADH/NADPH and flavins.



649 Phases of the yeast metabolic cycle

650 Based on chemostat studies, the YMC can be divided into two major phases:
651 an oxidative, high-oxygen consumption (OX/HOC) phase and a reductive, low-
652 oxygen consumption (RED/LOC) phase (Fig. 1.3).

653 Many authors (Slavov, Macinskas et al., 2011; D. B. Murray et al., 2011; Causton,
654 2018) use oxygen consumption rates, evidenced by the change of dissolved oxygen
655 concentrations over time, as a basis to refer to the YMC as a two-phase cycle (Fig.
656 1.4). In contrast, some authors (Machné and D. B. Murray, 2012) base their two-
657 phase model on the clustering of transcript level patterns. Krishna and Laxman
658 (2018) interpret the oxidative phase as a growth state, while the reductive phase
659 is a quiescent state.

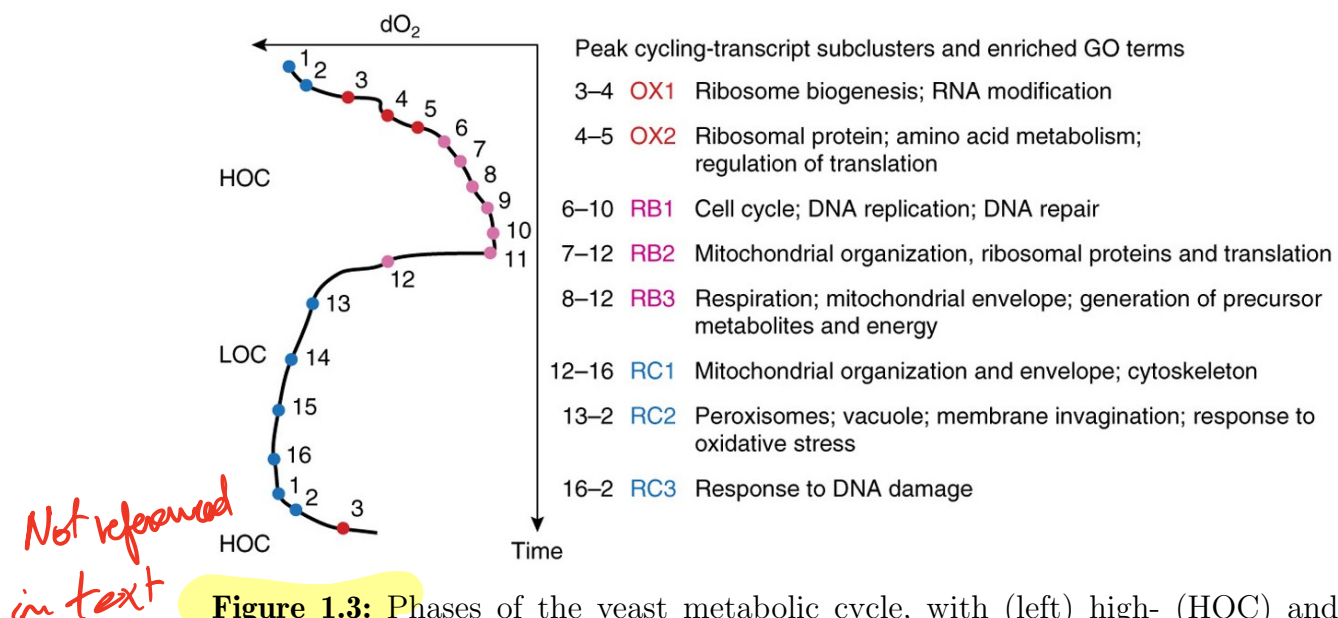
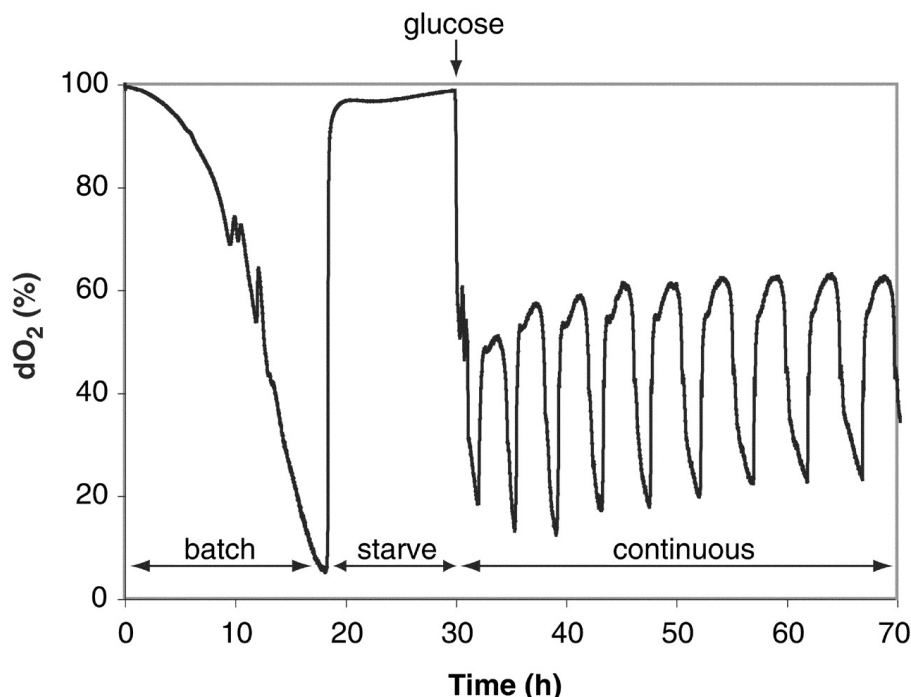


Figure 1.3: Phases of the yeast metabolic cycle, with (left) high- (HOC) and low-oxygen consumption (LOC) phases defined by changes in dissolved oxygen concentration (dO_2) over time in the chemostat and (right) oxidative (OX), reductive-building (RB) and reductive-charging (RC) phases defined by cycling of transcripts. Adapted from Mellor (2016).



→ odd
text in
between

Figure 1.4: The yeast metabolic cycle has been described as spontaneous respiratory cycles of 4–5 hours, as evidenced by regular oscillations of dissolved oxygen in the chemostat, after a starvation period. Adapted from Tu, Kudlicki et al. (2005).

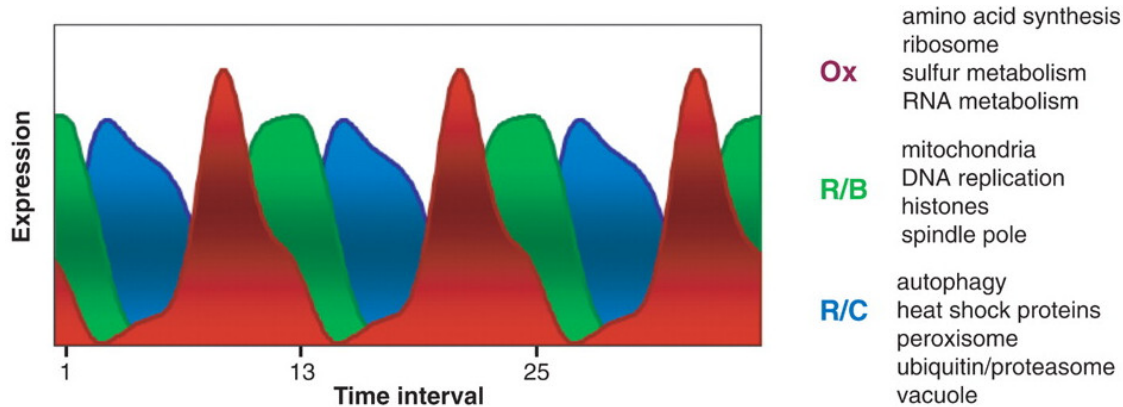


Figure 1.5: The yeast metabolic cycle is characterised by transcript cycling. Such transcripts are divided into three clusters based on their patterns and phase relationship. The peaking of these transcripts correspond to the three (OX, RB, RC) phases of the yeast metabolic cycle. Adapted from Tu, Kudlicki et al. (2005).

text to
space out
figures

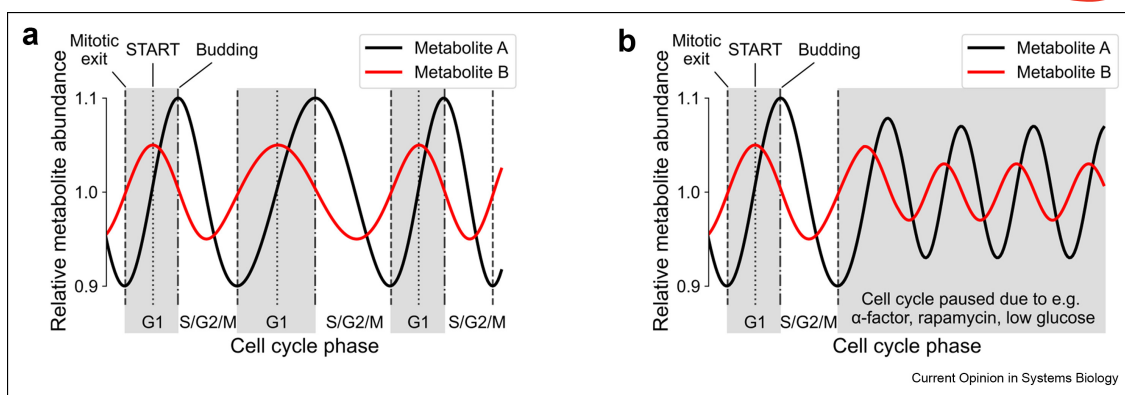


Figure 1.6: The yeast metabolic cycle seen as coordinated cycling of metabolites in the cell, generated autonomously of the cell division cycle, but are linked in permissive conditions. Adapted from Zylstra and Heinemann (2022).

- 660 In contrast to the two-phase model, some authors identify a three-phase model
 661 with a reductive-building (RB) phase and a reductive-charging (RC) phase within
 662 the reductive phase. This three-phase model is primarily based on cellular events,
 663 including clustering of transcript trajectories (Tu, Kudlicki et al., 2005) (Fig. 1.5)
 664 and of metabolite concentration trajectories (Tu, Mohler et al., 2007).

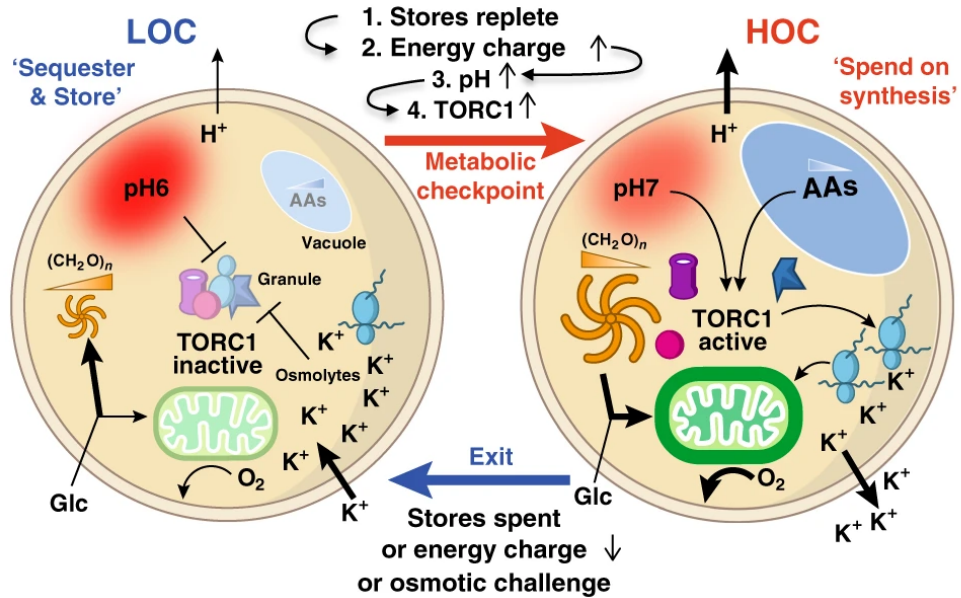


Figure 1.7: The yeast metabolic cycle seen as sequential scheduling of cellular processes into phases. Here, in the low-oxygen consumption (LOC) phase, the cell accumulates carbohydrates, amino acids, and solutes. In contrast, in the high-oxygen consumption (HOC) phase, the reverse is true: the cell uses its accumulated resources for biosynthesis and translation. Once reserves are exhausted, the cell resumes its LOC phase. Adapted from O' Neill et al. (2020).

665 Single-cell studies (Papagiannakis et al., 2017; Baumgartner et al., 2018) do not
 666 discuss phases as the single-cell microfluidic set-up does not allow live monitoring
 667 of transcription, and oxygen consumption rate can only be measured from chemo-
 668 stat cultures. Such studies define the metabolic cycle as autonomous oscillations
 669 in metabolite levels in individual cells over time (Fig. 1.6). In later chapters, I
 670 adhere to this single-cell definition because I perform a single-cell study of the
 671 yeast metabolic cycle. The two- or three-phase response may result from cellular
 672 adaptation to glucose limitation in chemostat cultures, and it is unknown whether
 673 these dynamics hold true in glucose-rich conditions, which cannot be created in
 674 a chemostat (Slavov and Botstein, 2011).

675 Cellular processes occur with the phases of the metabolic cycle (Fig. 1.7). In
676 the oxidative phase, cells consume oxygen at a high rate as respiration, fer-
677 mentation, and energy-demanding processes like biosynthesis and gene expression
678 occur. Biosynthesis and associated gene expression are confirmed by increased
679 transcripts from genes encoding components of the translation machinery and
680 amino acid biosynthesis (Tu, Kudlicki et al., 2005). ‘Redox state’ metabolites,
681 including NADH, NADPH, glutathione (Lloyd and D. B. Murray, 2005), and
682 flavins (FMN and FAD) (D. B. Murray et al., 2011) become most oxidised in
683 this phase. As cells transition from the oxidative to the reductive phase, 70% of
684 metabolite concentrations peak, when NAD(P)H autofluorescence peaks, and the
685 DNA synthesis rate is at its maximum (Lloyd and D. B. Murray, 2006).

686 In the reductive phase, cells consume oxygen at a low rate. During the reductive-
687 building phase, activities linked to mitochondrial growth occur. In the early
688 reductive-building phase, ethanol and acetate concentrations in the medium peak,
689 marking a transition from oxidative respiration to glycolytic metabolism (Tu,
690 Mohler et al., 2007). There is evidence to suggest that activities linked to cell
691 proliferation — such as initiation of the cell division cycle, DNA replication,
692 and spindle pole activity — are gated to the reductive-building phase for both
693 the short-period and long-period YMC. Such evidence includes budding activity
694 and the pattern of the expression of *YOX1*, which encodes a cell division cycle
695 repressor (Tu, Kudlicki et al., 2005).

696 Finally, during the reductive-charging phase, non-respiratory metabolism and
697 degradation processes occur to prepare the cell for the oxidative phase. This non-
698 respiratory metabolism includes glycolysis, ethanol and fatty acid metabolism,
699 and nitrogen metabolism. With these metabolic modes, under the regulation of
700 the transcription factors Msn2p and Msn4p (Kuang et al., 2017), acetyl CoA
701 accumulates so ATP can be produced in the oxidative phase (Tu, Kudlicki et al.,

702 2005). After acetyl CoA levels reach a threshold, it promotes histone acetylation
703 and thus induces the oxidative phase. These metabolic pathways also optimise
704 production of NADPH — based on the induction of *GND2* — to buffer against
705 oxidative stress in the oxidative phase. Genes associated with protein degradation,
706 ubiquitylation, peroxisomes, vacuoles, and the proteosome also peak in the
707 reductive-charging phase.

708 It has been hypothesised that gating activities linked to cell proliferation to
709 the reductive-building phase creates a temporal separation between oxidative
710 biochemical processes and the cell division cycle. This temporal separation may
711 prevent reactive oxygen species generated by oxidative process from damaging
712 DNA. However, measuring DNA content and oxygen consumption in cells grown
713 at different growth rates (Slavov and Botstein, 2011) showed that the S phase of
714 the cell cycle may occur in the oxidative phase if the cells have a slow growth
715 rate. This may be explained by the YMC gating the early and late cell cycle
716 independently, as evidenced by periodic localisation of the anaphase-promoting
717 complex and mitotic exit activator Cdc14 phosphatase in metaphase-arrested cells
718 (Y. Lu and Cross, 2010) and, conversely, the persistence of NAD(P)H cycling upon
719 arresting of the late cell cycle by depletion of Cdc14 (Papagiannakis et al., 2017),
720 all observed in single cells. This evidence indicates that the gating between the
721 YMC and the cell cycle is flexible. Although there is no consensus on the function
722 of such flexible gating, gating can aid the allocation of metabolites to different
723 temporal phases of both cellular oscillators.

724 History of evidence for the yeast metabolic cycle

725 Aspects of the YMC have been observed over decades. Nosoh and Takamiya
726 (1962) discovered that synchronised *S. cerevisiae* cultures show oscillatory oxygen
727 consumption. Kaspar von Meyenburg (1969) showed that gas metabolism and
728 energy generation increase upon budding, while Mochan and Pye (1973) described
729 a high-amplitude respiratory oscillation following a substrate shift from glucose
730 to ethanol. Satroutdinov et al. (1992) were the first to describe the metabolic
731 components of a 40-minute YMC for cells in continuous culture. Tu, Kudlicki
732 et al. (2005) first incorporated transcript cycling in the description of the YMC
733 and defined the YMC events based on a chemostat-based investigation of growth
734 of budding yeast on glucose-starved conditions.

735 The yeast metabolic cycle is longer and is more robust than a similar biological
736 oscillator, the glycolytic oscillation. The glycolytic oscillation has a period of
737 approximately 40 seconds (Olsen, Andersen et al., 2009). In contrast, the yeast
738 metabolic cycle has been described, using various definitions, to either exhibit
739 a 40-minute short-phase cycle (Lloyd and D. B. Murray, 2005; C. M. Li and
740 Klevecz, 2006; Lloyd and D. B. Murray, 2007), or a long-phase cycle, which is
741 most commonly described to be 4–5 hours (Tu, Kudlicki et al., 2005; Tu, Mohler
742 et al., 2007), but also ranges between 1.4 hours to 14 hours, depending on the
743 chemostat dilution rate (Beuse et al., 1998). Glycolytic oscillations are highly
744 damped, but yeast metabolic oscillations are robust, lasting for weeks (Lloyd
745 and D. B. Murray, 2007). Additionally, glycolytic oscillations have been observed
746 in anaerobic conditions (Lloyd, 2019), but yeast metabolic cycles have been ob-
747 served in aerobic conditions. Moreover, glycolytic oscillations are characterised by

748 fluctuations in NADH fluorescence and glycolytic intermediates. However, yeast
749 metabolic cycles consist of fluctuations in NADH fluorescence, flavin fluorescence,
750 and ATP concentrations as well as biosynthetic intermediates in TCA cycle,
751 amino acid, and nucleic acid metabolism (Tu, Mohler et al., 2007).

752 **1.2.2 Yeast metabolic cycles under perturbations**

753 Perturbations in growth conditions can affect the length of the metabolic cycle
754 and its relationship with other cellular events. The long-phase cycle may vary
755 from 1.4 to 14 hours (Causton, 2018). The main nutrient perturbations that have
756 been studied are perturbations in carbon sources and in nitrogen sources.

757 **Perturbations in growth conditions**

758 Perturbations in carbon sources are well-documented. Lower glucose concentra-
759 tions prolong the metabolic cycle, as evidenced by both chemostat studies that
760 assess the effect of changing the dilution rate (Burnetti et al., 2016; O' Neill et al.,
761 2020) and by single-cell studies that assess the effect of glucose concentrations
762 in the limiting region (Papagiannakis et al., 2017). For example, decreasing the
763 dilution rate decreases the growth rate, and in turn increases the duration of
764 the oxidative phase relative to the reductive phases (Slavov and Botstein, 2011),
765 thus prolonging the metabolic cycle. This effect is pronounced in the region of
766 glucose limitation. Increasing the glucose concentration beyond a certain point
767 does not produce an effect. Additionally, several studies (Slavov and Botstein,
768 2011; O' Neill et al., 2020) show that the duration of the low oxygen consumption
769 phase increases while the duration of the high oxygen consumption phase holds
770 constant if the metabolic cycle duration increases due to these reasons.

771 Such experimental observations could by explained by models such as K. D.
772 Jones and Kompala (1999), which suggest that as the dilution rate is decreased,
773 metabolic oscillations acquire greater amplitudes and longer periods, but if it
774 is low enough, metabolism becomes entirely oxidative, and metabolic oscilla-
775 tions disappear. However, non-fermentable carbon sources like pyruvate give long-
776 duration metabolic cycles in single cells, comparable to cells under limiting levels
777 of glucose (Papagiannakis et al., 2017).

778 In addition, bulk depletion or addition of a carbon source can reset the phase of
779 the YMC. Adding a bulk carbon source such as acetate, ethanol, or acetaldehyde
780 can reset the phase of the YMC (Kuang et al., 2017; Krishna and Laxman, 2018)
781 or eliminate it (K. D. Jones and Kompala, 1999).

782 Perturbations in nitrogen sources are less well-studied. Baumgartner et al. (2018),
783 based on single-cell observations, suggest that decreasing nitrogen concentration
784 prolongs the YMC, as evidenced by longer flavin oscillations when cells are grown
785 on lower concentrations of yeast nitrogen base (YNB) media or on urea, a non-
786 preferred nitrogen source.

787 In addition, perturbations outside nutrient sources also affect the YMC. For
788 example, externally applied hydrogen peroxide, as a source of oxidative stress,
789 shifts the YMC to the oxidative phase (Amponsah et al., 2021). The oscillation
790 period is insensitive to temperatures from 25 °C to 35 °C and media pH values from
791 2.9 to 6.0 (Lloyd and D. B. Murray, 2005) — though the period of dissolved-
792 oxygen oscillations decrease as pH decreases to below 2.9 and the oscillations
793 disappear when conditions are too acidic (O' Neill et al., 2020). Additionally, the
794 dissolved-oxygen oscillations are robust to media potassium ion concentrations
795 varying between 1 and 10 mM, but disappear when the potassium concentration
796 falls below 1 mM (O' Neill et al., 2020).

797 **Genetic perturbations**

798 Although the molecular basis of the yeast metabolic cycle is not well-characterised,
799 gene deletions shed light on it. Genes that control the cell division cycle and
800 metabolism have been deleted in studies.

801 Several deletions have been shown to remove the metabolic oscillations in chemo-
802 stats: *zwf1Δ* (Tu, Mohler et al., 2007), *gsy2Δ*, and *gph1Δ* (O' Neill et al., 2020)
803 (Figs. 1.8a, 1.8b).

804 *ZWF1* codes for glucose-6-phosphate dehydrogenase and is thus responsible for
805 entry into the pentose phosphate pathway and subsequently a major source of
806 NADPH generation. Therefore, deleting this gene may impair control of cel-
807 lular redox. However, because of its role, this gene deletion impairs adapting
808 to oxidative and pH stress and also causes methionine auxotrophy, so it may
809 be difficult to draw conclusions from this deletion in particular. Furthermore,
810 Idp2p and Ald6p catalyse reactions that generate NADPH and have shown to
811 compensate for the loss of *ZWF1* when cells are grown on lactate plates or on
812 liquid cultures with glucose as the carbon source (Minard and McAlister-Henn,
813 2005). This observation therefore raises the question of just how important *ZWF1*
814 is to the yeast metabolic cycle, and to what extent is NADPH generation needed
815 for control of cellular redox.

816 On the other hand, *GSY2* has a role in glucose storage and *GPH1* has a role in
817 glycogen mobilisation. The absence of dissolved oxygen cycles in the associated
818 deletions thus suggests that cycling of carbohydrate stores may be needed for
819 the function of the metabolic cycle. However, metabolic oscillations have been
820 observed in high-glucose conditions (Papagiannakis et al., 2017; Baumgartner et

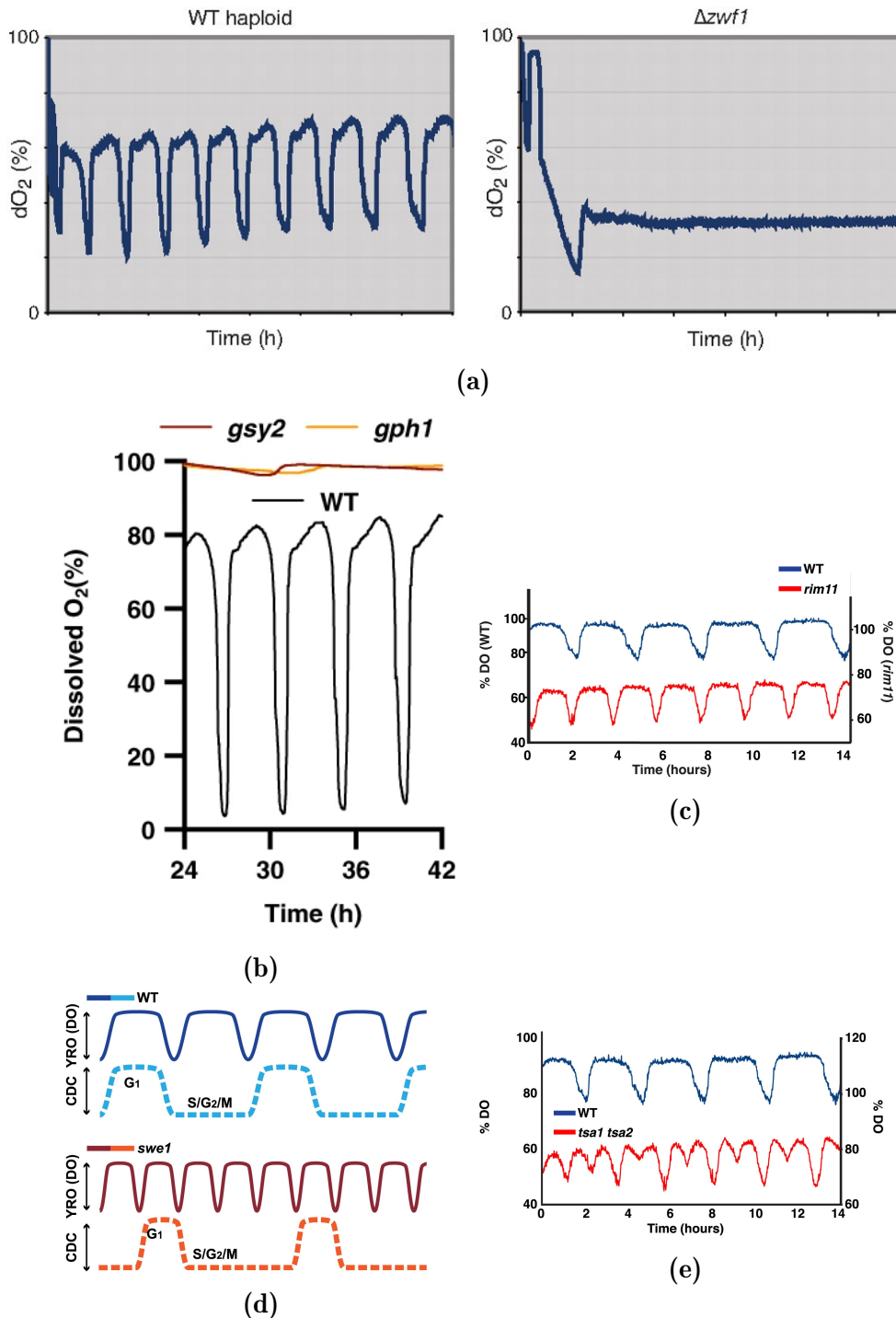


Figure 1.8: Effects of genetic perturbations on the yeast metabolic cycle, as evidenced by the dissolved oxygen cycles of deletion strains observed in the chemostat. **(1.8a)** $zwf1\Delta$ shows no dissolved oxygen cycles. Adapted from Tu, Mohler et al. (2007). **(1.8b)** $gsy2\Delta$ and $gph1\Delta$ show no dissolved oxygen cycles. Adapted from O' Neill et al. (2020). **(1.8c)** $rim11\Delta$ shows shorter dissolved oxygen cycles. Adapted from Causton et al. (2015). **(1.8d)** $swe1\Delta$ shows shorter dissolved oxygen cycles and a modified coupling ratio between the metabolic and cell division cycle oscillators. Adapted from Causton et al. (2015). **(1.8e)** $tsa1\Delta$ $tsa2\Delta$ shows dissolved oxygen cycles of a different shape. Adapted from Causton et al. (2015).

al., 2018) in which glycogen synthesis is repressed. These observations therefore suggest that glycogen cycling may play a more minor role in defining the yeast metabolic cycle and another nutrient cycling phenomenon may be more responsible.

In addition, *MSN2* and *MSN4* have been shown to regulate acetyl CoA accumulation in the reductive-charging phase, as evidenced by the lack of YMCs in deletion strains (Kuang et al., 2017). This observation suggests that genes involved in signalling pathways also play an important role in the integrity of the metabolic cycle.

Additionally, other deletions have been shown to change the frequency or shape of dissolved oxygen cycles. Causton et al. (2015) provide several examples, of which I discuss *rim11Δ*, *swe1Δ*, and *tsa1Δ tsa2Δ*.

Rim11p is the yeast homolog of the GSK3 β serine/threonine kinase, which regulates metabolism and plays a role in setting the speed of the circadian clock. The *RIM11* deletion has been shown to give shortened periods of dissolved-oxygen metabolic cycles in the chemostat, thus pointing towards a common mechanism for both biological oscillators (Fig. 1.8c).

Swe1p is a conserved cell division cycle regulator that functions at the G2/M checkpoint and has roles in coupling the cell division cycle with the circadian rhythm. Deleting *SWE1* also resulted in shortened periods of dissolved-oxygen metabolic cycles but with the same rate of DNA replication, suggesting a dysregulation in the coupling between the yeast metabolic cycle and the cell division cycle (Fig. 1.8d).

844 Tsa1p and Tsa2p are paralogous cytoplasmic thioredoxin peroxidases that cooper-
845 ate in the peroxiredoxin-thioredoxin system to eliminate reactive oxygen species
846 and have been shown to be a marker for circadian rhythms. A double deletion
847 of the two genes still results in metabolic cycles, but with an additional burst in
848 high oxygen consumption during what would otherwise be the reductive-charging
849 phase, showing that the peroxiredoxin-thioredoxin system is instrumental in the
850 integrity of the yeast metabolic cycle (Fig. 1.8e). In addition, Ampsonah et al.
851 (2021) show the presence of cycling peroxiredoxin oxidation during the YMC
852 using chemostat-based studies, with a corresponding cycling of hydrogen peroxide.
853 They also confirm that inactivating peroxiredoxins disrupts the metabolic cycle
854 and decouples it from the cell division cycle, through inducible degradation of an
855 additional cytosolic peroxiredoxin Ahp1p.

856 Taken together, these deletion studies show that regulators of other biological
857 rhythms and of redox metabolism play a role in the regulation of the YMC.
858 However, few genetic perturbation studies have been attempted in single-cell
859 studies. The most significant is in Baumgartner et al. (2018), in which by deleting
860 genes (*atp5Δ*, *cyt1Δ*) required for respiration, they showed that metabolic cycling
861 does not require respiration.

862 1.2.3 Modelling the yeast metabolic cycle

863 Mathematical models have been developed to explain the aspects of the YMC. An
864 early model is K. D. Jones and Kompala (1999) which uses differential equations
865 to simulate dynamic competition between three modes of metabolism: fermenta-
866 tion, glucose oxidation, and ethanol oxidation. This model predicts spontaneous
867 generation of oscillations in dissolved oxygen, cell mass, and storage carbohydrates
868 in continuous cultures. This prediction is consistent with chemostat-based studies
869 of the yeast metabolic cycle. Furthermore, the model predicts that, within a

870 window of dilution rate values, if the dilution rate decreases, then the dissolved
871 oxygen oscillations increase in amplitude and period. The increase in period agrees
872 with experimental studies such as O' Neill et al. (2020). However, the model also
873 predicts oscillations in the extracellular concentrations of glucose and ethanol.
874 In theory, such oscillations can only occur if there is a nutrient-consuming prey
875 species that is in turn consumed by two competing predators, or if there are two
876 competitors and an inhibitor added to the chemostat that inhibits only one of
877 the competitors (Smith and P. Waltman, 1995).

878 Krishna and Laxman (2018) use a frustrated bistability model to describe a
879 relaxation oscillator that explains how a population of yeast cells switches between
880 quiescent and growth states when faced with a limited amount of metabolic
881 resources. This model assumes that the cells retain hysteresis of their current state
882 and posits that cells of two populations communicate through diffused acetyl-
883 CoA to sustain population-level oscillatory behaviour. Burnett et al. (2016) also
884 propose that yeast cells committed to the metabolic cycle secrete metabolites
885 that induce other cells to enter the metabolic cycle, provided that they have
886 enough storage carbohydrates. Taken together, the models provide an attractive
887 cell-to-cell signalling explanation for the population-level behaviour observed in
888 the chemostat. However, such an explanation does not explain the presence of
889 metabolic cycling in single-cell conditions in which cells are physically separated
890 and thus signalling between cells cannot occur. Though, autonomous generation
891 of metabolic cycles and synchrony of metabolic cycles in a population can each
892 arise from mechanisms that are independent of each other.

893 Based on single-cell experimental observations, Özsezen et al. (2019) use a determ-
894 inistic Kuramoto model to explain the interaction between one metabolic oscil-
895 lator and three cell cycle oscillators at different stages. The study uses growth on
896 different carbon source conditions to determine parameters that define the natural

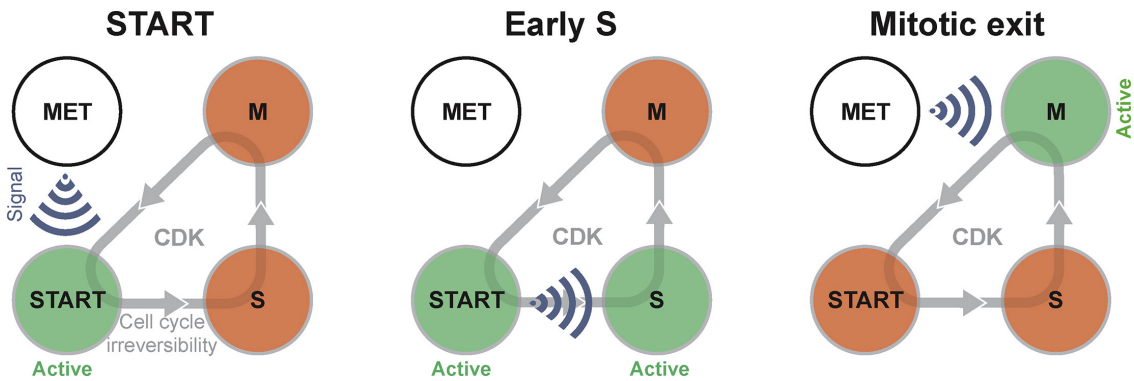


Figure 1.9: The relationship between the yeast metabolic cycle and the cell division cycle can be seen as a system of coupled oscillators. Namely, the cell division cycle is modelled as three oscillators (START, S, M), and the yeast metabolic oscillator (MET) gates entry into START and M phases, while progression from START to S is independent of the metabolic cycle. Adapted from Özsezen et al. (2019).

897 frequencies of the cell division cycle oscillators and the strength of the coupling
 898 between the four oscillators. Parameter optimisation predicts that the metabolic
 899 cycle most strongly influences the START point of the cell division cycle, and
 900 more weakly influences the M and S phases, while the three stages of the cell
 901 division cycle negligibly influence each other (Fig. 1.9). Under perturbations, the
 902 model system remains stable but shows a shift in oscillation frequency, agreeing
 903 with experimental observations, and also predicts the effects of Cdc20 and Cdc14
 904 dynamic depletions. However, a key criticism of this model-based study is that
 905 the Kuramoto model makes simplistic assumptions about the oscillators, which
 906 may be unrealistic, given how little is known about the mechanistic basis of the
 907 metabolic oscillator.

908 Taken together, modelling approaches have been able to predict some aspects of
909 the metabolic cycle. However, most models focus on specific aspects to the detri-
910 ment of other experimental observations, and none sufficiently reconcile observa-
911 tions from chemostat-based and single-cell studies. Constructing more accurate
912 models is complicated by the scant knowledge of the mechanistic basis of the
913 yeast metabolic cycle.

914 **1.2.4 Big picture/Hypothesis: a nutrient sensor than entrains the**
915 **cell division cycle?**

916 From existing evidence, we can create a big picture of the yeast metabolic cycle.
917 The yeast metabolic cycle is an autonomous biological oscillator that operates at
918 a range of frequencies in response to a range of permissive growth conditions, as
919 evidenced by how extreme conditions impair the oscillator. Based on chemostat-
920 based studies, such extreme conditions include poor nutrient quality, media being
921 too acidic, and potassium ion concentration being too low (O' Neill et al., 2020).
922 However, there is reason to believe that the metabolic oscillator can function
923 in some conditions previously deemed to be unfavourable. For example, single-
924 cell studies show that yeast cells show metabolic oscillations in high-glucose
925 conditions. Within the permissive growth conditions, different conditions affect
926 the frequency of the metabolic cycle. For example, a low concentration of glucose
927 or nitrogen source results in longer cycles, and bulk addition of certain compounds
928 can reset the phase of the metabolic cycle. These observations support the idea
929 that the metabolic oscillator includes the functionality of a nutrient sensor.

930 The observations suggest that the yeast metabolic cycle creates windows of op-
931 portunities for the cell to commit to START if conditions are favourable, for
932 example, good carbohydrate or lipid stores. Thus, this oscillator acts as a timing
933 mechanism for cellular processes, most importantly the cell division cycle and
934 biosynthetic/redox processes. The relationship between the metabolic cycle and
935 the cell division cycle is governed by the mathematical basis of coupled oscillators.
936 Most importantly, there is a small window of frequencies in which both oscillators
937 can be phase-locked, and that other, complicated relationships exist: e.g. multiple
938 metabolic cycles per cell division cycle.

939 **1.2.5 Disputes and unresolved questions with the yeast metabolic**
940 **cycle**

941 **Chemostat vs single-cell studies**

942 There is a dispute of whether the same conclusions can be drawn from chemostat-
943 based studies and from single-cell based studies. Most studies of the YMC arise
944 from chemostat experiments. Reconciling the two types of studies is difficult
945 because the readouts and conditions are different: chemostat studies produce
946 dissolved oxygen and transcript cycling readings, while single-cell experiments
947 cannot report on dissolved oxygen and chiefly report metabolite cycling. This
948 leads to differing definitions of the YMC. Some authors (Laxman et al., 2010;
949 Causton, 2018) only use the term metabolic cycle to refer to synchronised cycles
950 of dissolved oxygen concentrations observed in chemostat cultures that must have
951 gone through a starvation phase. In contrast, single-cell studies (Baumgartner et
952 al., 2018; Zylstra and Heinemann, 2022) define the metabolic cycle as metabolite
953 cycling and sequences of cellular events. This is because in such settings, the
954 cells are not synchronised by diffusible chemical signals and dissolved oxygen

concentrations cannot be measured. Additionally, these studies do not include the requirement of a starvation phase as part of their definition as they show that cell exhibit metabolite cycling even without having gone through a period of starvation.

I argue that there are three caveats to chemostat-based studies: the experimenter cannot assume that the chemostat is in steady-state, the chemostat obscures contributions from sub-populations, and the chemostat imposes glucose starvation. These caveats affect the interpretation of YMC studies.

There is a wide assumption that the chemostat is in steady-state, but it may not be true. A mathematical model shows that levels of solutes change over time (K. D. Jones and Kompala, 1999). In addition, observations of the metabolic cycle in chemostats may reflect individual cells' responses to the initial starvation imposed at the start of chemostat-based studies. The subsequent response to regularly changing media conditions could explain temporal segregation of physiological processes in phases of the YMC, and may not reflect cell-autonomous behaviour. In other words, the conditions of the chemostat may force the population of cells to behave in a certain way. However, temporal segregation of physiological process has also been reported in single-cell studies (Takhayev et al., 2023), suggesting that the cycling of solutes in the chemostat could affect some, but not all, temporal aspects of the metabolic cycle.

The chemostat obscures contribution of sub-populations of cells (Fig. 1.10). Burnetti et al. (2016) suggest that sub-populations within the yeast culture that enter the yeast metabolic cycle in a staggered manner can be responsible for the metabolic cycle and the cell division cycle appearing coupled one-to-one in the chemostat while having different periods. This proposition was information by observing one pulse of DNA replication per YMC and observing that a fraction

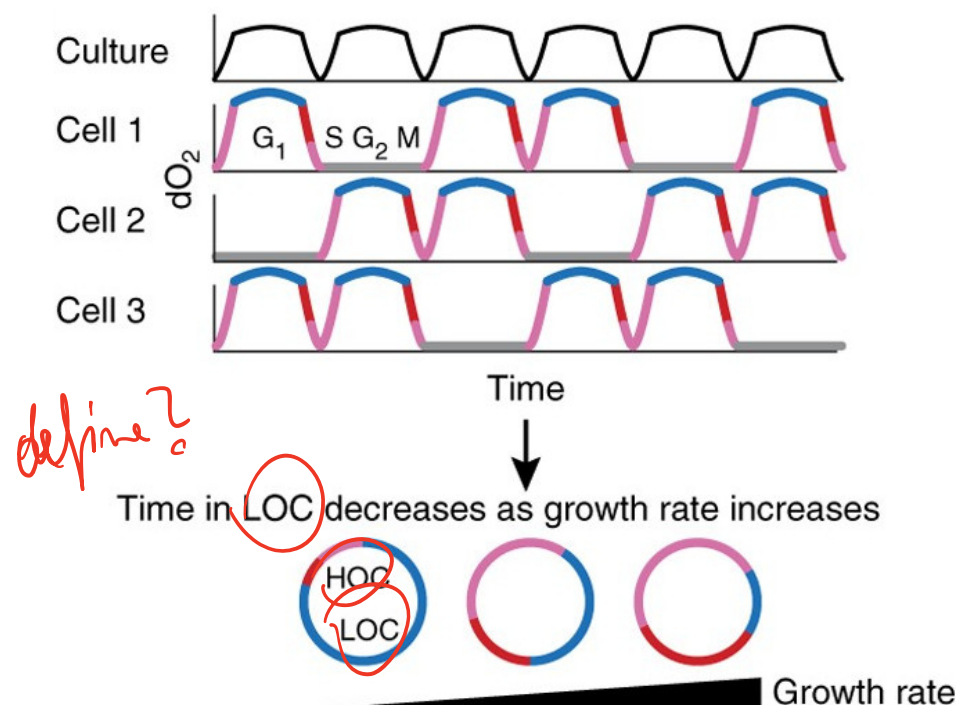


Figure 1.10: Model for how sub-populations of cells may account for oscillations of dissolved oxygen observed in the chemostat. Cells may enter the cell division cycle (pink-blue-red lines), gated by the metabolic cycle, in a staggered manner, and the combined effect of all cells may explain dissolved oxygen concentrations (black lines, top row). Adapted from Mellor (2016).

of cells that exhibit the YMC initiated cell division. Contributions from sub-populations of cells are further highlighted by Bagamery et al. (2020), who used a microfluidic platform to show that a group of genetically identical yeast cells divide themselves into two populations. Such a bet-hedging strategy results in some percentage of the population surviving in a glucose-starved or a glucose-rich condition, beneficial for long-term population survival. Taken together, it is possible that phenotypically different sub-populations in the chemostat culture may partially explain the observations in the chemostat so far.

In addition, there is the question of whether cells individually generate the metabolic cycle or is a diffusible chemical responsible for synchrony, as proposed by Krishna and Laxman (2018). Furthermore, Smith and P. Waltman (1995) show, ~~not~~, theoretically, if a chemostat has two competing species, and an inhibitor which inhibits one of the species is added, then the chemostat can generate oscillations.

In the case of the yeast metabolic cycle, the competitors can be genetically identical sub-populations of the yeast cells that have different levels of sensitivities to an inhibitor, perhaps a metabolic by-product. Bulk culture set-ups, including chemostats, are not able to address questions about cell sub-populations and autonomy of the metabolic cycle. However, single-cell set-ups may fill in such a technical gap.

Finally, the chemostat imposes glucose starvation, and single-cell studies with different carbon sources give a different picture in terms of metabolic requirements. Chemostat studies and related models suggest that glucose starvation and oxidative metabolism are required for oscillations in dissolved oxygen level that define YMCs. NAD(P)H oscillations have been recorded in non-fermentative conditions, such as pyruvate or low-glucose media (Papagiannakis et al., 2017). However, NAD(P)H (Papagiannakis et al., 2017; Özsezen et al., 2019) and flavin (Baumgartner et al., 2018) oscillations still occur in constant high-glucose condi-

1008 tions, and only within a window of periods, in contrast to the 1.4–14 hour range
1009 reported for chemostat-based studies. Furthermore, *ATP5* and *CYT1* deletions
1010 that impair oxidative respiration do not remove single-cell flavin-based metabolic
1011 oscillations (Baumgartner et al., 2018), thus giving additional evidence that ox-
1012 idative metabolism is not required for the YMC.

1013 Single-cell microfluidic studies are well-positioned to address the limitations of
1014 the chemostat, although there have been only few studies. Laxman et al. (2010)
1015 was an early attempt at using microfluidics to address the bulk vs single-cell issue.
1016 They cultured strains with fluorescent gene expression reporters for each phase
1017 (OX, RB, RC) of the metabolic cycle by transferring cells from a chemostat to
1018 a microfluidic device. The study showed that low glucose levels were required
1019 for the synchrony of metabolic cycles across cells. This study also shows the
1020 presence of quiescent cells, and then proposed that during OX phase, cells decide
1021 whether to commit to cell growth or enter a quiescent state, leading to a model
1022 of two sub-populations in the culture. However, it lacks quantitative time-series
1023 analysis; rather, it reports qualitative interpretations of fluorescence images. The
1024 microfluidic device did not truly physically separate each cell individually, thus
1025 it was unable to eliminate the possibility of cell-to-cell communication via a
1026 diffusible signalling chemical.

1027 Later microfluidics studies reveals additional features of the YMC in single cells.
1028 Papagiannakis et al. (2017) revealed that YMCs are an intrinsic feature of single
1029 cells and are autonomous with respect to the cell division cycle, based on measure-
1030 ments of the combined level of NADH and NADPH in single cells in microfluidic
1031 devices. Furthermore, by measuring flavin fluorescence in the cell, Baumgartner
1032 et al. (2018) demonstrated that YMCs persist in mutants deficient in oxidative

1033 phosphorylation, and that the cell division cycle inhibitor rapamycin desynchronizes
1034 the YMC and the cell division cycle. In sum, these single-cell studies address
1035 a small fraction of the knowledge covered by chemostat studies, and further such
1036 studies are required.

1037 **Molecular and genetic mechanisms**

1038 There are unknowns in the molecular mechanism that drives YMCs. Genome-
1039 wide transcript cycling has two superclusters that correspond to the oxidative
1040 and reductive-building phases (Machné and D. B. Murray, 2012). However, there
1041 has been no genome-wide analysis of genes that influence cycling (Mellor, 2016),
1042 though some genes seem to have key roles. As we lack proteome analysis, it is
1043 unclear how protein levels and post-translation modifications are affected.

1044 Metabolome cycling may play a role in the metabolic cycle and can explain se-
1045 quential scheduling of biosynthesis, but the evidence so far is indirect as it is based
1046 on the cell division cycle. Campbell et al. (2020) showed that lipid biosynthesis in
1047 budding yeast is periodic with the cell division cycle and peaks during S phase,
1048 as evidenced by an increase in the number of metabolites implicated in lipid
1049 metabolism in such phases, based on metabolomics analysis of prototrophic cells
1050 with synchronised cell division cycles. Ewald et al. (2016) also show that the cell
1051 division cycle machinery regulates trehalose mobilisation, showing the coupling
1052 between carbohydrate store levels and cellular oscillators. They also showed that
1053 lipid metabolism increased during S/G2/M, likely due to the synthesis of new cell
1054 membranes during bud growth, as evidenced by pathway enrichment analysis.
1055 Based on the coupling between the yeast metabolic cycle and the cell division

1056 cycle, lipid store cycling and perhaps to a lesser extent carbohydrate store cycling
1057 are likely instrumental to the yeast metabolic cycle. Though, investigation of how
1058 an impairment in lipid use affects the yeast metabolic cycle in single cells is needed
1059 to prove that such cycles are responsible for the metabolic cycle.

1060 **1.2.6 Implications of the metabolic cycle**

1061 The YMC shares regulatory mechanisms with the cell division cycle and the
1062 circadian rhythm, leading to the question of whether the metabolic cycle reflects
1063 a fundamental system. *that ...*

1064 Similar metabolic cycles have been described in other organisms. *E. coli* shows os-
1065 cillations in NAD(P)H fluorescence coupled to its cell division cycle, as evidenced
1066 by time-lapse microscopy of single cells (Z. Zhang et al., 2018). Addition of glucose
1067 or hydrogen peroxide to the medium results in global changes in autofluorescence,
1068 reflecting a response to nutrient conditions. In addition, metabolic cycles have
1069 been observed in mammalian cells. For example, Zhu (2022) describe a 12-hour
1070 metabolic cycle in liver cells that includes sequential scheduling of metabolic
1071 processes into energy homeostasis, genetic integrity maintenance processes, im-
1072 mune response, and gene expression — linking the processes to the circadian
1073 rhythm and the whole cycle to a more general 12-hour mammalian ultradian clock.
1074 Importantly, this hepatic metabolic cycle operates independently from the spatial
1075 organisation of cells in the liver, reminiscent of the cell-to-cell independence of
1076 the yeast metabolic cycle. In addition, HeLa cells with synchronised cell division
1077 have been shown to exhibit both NAD(P)H and ATP oscillations throughout the
1078 cell division cycle (Ahn et al., 2017), but the literature is conflicted about the
1079 these oscillations' dynamics across different mammalian cell types (Zylstra and
1080 Heinemann, 2022). There is reason to believe that a wide range of organisms

1081 exhibit biochemical phenomena similar to the yeast metabolic cycle, as the aims
1082 of controlling cell division to match environmental conditions along with the
1083 temporal coordination of biosynthesis and cellular redox state with cell division
1084 should be fundamental goals that apply to multiple domains of life.

1085 Metabolic oscillations may be the origins of biological timekeeping mechanisms.
1086 Lloyd and D. B. Murray (2007) assert that ultradian oscillations form the basis
1087 of longer-period biological oscillators like the circadian rhythm or the cell cycle,
1088 based on temperature compensation and sensitivity of the period. It is logical for
1089 a biological oscillation to have temperature compensation because temperature
1090 oscillates with a period of a day on most of the planet. Circadian rhythms can
1091 occur in cells of eukaryotes without transcription (J. S. O'Neill, van Ooijen et
1092 al., 2011; J. S. O'Neill and Reddy, 2011), refuting the idea that gene circuits are
1093 responsible for such rhythms. Additionally, the eukaryotic cell cycle evolved before
1094 cyclin-dependent kinases (Papagiannakis et al., 2017), so metabolic oscillations
1095 may have served to regulate the cell cycle before cyclin-dependent kinases evolved.
1096 Furthermore, YMCs share mechanisms with the circadian oscillator (Causton et
1097 al., 2015; Arata and Takagi, 2019), suggesting a common evolutionary origin.
1098 Thus, studying YMCs may shed light on the evolution of biological rhythms.

1099 A philosophical question that unites all biological oscillators is: why have oscilla-
1100 tions? The answers may differ for each type of biological oscillator.

1101 The answer is clear for circadian rhythms: circadian clocks evolved as an adapt-
1102 ation to the Earth's 24-hour rotation, and allow organisms to match biological
1103 processes that benefit from light or warmth to the time of day at which they occur
1104 (Millar, 2004). The selective advantage of such a system is highlighted by how
1105 circadian clocks of similar, negative-feedback gene circuit architectures evolved
1106 independently at least four times across kingdoms (A. N. Dodd et al., 2005).

1107 As a specific example, *Arabidopsis thaliana* plants with a clock period matched
1108 to the environment contain more chlorophyll, fix more carbon, grow faster, and
1109 survive better, as opposed to mutants with clock lengths that do not match
1110 environmental light-dark cycles (A. N. Dodd et al., 2005). The explanation is:
1111 light-harvesting complex proteins and chlorophyll are unstable in their unbound
1112 state. So, synthesising these components in sync with the light-dark cycle is
1113 advantageous for the plant. The plant can only do so with correct anticipation of
1114 dawn and dusk, and a circadian clock that matches the environmental light-dark
1115 cycle allows this to happen.

1116 The importance of coordinating the sequence of events in the cell division cycle
1117 was discussed in Section 1.1.1. Briefly, the cell division cycle is an energy-intensive
1118 and resource-intensive process that engages all compartments of the cell. In
1119 addition, maintaining genetic fidelity is important for ensuring that progeny cells
1120 are functional; therefore, cells need a robust system of tight control of the cell
1121 division cycle. The importance of the cell division cycle is highlighted by the
1122 conserved design of the cell division cycle across kingdoms. For example, cyclin-
1123 dependent kinases (CDKs) differ in their number in different organisms — one in
1124 budding yeast, but at least 11 classical CDKs in humans (Malumbres et al., 2009)
1125 — but their structure and function are conserved. The importance of linking the
1126 cell division cycle with cellular resource use is highlighted by the cell's systems
1127 of coupling the cell division cycle machinery with metabolic processes (Salazar-
1128 Roa and Malumbres, 2017). In particular, oxidative phosphorylation peaks upon
1129 S- and M-phase entry in plants and glycolysis peaks upon S-phase entry in
1130 lymphocytes. In addition, the CDKs regulate cycles of mitochondrial fusion and
1131 fission to ensure that mitochondria in the parent cell are divided to progeny

1132 cells based on their volumes. The importance of the cell division cycle control
1133 system is further highlighted by the result of impairments in the genetic control
1134 of the cell division cycle: uncontrolled cell proliferation, characteristic of cancers
1135 in multicellular organisms.

1136 The question of ‘why have oscillations?’ has been asked of the yeast metabolic
1137 cycle — specifically, why cycle metabolites and why cycle transcripts? It has
1138 been proposed that cycling of metabolites and metabolic activity serve to cre-
1139 ate ‘just-in-time’ biosynthesis of compounds when they are needed in the yeast
1140 metabolic cycle (Zylstra and Heinemann, 2022). For example, the HOC phase of
1141 the metabolic cycle is driven by the high energetic demands of protein synthesis
1142 in this phase, which is closely linked to the G₁ phase of the cell division cycle
1143 (O’Neill et al., 2020), and the evidence includes high protein synthesis rate and
1144 high ribosomal protein abundance. The rationale for cycling transcripts is less
1145 clear, however. Earlier studies propose that transcript cycling in clusters that
1146 peak according to three metabolic cycle phases reflect the metabolic demands in
1147 each phase and the translation of such transcripts lead to changes in metabolite
1148 concentrations (Tu, Kudlicki et al., 2005). However, Feltham et al. (2020) showed
1149 that although transcripts levels cycle, protein levels chiefly remain constant, but
1150 post-translational modifications cycle instead. This study then proposes that
1151 cyclic metabolic state changes cause post-translational modifications which then
1152 coordinate the metabolic cycle with cellular processes. The study therefore sug-
1153 gests that transcript cycling is effect of the metabolic cycle and have roles in the
1154 chromatin environment. Further clarification of the mechanistic basis of the yeast
1155 metabolic cycle is needed to answer the ‘why have oscillations’ question.

₁₁₅₆ **1.3 Flavins and flavoproteins**

₁₁₅₇ **1.3.1 Introduction to cellular autofluorescence**

₁₁₅₈ Cellular autofluorescence is the intrinsic fluorescence of a cell without fluorescent
₁₁₅₉ tags. It is caused by the autofluorescence of compounds that have light emission
₁₁₆₀ properties (Maslanka et al., 2018). Such endogenous fluorophores include coen-
₁₁₆₁ zymes, vitamins, and amino acids with aromatic chemical groups, flavins being
₁₁₆₂ one of them. However, autofluorescence poses a difficulty in cellular microscopy
₁₁₆₃ because its wavelengths can overlap with other fluorophores and therefore it is
₁₁₆₄ difficult to draw biochemical conclusions from the fluorescence signal alone. For
₁₁₆₅ example, flavin autofluorescence overlaps with the spectrum of the fluorescent
₁₁₆₆ glucose analogue 6-NBDG (Maslanka et al., 2018), and thus interferes with studies
₁₁₆₇ that use this analogue to study glucose uptake. Cellular autofluorescence can
₁₁₆₈ indicate of the physiology and metabolism of the cell. Autofluorescence thus offers
₁₁₆₉ an easy way to monitor cell physiology without engineering genetic constructs.

₁₁₇₀ **1.3.2 Biochemical basis of flavins and flavoproteins**

₁₁₇₁ Flavins are a group of organic compounds that share an aromatic moiety that
₁₁₇₂ allows redox reactions (Fig. 1.11). Specifically, the flavin moiety can exist in the
₁₁₇₃ oxidised, semiquinone, or reduced states. Flavins thus function as electron carriers
₁₁₇₄ in the cell.

₁₁₇₅ In *Saccharomyces cerevisiae*, flavin is present as FMN and FAD, which function
₁₁₇₆ as prosthetic groups in flavin-dependent proteins, or flavoproteins, whose genes
₁₁₇₇ account for 1.1% of the genome (Gudipati et al., 2014). FMN and FAD can be
₁₁₇₈ covalently bound to these proteins or be free (Mewies et al., 1998). FAD is a co-
₁₁₇₉ enzyme and has major roles in transferring electrons from the tricarboxylic acid

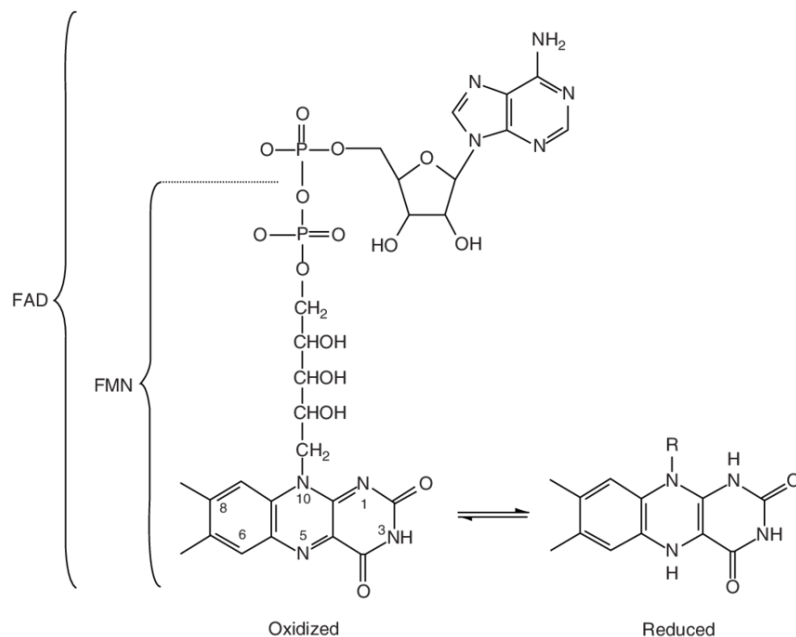


Figure 1.11: Chemical structure of FMN and FAD, with redox states of the aromatic flavin moiety shown. Adapted from Patel (2006).

cycle to the mitochondrial electron transport chain. Flavins in *Saccharomyces cerevisiae* are derived from riboflavin (Fig. 1.12). Riboflavin can be synthesised *de novo* from purine biosynthesis and the oxidative pentose phosphate pathway (Fig. 1.13). Based on the metabolism of flavins, the cell only synthesises new flavin for synthesis of FMN and FAD; therefore, monitoring of flavins monitors the combined pool of FMN and FAD in their oxidised states.

From a technical standpoint, the redox states of flavins reflect the emission and absorption of electromagnetic radiation by the flavin moiety. The redox biochemistry of flavins give rise to fluorescence, so monitoring flavin autofluorescence monitors the redox state of the cell. Flavins, in their oxidised forms (FMN and FAD), have a peak excitation frequency of ≈ 460 nm and a peak emission frequency of ≈ 535 nm (Maslanka et al., 2018; Wagnieres et al., 1998), displayed in Fig. 1.14. Comparison of *in vivo* autofluorescence in mammalian cells and the fluorescence spectrum of riboflavin in PBS confirms this fluorescence behaviour (Aubin, 1979).

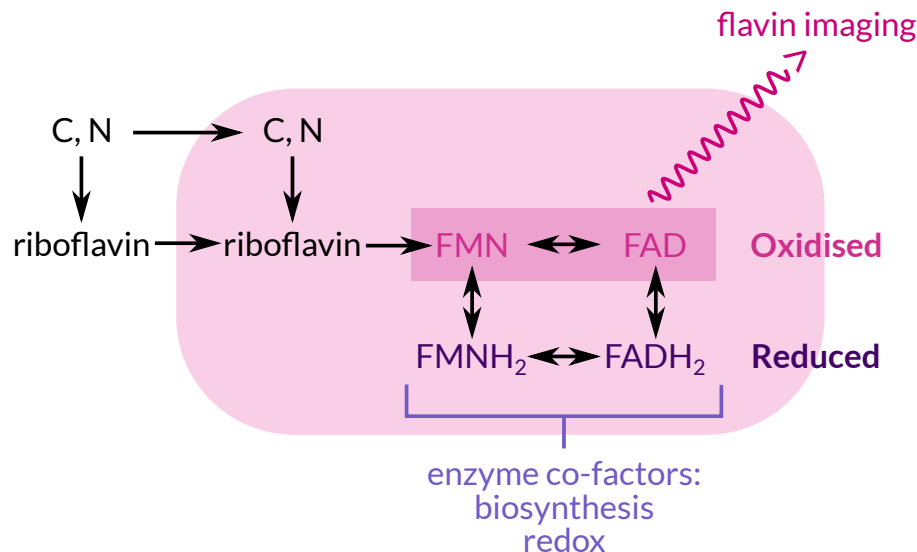


Figure 1.12: Simplified schematic of biosynthesis of flavins and detection of the oxidation states in fluorescence microscopy.

Text here

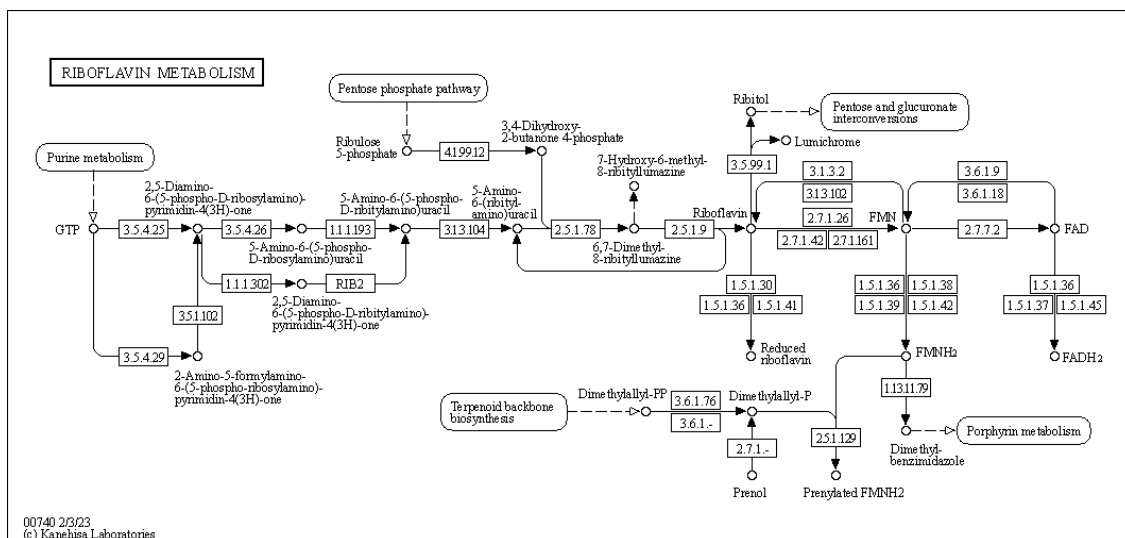


Figure 1.13: Reference pathway for biosynthesis of riboflavin and derivatives, KEGG pathway database (Kanehisa et al., 2023).

Text here

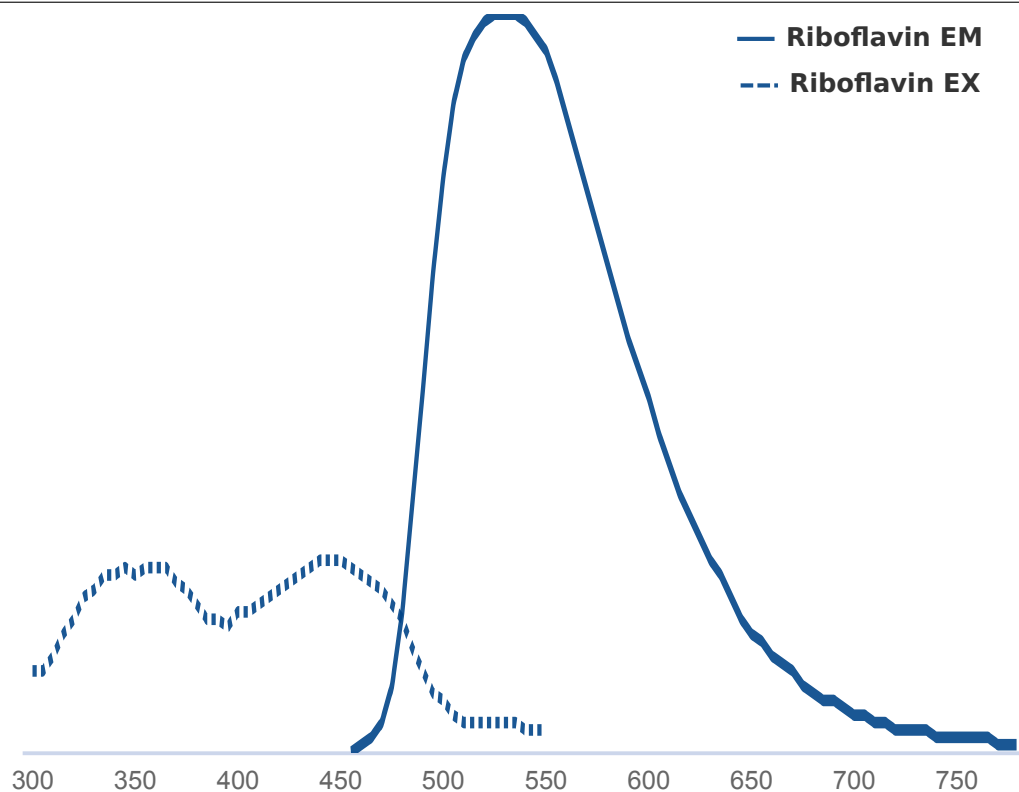


Figure 1.14: Fluorescence spectrum of riboflavin, (dotted line) excitation and (solid line) emission spectra shown, FPbase (Lambert, 2023).

¹¹⁹⁴ In contrast, the reduced forms FMNH_2 and FADH_2 have negligible fluorescence
¹¹⁹⁵ (Masters, 1994). Both chemostat-based (Sasidharan et al., 2012; D. B. Murray
¹¹⁹⁶ et al., 2011) and single-cell microfluidic studies (Baumgartner et al., 2018) have
¹¹⁹⁷ monitored flavin autofluorescence to study the YMC.

¹¹⁹⁸ **Descriptions of key flavoproteins and their roles**

¹¹⁹⁹ Gudipati et al. (2014) describe 68 genes that code for 47 flavoproteins in budding
¹²⁰⁰ yeast (Fig. 1.15). Of these, 35 require FAD, 15 require FMN, and 3 require both.
¹²⁰¹ In budding yeast, most flavins sit in the active site without covalent bonding. The
¹²⁰² biochemical and enzymatic properties of many flavoproteins are poorly charac-
¹²⁰³ terised (Koch et al., 2017).

Protein	Name	Reaction catalysed	Reference
Fas1	beta subunit of fatty acid synthetase	acetyl-CoA + malonyl-CoA + NADPH + ATP → palmitate	Singh et al. (2020)
Yhb1	nitric oxide oxidoreductase	2 NO + 2 O ₂ + NAD(P)H → 2 NO ₃ ⁻ + NAD(P) ⁺ + H ⁺	Bonamore and Boffi (2008)
Ura1	dihydroorotate dehydrogenase	dihydroorotic acid + fumarate → orotic acid + succinate	Zameitat et al. (2007)
Pst2	NAD(P)H-quinone oxidoreductase	NAD(P)H + H ⁺ + quinone → NAD(P) ⁺ + hydroquinone	Koch et al. (2017)
Trr1	cytoplasmic thioredoxin reductase	H ⁺ + NADPH + thioredoxin disulfide → NADP ⁺ + thioredoxin	Machado et al. (1997)
Ilv2	acetolactate synthase	2 pyruvate → 2-acetolactate + CO ₂	Pang et al. (2002)
Oye2	NADPH oxidoreductase	NADPH + H ⁺ + acceptor ⇌ NADP ⁺ + reduced acceptor	Odat et al. (2007)
Dld3	2-hydroxyglutarate transhydrogenase	D-2-hydroxyglutarate + pyruvate → α-ketoglutarate + lactate	Becker-Kettner et al. (2016)
Pdx3	pyridoxine phosphate oxidase	pyridoxamine 5-phosphate + H ₂ O + O ₂ → pyridoxal 5-phosphate + NH ₃ + H ₂ O	Tsuge et al. (1979)
Erg1	squalene epoxidase	squalene + H ⁺ + NADPH + O ₂ → 2,3-oxidosqualene + NADP ⁺ + H ₂ O	Satoh et al. (1993)
Lpd1	dihydrolipoamide dehydrogenase	dihydrolipoamide + NAD ⁺ → lipoamide + NADH ⁺ + H ⁺	Morrison (2021)

Table 1.1: Roles of the most abundant flavoproteins.

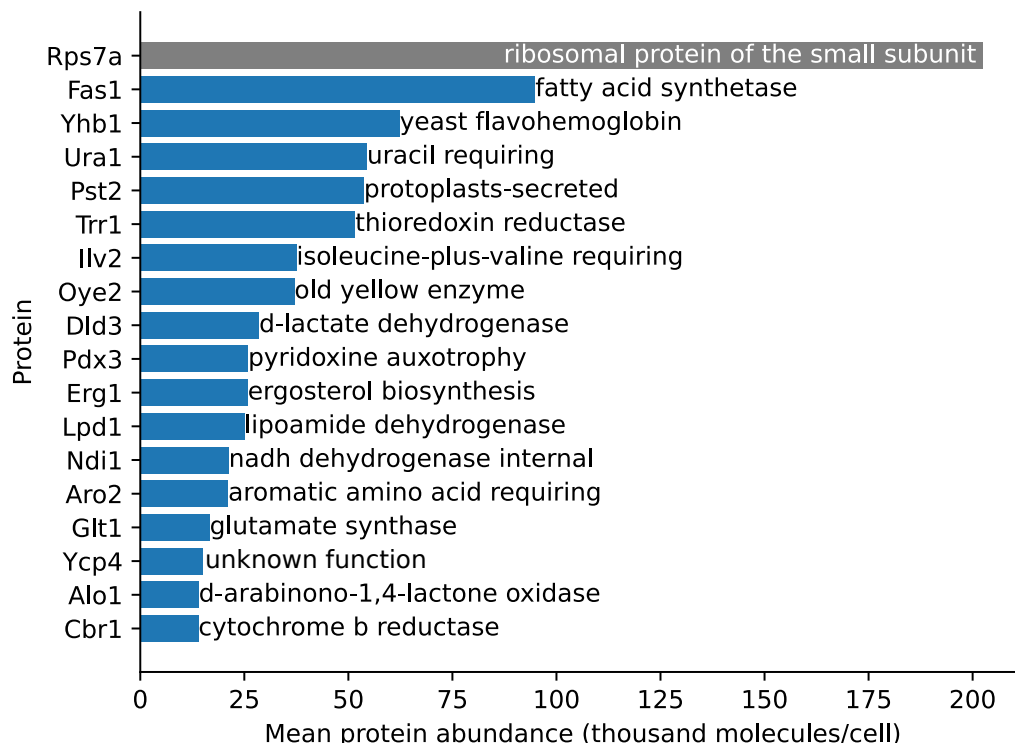


Figure 1.15: Flavoproteins (blue bars) shown by abundance (Ho et al., 2018), with Rps7ap (grey bar) shown as reference. Only the 17 most abundant flavoproteins are shown.

1204 The most abundant flavoproteins catalyse redox reactions (Table 1.1). Specifically,
 1205 these reactions include reduction of reactive chemical species to respond to oxidat-
 1206 ive stress — though not all enzymes involved in the response to reactive chemical
 1207 species have flavin co-factors. Additionally, the reactions include biosynthetic
 1208 reactions. Many of these reactions require NADPH or NADH to donate electrons,
 1209 suggesting a link between flavins and NAD(P)H in regulating the cellular redox
 1210 state. In particular, Oye2p catalyses the NADPH redox reaction, thus providing
 1211 a link between flavins and NAD(P)H. One exception flavoprotein is Ilv2p, which
 1212 does not catalyse a redox reaction. It has been hypothesised that an ancestral form
 1213 of Ilv2p catalysed a redox reaction, but the argument is weak because it is inferred
 1214 from the presence of FAD (Pang et al., 2002). To maintain the cellular redox state,
 1215 it is thus reasonable to assume that the redox equilibrium of all flavoprotein-
 1216 catalysed reactions are in the same direction at any point of the YMC. Supporting

1217 this, Siano and Mutharasan (1989) show that NAD(P)H fluorescence and the
1218 fluorescence of lipoamide dehydrogenase, a flavoprotein, indicate simultaneous
1219 reduction in response to lowered dissolved oxygen. They further show redox
1220 equilibrium in both fluorophores in response to glucose addition.

1221 It is important to rule out the possibility that flavin cycling is merely a function
1222 of the cell division cycle to make sure that flavin monitoring monitors the YMC.
1223 None of these flavoproteins are strictly cell division cycle proteins, but this does
1224 not exclude cycling of flavin autofluorescence linked to the cell division cycle. For
1225 example, fatty acid synthesis proteins should cycle along with the cell division
1226 cycle as cell synthesises more plasma membranes.

1227 **1.3.3 Flavins and flavoproteins in the yeast metabolic cycle**

1228 Flavin fluorescence can be used to monitor the metabolic cycle. The biological
1229 basis of flavins justifies this use. Flavins are linked to NAD(P)H via nitric ox-
1230 ide oxidoreductase (Yhb1p), as discussed in Section 1.3.2, and NAD(P)H cycles
1231 have been implicated in bulk-culture (Tu, Kudlicki et al., 2005) and single-cell
1232 (Papagiannakis et al., 2017) studies of the YMC, as discussed in Section 1.2.1.
1233 The oxidation of flavin is at its maximum at the start of the reductive state of
1234 the YMC, as evidenced by how flavin fluorescence peaks just before dissolved
1235 oxygen concentration in the chemostat (D. B. Murray et al., 2011; Sasidharan et
1236 al., 2012). Riboflavin abundance in the cell has been shown to oscillate and peak
1237 in the oxidative state of the YMC, while FAD abundance is at its maximum in
1238 the reductive-building phase, as evidenced by metabolic profiling of extracts from
1239 chemostat cultures taken at evenly-spaced intervals (Tu, Mohler et al., 2007).

1240 Flavoproteins may have roles linked to the YMC. The most abundant is Fas1
1241 (fatty acid synthetase). Because there is evidence that cycles of fatty acid stores
1242 are implicated in metabolic cycling in yeast (Campbell et al., 2020), it is likely
1243 that fatty acid synthetase is heavily implicated. Following this, the second most
1244 abundant is Yhb1, which may play a major role as discussed earlier.

1245 So, for these reasons, I expect flavin autofluorescence to be oscillatory and be
1246 a useful readout of the yeast metabolic cycle. Few studies have characterised
1247 how such flavin oscillations respond to changing nutrient conditions or to gene
1248 deletions. Thus, filling in this knowledge gap is an avenue for further research.

1249 Nevertheless, there are caveats to using flavin autofluorescence. Riboflavin fluo-
1250 rescence is captured too, though its intracellular abundance is two order of mag-
1251 nitudes lower than that of FMN and that of FAD, and these two flavin derivatives
1252 are present at the same order of magnitude (Tu, Mohler et al., 2007). In addition,
1253 different concentrations of riboflavin influence the autofluorescence signal and
1254 influence the physiological state of the cell (Maslanka et al., 2018). However,
1255 the experimenter can eliminate the effects of riboflavin by using riboflavin-free
1256 minimal media (Verduyn et al., 1992). Additionally, flavin fluorescence is the
1257 aggregate of many flavoprotein components, therefore it cannot be concluded
1258 that flavin fluorescence is the readout of one protein in particular — one can
1259 only draw conclusions about the overall redox state. Furthermore, the changes in
1260 flavin fluorescence can be because of changes in the ‘flavin pool’ — the amount
1261 of flavin-derived moieties in a cell across all their redox states — or due to global
1262 changes in intracellular flavin redox state, as a function of intracellular redox
1263 state. Most studies assume a constant flavin pool and see oscillations as periodic

¹²⁶⁴ shifts in redox equilibrium. These caveats are not unique to flavin fluorescence,
¹²⁶⁵ but are shared limitations with other auto-fluorescing cellular components like
¹²⁶⁶ NAD(P)H, and the benefits of having a non-invasive method to monitor cellular
¹²⁶⁷ metabolism outweighs the caveats.

1268

Chapter 2

1269

Methods

1270 2.1 Laboratory methods

1271 2.1.1 Strains and media

1272 The *Saccharomyces cerevisiae* strains used in this thesis are described in table 2.1.

1273 The minimal medium described by Verduyn et al. (1992) was used unless other-
1274 wise stated. This minimal medium does not contain riboflavin, thus minimising its
1275 effect on flavin autofluorescence imaging, and its composition is known and easily
1276 controlled. Specifically, the composition of the carbon source-limiting medium are
1277 described in Tables 2.2–2.4, and the media pH was adjusted to 6.0 using potassium
1278 hydroxide, or sodium hydroxide for potassium-free media. For auxotrophic strains,
1279 supplements were added according to Table 2.5. Then, a carbon source is added
1280 as appropriate to create the growth medium.

Name	Background	Genotype	Origin	Notes
FY4	FY4	-	EUROSCARF	Winston et al. (1995)
htb2::mCherry	FY4	HTB2::mCherry	In-house, CRISPR	-
BY4741	BY4741	<i>MATA his3Δ1 leu2Δ0 met15Δ0 ura3Δ0</i>	EUROSCARF	Brachmann et al. (1998)
<i>zwf1Δ</i>	BY4741	<i>zwf1Δ::KAN</i>	Edinburgh Genome Foundry	Yeast deletion collection
BY4742	BY4742	<i>MATA his3Δ1 leu2Δ0 lys2Δ0 ura3Δ0</i>	Bruce Morgan	Calabrese et al. (2019)
<i>tsa1Δ tsa2Δ</i>	BY4742	<i>tsa1Δ::natNT2 tsa2Δ::kanMX4</i>	Bruce Morgan	Calabrese et al. (2019)
CEN.PK113-7D	CEN.PK113-7D	-	Peter Kötter	Nijkamp et al. (2012)

Table 2.1: Strains used in this thesis.

Reagent	Concentration	Remarks
KH_2PO_4	3 g L^{-1}	
$\text{MgSO}_4 \cdot 7 \text{ H}_2\text{O}$	0.5 g L^{-1}	
$(\text{NH}_4)_2\text{SO}_4$	5 g L^{-1}	
Trace metals	1 mL L^{-1}	See Table 2.3
Vitamins	1 mL L^{-1}	See Table 2.4. Add upon use.
Carbon source	variable	Add upon use.

Table 2.2: Composition of base minimal medium. For potassium-free media, replace KH_2PO_4 with $2.65 \text{ g L}^{-1} \text{ NaH}_2\text{PO}_4$, which gives the same molarity.

Reagent	Formula	Concentration [g L^{-1}]
EDTA	$\text{C}_{10}\text{H}_{14}\text{N}_2\text{Na}_2\text{O}_8 \cdot 2 \text{ H}_2\text{O}$	15.00
Zinc sulfate	$\text{ZnSO}_4 \cdot 7 \text{ H}_2\text{O}$	4.50
Manganese (II) chloride	$\text{MnCl}_2 \cdot 2 \text{ H}_2\text{O}$	0.84
Cobalt (II) chloride	$\text{CoCl}_2 \cdot 6 \text{ H}_2\text{O}$	0.30
Copper (II) sulfate	$\text{CuSO}_4 \cdot 5 \text{ H}_2\text{O}$	0.30
Sodium molybdate	$\text{Na}_2\text{MoO}_4 \cdot 2 \text{ H}_2\text{O}$	0.40
Calcium chloride	$\text{CaCl}_2 \cdot 2 \text{ H}_2\text{O}$	4.50
Iron (II) sulfate	$\text{FeSO}_4 \cdot 7 \text{ H}_2\text{O}$	3.00
Boric acid	H_3BO_3	1.00
Potassium iodide	KI	0.10

Table 2.3: Composition of trace metal mix for minimal media described in Table 2.2.

Reagent	Formula	Concentration [g L ⁻¹]
D-(+)-biotin	C ₁₀ H ₁₆ N ₂ O ₃ S	0.05
D-pantothenic acid calcium salt	Ca(C ₉ H ₁₆ NO ₅) ₂	1.00
Nicotinic acid	C ₆ H ₅ NO ₂	1.00
<i>myo</i> -Inositol	C ₆ H ₁₂ O ₆	25.00
Thiamine chloride hydrochloride	C ₁₂ H ₁₅ ClN ₄ OS · HCl	1.00
Pyridoxal hydrochloride	C ₈ H ₁₂ ClNO ₃	1.00
4-aminobenzoic acid	C ₇ H ₇ NO ₂	0.20

Table 2.4: Composition of vitamin mix for minimal media described in Table 2.2.

Reagent	Concentration [mg L ⁻¹]
histidine	125
leucine	500
tryptophan	75
methionine	100
uracil	150

Table 2.5: Supplements to minimal media for BY4741-background auxotrophic strains, compositions derived from Pronk (2002). For BY4742-background strains, replace methionine with 100 mg L⁻¹ lysine-HCl.

¹²⁸¹ 2.1.2 Single-cell microfluidics

¹²⁸² Cells were grown from colonies on solid agar in a liquid culture composed of min-
¹²⁸³ imal media formulation appropriate for the experiment, supplements appropriate
¹²⁸⁴ for the strain's auxotrophy, and a carbon source (glucose or pyruvate) appropriate
¹²⁸⁵ for the experiment (see Section 2.1.1). The cells were incubated at 30 °C for 14 h
¹²⁸⁶ (overnight) if the carbon source is glucose or 48 h if the carbon source is pyruvate.
¹²⁸⁷ Subsequently, the cells were diluted so that the resulting culture had an OD₆₀₀ of
¹²⁸⁸ 0.10–0.20, and were then incubated for a further 4 h.

¹²⁸⁹ ALCATRAS microfluidics (Crane et al., 2014) devices were then prepared and
¹²⁹⁰ for an experiment, one device's multiple chambers were filled with growth media
¹²⁹¹ supplemented with 0.05% w/v bovine serum albumin. Cells were then loaded into
¹²⁹² the ALCATRAS chambers — different chambers can house cells from different

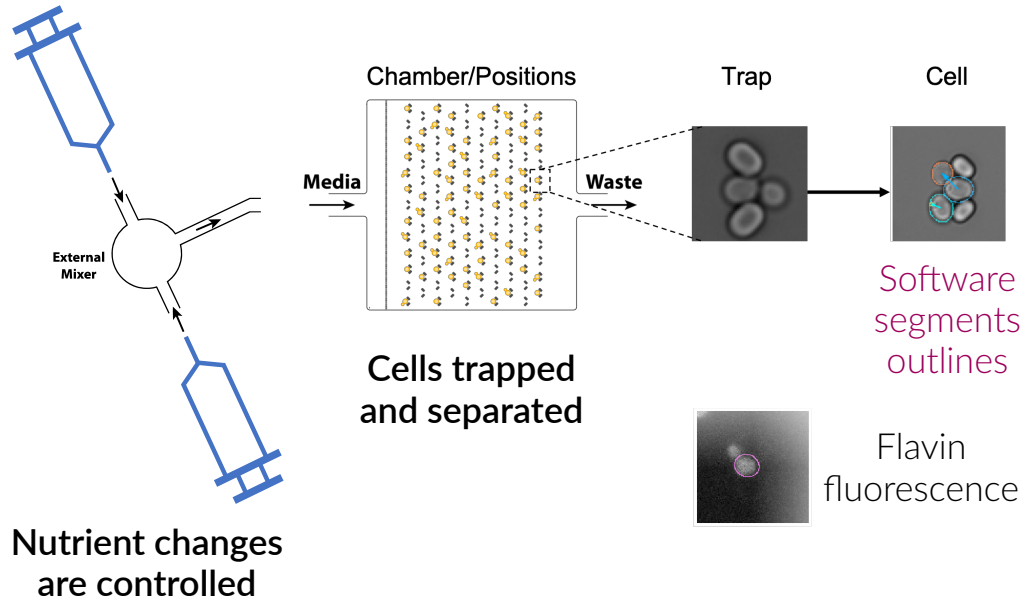


Figure 2.1: Overview of single-cell microfluidics set-up using the ALCATRAS system. Cells are loaded into chambers within devices, where they are trapped and separated (centre). The media composition the cells experience are controlled with syringe pumps (left). Brightfield and fluorescent images are taken at regular intervals, and then processed using *aliby* (Muñoz González, 2023) to obtain time series of fluorescence intensity changes for each parent cell.

1293 strains (Fig. 2.1). Syringe pumps containing media were programmed to produce
 1294 a constant flow of $4 \mu\text{L h}^{-1}$ into the chambers. As a consequence, parent cells are
 1295 held in place within traps, while progeny cells flow out of traps into the outflow
 1296 after the parents bud. There are two syringes that can contain different media,
 1297 and in experiments that require different nutrient conditions at different times,
 1298 the ALCATRAS system is programmed to switch between the two syringes. The
 1299 cells and ALCATRAS chambers were located in an incubation chamber (Oko-
 1300 labs) that was maintained at 30°C .

1301 Microscopy was performed using a $60 \times 1.4 \text{ NA}$ oil immersion objective (Nikon),
 1302 and the Nikon Perfect Focus System was used to ensure consistent focus. X-Y
 1303 spatial positions were defined for each chamber to maximise spatial coverage of
 1304 the chamber while ensuring that the microscope takes less time to move positions
 1305 and capture images than the interval period. Images were taken every 5 min,

and the duration of image acquisition varied for each experiment. Brightfield and flavin images were captured in all strains and mCherry images were additionally captured for the HTB2::mCherry strain. Five z-slices were taken for brightfield images, with a spacing of 0.6 µm between slices. Fluorescence imaging was performed with an OptoLED light source (Cain Research), and LED voltage was optimised for maximum signal intensity without LED cut-off prior to experiments. For flavin imaging, the excitation filter was set to 430/24 (418 nm to 442 nm), the emission filter was set to 535/30 (520 nm to 550 nm), and the exposure time was 60 ms. One z-slice was taken for each flavin image in each position. For mCherry imaging, the excitation filter was set to 555 nm to 590 nm, the emission filter was set to 632/60 (602 nm to 682 nm) and the exposure time was 100 ms. Five z-slices were taken for mCherry images, with a spacing of 0.6 µm between slices.

2.2 Image analysis methods

I used *aliby* (Muñoz González, 2023), an end-to-end Python-based software package developed for time-lapse microscopy, to process the microscope images in order to obtain flavin and mCherry time series for further analysis.

aliby tracks tiles that correspond to a trap across time-lapse images to account for expected spatial drifting in the microscope. It then uses *BABY* (Pietsch et al., 2023) to segment the images of traps to identify the outlines of cells and to track cells from one time point to another, creating a lineage of cells. *aliby* then overlays the cell outlines onto the fluorescence (flavin and mCherry) images to extract fluorescence intensity, and assigns a fluorescence value to each cell at each time point based on the mean intensity of pixels within the cell's outline. The background fluorescence is also computed, based on the pixel intensity outside cell outlines, and is then subtracted from the cell fluorescence. Flavin fluorescence

1331 thus represents the oxidation of flavins throughout the yeast metabolic cycle (see
1332 Section 1.3), and mCherry fluorescence thus represents the amount of histone
1333 proteins as a proxy for cell division cycle progression (Garmendia-Torres et al.,
1334 2018).

1335 2.3 Computational methods

1336 2.3.1 Classical periodogram

1337 To detect rhythmicity in time series, I computed the classical periodogram and
1338 used a statistical test for rhythmicity based on Glynn et al. (2006), described as
1339 follows:

- 1340 1. Let the data have \mathcal{G} cells. Let cell $g = 1, \dots, \mathcal{G}$ have a time series with N_g
1341 time points. The time series is thus denoted $Y_g(t) = y_g(t_1), \dots, y_g(t_{N_g})$.
- 1342 2. For each time series, I define a range of test frequencies linearly from $\frac{1}{N_g}$ to
1343 the Nyquist limit (i.e. half the rate of image acquisition).

1344 With this definition, I compute the classical periodogram for each time
1345 series:

$$P_g(\omega) = \frac{N_g}{2\sigma^2} \left| \int_{-\infty}^{\infty} Y_g e^{-2\pi i t} dt \right|, \quad (2.1)$$

1346 where σ^2 is the sample variance of Y_g . In this equation, the periodogram
1347 is normalised by the coefficient $N_g/2\sigma^2$ so that the area under the period-
1348 ogram is constant across all time series. The Lomb-Scargle periodogram is
1349 equivalent to the classical periodogram if the time points are equally spaced
1350 (Lomb, 1976), as is the case for the vast majority of my data.

- 1351 3. For each cell g , I denote the peak $h_g = \max_j P_g(\omega)$. The peak of the
1352 normalised classical periodogram of each time series was used as a proxy
1353 for the quality of oscillation.

- 1354 4. I define an effective number of independent frequencies $M = f_{max}N_g$ for
 1355 each time series, where f_{max} is the Nyquist limit (VanderPlas, 2018). I then
 1356 calculate the p -value of testing the null hypothesis that such a peak is due
 1357 to chance:

$$p_g = 1 - (1 - e^{-h_g})^M \quad (2.2)$$

1358 This formula is based on the exponential distribution of the power at a
 1359 given frequency in the periodogram (Scargle, 1982).

- 1360 5. I order the cells by p -values: $p_{(1)} \leq p_{(2)} \leq \dots \leq p_{(\mathcal{G})}$. This order thus ranks
 1361 the cells by oscillation quality.
- 1362 6. To control the false discovery rate (Benjamini and Hochberg, 1995), I find
 1363 \hat{k} according to:

$$\hat{k} = \arg \max_{1 \leq k \leq \mathcal{G}} \{k : p_{(k)} \leq qk/\mathcal{G}\} \quad (2.3)$$

- 1364 where q is a defined false discovery rate.
- 1365 7. Cells whose p -values correspond to $p_{(1)}, p_{(2)}, \dots, p_{(\hat{k})}$ are thus denoted to
 1366 have statistically significant oscillatory behaviour for the false discovery
 1367 rate q .
- 

1368 2.3.2 Autoregressive model

1369 As an alternative method to detect rhythmicity in time series, I fitted an autore-
 1370 gressive model and used its parameters to compute an analytically-defined peri-
 1371 odogram, based on Jia and Grima (2020), as follows:

- 1372 1. The algorithm relies on fitting a single time series $n(0), n(1), \dots, n(M-1)$
 1373 with an autoregressive model $AR(P)$ with order P :

$$\phi_0 n_t + \phi_1 n_{t-1} + \phi_2 n_{t-2} + \dots + \phi_P n_{t-P} = \theta_0 \epsilon_t \quad (2.4)$$

1374 where ϵ_t is a white noise satisfying $\langle \epsilon_t \rangle = 0$, $\phi_0 = 1$, and ϕ_1, \dots, ϕ_P are real
 1375 numbers such that the complex zeros of the polynomial $\Phi(z) = \sum_{k=0}^P \phi_k z^k$
 1376 lie outside the unit circle.

1377 2. The sample mean of the time series is estimated by:

$$\langle n \rangle = \frac{1}{M} \sum_{k=0}^{M-1} n(k) \quad (2.5)$$

1378 3. The sample autocorrelation function is estimated as:

$$R_i = \frac{1}{M} \sum_{k=0}^{M-1-i} (n(k) - \langle n \rangle)(n(k+i) - \langle n \rangle) \quad (2.6)$$

1379 4. The coefficients ϕ_1, \dots, ϕ_P are estimated by solving the Yule-Walker equa-
 1380 tion:

$$\begin{bmatrix} R_0 & R_1 & \dots & R_{P-1} \\ R_1 & R_0 & \dots & R_{P-2} \\ \vdots & \vdots & \ddots & \vdots \\ R_{P-1} & R_{P-2} & \dots & R_0 \end{bmatrix} \begin{bmatrix} \phi_1 \\ \phi_2 \\ \vdots \\ \phi_P \end{bmatrix} = \begin{bmatrix} R_1 \\ R_2 \\ \vdots \\ R_P \end{bmatrix} \quad (2.7)$$

1381 5. The parameter θ_0 is estimated as:

$$\theta_0^2 = R_0 - \sum_{k=1}^P \theta_k R_k \quad (2.8)$$

1382 6. The order P is determined by minimising the Akaike information criterion:

$$\text{AIC}(P) = \log \theta_0^2(P) + 2 \frac{P}{M} \quad (2.9)$$

1383 where $\theta_0(P)$ is the estimated θ_0 (Eq. 2.8) for a specific P . In this step, P
 1384 is varied with $1 \leq P \leq 3\sqrt{M}$, and the optimum order (P) is the one that
 1385 gives the smallest value of $\text{AIC}(P)$

- 1386 7. The power spectrum is thus estimated analytically using the parameters
 1387 found in earlier steps by:

$$G(\xi) = \frac{1}{2\pi} \cdot \frac{\theta_0^2}{|\sum_{k=0}^P \phi_k e^{-ik\xi}|^2}, -\pi \leq \xi \leq \pi \quad (2.10)$$

1388 where ξ represents frequency.

1389 2.3.3 Precision and recall

1390 To evaluate the performance of rhythmicity detection methods, precision and
 1391 recall are computed. The rhythmicity detection methods are seen as a binary
 1392 classifier that predicts a ‘positive’ or ‘negative’ label to each observation, and
 1393 these predicted labels are compared against true labels — in the context of this
 1394 thesis, manually-defined labels of whether a time series is oscillatory or not.

1395 Given the confusion matrix:

		Predicted labels	
		Positive	Negative
True labels	Positive	True positives (TP)	False negatives (FN)
	Negative	False positives (FP)	True negatives (TN)

Table 2.6: Confusion matrix

1396 Precision is defined as:

$$\text{Precision} = \frac{\text{TP}}{\text{TP} + \text{FP}} \quad (2.11)$$

1397 And recall is defined as:

$$\text{Recall} = \frac{\text{TP}}{\text{TP} + \text{FN}} \quad (2.12)$$

1398 Precision and recall can be used with datasets with class imbalance, i.e. if the
1399 two labels are not ~~split~~ evenly across observations.

split

1400 2.3.4 Cross-correlation function

1401 To estimate the periodicity of signals and to detect the synchrony between two
1402 types of signals, I adapted the cross-correlation function as used in Pietsch et al.
1403 (2023), as follows:

- 1404 1. Let the data have M cells. Each cell i in the population of M cells has a time
1405 series $x_1^{(i)}, \dots, x_j^{(i)}, \dots, x_N^{(i)}$ of quantity x and a time series $y_1^{(i)}, \dots, y_j^{(i)}, \dots, y_N^{(i)}$
1406 of quantity y . Let both time series have a sampling interval of Δt .
- 1407 2. The deviation from the population mean for each time series is computed.
1408 This population mean is calculated over replicates at each time point. The
1409 caveat of this calculation is that the signals must be out-of-phase, and I
1410 ensure this by generating synthetic signals with a random phase. Otherwise,
1411 the underlying signal will be subtracted from all time series and the cross-
1412 correlation of noise will be computed — this is undesired.

$$\delta x_t^{(i)} = x_t^{(i)} - \frac{1}{M} \sum_j x_t^{(j)} \quad (2.13)$$

$$\delta y_t^{(i)} = y_t^{(i)} - \frac{1}{M} \sum_j y_t^{(j)} \quad (2.14)$$

- 1413
- 1414 3. Based on Kiviet et al. (2014), the cross-covariance of the two time series x
1415 and y at a time lag of $r\Delta t$, is thus given by:

$$C_{xy}^{(i)}(r\Delta t) = \begin{cases} \frac{1}{N-r} \sum_{t=1}^{N-r} \delta x_t^{(i)} \cdot \delta y_{t+r}^{(i)} & \text{if } r \geq 0 \\ C_{yx}^{(i)}(-r\Delta t) & \text{if } r < 0 \end{cases} \quad (2.15)$$

¹⁴¹⁶ 4. $C_{xx}^{(i)}(0)$ and $C_{yy}^{(i)}(0)$ thus give the variances of x and y . The cross-correlation
¹⁴¹⁷ is thus given, with normalising by the standard deviation, by:

$$R_{xy}^{(i)}(r\Delta t) = \frac{C_{xy}^{(i)}(r\Delta t)}{\sqrt{C_{xx}^{(i)}(0)C_{yy}^{(i)}(0)}} \quad (2.16)$$

¹⁴¹⁸ The autocorrelation of a time series x is thus the cross-correlation of the time
¹⁴¹⁹ series with itself, i.e. $R_{xx}^{(i)}(r\Delta t)$.

¹⁴²⁰ 2.3.5 ~~Generation of synthetic oscillatory data.~~ Synthetic oscillations

¹⁴²¹ To understand the effect of the shape and noise properties present in biological
¹⁴²² time series on the cross-correlation function, I emulated such time series by
¹⁴²³ generating synthetic time series using the harmonic (sinusoid) and FitzHugh-
¹⁴²⁴ Nagumo oscillators (FitzHugh, 1961).

¹⁴²⁵ The harmonic oscillator $y(t)$ is defined as the solution of:

$$\frac{d^2y}{dt^2} = -\omega^2y \quad (2.17)$$

¹⁴²⁶ where the sole parameter ω represents the angular frequency.

¹⁴²⁷ The FitzHugh-Nagumo oscillator $v(t)$ is defined as a solution of the system:

$$\begin{aligned} \frac{dv}{dt} &= v - \frac{v^3}{3} - w + RI_{\text{ext}} \\ \tau \frac{dw}{dt} &= v + a - bw \end{aligned} \quad (2.18)$$

¹⁴²⁸ where RI_{ext} , τ , a , and b are constant parameters to be determined.

¹⁴²⁹ In addition, I emulated noise by generating Gaussian and Gillespie noise.

¹⁴³⁰ Gaussian noise was generated by randomly drawing samples from the normal
¹⁴³¹ distribution $\mathcal{N}(0, \sigma^2)$. Here, σ denotes the standard deviation of the distribution
¹⁴³² and thus controls the size of the noise.

¹⁴³³ Gillespie noise emulates noise from biological systems. Gillespie noise was gener-
¹⁴³⁴ ated using the direct method of the Gillespie algorithm (Gillespie, 1977) on the
¹⁴³⁵ birth-death process model (Appendix A.4).

¹⁴³⁶ The birth-death process is a simple stochastic model used for the modelling of
¹⁴³⁷ gene expression. The model describes a species that is produced at a linear birth
¹⁴³⁸ rate k_0 and destroyed at a linear death rate d_0 , and is defined by the system of
¹⁴³⁹ equations Eq. 2.19:



¹⁴⁴⁰ To produce Gillespie noise, a stochastic simulation employing the direct method
¹⁴⁴¹ of the Gillespie algorithm was performed on the birth-death process model with
¹⁴⁴² defined k_0 and d_0 parameters. The final time was defined in such a way that allows
¹⁴⁴³ the trajectory of the amount of P over time to reach a steady state (Fig. 4.16b).
¹⁴⁴⁴ This time varied depending on the k_0 and d_0 values, but the final time of 1500
¹⁴⁴⁵ was chosen as it was long enough to have the trajectory each steady state for the
¹⁴⁴⁶ k_0 and d_0 values used in this study.

¹⁴⁴⁷ The latter half of the trajectory was taken and then put on a grid with 1000
¹⁴⁴⁸ regularly-spaced time points, equal to the number of time points for the synthetic
¹⁴⁴⁹ oscillators (harmonic and FitzHugh-Nagumo). The time series was then normal-
¹⁴⁵⁰ ised by subtracting the mean (k_0/d_0) and then dividing by $\sqrt{1/d_0}$ to create a time

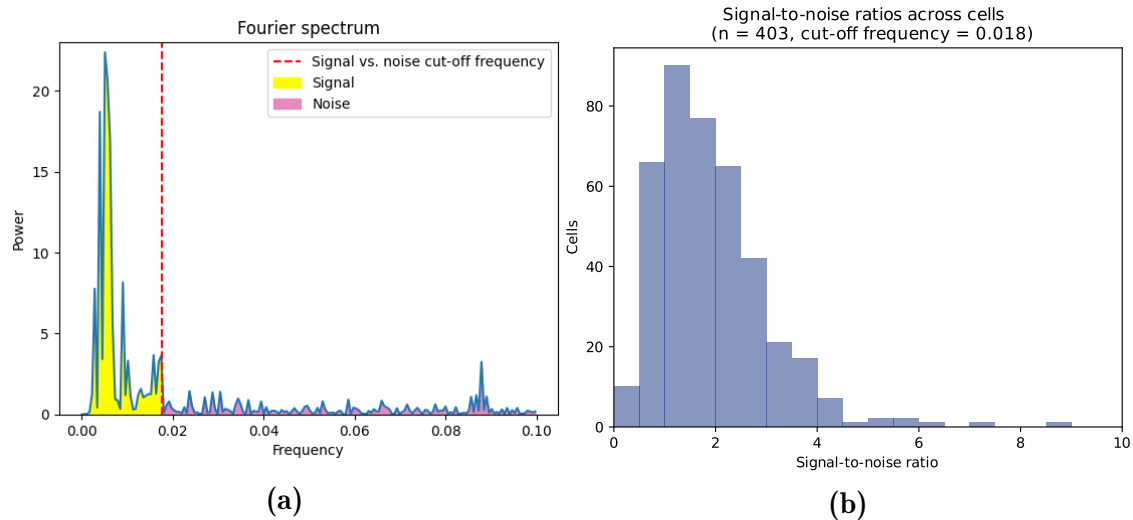


Figure 2.2: (2.2a) Illustration of signal-to-noise ratio. The signal-to-noise ratio is defined (Eqs. 2.20–2.23) as the area under the periodogram below a cut-off frequency (yellow) divided by the area under the periodogram above a cut-off frequency (pink). (2.2b) Histogram of signal-to-noise ratios from a sample experiment ($n = 403$).

series representing Gillespie noise with mean 0 and standard deviation $\sqrt{k_0}$. This
 Gillespie noise thus has a standard deviation of noise amplitude $A = \sqrt{k_0/d_0}$ and
 noise timescale $\tau = 1/d_0$ — in other words, the rate parameters of the birth-death
 process control the noise properties of this Gillespie noise.

2.3.6 Signal-to-noise ratio

To evaluate the quality of oscillatory time series in a dataset and to indirectly measure the amplitude of the oscillations, I computed a signal-to-noise ratio for each time series. Assuming a constant noise introduced by the combination of intrinsic noise (stochasticity in biochemical processes) and extrinsic noise (variations introduced by measurement instruments), a low signal-to-noise ratio suggests a low oscillation amplitude, and the reverse is true for a high signal-to-noise ratio.

The signal-to-noise ratio can be defined as follows:

¹⁴⁶⁴ Given a time series $x(t) = x(t_1), x(t_2), \dots, x(t_N)$, the normalised classical period-
¹⁴⁶⁵ ogram (Fourier spectrum) is given by

$$P(\omega) = \frac{N}{2\sigma^2} \left| \int_{-\infty}^{\infty} x(t)e^{-2\pi i t} dt \right|, \quad (2.20)$$

¹⁴⁶⁶ where N is the number of time points in x and σ^2 is the sample variance of x .

¹⁴⁶⁷ The periodogram P is defined as a function of the angular frequency ω .

¹⁴⁶⁸ A critical frequency ω_c is then defined to divide signal and noise — that is, very
¹⁴⁶⁹ high-frequency components of the periodogram correspond to noise and lower-
¹⁴⁷⁰ frequency components correspond to the meaningful oscillations.

¹⁴⁷¹ The signal to noise ratio $r_{s/n}$ (Fig. 2.2) is thus defined as

$$r_{s/n} = \frac{s}{n} \quad (2.21)$$

¹⁴⁷² where the signal s is defined as

$$s = \int_0^{\omega_c} P(\omega) d\omega \quad (2.22)$$

¹⁴⁷³ and the noise n is defined as

$$n = \int_{\omega_c}^{\infty} P(\omega) d\omega \quad (2.23)$$

¹⁴⁷⁴ In this thesis, I define $\omega_c = 0.018 \text{ min}^{-1}$ because this frequency is lower than
¹⁴⁷⁵ the frequencies of all oscillations of flavin autofluorescence I observed in my
¹⁴⁷⁶ experiments.

Chapter 3

1477

1478

1479

1480

Microfluidics and fluorescence microscopy for cellular metabolic cycles

1481 Few published studies have investigated the YMC in cells isolated from each
1482 other (Silverman et al., 2010; Papagiannakis et al., 2017; Baumgartner et al.,
1483 2018; Özsezen et al., 2019). Most studies instead have examined the YMC from
1484 a population of cells in a chemostat (Tu, Kudlicki et al., 2005; Tu, Mohler et al.,
1485 2007; D. B. Murray et al., 2011; Causton et al., 2015; Mellor, 2016; O' Neill et al.,
1486 2020; Amponsah et al., 2021). However, such chemostat-based studies are unable
1487 to account for cell-to-cell heterogeneity. Furthermore, in such conditions, cell
1488 density and environmental conditions are far removed from the natural habitat
1489 of budding yeast.

1490 To reconcile the evidence about the characteristics of the yeast metabolic cycle
1491 (YMC) from single-cell and chemostat experiments, I sought to use a single-
1492 cell experimental platform to address whether cellular metabolic cycles confirm
1493 chemostat-based studies.

1494 In this chapter, I use single-cell microfluidics to physically separate budding yeast
1495 cells. In these experiments, I use fluorescence microscopy to monitor the yeast
1496 metabolic cycle and the cell division cycle.

¹⁴⁹⁷ Specifically, I aim to evaluate these hypotheses:

- ¹⁴⁹⁸ 1. Yeast cells independently generate yeast metabolic cycles. Each cell generates the metabolic cycle autonomously of other cellular oscillators, but the metabolic cycle can phase-lock the cell division cycle.
- ¹⁴⁹⁹ 2. The yeast metabolic cycle is retained in different nutrient and genetic perturbations, but characteristics of the cycle change in response.
- ¹⁵⁰⁰ 3. Flavin autofluorescence of single yeast cells recapitulate oscillations in dissolved oxygen in the chemostat. If there are discrepancies between these two manifestations of the yeast metabolic cycle, they may be explained by individual cells continuing to generate the metabolic cycle but without synchrony between cells.

¹⁵⁰¹ In this chapter, I show that metabolic cycles are generated autonomously and are coupled to the cell division cycle in permissive conditions, confirming previous ¹⁵⁰² single-cell studies (Papagiannakis et al., 2017; Özsezen et al., 2019). To decouple ¹⁵⁰³ the metabolic and cell division oscillators, confirming that the metabolic oscillator is independently and autonomously generated, I used fast nutrient switching to ¹⁵⁰⁴ induce starvation. I further show that the metabolic cycle is robust across nutrient ¹⁵⁰⁵ and genetic perturbations, but with changes to its oscillatory parameters. Finally, ¹⁵⁰⁶ to address whether single-cell metabolic cycles confirm findings from chemostat-¹⁵⁰⁷ based studies, I emulated situations known to affect dissolved-oxygen traces. ¹⁵⁰⁸ These situations include potassium deficiency and deletions of genes with roles in ¹⁵⁰⁹ metabolism and biological timekeeping.

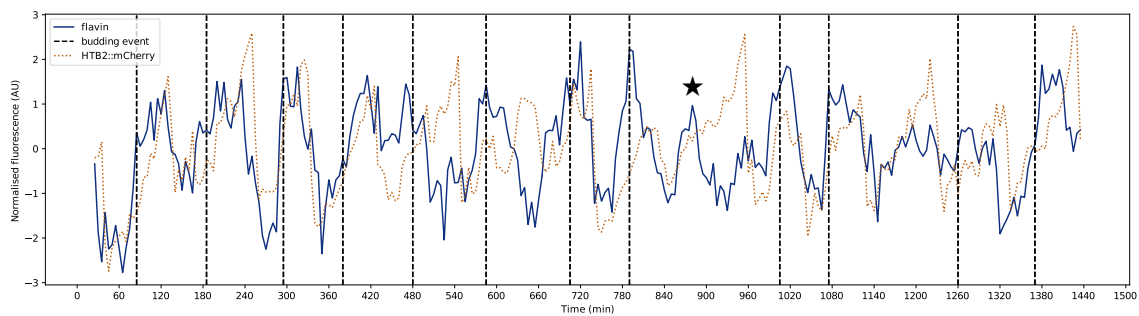


Figure 3.1: Flavin fluorescence (blue, solid lines) and histone 2B (orange, dotted lines) levels in a single, representative FY4 HTB2::mCherry cell grown in 20 g L^{-1} glucose. Vertical lines (black, dashed) indicate budding events. Star (*) indicates a flavin oscillation without a corresponding cell division cycle.

1519 3.1 Coupled oscillations in permissive conditions

1520 To show that metabolic cycles are generated autonomously and are coupled to
 1521 the cell division cycle, I replicated the single-cell flavin oscillations observed by
 1522 Baumgartner et al. (2018). Replicating results from a previous flavin-based micro-
 1523 fluidics study is important to confirm that my use of ALCATRAS (Crane et al.,
 1524 2014) monitored the yeast metabolic cycle, especially given that the microfluidics
 1525 set-up differed from previous studies (Papagiannakis et al., 2017; Baumgartner
 1526 et al., 2018).

1527 Fig. 3.1 shows that oscillations in flavin fluorescence peak when a bud forms
 1528 shortly before G_2/M , as evidenced by prototrophic FY4 HTB2::mCherry cells
 1529 grown in minimal medium supplemented with 20 g L^{-1} glucose. The HTB2::mCherry
 1530 insertion allows monitoring phases of the cell division cycle through quantifying
 1531 over time the intensity of the fluorescence of the inserted protein (Garmendia-
 1532 Torres et al., 2018) (Fig. 3.2), while also allowing monitoring flavin fluorescence
 1533 by avoiding the overlap of flavin and GFP emission spectra.

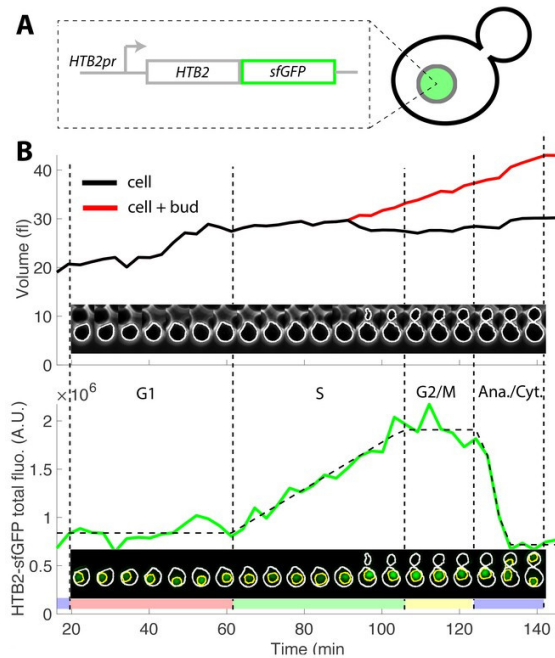


Figure 3.2: (A) Engineering a fluorescent protein cassette fused to *HTB2* (B) allows the identification of phases of the cell division cycle through monitoring changes in fluorescence of the fluorescent protein. Adapted from Garmendia-Torres et al. (2018).

Fig. 3.1 also shows that in some cases, a metabolic oscillation occurred without cell division cycle progression or bud formation. Such cases, also revealed by Papagiannakis et al. (2017) via cycles of NAD(P)H fluorescence, confirmed that the metabolic cycle is generated autonomously from the cell division cycle.

As observed, oxidation of flavin upon budding was expected for these reasons:

1. Flavin fluorescence peaks (becomes most oxidised) and NAD(P)H fluorescence peaks (becomes most reduced) at the same time in chemostat cultures (D. B. Murray et al., 2011).
2. NAD(P)H is in the reduced form when buds form (Papagiannakis et al., 2017).
3. The flavoprotein lipoamide dehydrogenase, coded by the gene *LPD1*, is in redox equilibrium with NAD(P)H (Siano and Mutharasan, 1989).

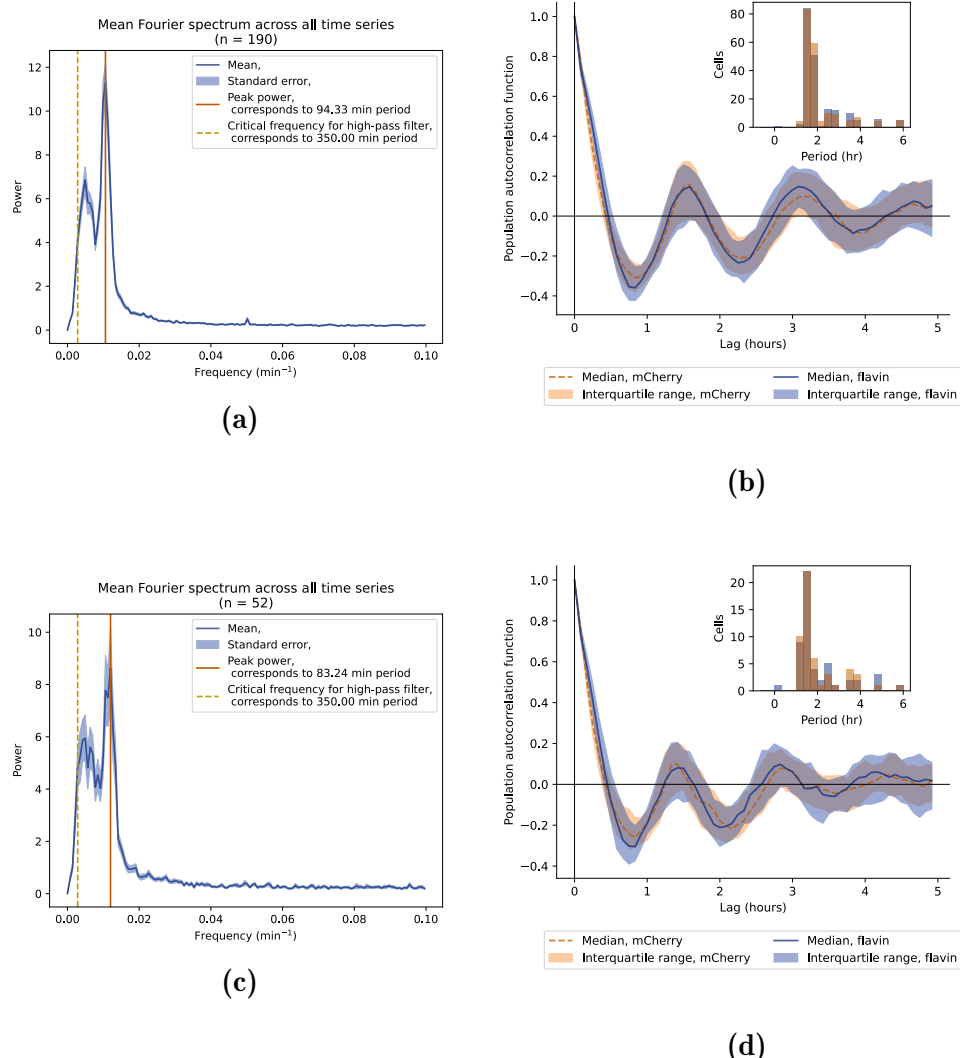


Figure 3.3: (3.3a, 3.3c) Mean Fourier spectrum of flavin fluorescence time series across cells. (3.3b, 3.3d) Median autocorrelation functions of flavin fluorescence (blue) and histone 2B levels (orange) time series, along with (*insets*) the periods of each oscillator across cells as determined by the frequency with the greatest power in each signal's Fourier spectrum. Data are from FY4 HTB2::mCherry cells under 20 g L^{-1} glucose; two experiment repeats shown.

1546 To quantify the period of the oscillators, I combined time series analysis methods.
1547 Fig. 3.3 shows that flavin fluorescence oscillated at a period of approximately
1548 90 min, based on the mean Fourier spectrum and median autocorrelation function.
1549 Figs. 3.3b and 3.3d additionally show that the cell division cycle proceeded
1550 at the same period, as evidenced by the autocorrelation function of mCherry.
1551 The duration of the cell division cycles agrees with previously reported values
1552 (Herskowitz, 1988).

1553 To visualise the relationship between the metabolic cycle and the cell division
1554 cycle, Fig. 3.4 shows that budding events synchronise with peaks in fluorescence
1555 and that the cell division cycle varies between cells, with most just under 2 h,
1556 agreeing with Fig. 3.3b (inset). The oscillatory shape of the median flavin fluo-
1557 rescence time series when aligned to the first budding event (Fig. 3.4b) further
1558 confirms the synchrony between the metabolic cycle and budding events.

1559 Finally, to quantify the relationship between the metabolic cycle and the cell
1560 division cycle, I computed the cross-correlation function between the flavin and
1561 mCherry signals across the population (Fig. 3.4c). The flavin signal peaks, on
1562 average, precede the mCherry signal peaks by 5 min, as evidenced by the location
1563 of the peak of the cross-correlation function that is closest to the vertical axis.
1564 The cross-correlation function thus demonstrates the coincidence between peaks
1565 of flavin oscillations and mitosis.

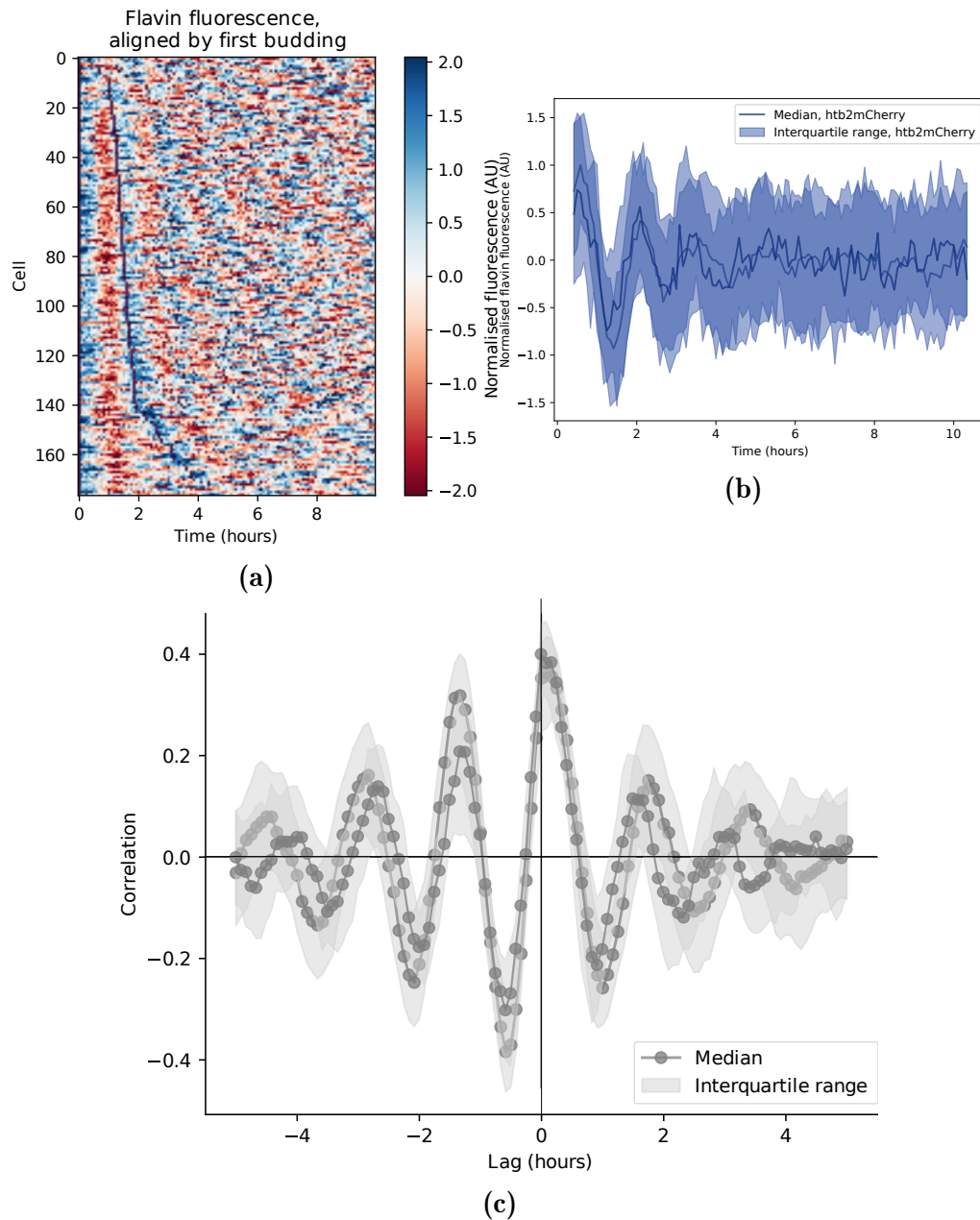


Figure 3.4: **(3.4a)** Heatmap showing the flavin fluorescence (pixels on a red-blue scale) and budding events (black pixels) of each cell over time. Signals are aligned by the first budding event. **(3.4b)** Median flavin fluorescence signal across cells, aligned to first budding event (two repeats: $n_1 = 361$, $n_2 = 144$). **(3.4c)** Median cross-correlation function between flavin and histone 2B signals (two repeats: $n_1 = 392$, $n_2 = 170$). Data are from FY4 HTB2::mCherry cells in 20 g L^{-1} glucose.

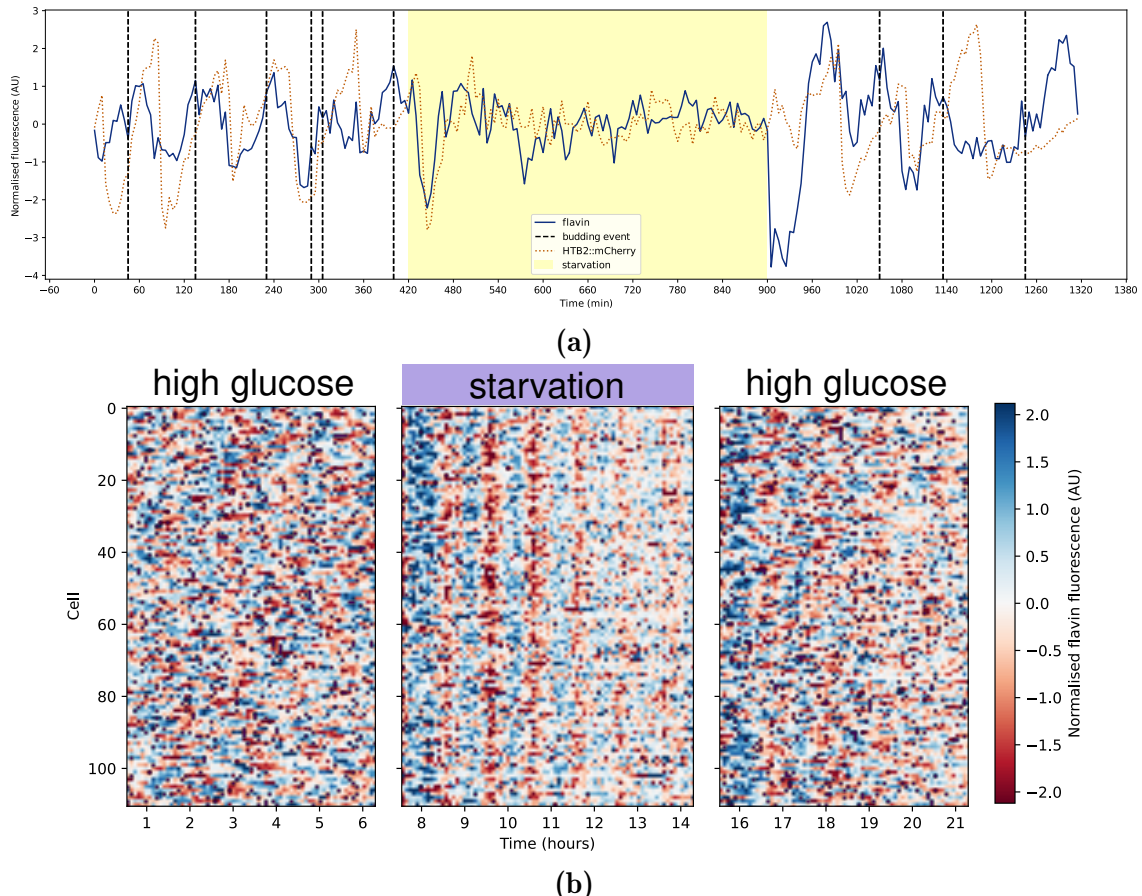


Figure 3.5: **(3.5a)** Flavin fluorescence (blue, solid lines) and histone 2B (orange, dotted lines) levels in a single, representative FY4 HTB2::mCherry cell. Vertical lines (black, dashed) indicate budding events. Shading (yellow) indicates glucose starvation. **(3.5b)** Heatmap showing the flavin fluorescence (pixels on a red-blue scale) and budding events (black pixels) of each cell. Data are from FY4 and HTB2::mCherry cells, subject to 7.5 g L^{-1} glucose for 7 h before being abruptly switched to 0 g L^{-1} glucose for 8 h and then resumed to 7.5 g L^{-1} glucose for 7 h.

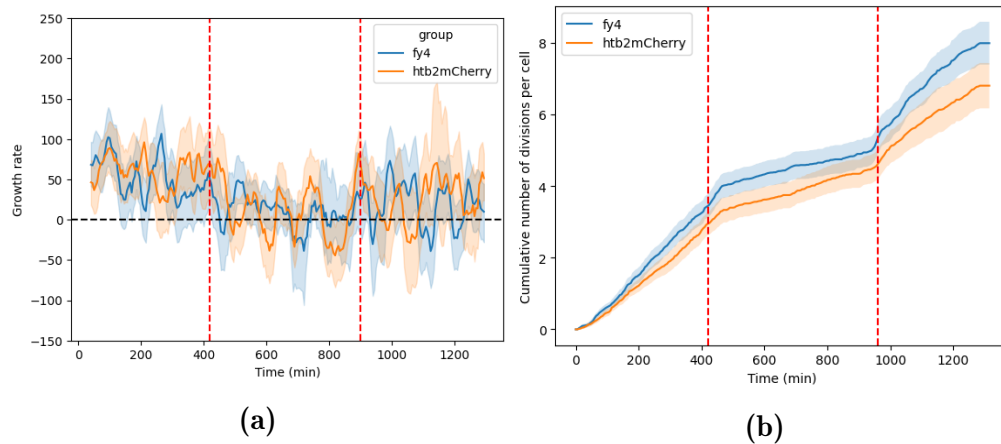


Figure 3.6: (3.6a) Mean growth rate, derived from changes in the sum of estimated parent cell and bud volumes (shading: 95% confidence intervals) and **(3.6b)** mean cumulative number of budding events per cell (shading: confidence intervals from bootstrapping, $n = 30$) of FY4 (blue) and HTB2::mCherry (orange) strains over time during the glucose-starvation experiment. Vertical lines (red) show changes in the nutrient medium.

1566 3.2 Decoupling between the metabolic and cell divi- 1567 sion cycles

1568 To provide additional evidence that cells generate metabolic oscillations autonom-
1569 ously of the cell division cycle, I created a condition in which cells did not
1570 undergo cell division. Specifically, I did so by inducing starvation: I cultured FY4
1571 and HTB2::mCherry cells in 7.5 g L^{-1} glucose for 7 h, switching them to 0 g L^{-1}
1572 glucose for 8 h, and then resumed 7.5 g L^{-1} glucose for 7 h. This abrupt induction
1573 of starvation is similar to experiments described by Bagamery et al. (2020), which
1574 showed that a population of genetically identical budding yeast cells, upon glucose
1575 starvation, formed two sub-populations that had different cellular physiology.

1576 Fig. 3.5 shows that when cells were in high glucose, metabolic oscillations were
1577 asynchronous, consistent with Section 3.1, Papagiannakis et al. (2017), and Baumgart-
1578 ner et al. (2018). When cells grown in high glucose were abruptly starved of
1579 glucose, their flavin oscillations reset their phase. Fig. 3.6 further shows that

1580 during starvation, these flavin oscillations continued, while growth rate dropped
1581 and budding events were sparse. The partial, rather than full, recovery of growth
1582 rate after starvation may be explained by accumulated phototoxicity over the
1583 course of the experiment generated by fluorescence imaging, with similar pat-
1584 terns across all experiments. Alternatively, the partial recovery of growth rate
1585 could also be explained by memory of glucose starvation. In addition, the lower
1586 cumulative number of budding events in the HTB2::mCherry strain, consistent
1587 across all experiments, may be explained by the increased phototoxicity generated
1588 by mCherry imaging in five z-slices (Methods Section 2.1.2).

1589 The results show that metabolic oscillations can be generated when the cell
1590 division cycle is halted, providing strong evidence that the metabolic cycle is
1591 generated autonomously and independently of the cell division cycle. In addition,
1592 the results show that each cell can individually reset the phase of its metabolic
1593 cycle in response to abrupt changes in environmental conditions. Similar phe-
1594 nomena have been observed upon bulk addition of carbon sources (Kuang et al.,
1595 2017; Krishna and Laxman, 2018). Importantly, the results suggest that diffusion
1596 of signalling chemicals between cells is not required for generation of metabolic
1597 cycles. Combined with results from the previous section, my data suggest that
1598 the metabolic cycle responds to external conditions and create windows of op-
1599 portunity for initiating the cell division cycle, if conditions are favourable for
1600 growth.



1601 The model in which the metabolic cycle creates windows of opportunity for the
1602 cell division cycle implies that, upon starvation, cell division cycles progress
1603 to the next gap phase (G_1 or G_2/M) while the metabolic cycle continues. To
1604 test this implication, Fig. 3.7 shows that cells may remain in G_1 (Fig. 3.7a), as
1605 evidenced by low mCherry intensity, or in G_2/M (Fig. 3.7b), as evidenced by high
1606 mCherry intensity. Extending this investigation across a population of cells, Fig.

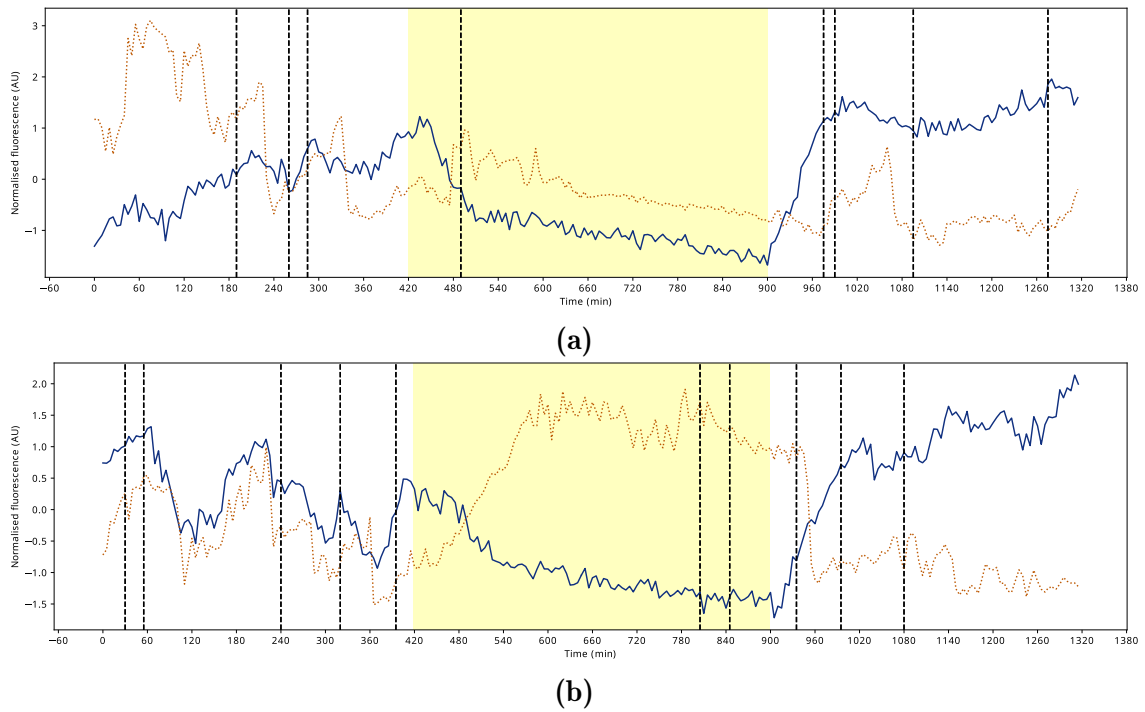


Figure 3.7: Flavin fluorescence (blue, solid lines) and histone 2B (orange, dotted lines) levels in two sample FY4 HTB2::mCherry cells in the glucose starvation experiment. Vertical lines (black, dashed) indicates budding events. Shading (yellow) indicate glucose starvation. **(3.7a)** is an example of a cell with a low intensity of mCherry during starvation, while **(3.7b)** is an example with a high intensity of mCherry. The flavin and mCherry time series were normalised to give a mean of 0 and standard deviation of 1 so that they can be plotted on the same vertical axes, but the high-pass Butterworth filter was not applied.

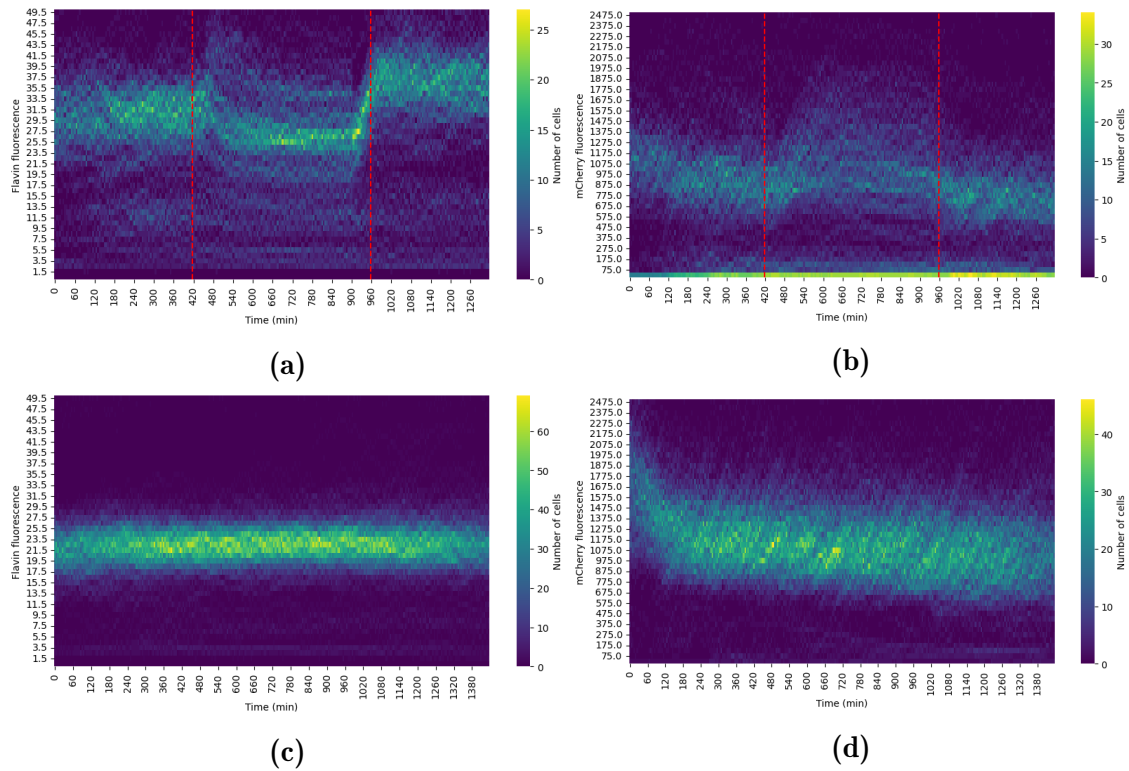


Figure 3.8: Distributions of (3.8a) flavin and (3.8b) mCherry fluorescence over time, for the glucose-starvation experiment. Vertical lines (red, dashed), indicate times of medium changes. As a control, distributions of (3.8c) flavin and (3.8d) mCherry fluorescence over time for the high glucose (20 g L^{-1}) experiment are also shown. Raw time series were used to calculate the distributions.

1607 3.8b shows that the distribution of mCherry intensity becomes broader during
1608 starvation before resuming to a distribution resembling the initial condition upon
1609 restoration of glucose. This observation can be explained by a larger proportion
1610 of cells in G₂/M, giving high mCherry intensity, in contrast to the usually short
1611 time cells spend in G₂/M relative to the rest of the cell division cycle (Fig. 3.2).
1612 In contrast, Fig. 3.8a suggests that during starvation, the distribution of flavin
1613 intensity became narrower. This observation can be explained by lower-amplitude
1614 oscillations during starvation, which was evidenced by a lower signal-to-noise ratio
1615 ($\bar{x}_{\text{before}} = 2.86$, $\bar{x}_{\text{starvation}} = 2.17$, $\bar{x}_{\text{after}} = 4.09$; two-sided Kolmogorov-Smirnov
1616 test: starvation vs before $p = 6.9 \times 10^{-15}$, starvation vs after $p = 6.6 \times 10^{-18}$). In
1617 addition, the overall higher intensity of flavin signals after starvation compared
1618 to before starvation suggest some memory of starvation.

Explain
how this
links to
figures

1619 3.3 Metabolic cycles in different genetic backgrounds

1620 To show that the metabolic cycle is robust, I monitored flavin autofluorescence
1621 signals from the auxotrophic BY4741 strain. Cells of this strain were grown in
1622 minimal medium supplemented with uracil and the amino acids required for this
1623 strain to grow, in addition to 10 g L⁻¹ glucose as the carbon source. Showing
1624 that metabolic cycles occur in an auxotroph is important because it shows that
1625 many cellular aspects must be impaired for the cycle to disappear, thus suggesting
1626 that the metabolic cycle is an intrinsic property of budding yeast. Similar to FY4
1627 HTB2::mCherry cells, BY4741 cells showed robust, consistent oscillations in flavin
1628 fluorescence that peak upon budding (Fig. 3.9), although metabolic cycles have a
1629 period of ≈ 75 min in this case. The shorter period may be explained by a lack of
1630 burden caused by a lack of an mCherry insertion, and by nutritional supplements.

✓

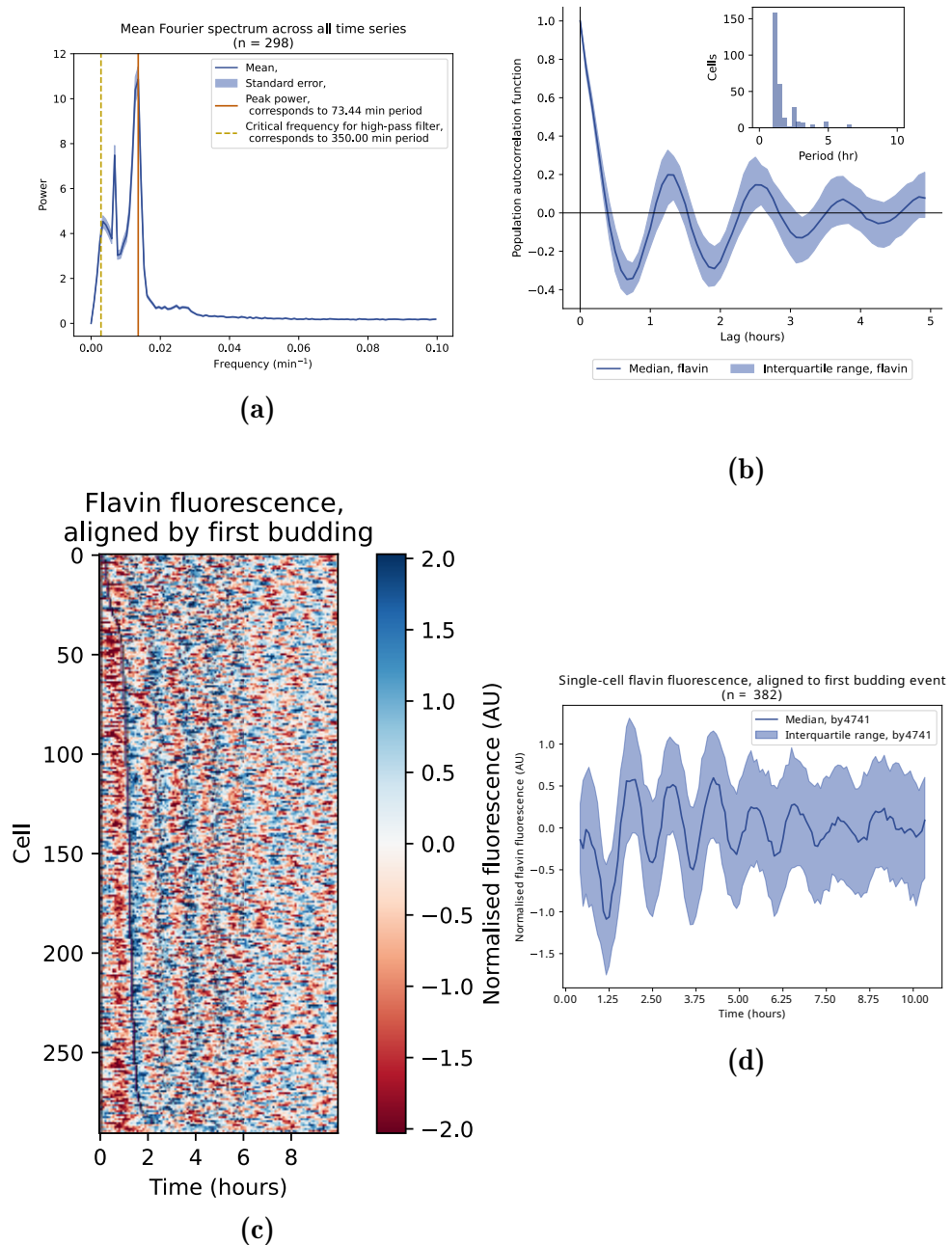


Figure 3.9: (3.9a) Mean Fourier spectrum of flavin fluorescence time series across cells. (3.9b) Median autocorrelation function of flavin fluorescence time series, along with (*inset*) the periods across cells as determined by the frequency with the greatest power in each signal's Fourier spectrum. (3.9c) Heatmap showing the flavin fluorescence (pixels on a red-blue scale) and budding events (black pixels) of each cell. Signals are aligned by the first budding event. (3.9d) Median flavin fluorescence signal across cells, aligned to first budding event. Data are from BY4741 cells in 10 g L^{-1} glucose.

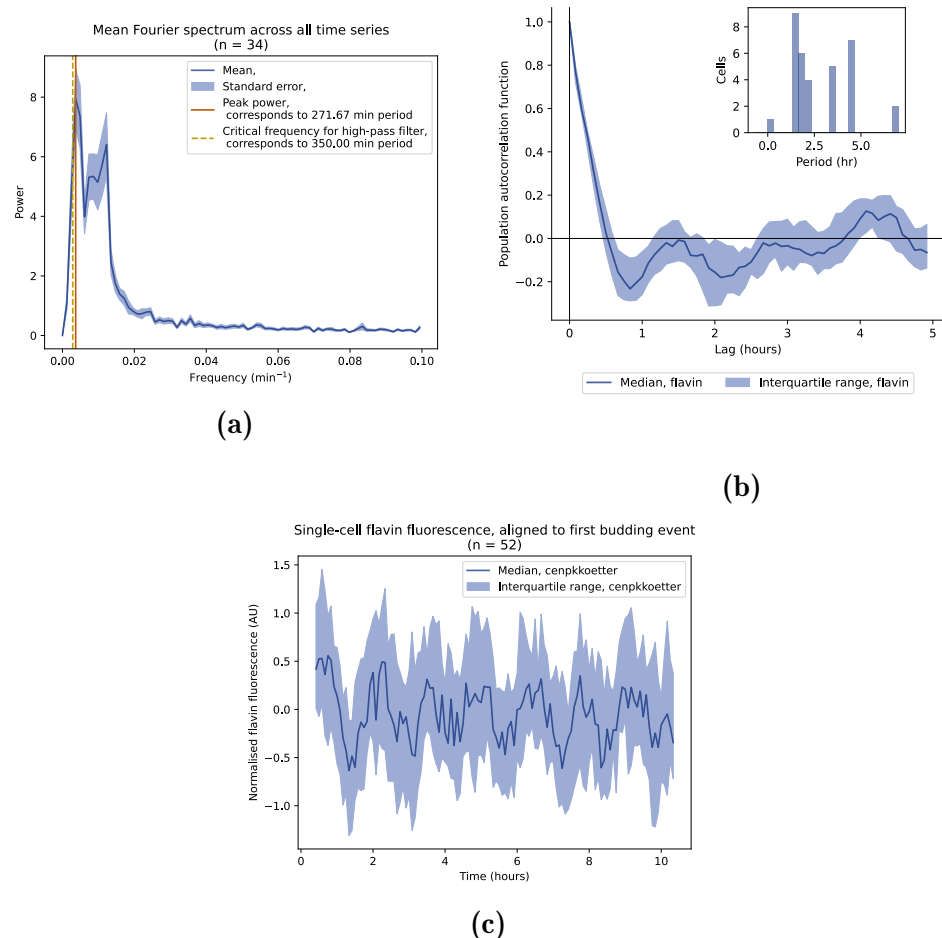


Figure 3.10: **(3.10a)** Mean Fourier spectrum of flavin fluorescence across cells. **(3.10b)** Median autocorrelation function of flavin fluorescence time series, along with (*inset*) the periods across cells as determined by the frequency with the greatest power in each signal's Fourier spectrum. **(3.10c)** Median flavin fluorescence signal across cells, aligned to first budding event. Data are from CEN.PK113-7D cells in 10 g L^{-1} glucose.

FY4 and BY4741 both derive from the S288c background strain. To show that the metabolic cycle is generated from a budding yeast strain other than S288c background strains, I performed a similar experiment with the prototrophic CEN.PK strain grown in minimal medium. Showing that metabolic cycles additionally occur in a different genetic background is important to emphasise that the cycles are intrinsic to budding yeast. CEN.PK is an important background to consider because it harbours genetic differences relative to S288c that results in physiological differences, including biotin prototrophy and malate metabolism (Nijkamp et al., 2012). Furthermore, CEN.PK has greater mitochondrial stability and a better gene regulatory response to levels of oxygen, owing to the insertion mutation that deactivates the *HAP1* gene in S288c (Gaisne et al., 1999). Fig. 3.10 suggests that CEN.PK113-7D cells exhibited 90 min flavin oscillations that were synchronised with budding events, similar to FY4 cells, thus further confirming the robustness of the metabolic cycle across genetic backgrounds.

3.4 Metabolic cycles in different carbon sources

To show that the metabolic cycle responds to nutrient conditions and, accordingly, adjusts the cell's metabolism and cell division cycle, I cultured cells in pyruvate and in a growth-limiting glucose concentration. These experiments are important as they confirm conclusions about varying nutrient conditions made by Papagiannakis et al. (2017), but using flavin autofluorescence. Specifically, pyruvate provided an example of a non-fermentable carbon source to test whether the switch from fermentative to respiratory metabolism affected the metabolic cycle. Additionally, a growth-limiting glucose concentration emulated low-glucose concentrations in a chemostat and was thus used to test whether long YMCs observed in such conditions can be replicated in a microfluidics platform.

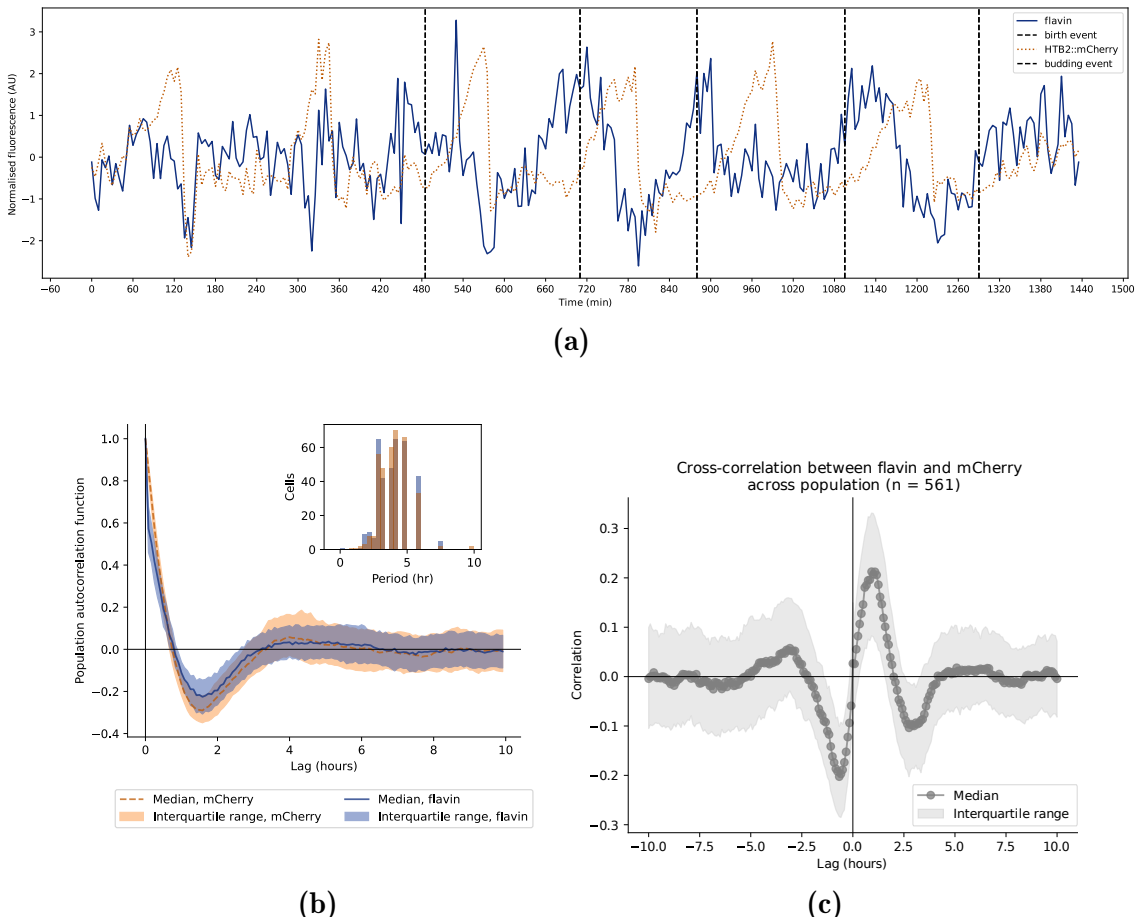


Figure 3.11: (3.11a) Flavin fluorescence (blue, solid lines) and histone 2B (orange, dotted lines) levels in a single, representative FY4 HTB2::mCherry cell grown in 20 g L^{-1} pyruvate. Vertical lines (black, dashed) indicate budding events. (3.11b) Median autocorrelation functions of flavin fluorescence (blue) and histone 2B levels (orange) time series, along with (*inset*) the periods of each oscillator across cells as determined by the frequency with the greatest power in each signal's Fourier spectrum. (3.11c) Median cross-correlation function between flavin and histone 2B signals. Data are from FY4 HTB2::mCherry cells in 20 g L^{-1} pyruvate.

1656 Fig. 3.11 shows that FY4 HTB2::mCherry cells had longer metabolic cycles and
1657 cell division cycles (approximately 4 h) when grown in minimal media supplemen-
1658 ted with 20 g L^{-1} pyruvate, compared to growth in high glucose. Furthermore, the
1659 synchrony between the metabolic cycle and cell division cycle remained, but with
1660 a longer lag (60 min) of the mCherry signal peak with respect to the flavin signal
1661 peak (Fig. 3.11c). Fig. 3.11a shows that the longer cell division cycles were because
1662 of longer G₁ phases but unchanged S/M phases, as evidenced by the longer flat
1663 regions of the mCherry signal.

1664 Fig. 3.12 shows that FY4 HTB2::mCherry cells had longer metabolic cycles when
1665 grown in minimal media supplemented with 0.010 g L^{-1} glucose. Additionally,
1666 Fig. 3.13 shows that the growth rate and the rate of bud formation of cells on
1667 limiting glucose was lower than on high glucose (20 g L^{-1}). Furthermore, Fig.
1668 3.14 shows that the amplitude of the flavin oscillations in this glucose-limiting
1669 condition was low relative to other conditions, as evidenced by the lower signal-
1670 to-noise ratios (two-sided Kolmogorov-Smirnov test: low-glucose vs pyruvate $p =$
1671 1.6×10^{-82} , low-glucose vs high-glucose $p = 1.9 \times 10^{-171}$) Finally, Fig. 3.12b
1672 shows that measurements of the metabolic cycle and the cell division cycle lost
1673 synchrony in limiting glucose. This was evidenced by a 2.5 h average metabolic
1674 cycle, though not robust, but an absence of consistent oscillations in mCherry
1675 intensity. This decoupling can be explained by a lack of cell division cycle events.

X

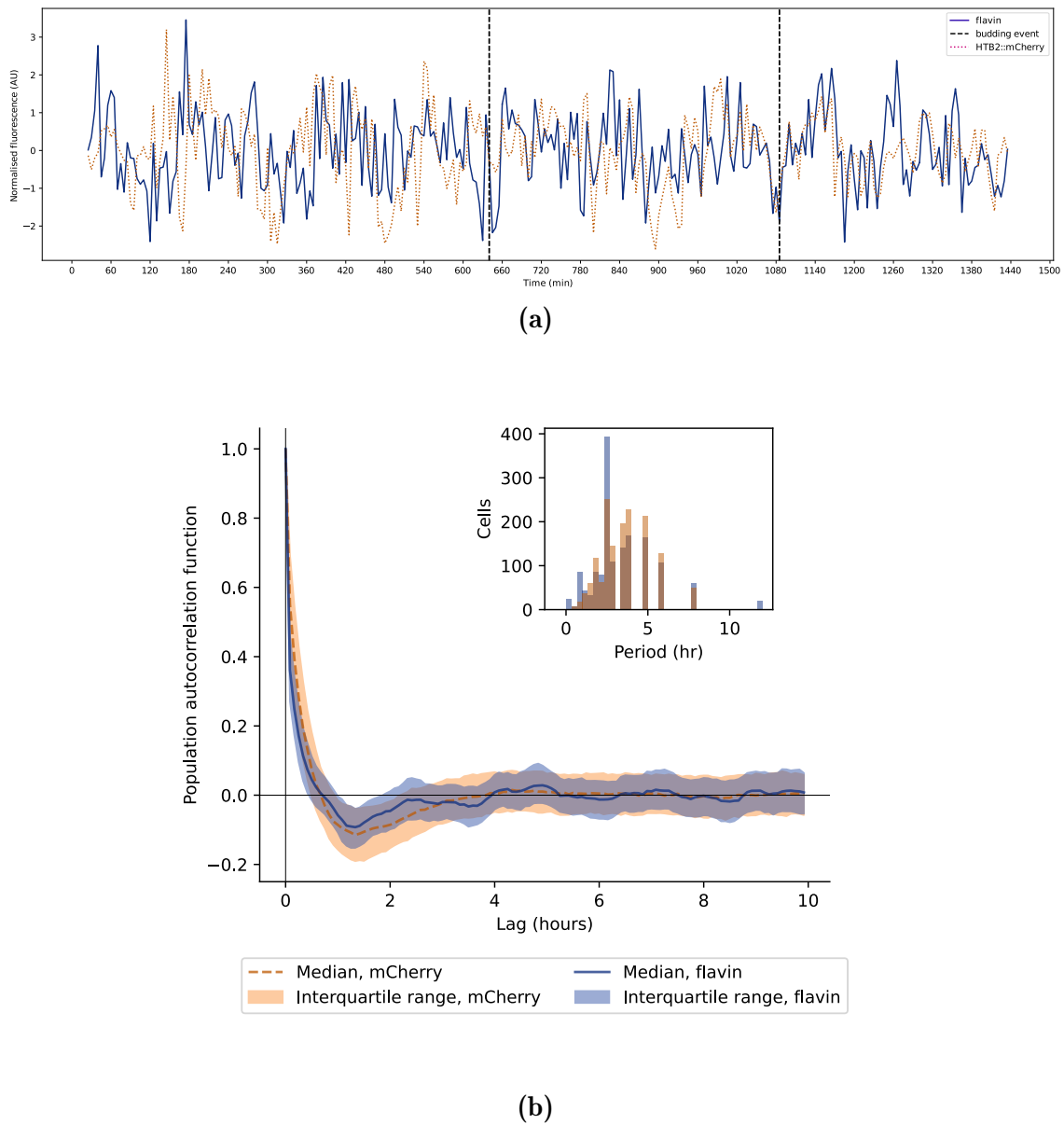


Figure 3.12: **(3.12a)** Flavin fluorescence (blue, solid lines) and histone 2B (orange, dotted lines) levels in a single, representative FY4 HTB2::mCherry cell grown in 0.010 g L^{-1} glucose. Vertical lines (black, dashed) indicate budding events. **(3.12b)** Median autocorrelation functions of flavin fluorescence (blue) and histone 2B levels (orange) time series, along with (*inset*) the periods of each oscillator across cells as determined by the frequency with the greatest power in each signal's Fourier spectrum. Data are from FY4 HTB2::mCherry cells in 0.010 g L^{-1} glucose.

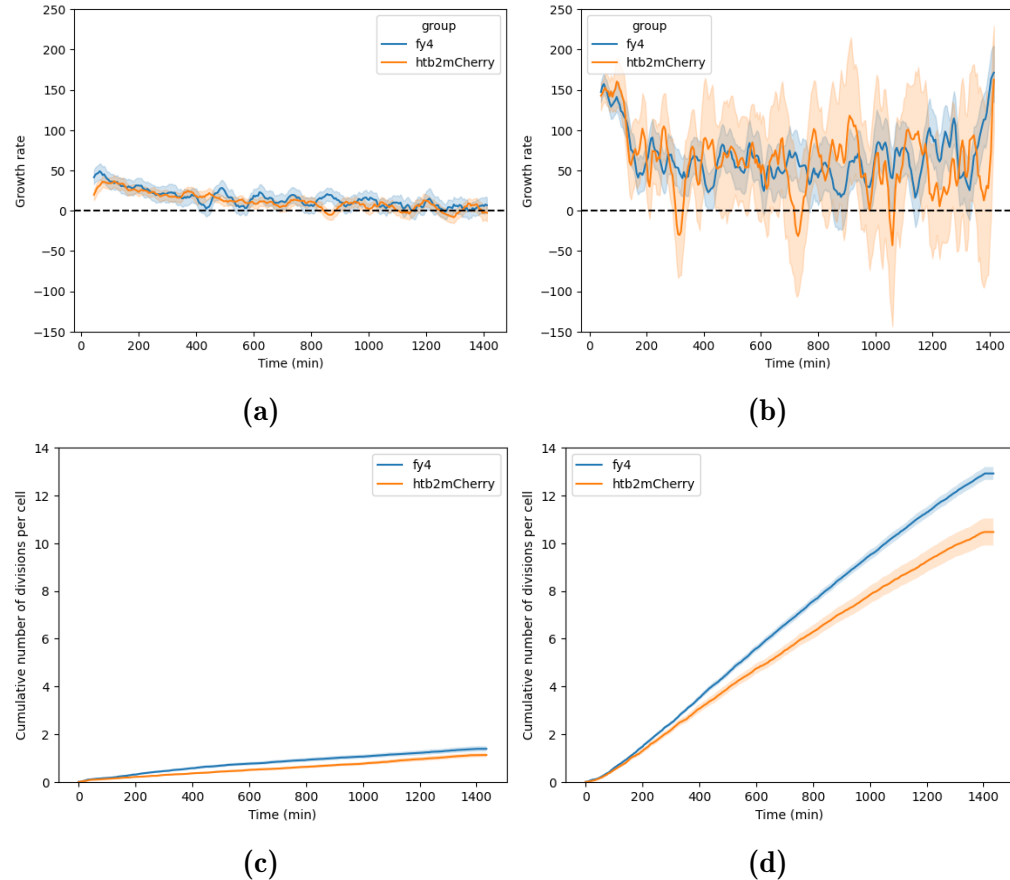


Figure 3.13: Mean growth rate, derived from changes in the sum of estimated parent cell and bud volumes (shading: 95% confidence intervals) of FY4 (blue) and HTB2::mCherry (orange) strains over time, for (3.13a) the glucose-limiting condition (0.010 g L^{-1}) and (3.13b) the high glucose condition (20 g L^{-1}). Similarly, the mean cumulative number of budding events per cell (shading: confidence intervals from bootstrapping, $n = 30$), of the same strains for (3.13c) the glucose-limiting condition and (3.13d) the high glucose condition.

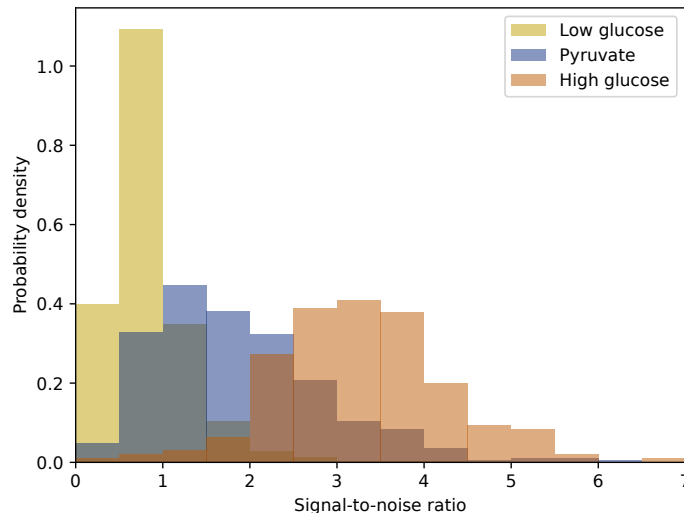


Figure 3.14: Distributions of signal-to-noise ratios of flavin signals from cells in (yellow) 0.010 g L^{-1} glucose, (blue) 20 g L^{-1} pyruvate, and (orange) 20 g L^{-1} glucose. Vertical axis shows probability density, computed by dividing the number of cells in each bin by the total number of cells and then by the bin width.

1676 3.5 Metabolic cycles persist in potassium-deficient me- 1677 dia

1678 To address whether single-cell flavin traces from microfluidic experiments re-
1679 capitulate dissolved-oxygen yeast metabolic cycles in chemostats, I replicated
1680 conditions of chemostat-based studies in which nutrient or genetic perturba-
1681 tions severely affected the metabolic cycle. These nutrient conditions included
1682 potassium deficiency and deletion strains included *zwf1Δ* and *tsa1Δ tsa2Δ*. Rep-
1683 licating conditions of chemostat-based studies is important in showing that the
1684 single-cell metabolic cycle and the chemostat metabolic cycle are the same cycle,
1685 or to prove otherwise. Chemostat experiments obscure the behaviour of individual
1686 cells, and single-cell microfluidics experiments can provide a bottom-up explan-
1687 ation of high-level observations of the metabolic cycle in the chemostat. Such
1688 single-cell experiments could address, for example, whether the cellular behaviour
1689 of the yeast metabolic cycle explains the changes in dissolved-oxygen oscillations.

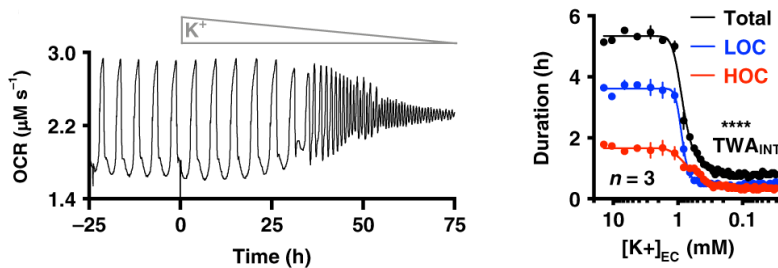


Figure 3.15: Decreasing extracellular potassium (K^+) concentration shortens, then under 1 mmol dm^{-3} , destroys metabolic oscillations in the chemostat. Adapted from O’Neill et al. (2020).

To test whether potassium deficiency eliminates metabolic cycles, I treated cells with potassium-deficient minimal medium, replacing monopotassium phosphate (KH_2PO_4) in the minimal medium with an equivalent molarity of monosodium phosphate (NaH_2PO_4), as described in table 2.2, with both media supplemented with 20 g L^{-1} glucose as a carbon source. O’Neill et al. (2020) suggested that, in chemostat cultures, as potassium in the nutrient medium is gradually replaced with sodium, the period and amplitude of dissolved-oxygen oscillations decrease until the oscillations disappear (Fig. 3.15). Fig. 3.16a shows that FY4 HTB2::mCherry cells retained synchronised metabolic cycles and cell division cycles when cells were abruptly switched from potassium-containing to potassium-deficient minimal medium. Such cycles were longer and were generated less reliably as in the normal growth medium (Fig. 3.16b). In addition, the distribution of signal-to-noise ratios of time series before potassium-deficiency and during potassium-deficiency were identical (Fig. 3.17; two-sided Kolmogorov-Smirnov test, $p = 0.10$), indicating an unchanged amplitude of flavin signal; however, the same was not true when comparing time series during potassium-deficiency and after potassium-deficiency (two-sided Kolmogorov-Smirnov test, $p = 4.09 \times 10^{-7}$).

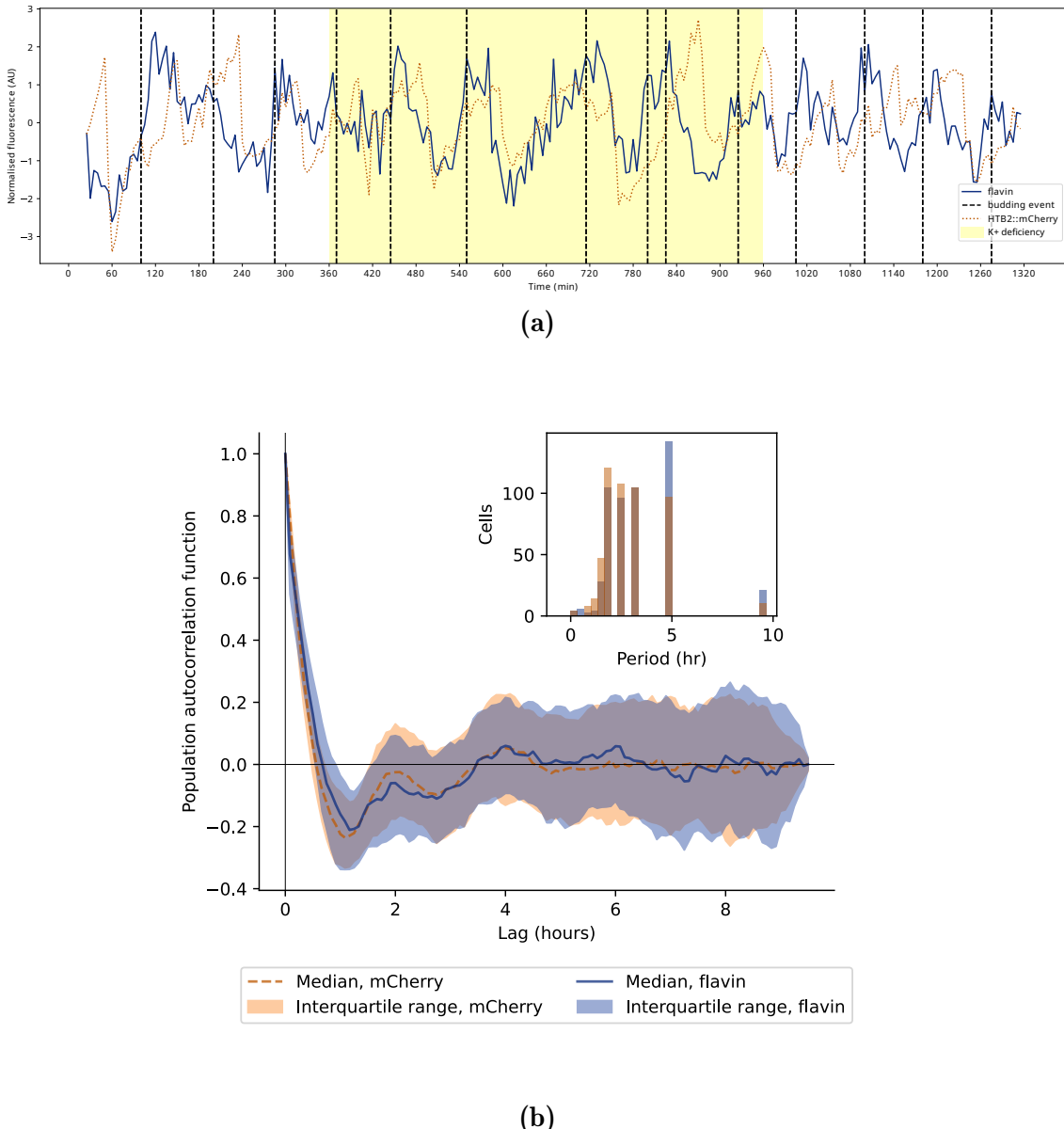


Figure 3.16: (3.16a) Flavin fluorescence (blue, solid lines) and histone 2B (orange, dotted lines) levels in a single, representative FY4 HTB2::mCherry cell. Vertical lines (black, dashed) indicate budding events. Shading (yellow) indicates the potassium-deficient period. (3.16b) Median autocorrelation functions of flavin fluorescence (blue) and histone 2B levels (orange) time series, along with (*inset*) the periods of each oscillator across cells as determined by the frequency with the greatest power in each signal's Fourier spectrum. Data are from FY4 and HTB2::mCherry cells; autocorrelation functions only used time points from the potassium-deficient condition (6 h to 16 h).

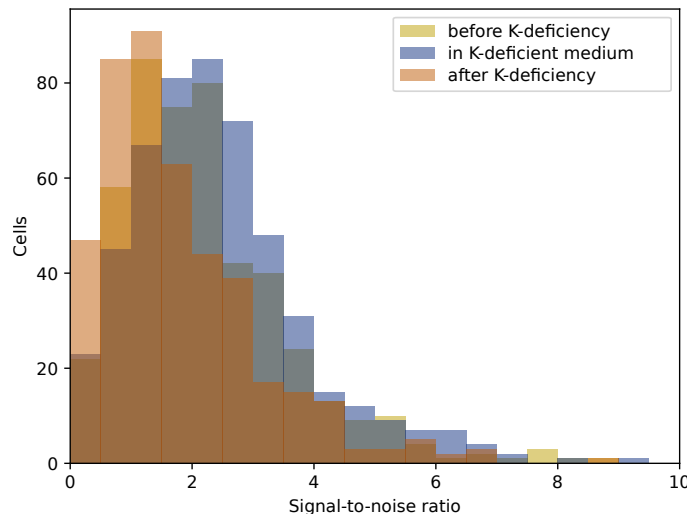


Figure 3.17: Distributions of signal-to-noise ratios of flavin signals from cells before, during, and after potassium-deficiency.

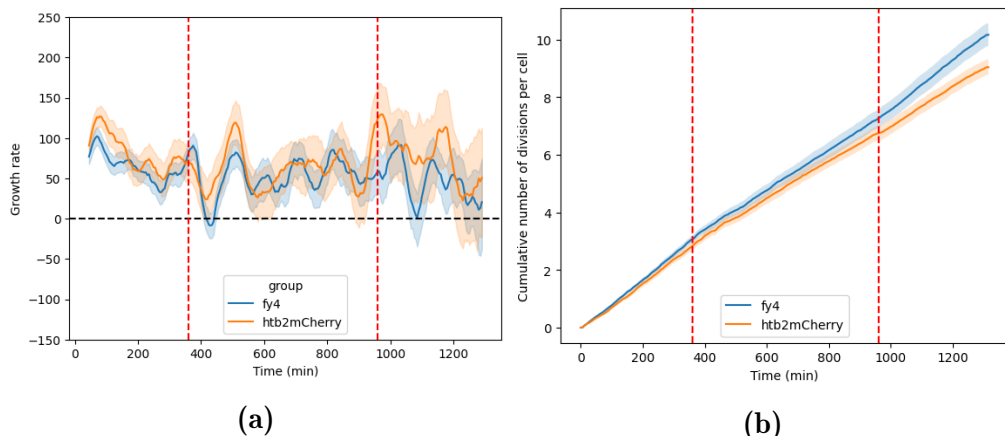


Figure 3.18: (3.18a) Mean growth rate, derived from changes in the sum of estimated parent cell and bud volumes (shading: 95% confidence intervals) and (3.18b) mean cumulative number of budding events per cell (shading: confidence intervals from bootstrapping, $n = 30$) of FY4 (blue) and HTB2::mCherry (orange) strains over time during the potassium-deficient experiment. Vertical lines (red) show changes in the nutrient medium.

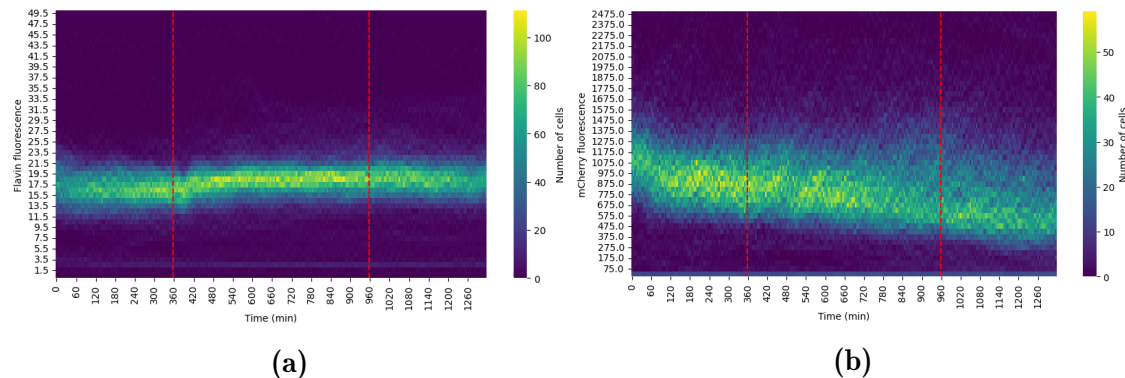


Figure 3.19: Distributions of (3.19a) flavin and (3.19b) mCherry fluorescence over time, for the potassium-deficient experiment. Vertical lines (red, dashed), indicate times of medium changes. Raw time series were used to calculate the distributions.

1707 In addition, to test whether potassium deficiency affected cell growth and division,
 1708 Fig. 3.18a shows that growth rates recovered soon after a sharp decrease upon
 1709 the abrupt switch to the potassium-deficient medium. This global response across
 1710 cells is suggestive of an osmotic response as a result of intracellular potassium
 1711 leaking out the cell, though the change and recovery of growth rate is slower than
 1712 the change and recovery of cell volume in response to osmotic stress reported
 1713 by Granados et al. (2017). Fig. 3.18b further shows that the rate of budding
 1714 was unaffected during potassium-deficiency, in contrast to a pause under glucose
 1715 starvation (Fig. 3.6b). Finally, in contrast to glucose starvation, Fig. 3.19 suggests
 1716 that potassium deficiency did not affect the time each cell spent in each phase of
 1717 the metabolic and cell division cycles as they progressed through growth.

1718 My results thus show that even though there was an initial response to potassium
 1719 depletion, cells resumed growth, division, and generation of metabolic cycles
 1720 soon after. My observations indicate that the metabolic cycle still occurs with
 1721 a consistent amplitude, as evidenced by signal-to-noise ratios, in a drastically

1722 changed nutrient condition, in contrast to O' Neill et al. (2020). Furthermore,
1723 the significance of the potassium-deficient, sodium-containing nutrient condition
1724 is highlighted by the toxicity of sodium ions for budding yeast (Ariño et al., 2010;
1725 Casey et al., 2013; Watcharawipas et al., 2018).

1726 3.6 Metabolic cycles in deletion strains

1727 To continue the investigation of whether single-cell flavin-based metabolic cycles
1728 recapitulate dissolved-oxygen metabolic cycles, I investigated the *zwf1Δ* and *tsa1Δ*
1729 *tsa2Δ* deletion strains. The investigation of deletion strains is important as they
1730 can lead to mechanistic explanations of the YMC.

1731 To investigate whether the *zwf1Δ* strain shows abolition of the metabolic cycle
1732 in single-cell microfluidics, I used a *zwf1Δ* strain with the BY4741 background.
1733 Chemostat-based studies have suggested that in the *zwf1Δ* strain, metabolic
1734 cycles are abolished but with little change in growth rate (Tu, Mohler et al.,
1735 2007). Cells were pre-cultured in 20 g L⁻¹ pyruvate over 48 h and then cultured in
1736 10 g L⁻¹ glucose in the microfluidic device because higher glucose concentrations
1737 disfavour growth in this strain. As the strain had an auxotrophic background, the
1738 required nutrient supplements were also added. Fig. 3.20 shows that the *zwf1Δ*
1739 cells showed oscillations of approximately 3 h, but with low robustness and a wide
1740 distribution of signal-to-noise ratios, while the reference BY4741 strain showed
1741 robust flavin oscillations of approximately 1.5 h. These results conflict with the
1742 results from the chemostat-based study (Tu, Mohler et al., 2007) that suggested
1743 that metabolic cycles are abolished in this strain.

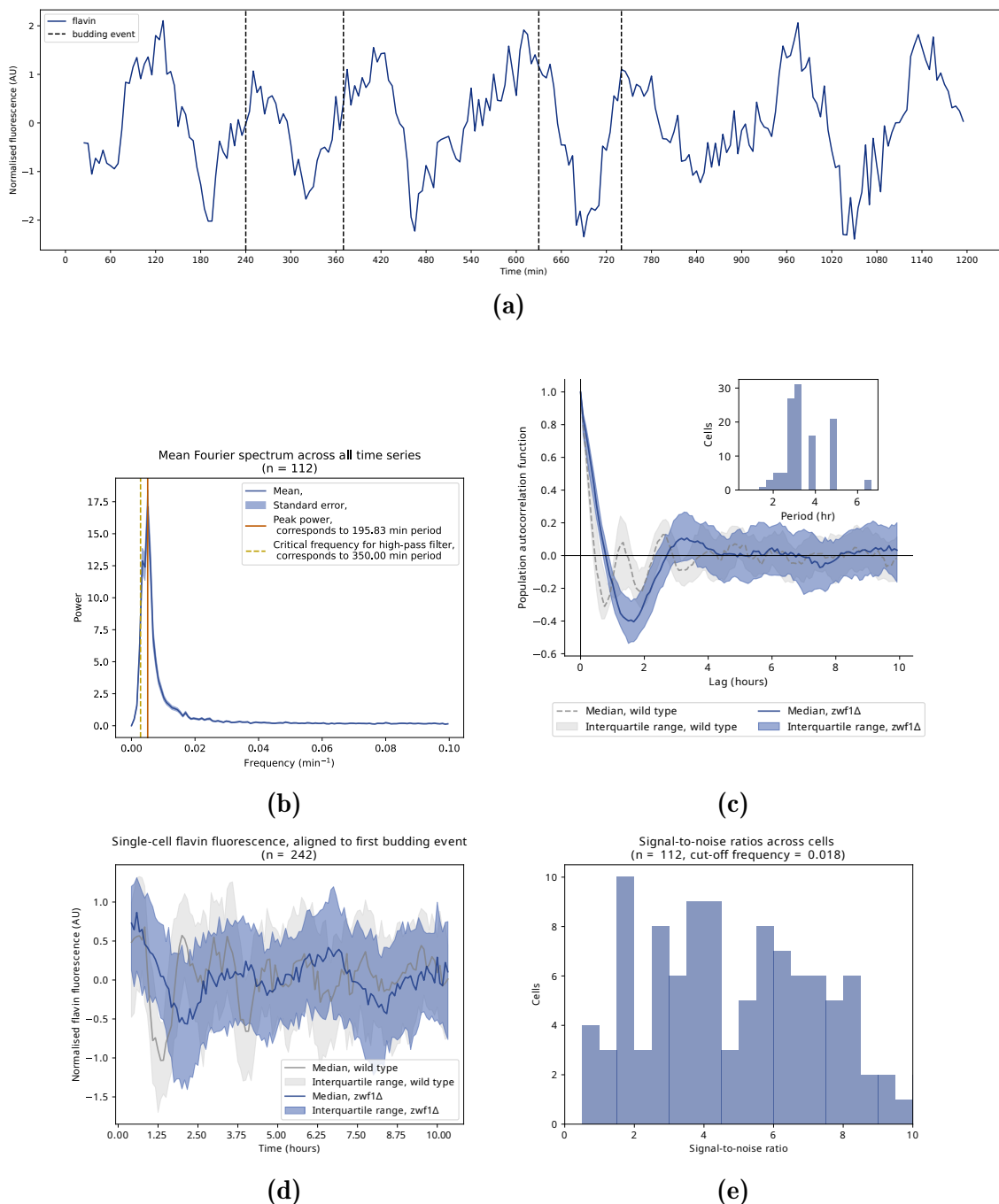


Figure 3.20: **(3.20a)** Flavin fluorescence (blue, solid lines) levels in a single, representative $zwf1\Delta$ cell. Vertical lines (black, dashed) indicate budding events. **(3.20b)** Mean Fourier spectrum of flavin fluorescence across cells. **(3.20c)** Median autocorrelation function of flavin fluorescence time series, along with (*inset*) the periods across cells as determined by the frequency with the greatest power in each signal's Fourier spectrum. **(3.20d)** Median flavin fluorescence signal across cells, aligned to first budding event. **(3.20e)** Distribution of signal-to-noise ratios of flavin signals from cells. Data are from $zwf1\Delta$ (BY4741) cells in 10 g L^{-1} glucose.

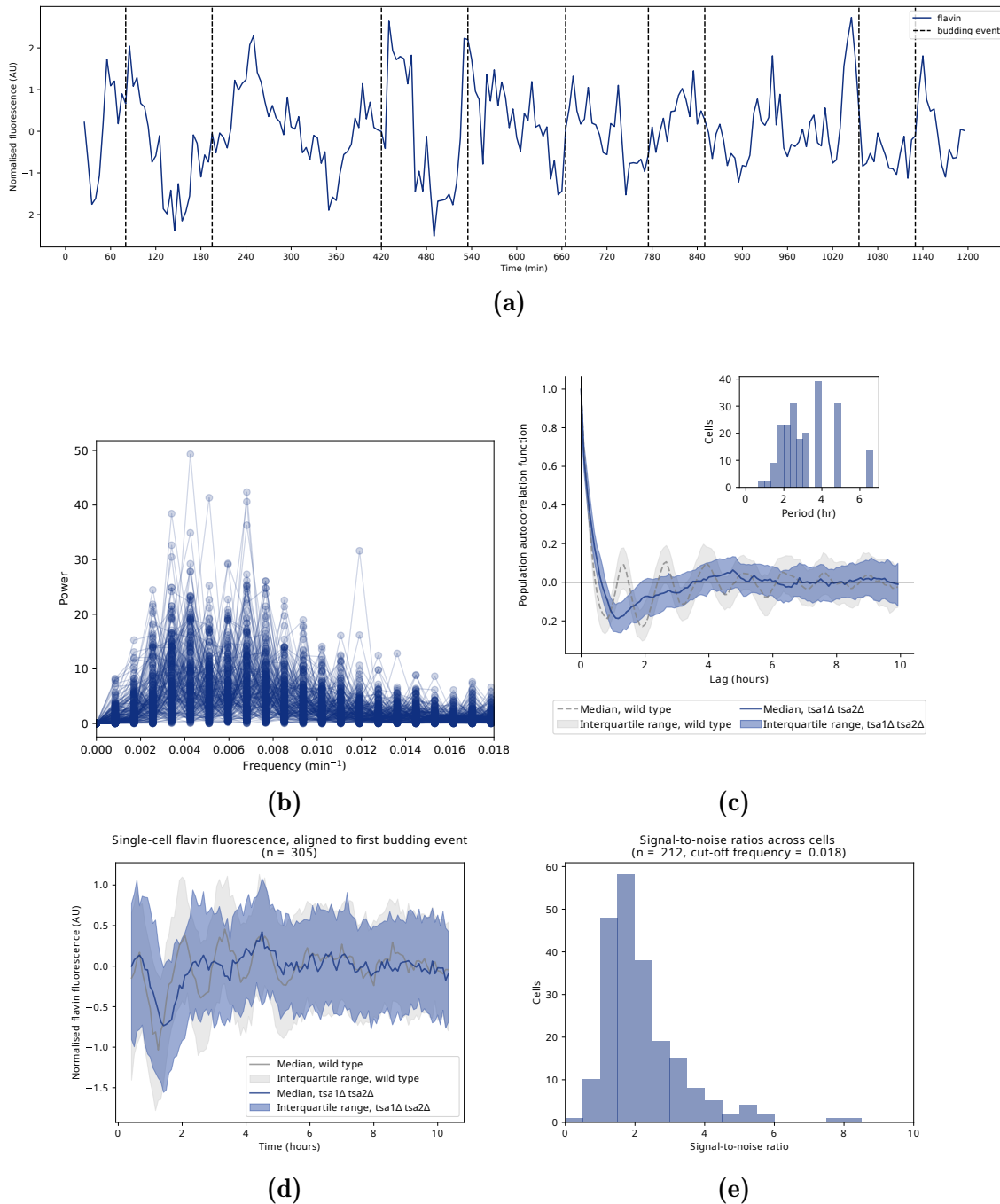


Figure 3.21: (3.21a) Flavin fluorescence (blue, solid lines) levels in a single, representative $tsa1\Delta tsa2\Delta$ cell. Vertical lines (black, dashed) indicate budding events. (3.21b) Overlaid Fourier spectra of flavin fluorescence across cells ($n = 212$). (3.21c) Median autocorrelation function of flavin fluorescence time series, along with (*inset*) the periods across cells as determined by the frequency with the greatest power in each signal's Fourier spectrum. (3.21d) Median flavin fluorescence signal across cells, aligned to first budding event. (3.21e) Distribution of signal-to-noise ratios of flavin signals from cells. Data are from $tsa1\Delta tsa2\Delta$ (BY4742) cells in 10 g L^{-1} glucose.

1744 To investigate whether the *tsa1Δ tsa2Δ* strain shows metabolic oscillations of a
1745 different waveform in single-cell microfluidics, I used a *tsa1Δ tsa2Δ* strain with the
1746 BY4742 background. Chemostat-based studies suggest that in the *tsa1Δ tsa2Δ*
1747 strain, metabolic cycles are shorter and exhibit an M-shaped dissolved oscillation
1748 trace due to an additional dip of oxygen consumption in the reductive-charging
1749 phase (Causton et al., 2015). To be consistent with *zwf1Δ*, cells were pre-cultured
1750 and cultured in the same conditions, but with the appropriate supplements for
1751 the auxotrophy of BY4742.

1752 Fig. 3.21 suggests that the metabolic cycles generated from the auxotrophic *tsa1Δ*
1753 *tsa2Δ* strain were not consistent, likely due to multiple periods. Specifically,
1754 the Fourier spectra (Fig. 3.21b) suggest that 2.45 h and 3.92 h oscillations were
1755 prominent in the population. These two prominent periods were obscured by
1756 the median fluorescence signal aligned by first budding event (Fig. 3.21d), which
1757 merely suggests that a 3 h oscillation was prominent in the population, and by the
1758 median autocorrelation function (Fig. 3.21c), which suggests that the oscillations
1759 were not at a consistent frequency across the population, in contrast to the
1760 BY4742 wild-type that showed robust 1.5 h oscillations. Fig. 3.21e additionally
1761 shows that the amplitudes and qualities of oscillations were retained, as evidenced
1762 by signal-to-noise ratios comparable to the FY4 strain cultured in pyruvate (Fig.
1763 3.14).

1764 Taken together, there are striking discrepancies between the metabolic cycle
1765 observed as dissolved oxygen oscillations from the chemostat and the metabolic
1766 cycle observed as flavin autofluorescence oscillations in single-cell conditions in
1767 the *zwf1Δ* and *tsa1Δ tsa2Δ* deletion strains. These discrepancies warrant further
1768 explanation.

₁₇₆₉ **3.7 Discussion**

₁₇₇₀ **3.7.1 Interpretation of results**

₁₇₇₁ This chapter confirms the presence of flavin-based single-cell metabolic cycles,
₁₇₇₂ and further confirm that they are autonomous and may gate the cell division
₁₇₇₃ cycle across nutrient and genetic perturbations.

₁₇₇₄ My results suggest that yeast cells independently generate the metabolic cycle
₁₇₇₅ which locks the cell division cycle in-phase. This conclusion was supported by the
₁₇₇₆ observation that flavin cycles were asynchronous between cells and peaks coincide
₁₇₇₇ with bud formation. These observations were consistent with Papagiannakis et al.
₁₇₇₈ (2017) and Baumgartner et al. (2018).

₁₇₇₉ Results in pyruvate additionally reveal that as the metabolic cycle lengthens, G₁
₁₇₈₀ lengthens but S/M stays the same length, suggesting a model in which a specific
₁₇₈₁ phase of the metabolic cycle gates entry into the cell division cycle. Importantly,
₁₇₈₂ metabolic cycles still occurred even when cells did not divide. This holds true for
₁₇₈₃ one-off skipping of cell division and conditions in which cells pause cell division
₁₇₈₄ for long periods of time.

₁₇₈₅ My results additionally show that the metabolic cycle and the cell division cycle
₁₇₈₆ can be decoupled, reinforcing the idea that the metabolic cycle is autonomous
₁₇₈₇ from other cellular oscillators. In particular, I observed that single-cell flavin
₁₇₈₈ oscillations could synchronise and reset phase in response to abrupt starvation,
₁₇₈₉ while the cell division cycle was paused. This observation also suggests that
₁₇₉₀ the metabolic cycle is individually generated across cells without the need of a

1791 diffusible metabolite as proposed by Krishna and Laxman (2018). The conclusion
1792 that the metabolic cycle is generated independently across cells is evidenced by
1793 the continued presence of metabolic cycles during starvation even though the cells
1794 were physically separated, with nutrient media perfused across them.

1795 The distributions of flavin and mCherry signals during starvation provided some
1796 mechanistic basis for the coupling or decoupling between the two oscillators. This
1797 observation suggests that if starvation occurs before START, the cell remains in
1798 the G₁ phase. Otherwise, the cell proceeds through the cell division cycle until it
1799 pauses in the G₂ phase. Such observations strengthen the idea that the metabolic
1800 cycle independently gates the early (START) and the late (mitotic exit) phases of
1801 the cell division cycle (Özsezen et al., 2019). However, the biochemical mechanism
1802 by which the cell uses to reset the phase of its metabolic cycle remains unclear.

1803 My observations confirm that cells adapt their metabolic cycle to nutrient condi-
1804 tions: the metabolic cycle lengthened when cells were grown on pyruvate, while
1805 the cycle exhibited a lengthened period and a lower amplitude when cells were
1806 grown on low glucose. A possible explanation is that nutrient conditions that
1807 favour respiration over fermentation — and thus slower growth rate — leads to
1808 slower YMCs.

1809 My results suggest discrepancies between chemostat and single-cell studies of the
1810 metabolic cycle, in particular, with regards to potassium-deficient conditions and
1811 the *zwf1Δ* and *tsa1Δ tsa2Δ* deletion strains. Such discrepancies warrant models
1812 to explain the observations. Alternatively, these discrepancies may represent ad-
1813 ditional cases in which the metabolic cycle is observed in single cells in conditions
1814 previously thought to be unfavourable based on chemostat observations, as was
1815 the case for metabolic cycles in high-glucose conditions.

1816 I observed that metabolic cycles persist in potassium-deficient conditions, in
1817 contrast to O' Neill et al. (2020) which suggested that the oscillations disappear.
1818 The disappearance of dissolved oxygen cycles can alternatively be explained by
1819 a loss of synchrony in the population. However, while O' Neill et al. (2020)
1820 gradually replaced potassium with sodium over a longer period of time, my
1821 experiments included an abrupt potassium depletion but over a shorter period of
1822 time. Therefore, the carbohydrate or amino acid stores that O' Neill et al. (2020)
1823 proposed were responsible for metabolic oscillations may still have been sufficient
1824 to drive metabolic oscillations during potassium-deficiency in my experiment.

1825 I also observed that *zwf1Δ* exhibited metabolic cycles, though with varying amp-
 1826 ^{with}litudes. This contrasts Tu, Mohler et al. (2007), which suggested that metabolic
1827 cycles in this strain were abolished To reconcile findings, a potential explanation
1828 is that cells lose synchrony or the ability to reset phase, while growth is still
1829 maintained. *ZWF1* codes for glucose-6-phosphate dehydrogenase, which catalyses
1830 the first step of the pentose phosphate pathway involving the reduction of NADP⁺
1831 to produce NADPH, a key metabolite in the YMC (Nogae and Johnston, 1990).
1832 Thus, it is expected that the *zwf1Δ* deletion should affect a broad range of
1833 metabolic processes, including flavin oscillations, owing to the role of NAD(P)H
1834 redox in the function of the most abundant flavoproteins (Gudipati et al., 2014).
1835 However, some of the deleterious effects of *zwf1Δ* deletion may be compensated by
1836 *ALD6* and *IDP2* as they also catalyse reactions that produce NADPH (Minard
1837 and McAlister-Henn, 2005), therefore, explaining why growth is retained in the
1838 *zwf1Δ* strain.

1839 My results additionally suggest that *tsa1Δ tsa2Δ* exhibits a range of metabolic
1840 cycle frequencies. This observation can be reconciled with the M-shaped dissolved
1841 oxygen cycles described by Causton et al. (2015) through a potential explanation:
1842 there are at least two substantial cell populations that each produce a different

1843 frequencies of metabolic oscillations, and the changed M-shaped waveform is the
1844 sum of the effect of individual cells. *TSA1* and *TSA2* are paralogous genes that are
1845 involved in redox metabolism. Specifically, these genes code for peroxiredoxins as
1846 part of the peroxiredoxin-thioredoxin system, which functions to reduce intracellu-
1847 lar reactive oxygen species (Wong et al., 2002). In addition, these genes have been
1848 suggested to be linked to the circadian rhythm, as evidenced by an approximately
1849 24 h oscillation in oxidation patterns (Edgar et al., 2012). Therefore, deletion of
1850 these genes may lead to loss of regulation of timekeeping, leading to the different
1851 oscillation frequencies.

1852 Taken together, the discrepancies between chemostat and single-cell studies high-
1853 light the role of sub-populations that cannot be captured in the chemostat, but
~~1854 possibly~~ in single-cell studies.

1855 3.7.2 Study caveats and future directions

1856 Characteristics of the single-cell metabolic cycle

1857 Time series of NAD(P)H oscillations, especially if recorded alongside flavin in
1858 the same cells, would strengthen the evidence that flavin autofluorescence oscilla-
1859 tions are equivalent to the single-cell metabolic oscillations described by previous
1860 microfluidics studies. Such data would also provide a novelty: two fluorophores
1861 that act as read-outs of the metabolic cycle have, to my knowledge, never been
1862 recorded from the same cell.

1863 To explore the link between the components of flavin autofluorescence and cycling
1864 of storage lipids as a proposed biochemical mechanism of the metabolic cycle, the
1865 *fas1Δ* strain may be studied. *FAS1* codes for the most abundant flavoprotein,
1866 the beta subunit of fatty acid synthetase, which has a role in lipid metabolism

1867 (Gudipati et al., 2014). The investigation may be strengthened with a rescue ex-
1868 periment using lipid sources such as glycerol trihexanoate or glycerol trioctanoate.
1869 This avenue of exploration may lead to additional insight on the biochemical basis
1870 of the yeast metabolic cycle, which is still poorly characterised.

1871 To explore the conditions that make budding yeast cells reset their metabolic cycle
1872 phases, future experiments may include adding carbon sources in bulk, using the
1873 media-switching system of ALCATRAS. Such experiments could include acetate,
1874 acetaldehyde, or ethanol (Kuang et al., 2017; Krishna and Laxman, 2018). Insights
1875 from such experiments may lead to a broader understanding of the control of the
1876 sequence of events in the metabolic cycle.

1877 **Chemostat vs single-cell**

1878 Additional nutrient conditions can be used to address the discrepancies between
1879 the chemostat and single-cell microfluidics, namely, low glucose conditions and
1880 feast-and-famine conditions.

1881 Low glucose conditions emulate conditions in the chemostat and may lead to long
1882 metabolic cycles, thus explaining why cycles with periods up to 14 h have been
1883 observed in chemostats. However, the glucose concentrations in chemostats are
1884 below the tolerance of measurement with current technologies; therefore, I propose
1885 that the limiting concentration of 0.010 g L^{-1} is used. Experiments with deletion
1886 strains can then be performed under these low-glucose conditions to investigate
1887 whether such conditions lead to a closer equivalence between chemostat and
1888 single-cell studies.

1889 Feast-and-famine conditions have been modelled in chemostat cultivation of yeast
1890 (K. D. Jones and Kompala, 1999). Further experiments can therefore use rapid
1891 media-switching in ALCATRAS to produce regular glucose pulsing. In this type
1892 of experiment, cells are fed with a glucose-limited medium for an amount of
1893 time, then switched on to a glucose-rich medium for a short period of time
1894 (approximately 10 min), and the cycle repeats. The interval between glucose
1895 pulses can be varied to investigate the effect of an external entraining mechanism
1896 on the system of coupled oscillators that defines the yeast metabolic cycle. This
1897 design would be similar to Charvin et al. (2009), which investigated the effect of
1898 intervals of glucose pulsing on the cell division and circadian cycles in budding
1899 yeast. A glucose pulsing experiment can thus also lead to a mathematical model
1900 of coupled oscillations in the yeast metabolic cycle.



Chapter 4

1901

1902 **Analysis of oscillatory time series in** 1903 **the yeast metabolic cycle**

1904 Short and noisy oscillatory time series are challenging to analyse to give usable
1905 characteristics such as period and phase, especially because of the limited in-
1906 formation they encode. Microfluidics experiments capture up to 5–10 periods of
1907 metabolic cycles, so a Fourier spectrum gives period estimates at low resolution.
1908 In addition, there is no standard method of analysing oscillatory time series such
1909 as those that arise from the yeast metabolic cycle.

1910 To characterise the properties of large sets of time series generated by microfluidics
1911 experiments, I sought to develop a pipeline of time series analysis methods.

1912 Here, I propose steps for the analysis of datasets of 100–1000 time series related
1913 to the yeast metabolic cycle from single cells, using my experimental data as an
1914 example case.

1915 Specifically, this chapter focuses on:

- 1916 1. Data cleaning: choosing data and filtering out long-term trends that may
1917 confound analysis.
- 1918 2. Visualising groups in a dataset: identifying groups within a population of
1919 time series based on their similarities. Such a relationship may include
1920 groupings or structures within the population of time series.

- 1921 3. Detection of rhythmicity: determining whether a time series exhibits oscil-
1922 lations.
- 1923 4. Period estimation: identifying the period of a single time series.
- 1924 5. Detection of synchrony: identifying whether two types of signal from the
1925 same cell are synchronous, and to what extent.
- 1926 In this chapter, I show that a high-pass Butterworth filter gives control over fre-
1927 quencies when filtering out long-term trends. To discover structure within a data-
1928 set, I show that UMAP, a dimension-reduction technique, and modularity clus-
1929 tering, a community detection technique, led to similar groupings. Subsequently,
1930 I compared three approaches to rhythmicity detection: a statistical test based on
1931 a spectral method, model-fitting and analytically computing a periodogram, and
1932 a simple machine learning model. To estimate the period and noise parameters
1933 of time series, I then explored the effect of noise on the autocorrelation function
1934 of synthetic time series. Finally, I used the cross-correlation function to detect
1935 synchrony and to quantify the relationship between two types of oscillators.

1936 4.1 Analysing time series in a biological context

1937 Previous studies have described computational pipelines that included mathem-
1938 atical methods to analyse biological time series. Zieliński et al. (2022) described
1939 a software pipeline (BioDare/BioDare2), catered to circadian rhythm studies, to
1940 estimate the period and detect rhythmicity in time series. This pipeline includes
1941 choices of methods to detrend and normalise time series, followed by a choice
1942 of methods to estimate the period, phase, and amplitude of the time series.
1943 Furthermore, the pipeline also includes statistical tests for the presence of an
1944 oscillation in a time series: an implementation of the JTK_CYCLE test (Hughes
1945 et al., 2010) along with an empirical derivative (Hutchison et al., 2015).

1946 The software BioDare2 builds upon Zielinski et al. (2014), which compared and
1947 contrasted a set of period-estimation methods — FFT-NLLS, mFourFit, MESA,
1948 the Enright periodogram, the Lomb-Scargle periodogram, and spectrum resampling
1949 — to conclude with recommendations on time series analysis.

1950 Studies of biological rhythms have used the BioDare pipeline to quantify features
1951 of oscillations of fluorescence. These included using FFT-NLLS to calculate the
1952 period and amplitude error of fluorescence in mouse brain sections to determ-
1953 ine the mechanistic basis of the synchronisation of the suprachiasmatic nucleus
1954 (Hamnett et al., 2019). Another study used linear detrending of data followed by
1955 FFT-NLLS and spectral resampling to estimate the period and amplitude error of
1956 delayed fluorescence of chloroplasts in *Kalanchoë fedtschenkoi* leaves to determine
1957 whether phosphorylation of phosphoenolpyruvate affects robustness of circadian
1958 rhythms (Boxall et al., 2017).

1959 In addition, Fulcher and N. S. Jones (2017) described a software pipeline, termed
1960 *hctsa*, that computes over 7700 time series features for input time series. The
1961 resulting feature matrix — a row for each time series and a column for each feature
1962 — could then be used to identify sets of features that are useful to discriminate
1963 between sets of time series or to identify clusters of time series based on their
1964 properties. The publication then showed that *hctsa* could be used to distinguish
1965 five *Caenorhabditis elegans* strains based on their movement patterns, and to
1966 identify clusters in the feature space of time series of *Drosophila melanogaster*
1967 movement patterns which correspond well to experimental groups. To reduce
1968 computation time, Lubba et al. (2019) identified 22 features, termed *catch22*, of
1969 *hctsa* that performed well in time series classification tasks based on 93 datasets
1970 (Table A.1 in Appendix A.1).

1971 Taken together, the two examples of BioDare and *hctsa* demonstrate two ap-
1972 proaches to analysis of time series: on one end, relying on mathematical methods,
1973 and on the other end, a data science approach to time series classification tasks.

1974 4.2 Data cleaning: filtering out long-term trends

1975 Biological time series often have long-term trends. In my study of the yeast
1976 metabolic cycle, such trends include slow, global changes in flavin autofluor-
1977 escence, which must be removed to uncover the periodic behaviour of flavin
1978 autofluorescence that is a component of the metabolic cycle. To determine the
1979 detrending method that is most appropriate for my data, I compared a frequency
1980 filtering method with a sliding-window detrending method.

1981 To demonstrate the use of a method that modifies the frequency profile of time
1982 series to remove trends, Figs. 4.1a–4.1b show how a time series and its Fourier
1983 spectrum changes after the application of a high-pass Butterworth filter with
1984 a critical frequency of $2.86 \times 10^{-3} \text{ min}^{-1}$, corresponding to a period of 350 min.

1985 Defining a signal filter offers direct control over frequencies. The critical frequency
1986 was chosen as a reasonable upper limit of periods of the yeast metabolic cycle,
1987 based on my observations in single-cell microfluidics experiments. Defining the
1988 critical frequency in this way excludes the possibility of metabolic cycles that have
1989 very long periods in favour of emphasising metabolic oscillations of an expected
1990 frequency.

1991 To show how sliding-window methods may adversely affect the frequency profile
1992 of time series when used for detrending, I computed the Fourier spectrum of time
1993 series detrended using the moving average method. Sliding-window methods are
1994 common in detrending biological time series. For example, Cuny et al. (2022)

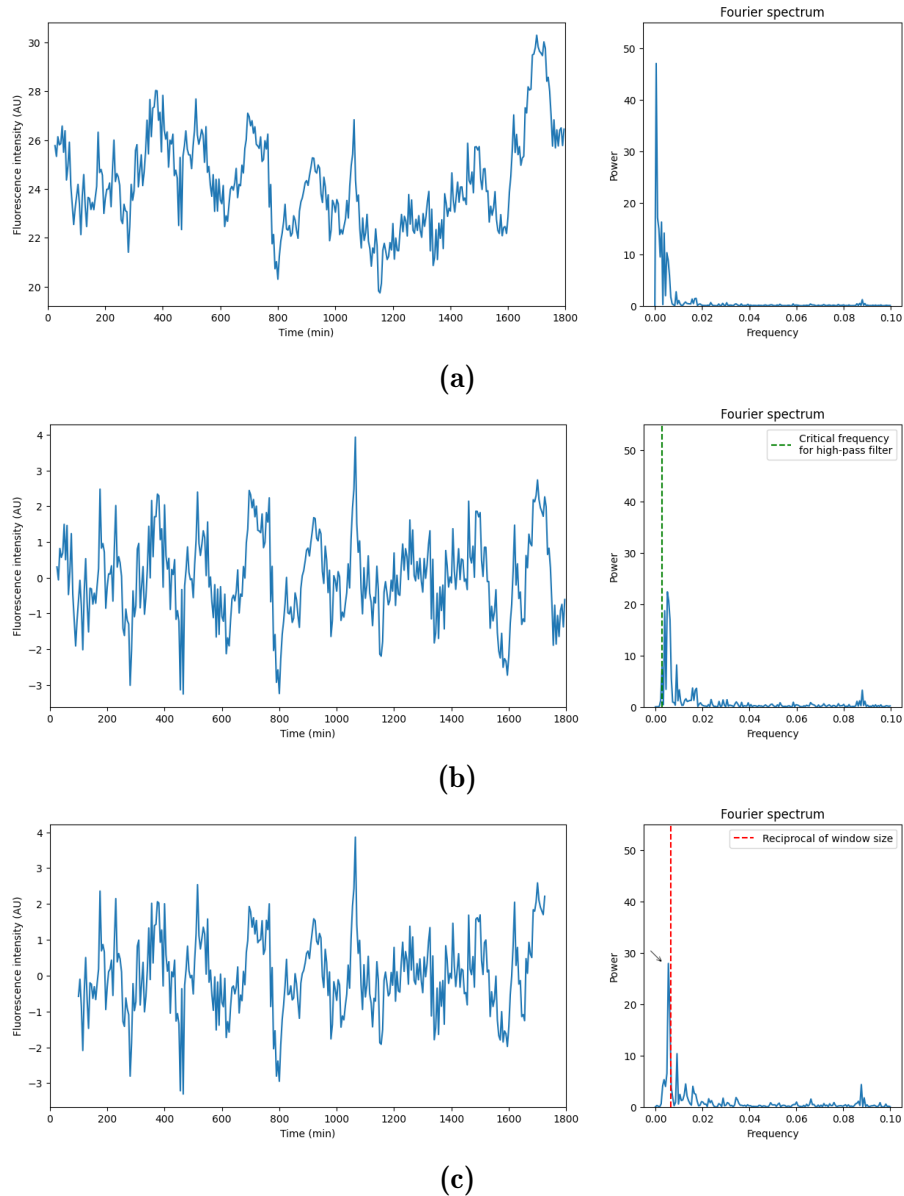


Figure 4.1: (Left panels) Time series and (right panels) Fourier spectra corresponding to (4.1a) a sample raw time series of flavin autofluorescence, (4.1b) the time series processed by a high-pass Butterworth filter with a critical frequency $2.86 \times 10^{-3} \text{ min}^{-1}$, and (4.1c) the time series detrended using a moving average (window size 30 time points). Arrow (\searrow) indicates artefact.

1995 used a moving average: a constant, defined sliding window to smooth time series
1996 of yeast cell mass during growth. Fig. 4.1c shows that the moving average method
1997 introduced an artefact in the frequency spectrum near the reciprocal of the
1998 window size and decreases the number of time points.

1999 4.3 Visualising groups in the dataset

2000 To identify structures in datasets of time series, I implemented UMAP, a dimension-
2001 reduction method, and modularity clustering, a graph-based clustering method.
2002 Such data visualisation methods are important because the structures they show
2003 may identify differences between groups that are biologically relevant — for
2004 example, sub-populations of oscillations with similar properties. Previous efforts
2005 in using computational methods to identify groups in a set of biological time series
2006 include using k -means clustering to identify clusters of transcript cycling patterns
2007 that correspond to phases of the YMC (Tu, Kudlicki et al., 2005), development of
2008 a method to cluster featurised multivariate time series based of videos of human
2009 motion (Wang et al., 2007), and using signal entropy to featurise fMRI signals
2010 followed by modularity clustering to partition the signals into brain regions.

2011 To demonstrate the data visualisation methods, I used time series of flavin auto-
2012 fluorescence oscillations from one experiment with both the wild-type BY4741
2013 strain ($n = 206$) and the mutant $zwf1\Delta$ strain ($n = 425$). These time series had
2014 time points sampled every 5 min in the experiment, for a total of 163 time points.
2015 I manually labelled the time series to indicate whether they were oscillatory or
2016 not, with 142 of the 206 BY4741 time series classed as oscillatory and 224 of the
2017 425 $zwf1\Delta$ classed as oscillatory.

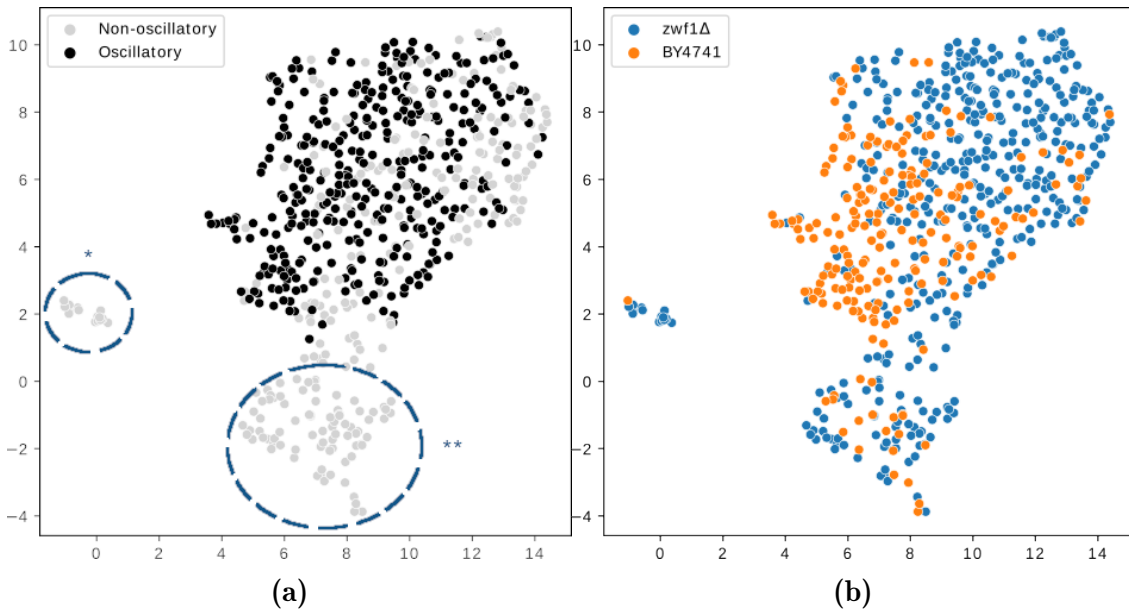


Figure 4.2: UMAP embedding ($n = 5$, $\text{min_dist} = 0.5$, $d = 2$, Euclidean distance as the metric) of a dataset of time series featurised using *catch22*. Each node represents a time series, coloured either by (4.2a) whether each is oscillatory or not, human-labelled (* and ** indicating two groups of non-oscillatory nodes of interest), or by (4.2b) strain ('BY4741' or 'zwf1 Δ ').

2018 4.3.1 UMAP

2019 UMAP (McInnes et al., 2020) is an unsupervised dimension reduction method
 2020 that can be used to visualise structure in a dataset. Specifically, UMAP aims to
 2021 find a manifold structure of the input observations and compute a low-dimensional
 2022 embedding that preserves the topological structure of the manifold. This embed-
 2023 ding thus serves as coordinates to plot the data onto a low-dimensional space.

2024 To evaluate whether UMAP was able to discover a structure within the BY4741
 2025 & zwf1 Δ dataset that corresponded to meaningful divisions, I featurised the time
 2026 series with *catch22*, then used UMAP to compute two-dimensional embeddings.
 2027 Fig. 4.2a demonstrates that UMAP suggested a small group of non-oscillatory
 2028 time series that differed markedly from the rest (*) in figure), and a larger group
 2029 that was more similar to oscillatory time series (** in figure). In addition, Fig.
 2030 4.2b demonstrates that UMAP suggested that the BY4741 time series were more

similar to each other. In contrast, *zwf1Δ* occupied larger regions of the embedding space. These embeddings agreed with my observation that time series from the *zwf1Δ* strain had a larger variety of shapes and oscillation quality than the BY4741 strain. Thus, UMAP may have potential to separate oscillatory and non-oscillatory time series, or time series of different shapes.

To improve the visualisation, I performed a grid search of the *n* and *min_dist* UMAP hyperparameters (Appendix A.2) to find the best combination. Fig. 4.3 suggests that $50 \leq n \leq 150$ and $0.25 \leq \text{min_dist} \leq 1$ resulted in a good separation between the BY4741 and *zwf1Δ* nodes. In addition, non-oscillatory time series were consistently displayed into groups separate from the rest as the hyperparameters were varied.

4.3.2 Graph-based clustering

Modularity clustering is a mathematical method that partitions a graph into groups to optimise a ‘modularity’ value, defined so that the method finds a trade-off between maximising the connections within a cluster and minimising the connections between clusters (Newman, 2006). This optimisation problem is computationally difficult, so approximations such as the Louvain algorithm are needed for large networks (Blondel et al., 2008), with the Leiden algorithm (Traag, L. Waltman et al., 2019) subsequently developed to ensure that communities are well-connected and to provide an optimum number of communities. Furthermore, the intrinsic scale of modularity scales with the square root of the number of connections in the network; therefore, if the network is large, there is a large resolution limit, preventing a modularity clustering algorithm from detecting

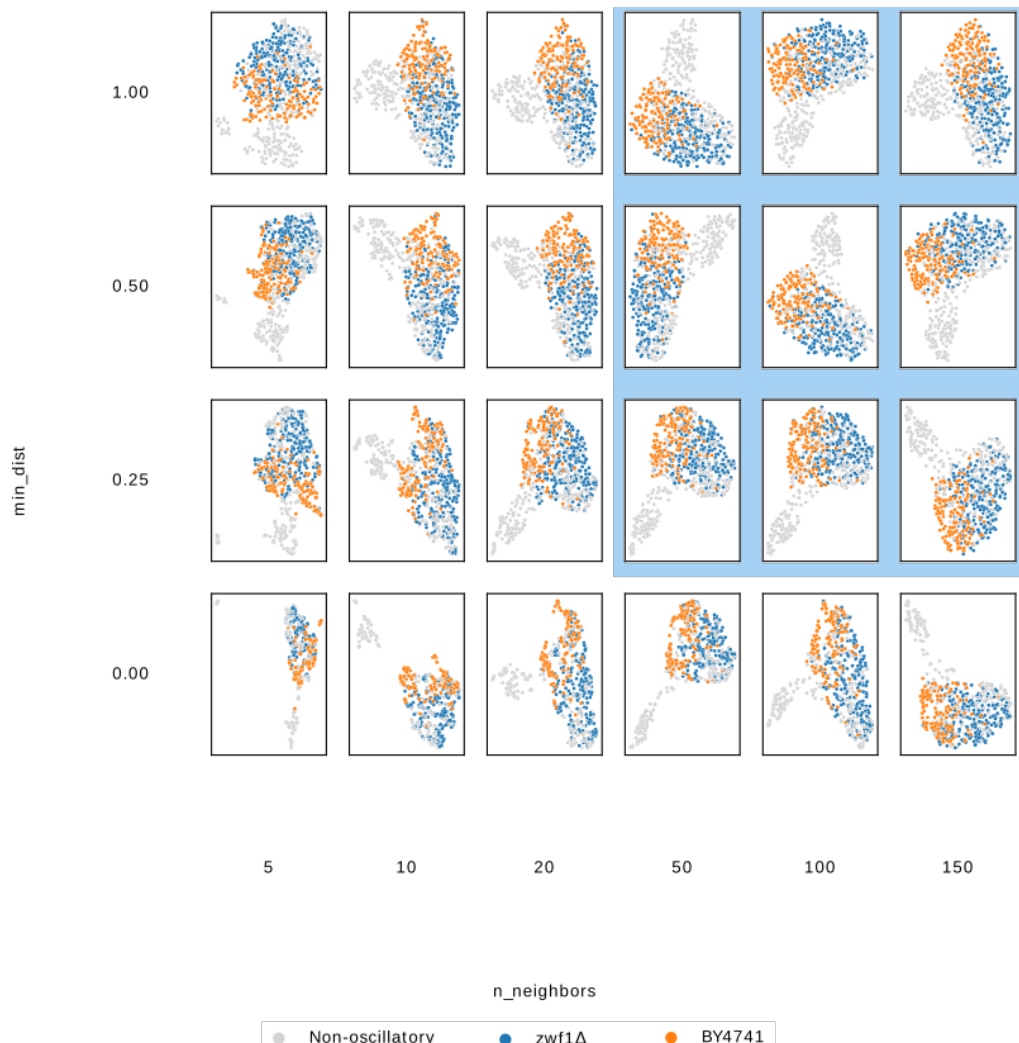


Figure 4.3: Grid search of UMAP hyperparameters: number of neighbours along the horizontal axis and minimum distance along the vertical axis. Data points are coloured according to category: grey indicates non-oscillatory time series, blue indicates oscillatory time series from *zwf1Δ* cells, and orange indicates oscillatory time series from BY4741 cells.

2054 small-scale structures (Fortunato and Barthélemy, 2007; Traag, Van Dooren et
2055 al., 2011). To remedy this, algorithms that implement a resolution parameter
2056 (γ), were devised; the value of this parameter thus controls the scale at which
2057 communities are detected (Reichardt and Bornholdt, 2004; Kumpula et al., 2007).

2058 To assess the performance of a graph-based clustering method in identifying
2059 clusters in time series data, I represented a dataset of time series as a graph
2060 before using modularity clustering to identify clusters. Fig. 4.4 illustrates this
2061 process, specifically:

- 2062 1. *Constructing a graph representation*: Each time series was represented as
2063 a vector of features in n -dimensional space, where n is the length of the
2064 vector. Here, I represented each time series with a vector of 22 features using
2065 *catch22*. The cosine distances between each pair of vector was computed,
2066 and became the edge weights of a complete graph with each time series as
2067 a node.
- 2068 2. *Pruning*: The complete graph was pruned by deleting edges, so that each
2069 node was connected to at least the k nearest neighbours. I used $k = 10$.
- 2070 3. *Modularity clustering*: Modularity clustering was performed on the graph
2071 to partition the pruned graph into communities. In this step, I used the
2072 constant Potts model (Traag, Van Dooren et al., 2011) and the Leiden
2073 algorithm (Traag, L. Waltman et al., 2019).

2074 Fig. 4.5a shows that construction of a pruned graph based on similarities between
2075 time series highlights two groups of non-oscillatory time series. Subsequently,
2076 Figs. 4.5b–4.5d show that the resolution parameter (γ) controls the number of
2077 communities detected. Non-oscillatory time series were assigned to a separate
2078 group when $\gamma = 0.01$, and the two sub-groups of non-oscillatory time series
2079 were separated when $\gamma = 0.02$; however, when $\gamma = 0.03$, the divisions changed.
2080 The Leiden algorithm (Traag, L. Waltman et al., 2019) suggested 10 as the

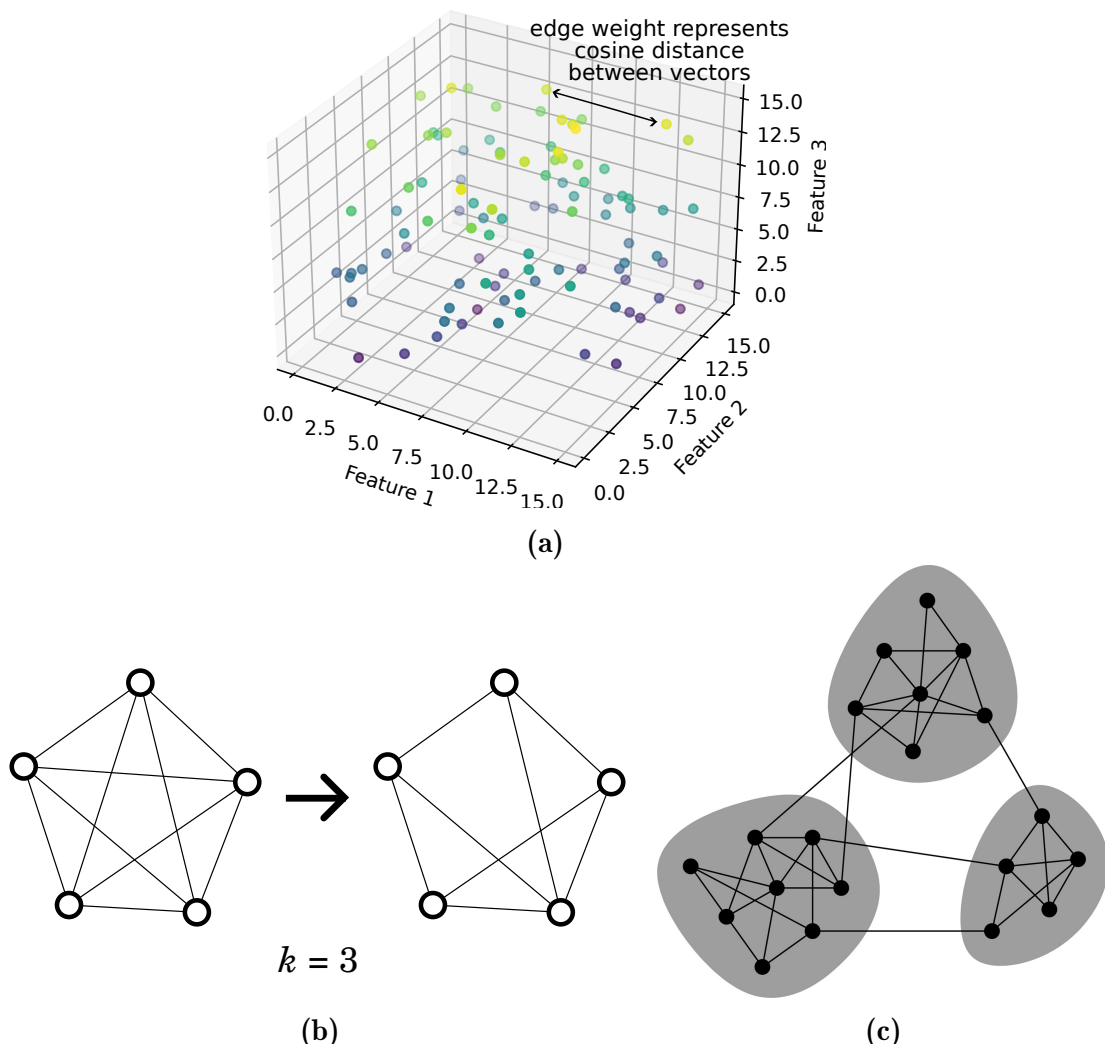


Figure 4.4: Process of preparing a dataset of time series for modularity clustering. **(4.4a)** Constructing a graph representation: each time series was featurised and the cosine distances in feature space became edge weights. **(4.4b)** Pruning the complete graph so that each node had at least the k nearest neighbours. **(4.4c)** Modularity clustering, using the Leiden algorithm (Traag, L. Waltman et al., 2019), to identify communities. 4.4c adapted from Newman (2006). In all subfigures, data are synthetic and only serve to illustrate the process.

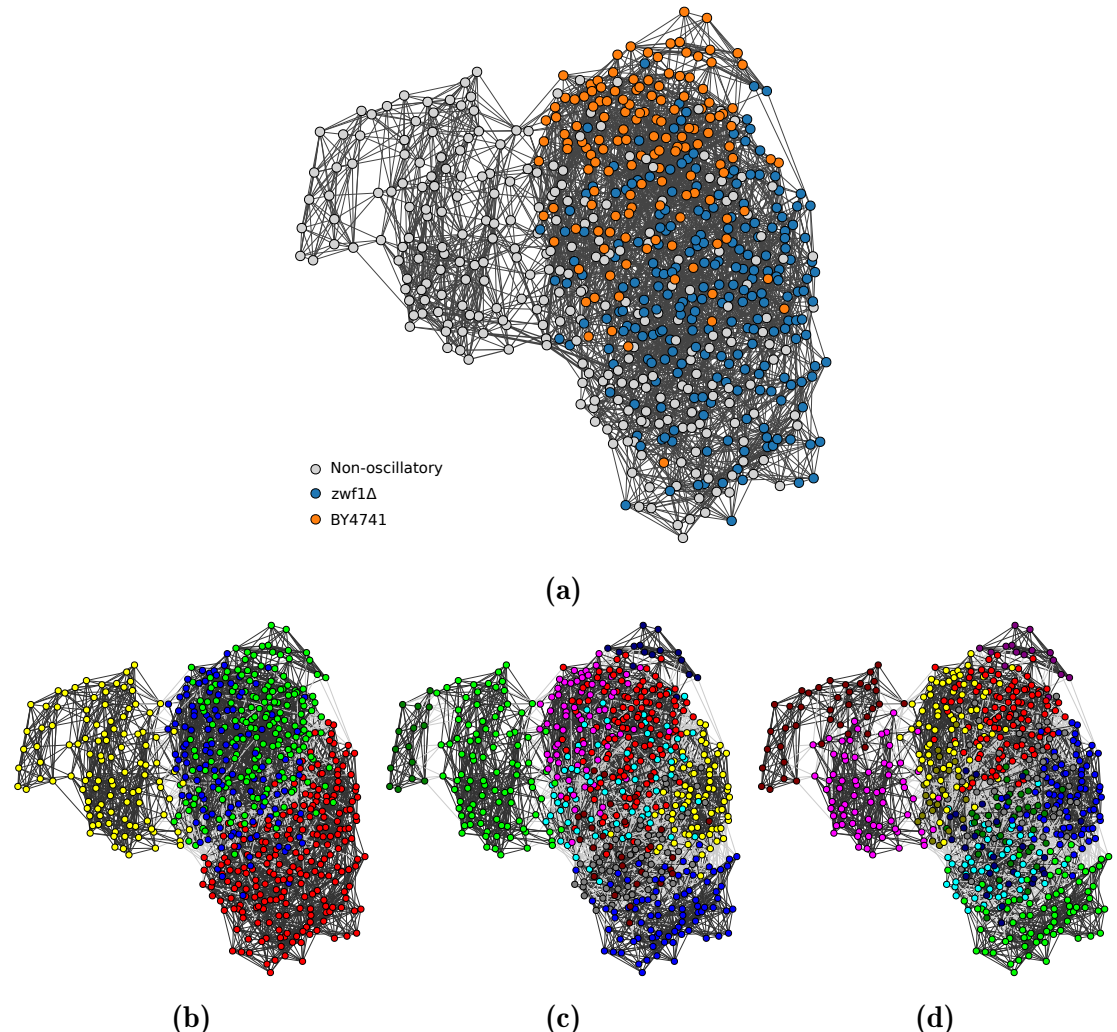


Figure 4.5: Pruned graph of BY4741 and *zwf1Δ* time series from the same experiment. **(4.5a)** Nodes coloured by group: grey, non-oscillatory; blue, oscillatory *zwf1Δ*; orange, oscillatory BY4741. Thickness of edges represent edge weights, scaled by similarity found by cosine distances. Additionally, nodes coloured by community as found by the constant Potts model (Traag, Van Dooren et al., 2011) as the resolution parameter (γ) was varied: **(4.5b)** $\gamma = 0.01$ (4 communities), **(4.5c)** $\gamma = 0.02$ (10 communities), and **(4.5d)** $\gamma = 0.03$ (12 communities).

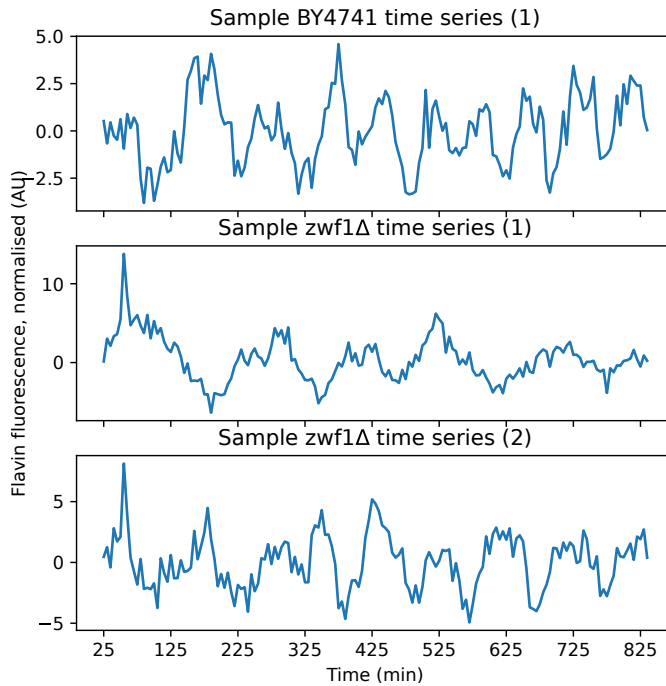


Figure 4.6: Sample time series from BY4741 and *zwf1* Δ cells. *zwf1* Δ sample 1 does not resemble the BY4741 sample, while *zwf1* Δ sample 2 does.

2081 optimal number of communities, which was realised by $\gamma = 0.02$. For all γ values,
 2082 modularity clustering was able to further show communities among the oscillatory
 2083 time series. However, such communities did not divide along the division between
 2084 BY4741 and *zwf1* Δ cells, suggesting that time series features alone were not able
 2085 to divide these two strains. This agreed with my observation that some oscillatory
 2086 *zwf1* Δ time series resembled BY4741 time series (Fig. 4.6).

2087 In sum, the general agreement between UMAP and modularity clustering shows
 2088 that the BY4741 & *zwf1* Δ dataset had internal structure defined by rhythmicity
 2089 of time series. However, it was not clear from UMAP whether there were sub-
 2090 populations among the BY4741 and *zwf1* Δ time series whose members exhibit
 2091 similar types of oscillations. In contrast, while modularity clustering suggests
 2092 that such sub-populations can be found based on connectivity between nodes,
 2093 the number of sub-populations depends on the value of a resolution parameter.

2094 **4.4 Detection of rhythmicity**

2095 To identify metabolic cycles from flavin autofluorescence signals, it is important
2096 to have a systematic method to determine whether a time series is oscillatory.
2097 To determine the time series classification method that is most appropriate for
2098 my data, I compared a spectral method, a model-fitting method, and a machine
2099 learning method.

2100 **4.4.1 Rhythmicity detection using spectral methods**

2101 In order to classify oscillatory and non-oscillatory time series, I modified a clas-
2102 sifier based on a spectral method that included a statistical test (Methods Sec-
2103 tion 2.3.1). This classifier was based on Glynn et al. (2006), which described
2104 a method that employed the peak power from the Lomb-Scargle periodogram
2105 (Lomb, 1976) to rank time series by the quality of oscillation and to perform a
2106 statistical test to determine whether a time series is oscillatory or non-oscillatory
2107 (Scargle, 1982), as shown by Eqs. 2.2–2.3.

2108 Figs. 4.7–4.8 suggest that the best- and worst-ranked time series according to the
2109 quality of their oscillatory signals conformed to subjective judgements of quality.
2110 Highest-ranked time series resembled sinusoids and therefore led to periodograms
2111 with a strong power corresponding to the frequency of the sinusoid that would
2112 model the time series. Conversely, lowest-ranked time series resembled white noise
2113 and led to periodograms with power equally spread across all frequencies, thus
2114 bringing down the height of the highest peak. However, some time series with
2115 irregular oscillations based on visual inspection (Fig. 4.7; ranks 2, 3) were given
2116 higher ranks than those with more regular oscillations based on visual inspection,
2117 thus calling into question the reliability of the ranking method.

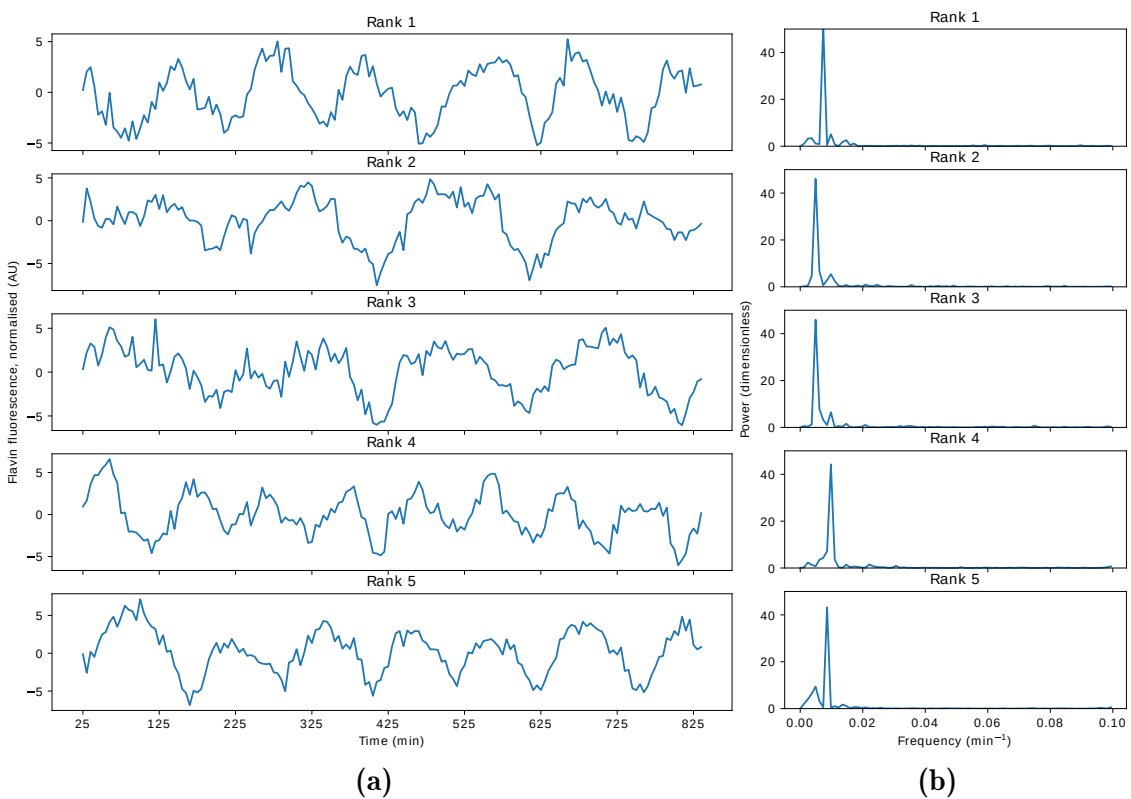


Figure 4.7: (4.7a) Best five time series in the $zwf1\Delta$ dataset and (4.7b) their periodograms, ranked by the quality of oscillation based on the maximum power in the periodogram (Glynn et al., 2006).

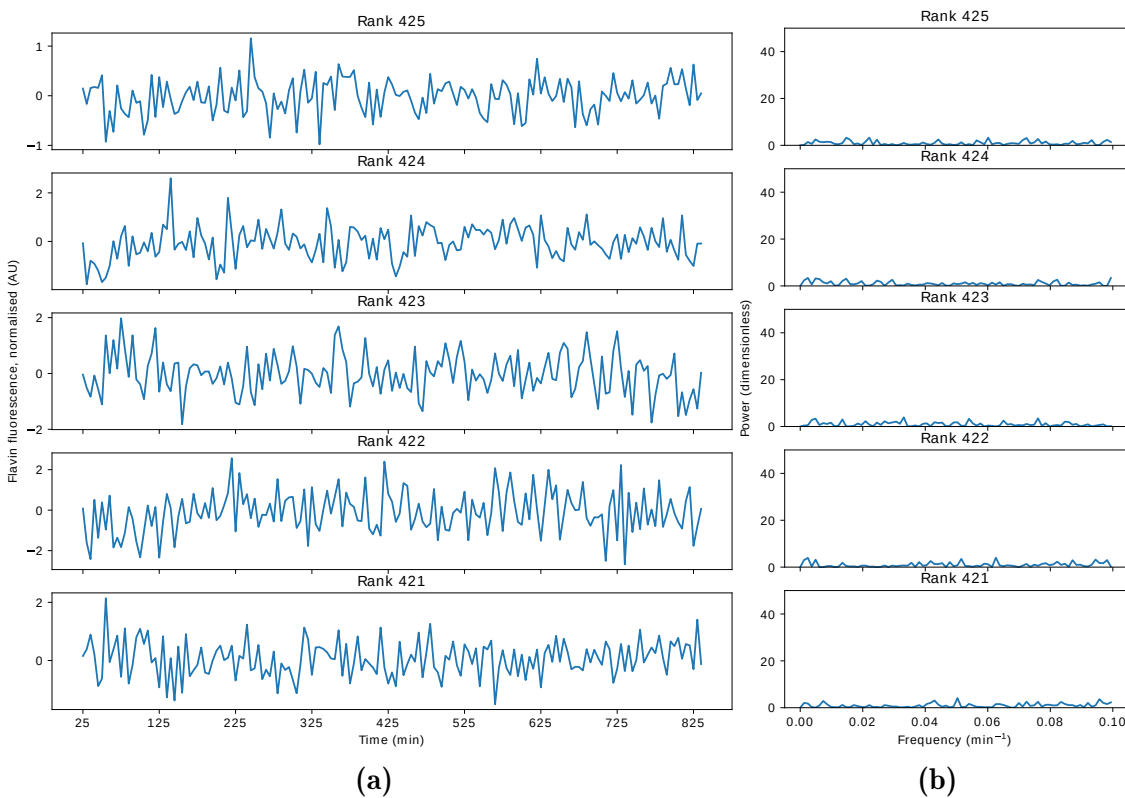


Figure 4.8: (4.8a) Worst five time series in the *zwf1Δ* dataset and (4.8b) their periodograms, ranked by the quality of oscillation based on the maximum power in the periodogram (Glynn et al., 2006).

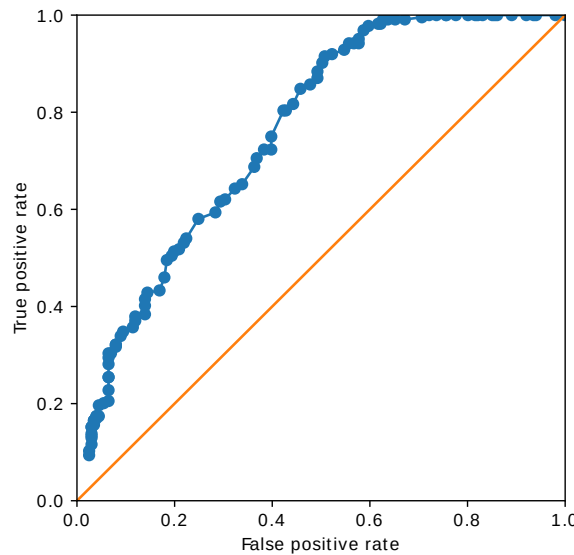


Figure 4.9: ROC curve of classifier based on Glynn et al. (2006) as the false discovery rate was varied. The true positive rate and false positive rates were computed based on the manual labels of the *zwf1Δ* dataset.

2118 To detect rhythmicity in one time series, Glynn et al. (2006) calculates the
2119 probability of the null hypothesis that a peak in the periodogram occurs due to
2120 chance. When extended across a population of time series, rhythmicity detection
2121 by this method thus becomes a task of testing multiple hypotheses. Glynn et al.
2122 (2006) thus proposed controlling the false discovery rate, defined as the proportion
2123 of cases in which the null hypothesis is true among all hypotheses in which
2124 the test is declared significant (see Methods, Section 2.3.1, specifically Eq. 2.3).
2125 Controlling the false discovery rate thus controls the expected proportion of
2126 oscillations that are classified as oscillatory.

2127 To assess the performance of this method as a classifier for rhythmicity detection,
2128 Fig. 4.9 shows the receiver operating characteristic (ROC) curve, created as the
2129 false discovery rate was varied. The area under the ROC curve (0.762) suggests
2130 that the classifier performed modestly well, especially for a large ($n = 425$) dataset
2131 of time series with a large variety of quality of oscillations.

2132 4.4.2 Rhythmicity detection using model fitting

2133 To assess the performance of a time series classification method based on the
2134 autoregressive model, I implemented the method described by Jia and Grima
2135 (2020), used to characterise synthetic time series of stochastic, oscillatory gene ex-
2136 pression in a dividing cell. In the implementation of the autoregressive model used
2137 by Jia and Grima (2020), each data point was expressed as a linear combination of
2138 a number of data points that precede it, and model parameters led to an analytical
2139 solution for the periodogram, thus giving an advantage over the low-resolution
2140 Fourier spectrum (Methods Section 2.3.2). The resulting power spectra fell into
2141 four categories, one of which corresponded to a lack of oscillations, characterised

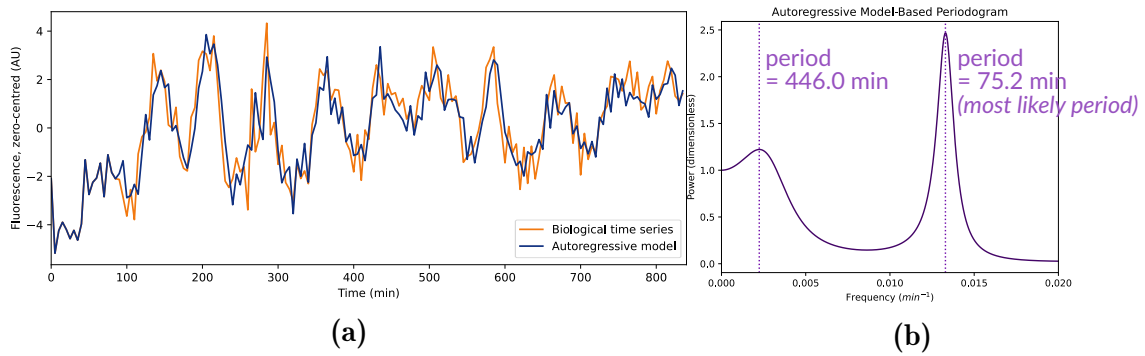


Figure 4.10: (4.10a) Sample time series (orange), with a fitted autoregressive model (blue) of order 18 computed according to Jia and Grima (2020). (4.10b) Periodogram defined based on parameters of the autoregressive model.

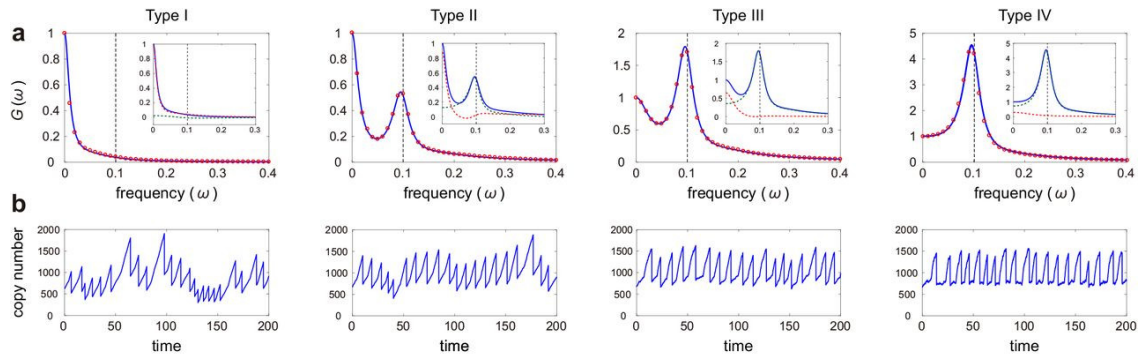


Figure 4.11: Power spectra (a) analytically derived from fitting an autoregressive model to time series (b) can be divided into four types. Type I lacks a local maximum and is denoted as lacking oscillations. Figure adapted from Jia and Grima (2020).

2142 by an absence of a local maximum in the power spectrum (Fig. 4.11). This method
 2143 thus allows computing the frequency of the oscillation from the location of the
 2144 peak in the periodogram and quality of the oscillation from the height of the
 2145 peak.

2146 Fig. 4.10 shows that the autoregressive model was able to correctly identify a
 2147 time series as oscillatory at a period of 75.2 min, as evidenced by the location of
 2148 a peak in the periodogram that the model predicted.

		Predicted by AR model		Total
		Positive	Negative	
Human-defined labels	Positive	141	83	224
	Negative	124	77	201
	Total	265	160	425

Table 4.1: Confusion matrix to evaluate the performance of using the autoregressive model (Jia and Grima, 2020) to detect rhythmicity in the *zwf1Δ* dataset.

2149 To assess the performance of the use of the autoregressive model for rhythmicity
 2150 detection across a dataset, I extended this method across the *zwf1Δ* dataset,
 2151 treating Type I power spectra (Fig. 4.11) as non-oscillatory. The confusion matrix
 2152 (Table 4.1) suggests that the method leads to poor performance (precision =
 2153 0.532, recall = 0.629, no-skill classifier: precision = recall = 0.527, see Methods
 2154 Section 2.3.3 for definitions), as it classed a large proportion of time series as
 2155 non-oscillatory.

2156 4.4.3 Rhythmicity detection using machine learning

2157 As an alternative to the mathematical methods previously discussed, I trained
 2158 a support vector classifier to classify oscillatory and non-oscillatory time series
 2159 from the *zwf1Δ* cells (Appendix A.3).

2160 To ensure that the dynamic ranges of the fluorescence signals do not affect
 2161 rhythmicity detection, I normalised each time series $x_i(t_1), \dots, x_i(t_j), \dots, x_i(t_N)$
 2162 to produce a processed time series $z_i(t_1), \dots, z_i(t_j), \dots, z_i(t_N)$ as follows:

$$z_i(t_j) = \frac{x_i(t_j) - \mu_i}{\sigma_i} \quad (4.1)$$

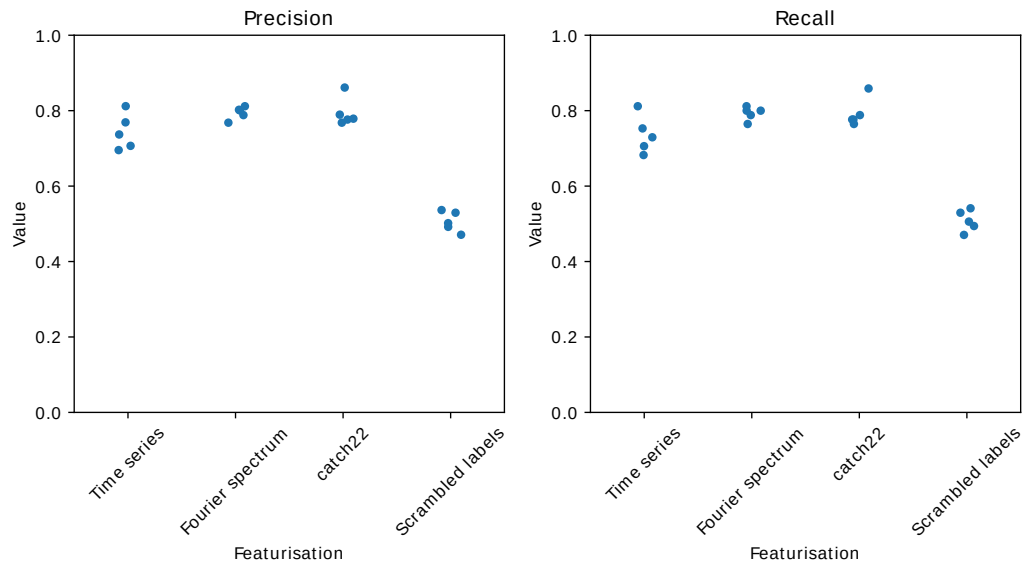


Figure 4.12: (Left) Precision and (right) recall from five-fold cross-validation of support vector classifiers trained using different featurisation methods: using the time points as features, using the power values in the Fourier spectrum as features, and using *catch22* features. As a control, the oscillatory and non-oscillatory labels were randomly reassigned to the time series and the time points were used as features.

2163 where μ_i is the mean value of x_i computed across all time points, and σ_i is
 2164 the standard deviation of x_i computed across all time points. As a result, each
 2165 normalised time series z_i has a mean of 0 and a standard deviation of 1. From
 2166 this input data, 75% of the time series formed the training set.

2167 To determine the most effective way to featurise the data, I computed the pre-
 2168 cision and recall (defined in Methods Section 2.3.3) of support vector classifiers
 2169 trained on data featurised using different methods. All support vector classifiers
 2170 were trained using a radial bias kernel, a kernel coefficient $\gamma = 1/N$, where N is
 2171 the number of features, and a regularisation parameter $C = 10$. Fig. 4.12 suggests
 2172 that featurisation using *catch22* and the Fourier spectrum gave comparably high
 2173 performances, as evidenced by high precision and recall, and with a low degree of
 2174 overfitting, as evidenced by a small variation of both metrics across the rounds
 2175 of cross-validation.

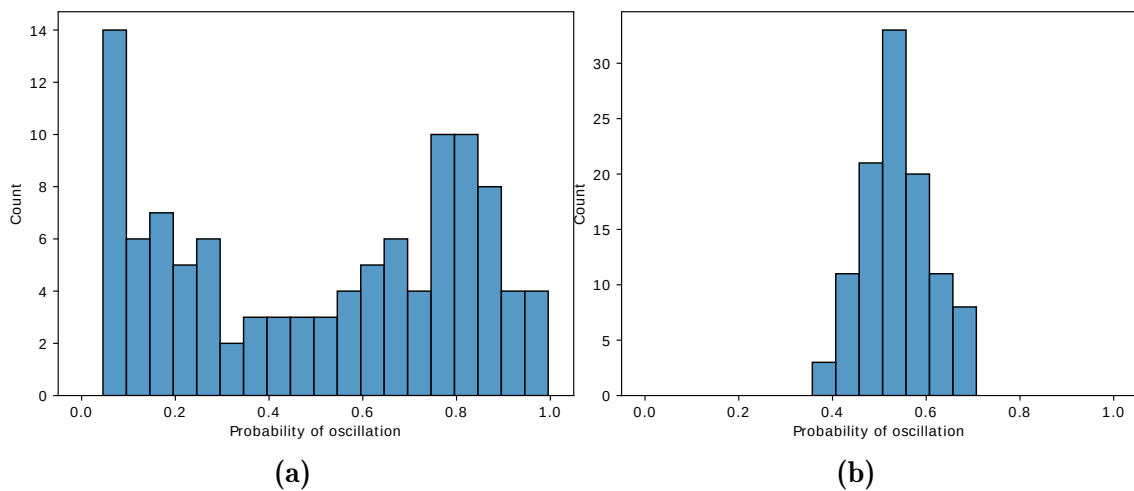


Figure 4.13: (4.13a) Histogram of probabilities of whether a time series in the test data set is classified as oscillatory by the SVC (featurisation with *catch22*, $\gamma = 1/22$, $C = 10$), and as a control (4.13b) with labels randomly reassigned.

2176 To predict the probability that each time series was oscillatory, I used Platt
 2177 scaling (Platt, 1999) with the support vector classifier, as implemented by the
 2178 `predict_proba` method in the Python package `scikit_learn`. Platt scaling in-
 2179 volves finding parameters for a logistic sigmoid function which approximates
 2180 the posterior class probability for a binary classifier. Fig. 4.13 suggests that the
 2181 classifier performed well in discriminating between the two classes, as evidenced
 2182 by the U-shaped histogram of probabilities (Fig. 4.13a), in contrast to the control
 2183 (Fig. 4.13b). In addition, Fig. 4.14 demonstrates that the probabilities can serve
 2184 as a good score to rank time series by oscillation quality.

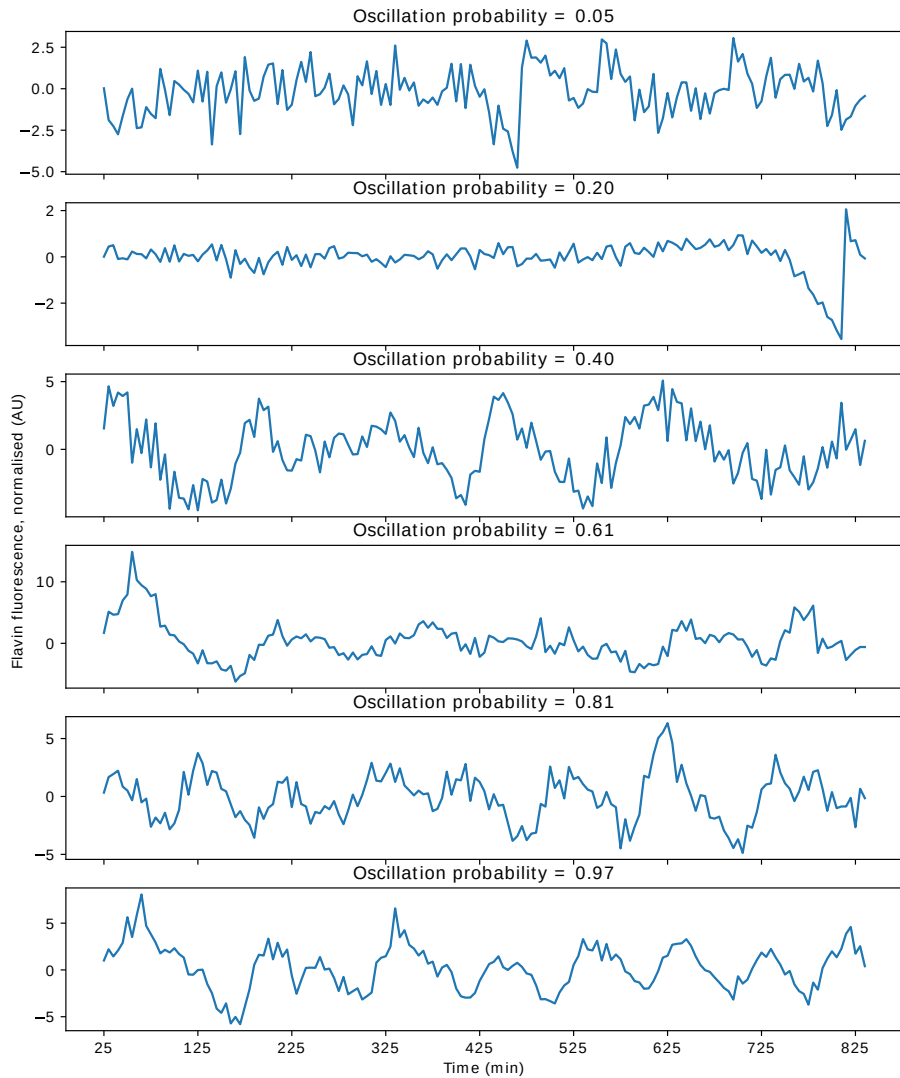


Figure 4.14: Sample time series arranged by probability that each is oscillatory, as predicted by the support vector classifier.

2185 **4.5 Period estimation using the autocorrelation func-**

2186 **tion**

2187 Estimating the period of oscillatory time series is important as it provides a
2188 quantitative measure of how yeast metabolic cycles respond to genetic nutrient
2189 perturbations as was previously used by (Papagiannakis et al., 2017). To show
2190 that the autocorrelation function can be used to estimate the period and noise
2191 properties of both symmetric and asymmetric oscillations, I adapted the auto-
2192 correlation function as used by Pietsch et al. (2023) (Methods Section 2.3.4).
2193 To calibrate the method, I generated synthetic oscillations — sinusoids and the
2194 FitzHugh-Nagumo oscillator (FitzHugh, 1961) — to investigate the effect of their
2195 properties on the autocorrelation function. Subsequently, I applied the autocorrel-
2196 ation function to characterise experimentally-recorded time series. Details on how
2197 the sinusoids and the FitzHugh-Nagumo oscillators were defined can be found in
2198 Methods Section 2.3.5.

2199 **4.5.1 Effect of noise parameters on the autocorrelation function**

2200 **of synthetic sinusoids**

2201 To compare the effect of Gaussian noise and Gillespie noise on the autocorrelation
2202 function, I computed the autocorrelation functions from a population of sinusoids
2203 with either type of noise added via element-wise sums.
2204 Fig. 4.15b shows that the autocorrelation function computed from a population
2205 of out-of-phase sinusoids could be modelled by a cosine with the same period
2206 as the sinusoids. Following this, Fig. 4.15d shows that the addition of Gaussian
2207 noise preserved the point $(0, 1)$, but the amplitude of the cosine that models the

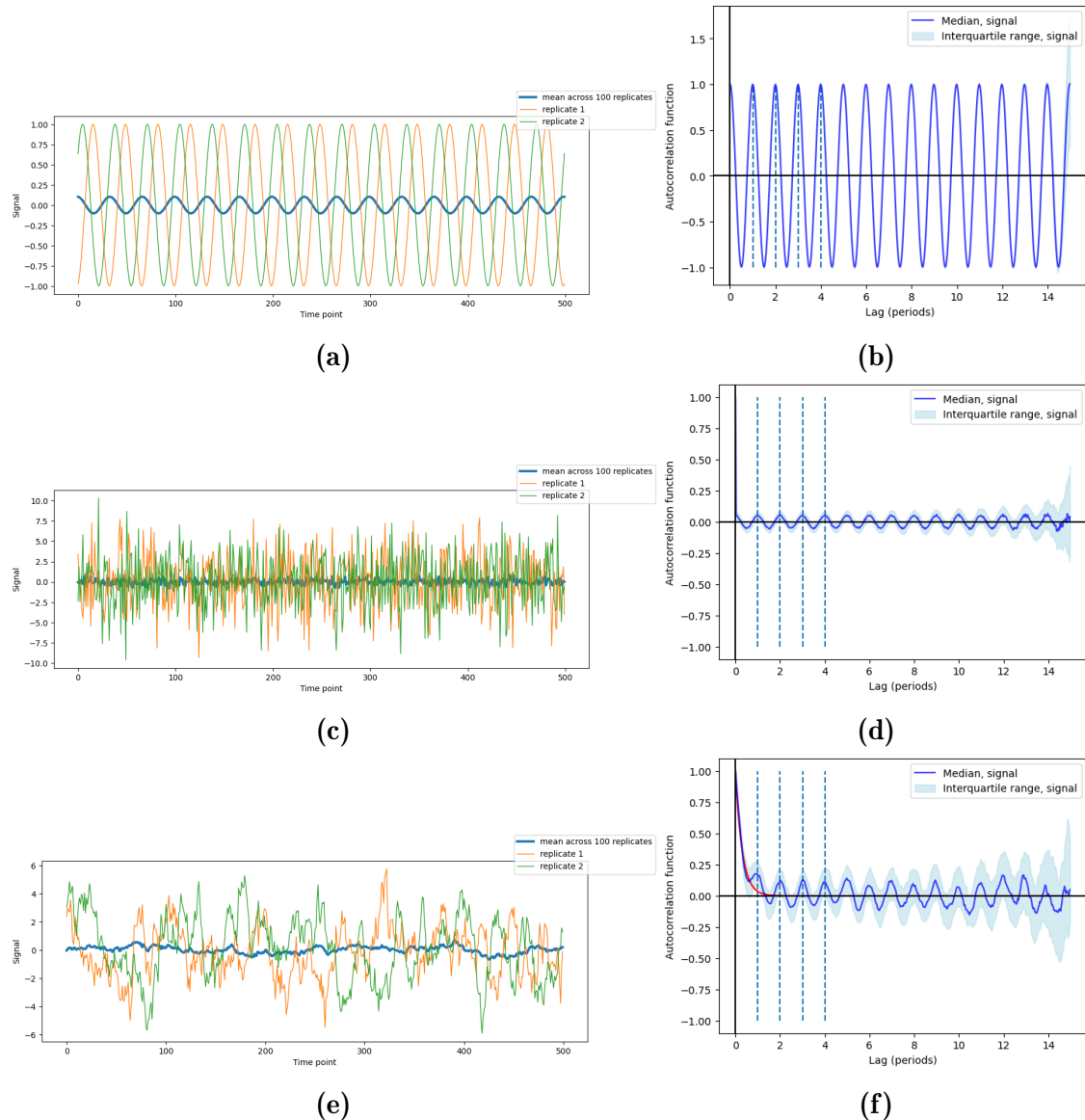


Figure 4.15: (4.15a) Sample sinusoids without noise, and (4.15b) its autocorrelation function. (4.15c) Sample sinusoids with Gaussian noise defined by drawing samples from $\mathcal{N}(0, \sigma^2 = 3)$, and (4.15d) its autocorrelation function. (4.15e) Sample sinusoids of with Gillespie noise ($k_0 = 5$ and $d_0 = 0.05$), and (4.15f) its autocorrelation function. Red line is defined by $y = e^{-2d_0T}$, where T represents the lag in units of period of the sinusoids. For each case, the frequency of the sinusoids was 0.03, and there were 100 repeats, randomly out-of-phase.

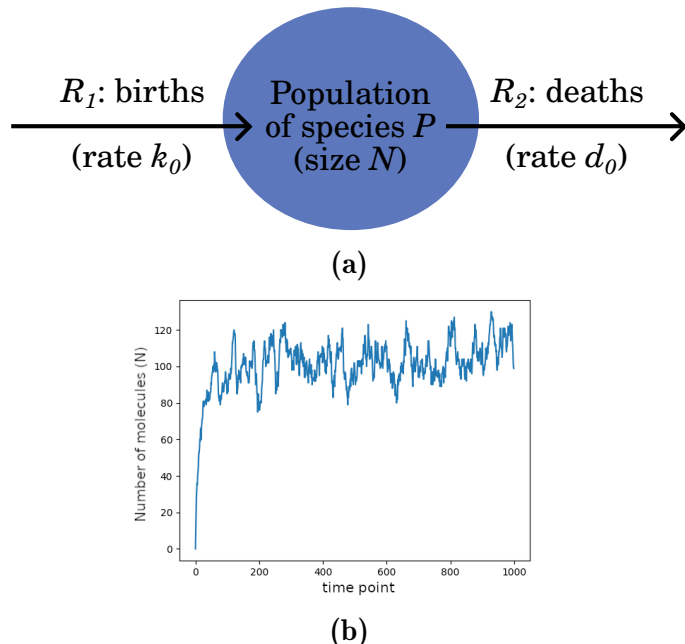


Figure 4.16: (4.16a) Illustration of the birth-death process. The birth-death process is defined by two reactions: birth ($R_1 : \emptyset \longrightarrow P$), with rate k_0 , and death ($R_2 : P \longrightarrow \emptyset$) with rate d_0 , both of which affect the number N of species P . Random firing of the birth and death reactions, simulated by the Gillespie algorithm (Gillespie, 2007), defines the trajectory of N over time, which in turn defines Gillespie noise. (4.16b) Sample trajectory of a substrate created and destroyed by the birth-death process, simulated by the Gillespie algorithm ($k_0 = 5$, $d_0 = 0.05$, $t_{\max} = 1500$).

autocorrelation function was decreased. Furthermore, the variation of the autocorrelation function among time series at long lags was increased, as evidenced by the interquartile range, because less data was used to compute the autocorrelation function at longer lags.

Gillespie noise is based on the birth-death process (Fig. 4.16), and its two parameters control noise parameters (Methods Section 2.3.5). Specifically, given a birth rate k_0 and a death rate d_0 , the noise has a standard deviation of noise amplitude $A = \sqrt{k_0/d_0}$ and noise timescale $\tau = 1/d_0$. Fig. 4.15f shows that when Gillespie noise was added to the sinusoids, the medium autocorrelation followed

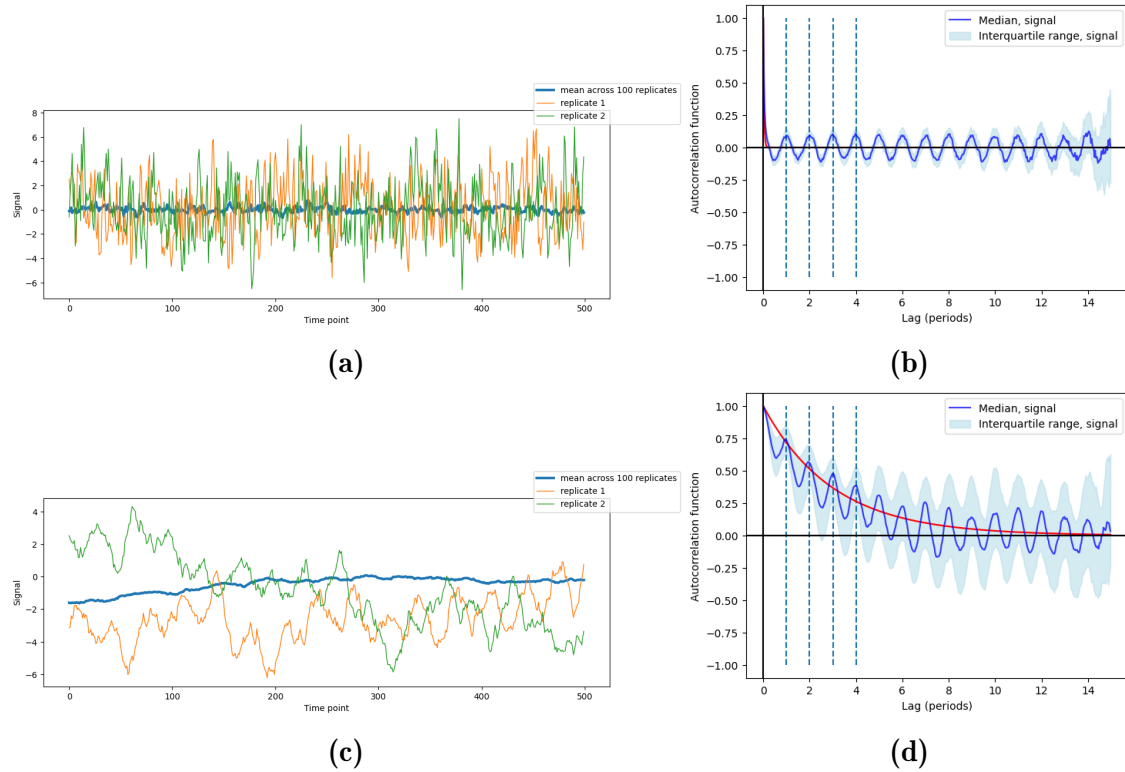


Figure 4.17: (4.17a) Sample sinusoids with Gillespie noise ($k_0 = 5$ and $d_0 = 0.5$), and (4.17b) its autocorrelation function. (4.17c) Sample sinusoids with Gillespie noise ($k_0 = 5$ and $d_0 = 0.005$), and (4.17d) its autocorrelation function. Red lines are defined by $y = e^{-2d_0 T}$, where T represents the lag in units of period of the sinusoids. For each case, the frequency of the sinusoids was 0.03, and there were 100 repeats, randomly out-of-phase.

the exponential decay function $y = e^{-2d_0 T}$, where T represents lag. In addition, the locations of the peaks of the autocorrelation function were preserved. The observation thus suggests that the death rate d_0 parameter of Gillespie noise controlled the shape of the autocorrelation function.

To quantify the effect of the noise timescale on the shape of the autocorrelation function, I varied the death rate parameter d_0 when generating Gillespie noise. Fig. 4.17 shows that a higher death rate decreased the decay timescale of the autocorrelation function (Fig. 4.17b), while a lower death rate introduced long-term trends in the simulated signals (Fig. 4.17c). A lower death rate also increased the variation between autocorrelation functions between replicates (Fig. 4.17d).

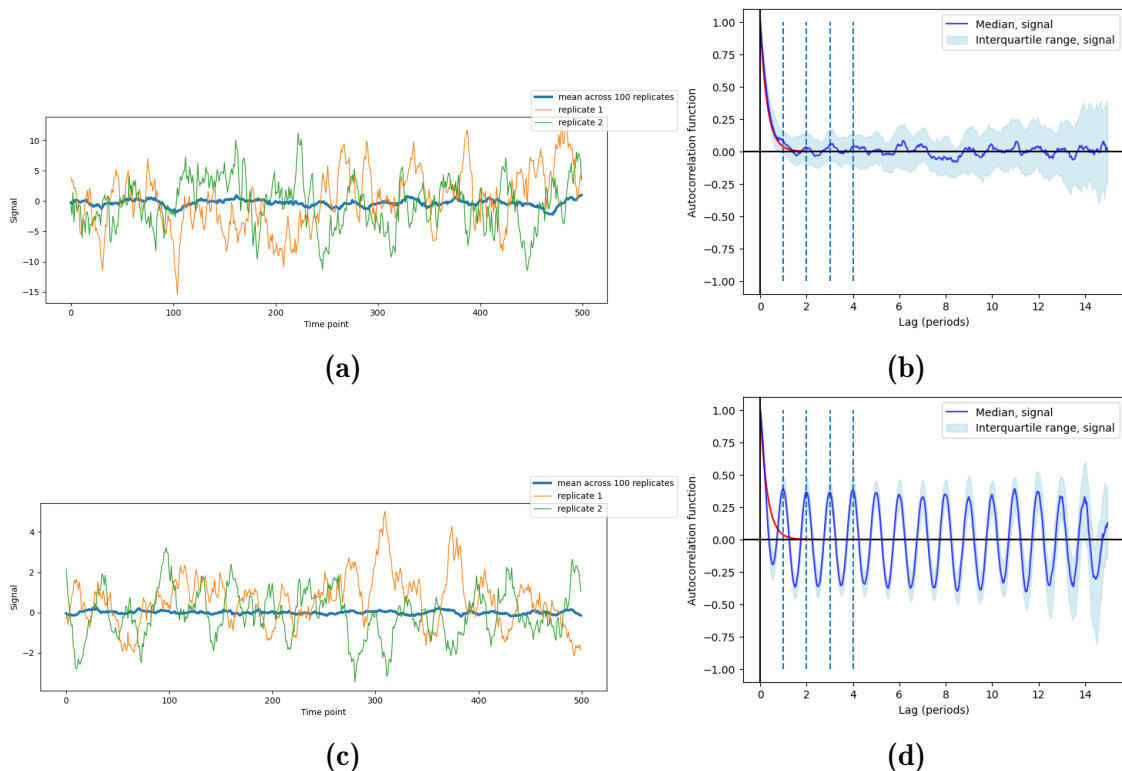


Figure 4.18: (4.18a) Sample sinusoids with Gillespie noise ($k_0 = 25$ and $d_0 = 0.05$), and (4.18b) its autocorrelation function. (4.18c) Sample sinusoids with Gillespie noise ($k_0 = 1$ and $d_0 = 0.05$), and (4.18d) its autocorrelation function. Red lines are defined by $y = e^{-2d_0 T}$, where T represents the lag in units of period of the sinusoids. For each case, the frequency of the sinusoids was 0.03, and there were 100 repeats, randomly out-of-phase.

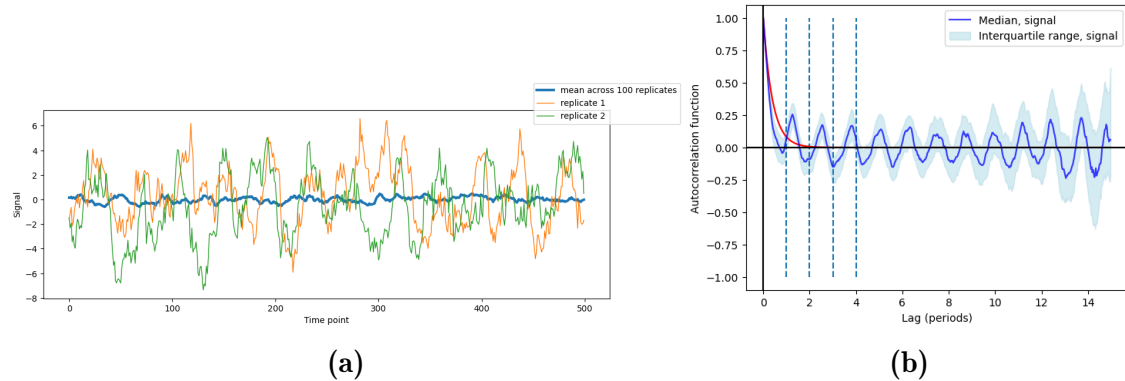


Figure 4.19: (4.19a) Sample FitzHugh-Nagumo oscillators ($RI_{\text{ext}} = 0.4$, $\tau = 12.5$, $a = 0.7$, $b = 0.82$) with Gillespie noise ($k_0 = 5$ and $d_0 = 0.05$), and (4.19b) its autocorrelation function. Red line is defined by $y = e^{-2d_0 T}$, where T represents the lag in units of period of the sinusoids. There were 100 repeats, randomly out-of-phase.

2227 To quantify the effect of the noise amplitude on the autocorrelation function,
 2228 I varied the birth rate parameter k_0 when generating Gillespie noise. Fig. 4.18
 2229 shows that a higher birth rate increased the amplitude of noise (Fig. 4.18a) and
 2230 increased the variation between replicate autocorrelation functions (Fig. 4.18b),
 2231 while the opposite was true for a higher birth rate (Figs. 4.18c–4.18d).

2232 4.5.2 FitzHugh-Nagumo oscillator: effect of oscillation shape

2233 To test whether Gillespie noise parameters can be estimated from the autocorrel-
 2234 ation function computed from an asymmetric oscillation, I added Gillespie noise
 2235 with varying d_0 and k_0 to FitzHugh-Nagumo oscillators as defined in the Methods
 2236 Section 2.3.5.

2237 Fig. 4.19b shows that when the oscillator had a different shape, the waves in the
 2238 autocorrelation function changed shape, becoming more pointed. Additionally,
 2239 the effect of noise parameters on the autocorrelation function is preserved when
 2240 the oscillators switch from sinusoid to FitzHugh-Nagumo oscillators.

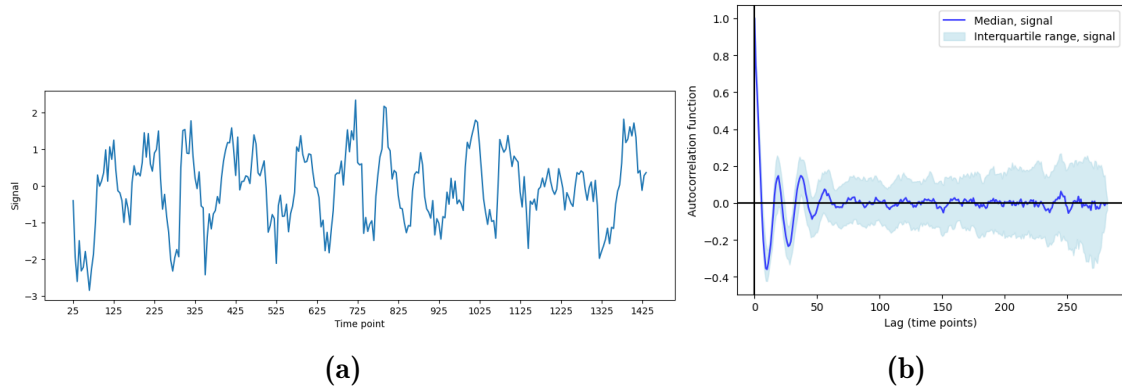


Figure 4.20: (4.20a) Sample time series of flavin autofluorescence. (4.20b) Autocorrelation function across a population of time series of flavin autofluorescence.

2241 4.5.3 Real data

2242 To deduce the period and noise parameters of a experimentally-recorded sinusoid-
 2243 like signal (Fig. 4.20a), I computed the autocorrelation functions of a population
 2244 of flavin autofluorescence time series (Fig. 4.20b). The autocorrelation function
 2245 suggests an average period of 19 time points, corresponding to 95 min, as expec-
 2246 ted from the nutrient conditions. However, estimation of noise parameters was
 2247 complicated by the damping in the autocorrelation function, giving a different
 2248 shape compared to the synthetic data and fewer peaks and troughs for fitting.
 2249 Nevertheless, relating the shape of the autocorrelation function to the effect of
 2250 noise parameters on synthetic sinusoids suggested a noise timescale of 7.35 and a
 2251 noise amplitude of 110.45.

2252 In addition to flavin autofluorescence, I also recorded time series of histone 2B
 2253 abundance as an indicator of the phases of the cell division cycle (Garmendia-
 2254 Torres et al., 2018), to investigate whether the flavin autofluorescence oscillations
 2255 and the cell division cycle synchronised. The abundance of histone 2B follow an
 2256 asymmetric oscillation (Fig. 4.21a).

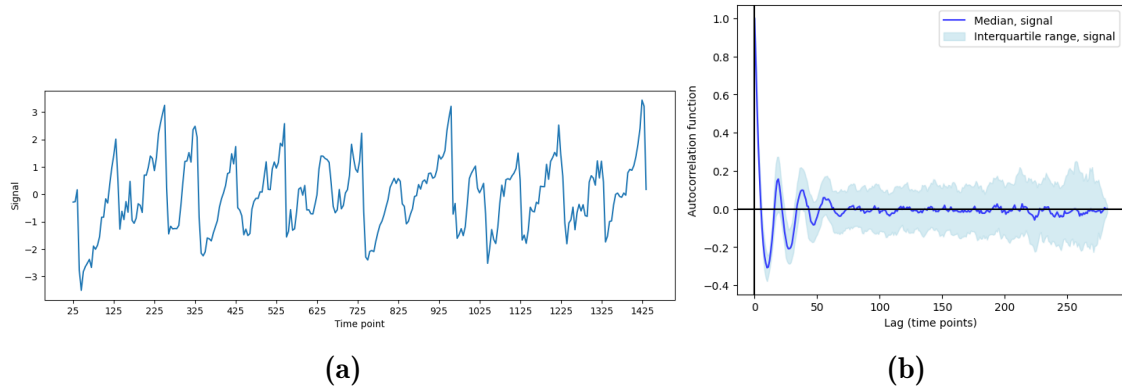


Figure 4.21: (4.21a) Sample time series of histone 2B abundance. (4.21b) Autocorrelation function across a population of time series of histone 2B abundance.

2257 Similar to the previous section, to deduce the period and noise parameters of this
 2258 signal, I computed the autocorrelation functions of a population of histone 2B
 2259 abundance time series (Fig. 4.21b). The autocorrelation function also suggests an
 2260 average period of 19 time points, corresponding to 95 min. As was the case for the
 2261 flavin autofluorescence time series, the damping in the autocorrelation function
 2262 complicated estimation of noise parameters, but the function suggested a noise
 2263 timescale of 9.35 and a noise amplitude of 168.12. The differences of these noise
 2264 parameters relative to the flavin autofluorescence time series suggest different
 2265 noise properties, which can be explained by the different fluorescence channels
 2266 and exposure times used to generate each type of signal.

2267 4.6 Detection of synchrony

2268 To test a method to detect the synchrony and quantify the temporal lag between
2269 two types of oscillations, I computed the cross-correlation functions of a popu-
2270 lation of sinusoid and FitzHugh-Nagumo oscillators. Cross-correlation has been
2271 used to investigate the relationship between the expression levels of two genes in a
2272 model feed-forward loop (Dunlop et al., 2008), and to investigate the relationship
2273 between instantaneous growth rate and the expression of *lac* genes of enzymes in
2274 central metabolism across a population of *E. coli* cells (Kiviet et al., 2014).

2275 4.6.1 Synthetic data

2276 Fig. 4.22b shows that the cross-correlation function identifies that the sinusoids,
2277 on average, peaked 20 time points before the FitzHugh-Nagumo oscillators, close
2278 to the actual value of 20.75 time points. This shift was evidenced by the position
2279 of the peak of the cross-correlation function closest to the vertical axis. The cross-
2280 correlation function further showed that synchrony between the two oscillators
2281 was maintained along the entire time series, across all time series. Furthermore,
2282 Fig. 4.22d suggests that even with strong Gillespie noise, the lag between the two
2283 oscillators could still be deduced from the cross-correlation function.

2284 4.6.2 Real data

2285 To show how the cross-correlation function can be used to quantify the synchrony
2286 between flavin autofluorescence oscillations and HTB2::mCherry levels in a popu-
2287 lation of cells, Fig. 4.23 displays a sample pair of time series (Fig. 4.23a) and the
2288 cross-correlation function from the population of cells (Fig. 4.23b). The cross-
2289 correlation function suggests that the histone 2B oscillations peaked after the
2290 flavin autofluorescence oscillations by an average of 5 min.

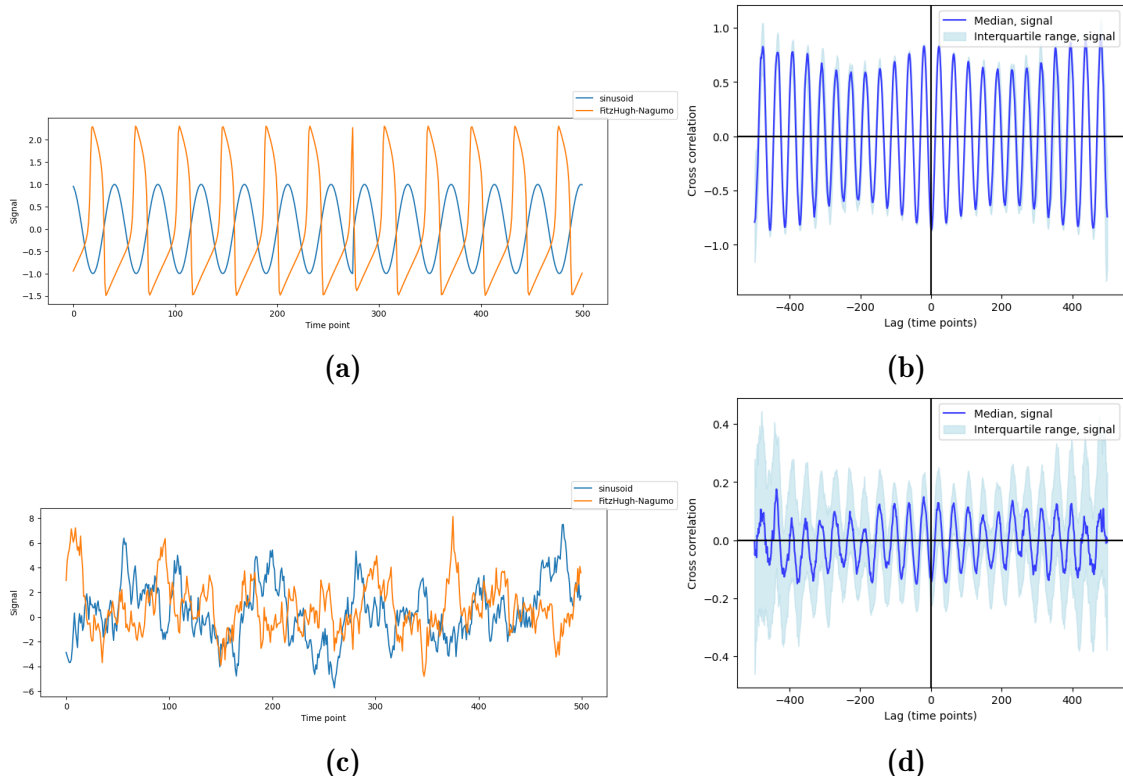


Figure 4.22: (4.22a) (Blue) Sample sinusoid ($f = 0.0235$) and (orange) FitzHugh-Nagumo oscillator ($RI_{\text{ext}} = 0.4$, $\tau = 12.5$, $a = 0.7$, $b = 0.82$) of the same frequency and without noise, and (4.22b) the cross-correlation function of the FitzHugh-Nagumo oscillators with respect to the sinusoids. (4.22c) (Blue) Sample sinusoid and (orange) FitzHugh-Nagumo oscillator with same parameters as 4.22a, but with Gillespie noise ($d_0 = 0.05$, $k_0 = 5$), and (4.22d) the cross-correlation function of the FitzHugh-Nagumo oscillators with respect to the sinusoids. For each case, there were 400 repeats, randomly out-of-phase.

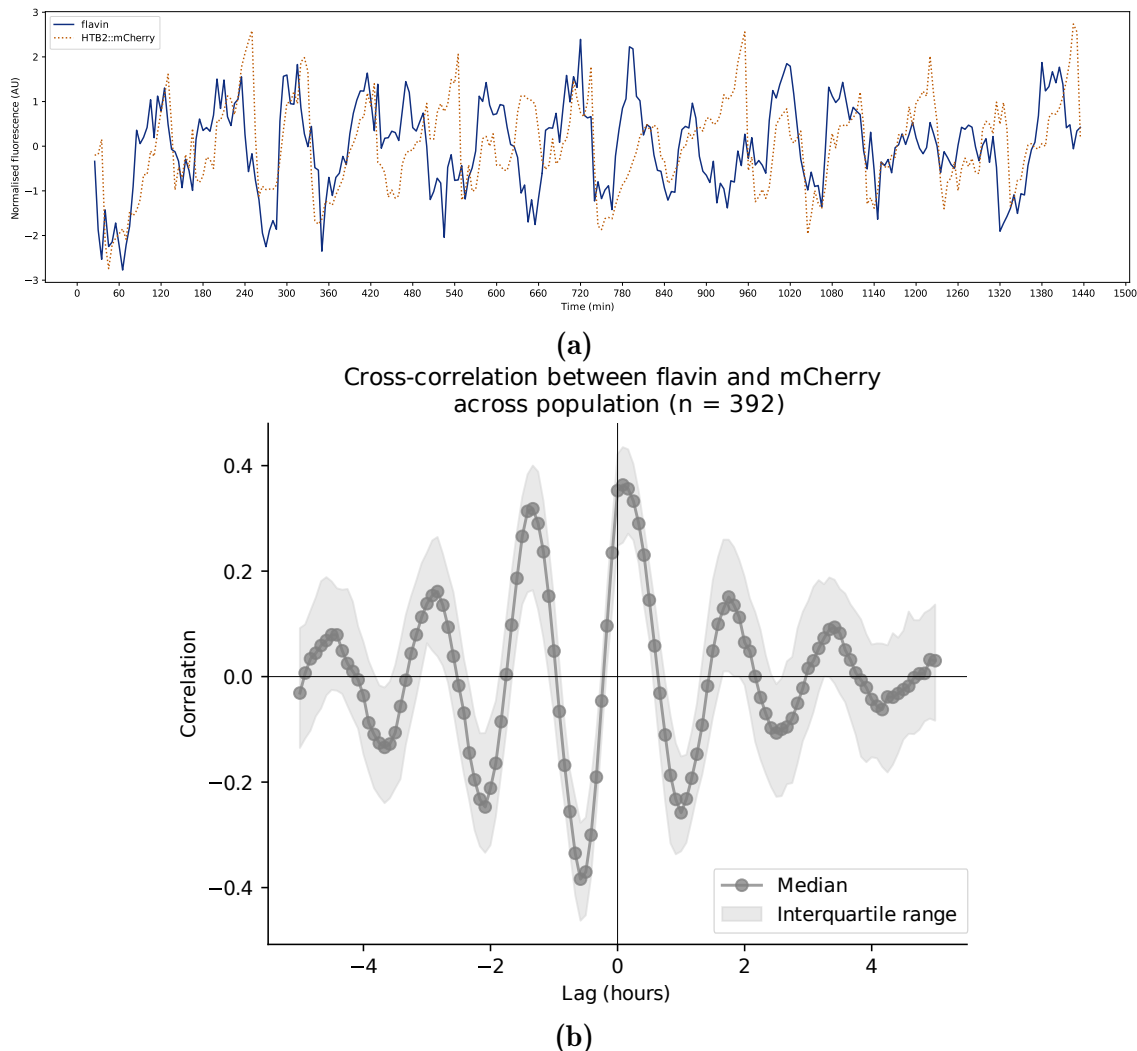


Figure 4.23: (4.23a) Sample time series of flavin autofluorescence (blue) and histone 2B abundance (orange). (4.23b) Cross-correlation function between the flavin autofluorescence time series and the histone 2B abundance time series.

2291 4.7 Discussion

2292 This chapter discusses methods to filter long-term trends in time series data, to
2293 visualise structures within a dataset of time series, to detect rhythmicity in a
2294 time series, to estimate period and noise parameters, and to detect the synchrony
2295 between two time series.

2296 My results suggest that using a high-pass Butterworth filter to filter out long-
2297 term trends in time series data gives better control over the frequency profile of
2298 the time series than moving-average methods, which is often used to detrend time
2299 series from biological oscillators. Such results highlight that a degree of caution
2300 is needed to choose methods for such a crucial step in data analysis.

2301 My exploration of UMAP and modularity clustering suggests that both methods
2302 were useful in discovering structure within time series, particularly in discrimin-
2303 ating between oscillatory and non-oscillatory time series. These methods further
2304 indicated sub-groups of time series that may have similar properties, such as shape
2305 or oscillation quality, which may correspond to sub-populations of metabolic
2306 cycle-producing cells in a culture. The consistency between the two methods
2307 strongly suggest that such groups in the dataset are meaningful.

2308 Subsequently, my exploration of three approaches to detect rhythmicity — deriv-
2309 ing a statistical test of a power spectrum, deriving a periodogram from an autore-
2310 gressive model, and a binary classifier — highlights the difficulty of rhythmicity
2311 detection in noisy biological time series. The spectral method described by Glynn
2312 et al. (2006) had a modest performance. The autoregressive model was able to

2313 identify the most likely period in some time series, but otherwise classified most
2314 time series as non-oscillatory, and lacked a tuning parameter. Finally, the support
2315 vector classifier suggests that a simple machine learning model could be adapted
2316 for rhythmicity detection, subject to a good feature set and training data.

2317 Ultimately, rhythmicity detection requires supplying a threshold in some form, be
2318 it a range of frequencies in which oscillations are expected (Zielinski et al., 2014),
2319 a parameter that controls the proportion of time series detected as oscillatory,
2320 or training labels. This is because there is no way to objectively specify a failure
2321 rate for a rhythmicity detection method as there is no independent method to
2322 estimate rhythmicity (Zielinski et al., 2014).

2323 My observations concerning the autocorrelation function confirms its use for
2324 estimating the period of an oscillatory time series, as used previously by Papagi-
2325 annakis et al. (2017). As periodicity-estimation methods have a limited ability to
2326 estimate the period of short, noisy time series owing to little input data, combining
2327 several such methods can be useful to produce a picture of the periodicity of
2328 oscillatory time series. For example, Potvin-Trottier et al. (2016) combines the
2329 autocorrelation function and the Fourier transform to study the changes in the
2330 periodicity of a modified model of the repressilator.

2331 Furthermore, I showed that the autocorrelation function may be used to esti-
2332 ate parameters to describe noise, assuming that the noise can be modelled by
2333 the birth-death process. However, further work, such as synthetic time series
2334 generated from a wider variety of parameters or additional estimation methods
2335 are likely required for adequate estimation of noise parameters from real data. In
2336 addition, it is possible that other types of noise better describe the noise from real
2337 data, and such types of noise may lead to different effects on the autocorrelation
2338 function.

²³³⁹ Finally, my results show that the cross-correlation function, as used by Dunlop
²³⁴⁰ et al. (2008), Kiviet et al. (2014), and Pietsch et al. (2023), can be used to
²³⁴¹ detect synchrony between two sets of time series and to quantify the temporal
²³⁴² relationship between the time series, even if the time series are very noisy.

²³⁴³ Taken together, the analysis methods discussed in this chapter can form the
²³⁴⁴ basis of a powerful data analysis pipeline to analyse large datasets of oscillatory
²³⁴⁵ biological time series.

2346

Chapter 5

2347

2348

Modelling yeast biosynthesis strategies under constraints

2349 To better understand the mechanistic basis of the YMC, I sought to build a model
2350 of how the cyclic sequence of cellular events respond to extracellular nutrient
2351 conditions. However, it is challenging to develop a fine-grained model for the
2352 aspects of the YMC, especially if the detailed molecular mechanisms are unclear.
2353 Further complicating the development of a fine-grained model is the fact that the
2354 main read-outs from single-cell studies — NAD(P)H and flavin autofluorescence
2355 — are aggregate signals from several biochemical phenomena.

2356 Thus, it is more feasible to construct coarse-grained models to answer biological
2357 questions about the YMC. One such question is whether a finite proteome is
2358 responsible for the sequence of events in the yeast metabolic cycle, especially
2359 considering the high energetic and resource requirements of protein synthesis (O'
2360 Neill et al., 2020; Zylstra and Heinemann, 2022).

2361 Here, I use a genome-scale metabolic model and flux balance analysis (FBA) to
2362 address whether cellular events in the metabolic cycle reflect a strategy in resource
2363 allocation that optimises growth.

2364 Specifically, I aim to evaluate these hypotheses:

- 2365 1. A finite proteome pool gives rise to sequential scheduling of the synthesis of
2366 biomass components during growth: lipid, carbohydrate, amino acids, and
2367 nucleic acids. In other words, as an adaption, the cell synthesises biomass
2368 components in sequence rather than in parallel. This would explain the
2369 timing of biosynthetic events in the phases of the yeast metabolic cycle.
- 2370 2. This resource allocation strategy remains advantageous in many nutrient
2371 conditions and deletion strains, which would explain the robustness of the
2372 yeast metabolic cycle.
- 2373 3. Synthesis of biomass components in parallel, as opposed to in sequence, may
2374 be advantageous if the processes of synthesising each biomass component
2375 share similar enzyme levels across biomass components.

2376 5.1 Introduction to flux balance analysis

2377 Metabolic network reconstructions are mathematical representations of a set of
2378 metabolic pathways in a living organism. Usually, each metabolite is represented
2379 as a node, and metabolites are connected to each other through reactions that are
2380 represented as links (B. Ø. Palsson, 2015). This information can be represented
2381 in a two-dimensional stoichiometric matrix, in which the rows of the matrix
2382 represent the metabolites, the columns represent the reactions, and the values
2383 of each element in the matrix show the stoichiometry of the reactions in the
2384 system.

2385 For example, if reaction R_1 is defined by:



2386 the elements in the stoichiometric matrix that correspond to the metabolite-
2387 reaction combinations (M_1, R_1) , (M_2, R_1) , and (M_3, R_1) are -1, -2, and 3, respect-
2388 ively.

2389 A genome-scale metabolic model is, in simple terms, a metabolic network recon-
2390 struction that aims to cover every biochemical reaction in a living system that
2391 is catalysed by a gene-encoded enzyme. In most of the reactions represented in
2392 a metabolic network reconstruction, one or more chemical species react to create
2393 a different set of chemical species as products. However, reactions in a metabolic
2394 network reconstruction may include processes that are not chemical reactions.
2395 Such processes may include exchange of nutrients, as well as a reaction that
2396 models biomass formation.

2397 Flux balance analysis (FBA) is a mathematical method that finds the steady-state
2398 flux of reactions through a metabolic network that is best for a given condition
2399 (Orth et al., 2010). These metabolic fluxes represent rates of chemical reactions.
2400 At its core, FBA is a method of solving the linear programming problem of finding
2401 the flux values that optimise the output value of an objective function, subject
2402 to biological constraints.

2403 Mathematically, the linear programming problem of FBA can be expressed as:

$$\max \mathbf{c}^\top \mathbf{v} \quad (5.2)$$

2404 subject to


$$\begin{aligned} \mathbf{S}\mathbf{v} &= \mathbf{0} \\ v_{i,\min} &\leq v_i \leq v_{i,\max} \end{aligned} \quad (5.3)$$

2405 where \mathbf{c} is a vector of weights such that $\mathbf{c}^\top \mathbf{v}$ defines the objective function, \mathbf{S}
2406 is the stoichiometric matrix, and \mathbf{v} is the vector of fluxes. The expression $v_{i,\min}$
2407 represents the lower bound and $v_{i,\max}$ represents the upper bound for each flux v_i
2408 in \mathbf{v} .

2409 The objective function is given as the task of maximising a mathematical expres-
2410 sion that is based on a subset of fluxes (Eq. 5.2). Most commonly, the objective
2411 function is maximising the flux of the biomass reaction, thus optimising the
2412 growth rate of the cell. The constraints for FBA are, in the most basic case,
2413 imposed by two factors: the stoichiometric matrix and reaction flux bounds (Eq.
2414 5.3). The stoichiometric matrix balances reaction inputs and outputs, while flux
2415 bounds impose upper and lower limits on the fluxes of each reaction. These
2416 constraints restrict the solution space for the FBA problem.

2417 FBA thus offers a computationally inexpensive way to simulate metabolism in
2418 a living system, as opposed to solving a large set of differential equations that
2419 describe the kinetics of biochemical reactions that are difficult to construct and
2420 parametrise.

2421 5.2 Modelling temporal scheduling of biosynthesis

2422 Previous studies have attempted to use FBA to model how each phase of the
2423 YMC has different metabolic requirements. Takhayev et al. (2023) showed that in
2424 different stages of the cell division cycle, the cell synthesises different components
2425 of its biomass at different levels. In the study, they blocked synthesis of each
2426 class of macromolecule and recorded the changes in single-cell NAD(P)H cycles,
2427 representing the YMC, to quantify the level of each class of macromolecule that
2428 the cell synthesises at each time point within a cell division cycle. Then, they

2429 used these activities as coefficients for a modified thermodynamic-stoichiometric
2430 metabolic model at each time point and used FBA to deduce biomass production
2431 rates. Additionally, Cesur et al. (2022) constructed a different FBA model for each
2432 YMC phase based on transcriptomic and epigenetic data. They did so using the
2433 GIMME algorithm (Becker and B. O. Palsson, 2008), which excludes reactions
2434 that correspond to genes that are not expressed at certain time points. Both
2435 studies model the metabolic state of the cell at each phase of the YMC, rather
2436 than predicting the time the cell takes to replicate or to synthesise biomass
2437 components.

2438 An attempt in extending FBA to solve a time-dependent resource allocation
2439 problem was Reimers et al. (2017). This study extended a genome-scale model
2440 of the cyanobacterium *Synechococcus elongatus* PCC7942 to find the temporal
2441 order of intracellular synthesis reactions which optimises the growth rate of the
2442 cell, under resource constraints. However, the model relies on an external oscil-
2443 lator — namely, the light-dark cycle. In contrast, the yeast metabolic cycle is
2444 autonomously generated. Therefore, it is difficult to extend the ideas in Reimers
2445 et al. (2017) to the study of the YMC.

2446 Traditional genome-scale models assume that the uptake rate of carbon source
2447 limits production. However, levels of each enzyme also restrict reaction fluxes,
2448 leading to the development of enzyme-constrained models. An enzyme-constrained
2449 model fits the assumption that there is a fixed number of amino acids the cell
2450 has to distribute (Weiße et al., 2015). Models like Sánchez, C. Zhang et al. (2017)
2451 and Elsemman et al. (2022) constrain the total sum of fluxes based on a defined
2452 total amount of enzyme. Elsemman et al. (2022) additionally impose a ribosome
2453 capacity constraint and compartment constraints.

In this chapter, I used an enzyme-constrained genome-scale model of *Saccharomyces cerevisiae* and performed FBA to simulate two strategies of scheduling of the synthesis of biomass components: in sequence and in parallel. To simulate the cell prioritising the synthesis of each biomass component in sequence, I ablated metabolites from the biomass reaction so that one biomass component remained, then optimised the model. To assess the advantage of sequential synthesis over parallel synthesis, I estimated the synthesis time for each biomass component based on ablation, then compared these times predicted by the unmodified model. To show that sequential synthesis is an adaptation for a finite proteome pool, I varied the size of the enzyme-available proteome pool to observe its effect on the cell's preferred scheduling strategy. Finally, to show how nutrient conditions affect the cell's scheduling strategy, I modelled changes in carbon and nitrogen source concentrations, then observed how the changes affect allocation of the proteome to metabolic enzymes.

5.3 The Yeast8 and ecYeast8 models and their formalisms

To impose proteome constraints, I used the enzyme-constrained Yeast8 (ecYeast8) model (H. Lu et al., 2019) and performed FBA. I used this model because it is recent, offers a good coverage of reactions, and is continuously updated in a well-characterised and well-documented software repository. Here, I used the model ecYeast8.6.0, the latest version for which both original and enzyme-constrained variants are available. ecYeast8 uses the GECKO formalism (Sánchez, C. Zhang et al., 2017) — specifically, GECKO 2 (Domenzain et al., 2022), the latest published version. GECKO applies an enzyme constraint by modifying

Keep

2478 the stoichiometric matrix of a genome-scale metabolic model. In addition, the
2479 model has ‘pseudometabolites’ defined by reactions that group specific chemical
2480 species in general classes. These formalisms allow studying each class of biomass
2481 component (e.g. lipid, protein, carbohydrate) individually.

2482 In this section, I discuss the formalisms used in ecYeast8 because they differ from
2483 the usual formalisms used in genome-scale metabolic models.

2484 ecYeast8 contains four formalisms relevant to this chapter:

- 2485 1. The biomass reaction is defined by having ‘pseudometabolites’ as reactants
2486 and a biomass species as a product. These pseudometabolites include lip-
2487 ids, proteins, carbohydrates, RNA, DNA, ions, and cofactors. This is in
2488 contrast to BiGG genome-scale models (Norsigian et al., 2020). In these
2489 models, biomass reactions have chemical species as reactants, and each has
2490 a stoichiometric coefficient that is equal to the species’ abundance in units
2491 of $\text{mmol g}_{\text{DW}}^{-1}$.
- 2492 2. The pseudometabolites are defined by ‘*isa*’ reactions, which group specific
2493 chemical species into classes of metabolites (Heavner et al., 2012). These re-
2494 actions account for how some KEGG definitions of reactions require generic
2495 compounds and these reactions also allow flexibility of biomass definition
2496 in different growth conditions. The *isa* reactions have chemical species as
2497 reactants, each with a stoichiometric coefficient representing the species’
2498 abundance in units of $\text{mmol g}_{\text{DW}}^{-1}$, and a pseudometabolite as a product. In
2499 effect, the species abundance information is shifted one reaction away from
2500 the biomass reaction.

Method

- 2501 3. The models implements SLIMER (Sánchez, F. Li et al., 2019), which Splits
2502 Lipids Into Measurable Entities, and adds constraints on lipid classes and
2503 acyl chain distribution. This formalism is needed because species of lipid
2504 backbones and acyl chain can combine to form lipids in more than a thou-
2505 sand ways, and the resulting lipid species are difficult to all be represented
2506 in a genome-scale metabolic model. SLIMER thus introduces reactions that
2507 split lipids into their basic components and lipid pseudoreactions to preserve
2508 the distribution of acyl chains. As a result, the definitions of lipids are
2509 flexible.
- 2510 4. GECKO was applied to Yeast8 to produce ecYeast8. GECKO modifies the
2511 stoichiometric matrix of a genome-scale metabolic model to account for
2512 enzyme abundances and kinetics. Specifically, it adds to enzyme-catalysed
2513 reactions enzyme species with a stoichiometric coefficient derived from its
2514 k_{cat} value. The formalism also adds reactions to model drawing enzymes
2515 from a pool. GECKO simulates an upper limit of amino acids available for
2516 enzyme production.

2517 Here, I detail how I apply these formalisms for this chapter. In particular, I detail
2518 GECKO (item 4) and computing molecular weights of pseudometabolites (based
2519 on items 1 and 2).

2520 **5.3.1 GECKO** *Keep*

2521 In a conventional genome-scale model, metabolic fluxes through reactions are
2522 constrained by lower and upper bounds. This constraint narrows the solution
2523 space when the objective function is optimised. GECKO imposes an additional
2524 constraint on the metabolic fluxes based on the concentration of the enzyme that
2525 catalyses the reaction (Fig. 5.1).

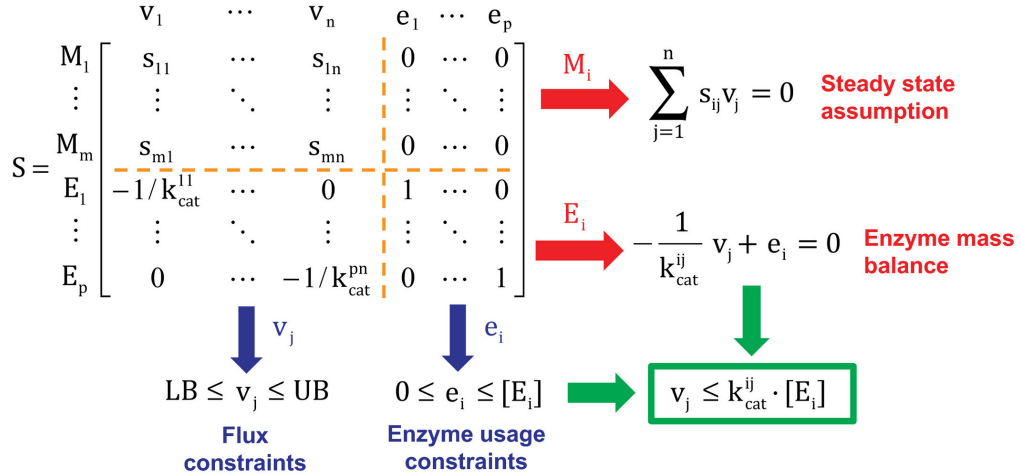


Figure 5.1: Modifications to the stoichiometric matrix of a genome-scale model that GECKO imposes. The original stoichiometric matrix S includes metabolites $M_1 \dots M_m$ and reactions $v_1 \dots v_n$. GECKO extends this matrix to include enzymes $E_1 \dots E_p$ and enzyme usage reactions $e_1 \dots e_p$. The new stoichiometric matrix can be seen as four submatrices concatenated together: the upper right submatrix is $\mathbf{0}$, the lower left submatrix encodes kinetic information, and the lower right submatrix is \mathbf{I} . Figure adapted from Sánchez, C. Zhang et al. (2017).

2526 GECKO modifies the linear programming of FBA as defined by Eq. 5.2 and 5.3
 2527 so that enzymes are expressed as metabolites that take part in reactions. This
 2528 can be expressed as:

$$\max \mathbf{c}^\top \mathbf{v} \quad (5.4)$$

2529 subject to

$$\begin{aligned} \mathbf{S}\mathbf{v} &= \mathbf{0} \\ v_{j,\min} \leq v_j &\leq v_{j,\max} \\ v_j &\leq k_{\text{cat}}^{ij} \cdot [E_i] \end{aligned} \quad (5.5)$$

2530 where v_j is the flux of each reaction R_j catalysed by enzyme E_i , k_{cat}^{ij} is the catalytic
 2531 constant of the enzyme E_i for reaction R_j , and $[E_i]$ represents the concentration
 2532 of the enzyme E_i . These constraints ensure that each v_j does not exceed the v_{\max}
 2533 of E_i . Each enzyme E_i may catalyse one or more reactions R_j .

2534 To illustrate how GECKO modifies chemical reactions, consider a simple example,
 2535 a reaction R_j catalysed by enzyme E_i :



2536 To apply the constraints described by Eq. 5.5, the chemical reaction in Eq. 5.6 is
 2537 modified by adding a term:



2538 with the stoichiometric coefficient $n_{ij} = 1/k_{\text{cat}}^{ij}$. GECKO takes k_{cat} values from
 2539 BRENDa (Chang et al., 2021).

2540 This transformation, adding the enzyme as a pseudometabolite, is based on the
 2541 intuition that the system uses some amount of enzyme at a specific time to
 2542 catalyse the flux through the reaction. Slightly different formalisms are applied
 2543 to reversible reactions, isozymes, promiscuous enzymes, and enzyme complexes
 2544 (Appendix B.1).

2545 To constrain overall enzyme levels in the model, GECKO defines a pseudoreaction



2546 where E_{pool} is a pseudometabolite that represents the proteome pool available for
 2547 enzymes. This pseudoreaction has a flux

$$e_{\text{pool}} \leq (P_{\text{total}} - P_{\text{measured}}) \cdot f \cdot \sigma \quad (5.9)$$

in units of $\text{g g}_{\text{DW}}^{-1}$, where P_{total} is the total protein fraction with respect to the dry weight of the cell, P_{measured} is the protein fraction of proteins whose weight are accounted for in the model, based on proteomic data, f represents the fraction of proteins that are enzymes, and σ is a parameter that represents the average saturation of enzymes. ecYeast8.6.0 assumes parameter values of $f = 0.5$, $P_{\text{total}} = 0.5$, and $\sigma = 0.5$. If no proteomic data is used, as is the case in this chapter, $P_{\text{measured}} = 0$.

Defining such parameters is a judgement call, especially when the protein fraction varies across growth rates (Elseman et al., 2022), but $f = 0.5$ is close to the protein mass fraction of ecYeast8.6.0. Subsequently, GECKO changes the carbohydrate composition based on the assumption that a change in the amino acid composition is offset by the reverse change in the carbohydrate composition; experimental data justifies this assumption (Nissen et al., 1997).

Then, for each enzyme E_i , GECKO defines enzyme usage pseudoreactions of the form



where MW_i represents the molecular weight of the enzyme in units of g mmol^{-1} . The flux of enzyme usage pseudoreactions are defined in units of $\text{mmol g}_{\text{DW}}^{-1}$. GECKO takes enzyme data from SWISSPROT (The UniProt Consortium, 2023) and KEGG (Kanehisa et al., 2023), including molecular weight of proteins and associated pathways.

Could this be on appendix?

2558 Taken together, the modelled cell thus has an enzyme pool in terms of a mass
 2569 fraction of the cell's dry weight, and the modelled cell allocates certain fractions
 2570 of this mass to the synthesis of each enzyme at steady-state. The mass of each
 2571 enzyme in the cell determines the amount (in moles) of each enzyme and therefore
 2572 its catalytic activity.

2573 5.3.2 Computing molecular weights of pseudometabolites

2574 To compute the synthesis time for each biomass component, the mass fractions of
 2575 each biomass component must be known. These quantities are typically stored as
 2576 molecular weights in a genome-scale model. As biomass components in ecYeast8
 2577 are pseudometabolites without specified molecular weights, I computed the mass
 2578 fractions of each biomass component based on their *isa* reactions (Appendix B.2).
 2579 Rather than using mass fractions based on experimental studies, I used mass frac-
 2580 tions based on the model because the mass fraction of each biomass component
 2581 varies according to strain and growth rate (Nilsson and Nielsen, 2016; Elsemman
 2582 et al., 2022).

notes

Metabolite	Computed molecular weight (g mol ⁻¹)	Biomass composition at growth rate 0.375 h ⁻¹ (g kg _{DW} ⁻¹)
Protein	504.37	505
Carbohydrate	350.37	237
RNA	64.04	105
Lipid	31.57	57
Cofactors	4.83	
DNA	3.90	5
Ions	2.48	
Total	961.57	

Table 5.1: Computed molecular weights of bulk metabolites in ecYeast8, compared to experimentally recorded biomass composition by Canelas et al. (2011).

2583 Table 5.1 summarises the molecular weight of the pseudometabolites. The ratio
2584 between the molecular weights are similar to the ratio between the mass of each
2585 class of macromolecule in the yeast cell dry weight shown by Canelas et al. (2011),
2586 thus validating my calculations.

2587 Adding together molecular weights of pseudometabolites gave a molecular weight
2588 of the biomass pseudometabolite of $961.57 \text{ g mol}^{-1}$, close to the 966 g mol^{-1} com-
2589 puted by Takhveev et al. (2023) from a different genome-scale model. In theory,
2590 this number should be 1000 g mol^{-1} because the stoichiometric coefficients of
2591 the species that form biomass components are expressed in terms of $\text{mmol g}_{\text{DW}}^{-1}$
2592 (Thiele and B. Ø. Palsson, 2010; B. Ø. Palsson, 2015), but the deviation from
2593 1000 could be explained by the SLIMEr formalism. In addition, the sum of
2594 stoichiometric coefficients are not always verified in genome-scale models (Chan
2595 et al., 2017).

2596 **5.4 Ablating pseudometabolites from the biomass re-**
2597 **action**

2598 **5.4.1 Definition of ablation**

2599 To simulate producing each class of biomass component in turn, I take advantage
2600 of pseudometabolites in ecYeast8 to remove them in turn from the biomass
2601 reaction — in other words, ablating pseudometabolites from the biomass reaction.

2602 Consider the objective function, the biomass reaction:

2603 $47.5883 \text{ atp_c} + 47.5883 \text{ h2o_c} + \text{lipid_c} + \text{protein_c} + \text{carbohydrate_c}$
2604 $+ \text{dna_c} + \text{rna_c} + \text{cofactor} + \text{ion}$
2605 $\rightarrow 47.5883 \text{ adp_c} + \text{biomass_c} + 47.5883 \text{ h_c} + 47.5883 \text{ pi_c}$

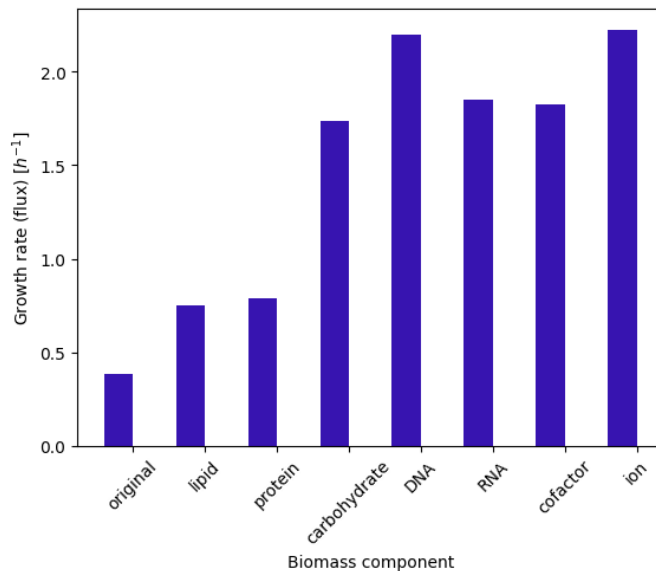


Figure 5.2: Growth rates from the original model (leftmost bar) and from the ablated versions of the model (other bars)

2606 There are seven pseudometabolites: lipid, protein, carbohydrate, DNA, RNA,
2607 cofactor, and ion.

2608 To simulate the cell prioritising biosynthesis of lipids, I set the stoichiometric
2609 coefficients of all pseudometabolites except for lipids to zero in the above equation,
2610 giving:

2611 $47.5883 \text{ atp_c} + 47.5883 \text{ h2o_c} + \text{lipid_c}$
2612 $\rightarrow 47.5883 \text{ adp_c} + \text{biomass_c} + 47.5883 \text{ h_c} + 47.5883 \text{ pi_c}$

2613 Using this modified reaction as the objective function, the model was optimised
2614 using FBA, and this process was repeated for the other pseudometabolites, res-
2615 ulting in different growth rates for each round of ablation (Fig. 5.2).

²⁶¹⁶ **5.4.2 Effect of ablation on allocation of proteome to enzymes**

²⁶¹⁷ To assess whether ablation leads to metabolic changes that reflect cellular bio-
²⁶¹⁸ chemistry, I quantified how proteome allocation to enzymes changes across rounds
²⁶¹⁹ of ablation. When the model prioritised a different biomass component in each
²⁶²⁰ round of ablation, the model partitioned the limited proteome available for en-
²⁶²¹ zyme production differently. In other words, in each round of ablation, the vector
²⁶²² of fluxes carried by each enzyme usage pseudoreaction (defined in Eq. 5.10) was
²⁶²³ different from each other and from the non-ablated case, in which all biomass
²⁶²⁴ components were synthesised in parallel.

²⁶²⁵ To quantify changes in proteome allocation across rounds of ablation, I computed
²⁶²⁶ the $\log_2(\text{FC})$ of fluxes relative to the non-ablated, parallel case. This is defined
²⁶²⁷ as:



$$\log_2(\text{FC}_{i,j}) = \log_2 \left(\frac{e'_{i,j}}{e'_{i,\text{par}}} \right) \quad (5.11)$$

²⁶²⁸ where, to ensure that $\log_2(\text{FC}_{i,j})$ can be defined for all i and j ,

$$e' = \begin{cases} \epsilon, & \text{if } |e| < \epsilon \\ e, & \text{otherwise} \end{cases} \quad (5.12)$$

where e' is either $e'_{i,j}$ or $e'_{i,\text{par}}$, e is the corresponding $e_{i,j}$ or $e_{i,\text{par}}$, and ϵ is the minimum flux of 1 molecule $\text{cell}^{-1} = 1.11 \times 10^{-10} \text{ mmol g}_{\text{DW}}^{-1}$, computed assuming a cell dry weight of 15 pg dry weight per cell (Sherman, 2002). Here, $e_{i,\text{par}}$ represents the flux of an enzyme usage reaction associated with each enzyme E_i in the model (defined in Eq. 5.8) in the non-ablated, parallel case, and $e_{i,j}$ represents the flux of the enzyme usage reaction when biomass component j is prioritised in a round of ablation.

If $\log_2(\text{FC}_{i,j}) > 0$, the cell allocates more of its proteome to produce enzyme E_i when biomass component j is prioritised; the reverse is true if $\log_2(\text{FC}_{i,j}) < 0$. In addition, if enzyme expression switches on ($e_{i,\text{par}} = 0$), $\log_2(\text{FC}_{i,j}) \ll 0$. Conversely, if enzyme expression switches off ($e_{i,j} = 0$), $\log_2(\text{FC}_{i,j}) \gg 0$.

Subsystem information aids interpretation of the changes in proteome allocation across rounds of ablation. Here, I matched the flux carried by each enzyme usage pseudoreaction to the enzyme-catalysed reaction that the enzyme is associated with. If an enzyme usage pseudoreaction is associated with multiple enzyme-catalysed reactions, data entries were duplicated accordingly. Then, the subsystem associated with each enzyme-catalysed reaction was taken from the gene-protein map, and noted. ?

To show that in each round of ablation, the cell re-allocated its finite proteome to enzymes with roles related to the synthesis of each biomass component, Fig. 5.3 categorises fold changes by subsystem. Specifically, the figure shows:

incomplete sentence



Figure 5.3: $\log_2(\text{FC})$ of enzyme usage reaction flux (Eq. 5.10) in rounds of ablation, according to biomass component prioritised. Each column shows the component that remains in each round of pseudometabolite ablation (labels on top). Each row represents an enzyme, and rows are grouped by subsystem (labels on left). Colours represent $\log_2(\text{FC})$ (defined in Eq. 5.11) showing how enzyme usage fluxes change in rounds of ablation: green shows an increase, while pink shows a decrease. Rows in which $|\log_2(\text{FC})| < 11$ for all biomass components are not shown to restrict the number of reactions ($n = 3897$) for visualisation.

5.4. Ablating pseudometabolites from the biomass reaction

147

- 2650 1. When any biomass component was prioritised, the cell de-allocated its
2651 proteome to most of its enzymes, as $\log_2(FC_{i,j}) < 0$ for most values of i, j .
2652 However, there were cases with strong increases in allocation ($\log_2(FC_{i,j}) >$
2653 0). For example, when cofactors were prioritised, there were strong increases
2654 in biosynthesis of unsaturated fatty acids and in riboflavin metabolism.
2655 Additionally, there were strong increases in oxidative phosphorylation when
2656 carbohydrate, DNA, RNA, cofactor, or ion was prioritised.
- 2657 2. When the *cell prioritised lipid biosynthesis*, it showed the least change relat-
2658 ives to the parallel (non-ablated case), compared to other biomass compo-
2659 nents. The changes included increases of fluxes in the subsystems of fatty acid
2660 biosynthesis, glycerolipid metabolism, glycerophospholipid metabolism, in-
2661 ositol phosphate metabolism, steroid biosynthesis, and terpenoid backbone.
2662 Given that these subsystems are directly related to lipid metabolism, such
2663 changes were expected. In addition, during lipid biosynthesis, the model
2664 showed decreases of fluxes in oxidative phosphorylation, the TCA cycle,
2665 and in amino acid metabolism, with fluxes varying depending on the amino
2666 acid.
- 2667 3. When the *cell prioritised protein biosynthesis*, it showed small increases
2668 in fluxes associated with amino acid metabolism, tRNA metabolism, and
2669 oxidative phosphorylation. Such increases were expected as these led to
2670 production of substrates that are required for translation. Conversely, when
2671 other biomass components (carbohydrate, ion, DNA, RNA, and cofactor)
2672 were prioritised, there were decreases in fluxes in glycine, serine, and threon-
2673 ine metabolism.

2674 4. When the cell prioritises carbohydrate biosynthesis, there were increases
2675 in fructose metabolism, mannose metabolism, N-glycan biosynthesis, and
2676 starch and sucrose metabolism. This was expected given that these reactions
2677 relate directly to pathways for synthesis of carbohydrates.

2678 5. When the cell prioritised RNA biosynthesis, there were increases in the
2679 purine metabolism and pyrimidine metabolism subsystems, along with a
2680 mixed picture in the pentose phosphate pathway. The increases were ex-
2681 pected given the presence of purines and pyrimidines in RNA and the role
2682 of the pentose phosphate pathway in generating the precursors for these
2683 compounds. However, these subsystems showed weak decreases in flux when
2684 DNA is prioritised, though the enzyme usage flux profile overall is similar
2685 to when RNA is prioritised.

2686 Results thus validate ablation of biomass components as a method to simulate
2687 sequential synthesis of biomass components by the cell, as the changes of fluxes
2688 reflect cellular biochemistry.

2689 5.5 Estimating timescale of biosynthesis

2690 To evaluate whether sequential or parallel synthesis of biomass components offers
2691 a time advantage during cell growth, I estimated the timescale of biosynthesis for
2692 either resource allocation strategy (Fig. 5.4).

2693 Based on the objective function of the unmodified model, the doubling time was
2694 computed as follows:

$$t_0 = \frac{\ln 2}{\lambda_0} \quad (5.13)$$

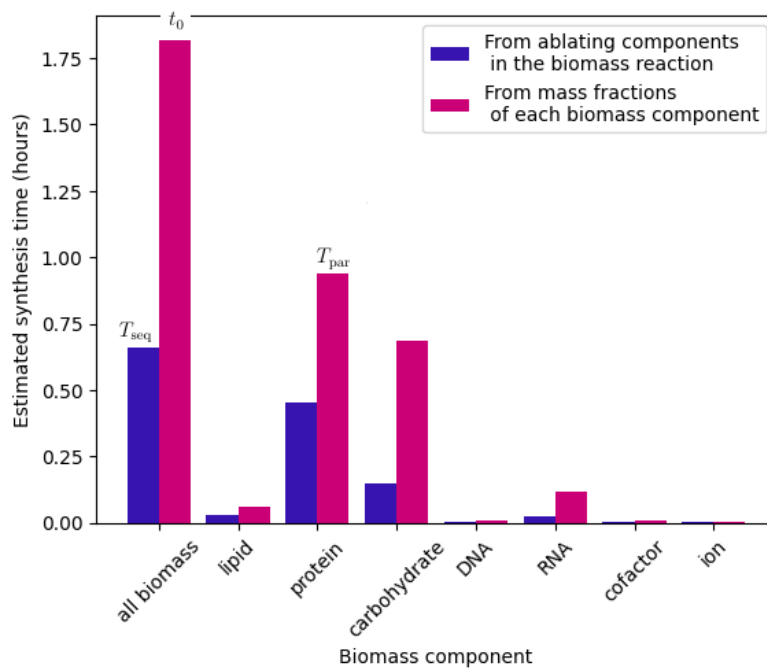


Figure 5.4: Estimated synthesis times of biomass components, from ablation (blue bars) and from scaling doubling time by mass fraction (red bars). Bars under ‘all biomass’ indicate (blue) T_{seq} (defined in Eq. 5.17) and (red) the doubling time t_0 (defined in Eq. 5.13). Other bars indicate (blue) $t_{\text{seq},i}$ (defined in Eq. 5.14) and (red) $t_{\text{par},i}$ (defined in Eq. 5.15); T_{par} is the greatest $t_{\text{par},i}$.

2695 where t_0 is the doubling time and λ_0 is the growth rate, equivalent to the optimised
 2696 flux of the biomass reaction.

2697 Based on the growth rates computed in rounds of ablation (Fig. 5.2), the synthesis
 2698 time of each biomass component was computed as follows:

$$t_{\text{seq},i} = f_i \cdot \frac{\ln 2}{\lambda_{\text{seq},i}} \quad (5.14)$$

2699 where i represents each of the biomass components (lipids, proteins, carbohydrates,
 2700 DNA, RNA, cofactors, and ions), $t_{\text{seq},i}$ is the predicted time for synthesis of each
 2701 biomass component, f_i is the mass fraction of each biomass component (shown
 2702 in Table B.3), and $\lambda_{\text{seq},i}$ is the optimal flux of the ablated biomass reaction. In
 2703 Eq. 5.14, f_i functions as a scaling factor so that the synthesis time of a biomass
 2704 component is proportional to the proportion of the biomass component in dry
 2705 cell mass.

2706 For comparison, I computed estimates of the time for each biomass component,
 2707 assuming that it is proportional to the mass fraction:

$$t_{\text{par},i} = f_i \cdot t_0 \quad (5.15)$$

2708 where t_0 is the doubling time found in Eq. 5.13.

2709 To determine whether sequential biosynthesis of biomass components or parallel
 2710 biosynthesis of biomass components is advantageous, I defined a ratio $\tau_{\text{seq}/\text{par}}$ that
 2711 represents the ratio between the total time predicted by ablation and the biomass
 2712 component that is predicted to take the most time:

$$\tau_{\text{seq}/\text{par}} = \frac{T_{\text{seq}}}{T_{\text{par}}} \quad (5.16)$$

²⁷¹³ where T_{seq} represents the predicted growth time assuming sequential biosynthesis
²⁷¹⁴ and T_{par} represents the limiting biomass synthesis time assuming parallel biosyn-
²⁷¹⁵ thesis. The quantities T_{seq} and T_{par} are defined:

$$T_{\text{seq}} = \sum_i t_{\text{seq},i} \quad (5.17)$$

$$T_{\text{par}} = \operatorname{argmax}_i t_{\text{par},i} \quad (5.18)$$

²⁷¹⁶ Because $f_{\text{protein}} = 0.525$ (Table B.3), $T_{\text{par}} = t_{\text{par,protein}}$.

²⁷¹⁷ Therefore,

dangling sentence?

$$\begin{aligned} \tau_{\text{seq/par}} &= \frac{T_{\text{seq}}}{T_{\text{par}}} \\ &= \frac{(\sum_i t_{\text{seq},i})}{(\operatorname{argmax}_i t_{\text{par},i})} \\ &= \frac{\left(\sum_i f_i \cdot \frac{\ln 2}{\lambda_{\text{seq},i}} \right)}{\left(f_{\text{protein}} \cdot \frac{\ln 2}{\lambda_0} \right)} \\ &= \left(\frac{f_{\text{lipid}}}{\lambda_{\text{seq,lipid}}} + \frac{f_{\text{protein}}}{\lambda_{\text{seq,protein}}} + \dots + \frac{f_{\text{ion}}}{\lambda_{\text{seq,ion}}} \right) \cdot \frac{\lambda_0}{f_{\text{protein}}} \end{aligned} \quad (5.19)$$

²⁷¹⁸ The expression in Eq. 5.19 means that the definition of the $\tau_{\text{seq/par}}$ ratio does not
²⁷¹⁹ reduce to a trivial expression and depends on the λ_0 and the $\lambda_{\text{seq},i}$ values, which
²⁷²⁰ are independent of each other. A $\tau_{\text{seq/par}} < 1$ means that synthesising biomass
²⁷²¹ components in sequence saves more time, and sequential biosynthesis is favoured.
²⁷²² Conversely, $\tau_{\text{seq/par}} > 1$ indicates that parallel synthesis of biomass components
²⁷²³ is favoured as synthesising biomass components in sequence does not save time.

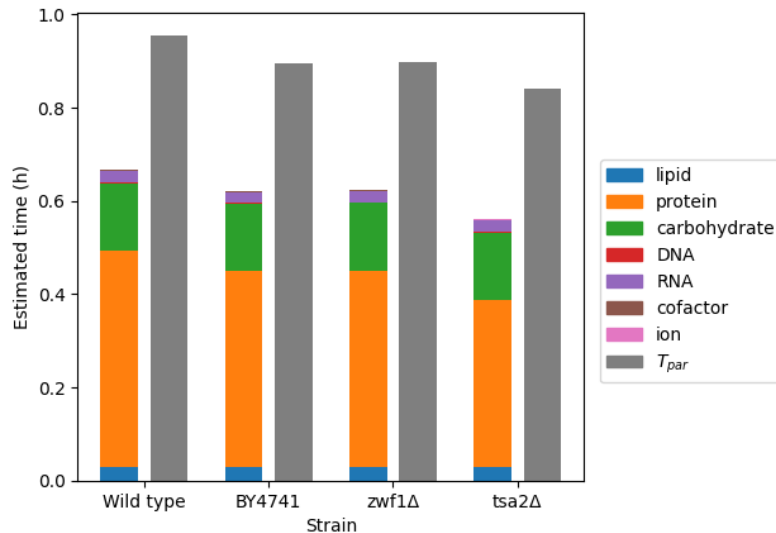


Figure 5.5: Estimated synthesis times of biomass components: from ablation and T_{par} , for wild-type (unmodified model) BY4741, $zwf1\Delta$ in the BY4741 background, and $tsa2\Delta$ in the BY4742 background

2724 To confirm that the advantage of the sequential biosynthesis strategy is retained
 2725 in other genetic backgrounds, I extended the computation $\tau_{seq/par}$ and related
 2726 quantities to models in which genes were deleted. To corroborate results from
 2727 Chapter 3, the BY4741 $zwf1\Delta$ and BY4742 $tsa2\Delta$ strains were simulated — the
 2728 latter was substituted for $tsa1\Delta$ $tsa2\Delta$ because the ecYeast8 model did not include
 2729 reactions that correspond to $TSA1$. The deletions were made by restricting to
 2730 zero the reaction fluxes that are associated with the deleted genes in the model.
 2731 For BY4741-background strains, supplements were simulated by allowing uptake
 2732 of histidine, leucine, tryptophan, methionine and uracil. The same applied to
 2733 BY4742-background strains, but lysine uptake replaced methionine uptake. Fig.
 2734 5.5 shows that $\tau_{seq/par} < 1$ still held for auxotrophs and deletion strains, suggest-
 2735 ing that the sequential biosynthesis strategy remained advantageous. Assuming
 2736 that temporal scheduling of the synthesis of biomass components during growth
 2737 explains the timing of biosynthetic events in the yeast metabolic cycle, these
 2738 observations supports results in Chapter 3 which shows that auxotrophs and
 2739 deletion strains have YMCs.

2740 5.6 Effect of restricting the enzyme pool

2741 The yeast cell has a finite enzyme-available proteome pool, so it must decide
2742 which enzymes to allocate the greatest proportions of the pool to. To study this
2743 effect using the ecYeast8 model, I imposed a constraint on the enzyme-available
2744 proteome pool by varying the value of the upper limit of the flux e_{pool} of the
2745 enzyme pool pseudoreaction (Eq. 5.8), taking advantage of a GECKO formalism
2746 that is easy to modify and interpret. With a smaller e_{pool} , the sum of fluxes of
2747 enzyme usage pseudoreactions must decrease, and the model must decide which
2748 enzyme usage pseudoreactions to allocate a higher flux to, modelling the biological
2749 response to a restricted enzyme pool.

2750 Fig. 5.6 shows that constraining the proteome pool available for enzymes leads to a
2751 greater advantage of sequential biosynthesis of biomass components over parallel
2752 biosynthesis. Within the range of e'_{pool} that gives realistic growth rates, this is
2753 evidenced by a decreasing $\tau_{\text{seq/par}}$ ratio if e'_{pool} decreases (Fig. 5.6a). Concurrently,
2754 as e'_{pool} decreases, the wild type growth rate (λ_0) decreases linearly to zero and
2755 ablated growth rates ($\lambda_{\text{seq},i}$) decrease in linear segments independently of each
2756 other and of the growth rate. These observations can be explained by considering
2757 Eq. 5.19 and modelling the changes of λ_0 and $\lambda_{\text{seq},i}$ with respect to $e'_{\text{pool}}/e_{\text{pool}}$ as
2758 linear equations (Appendix B.3).

2759 5.7 Effect of carbon and nitrogen sources

2760 To explore whether sequential synthesis of biomass components remains advant-
2761 ageous across nutrient conditions, I investigated how changes in the concentra-
2762 tions of nitrogen (ammonium) and carbon sources (glucose and pyruvate) affected
2763 the resource allocation strategies. Ammonium is the form of nitrogen in minimal

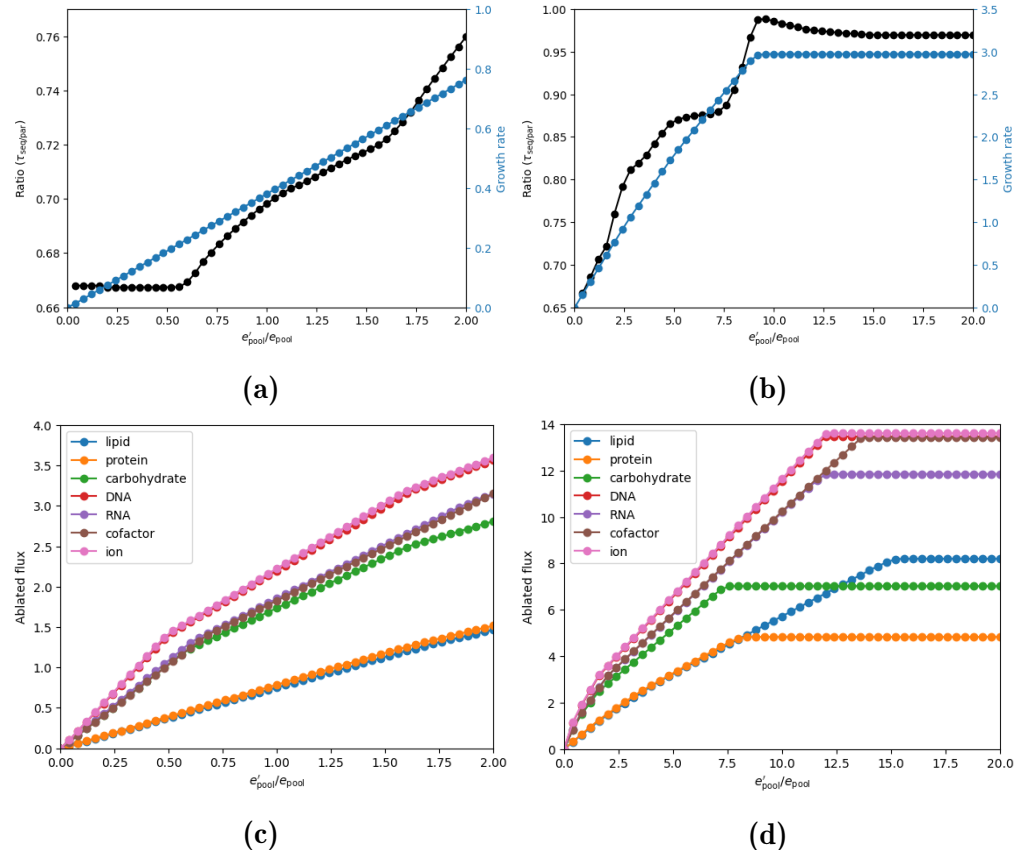


Figure 5.6: Effect of the size of the proteome pool available for enzymes (e'_pool) on (5.6a, 5.6b) $\tau_{\text{seq/par}}$, the growth rate, and (5.6c, 5.6d) the optimal flux of the ablated biomass reaction $\lambda_{\text{seq},i}$ in each round of ablation. (5.6a) and (5.6c) show $e'_\text{pool}/e_\text{pool} \leq 2$, while (5.6b) and (5.6d) show $e'_\text{pool}/e_\text{pool} \leq 20$.

2764 growth media. Glucose is the preferred carbon source for budding yeast, and as
2765 pyruvate is a non-fermentable carbon source, using it as a carbon source would
2766 show how substantial changes to central carbon metabolism affected resource
2767 allocation strategies.

2768 **5.7.1 Saturation of exchange reactions**

2769 Investigating the effect of carbon and nitrogen sources requires finding ranges
2770 of concentrations of each source to be used in an FBA problem that leads to
2771 biologically informative results. The saturation point of the nutrient, defined as
2772 the concentration of the nutrient at which the growth rate reaches its maximum,
2773 thus serves as a biologically relevant reference point. Although genome-scale
2774 metabolic models have nutrient exchange reactions that simulate the presence
2775 or absence of nutrients, saturation points from experimental studies cannot be
2776 directly used as flux bounds for these reactions because FBA does not account
2777 for substrate concentrations. Instead, I constrained the flux of exchange reactions
2778 so that the optimised growth rate matched experimental observations, as was
2779 performed in previous FBA-based studies (Elsemman et al., 2022; Famili et al.,
2780 2003).

2781 To model the effect of nutrient concentrations on growth rate, I created saturation
2782 curves that show how the effect of nutrient exchange flux on the objective func-
2783 tion. Figs. 5.7a and 5.7b show that the saturation curves of glucose and pyruvate
2784 had different shapes. In addition, the maximum growth rate on glucose (0.38 h^{-1})
2785 was greater than the maximum growth rate on pyruvate (0.25 h^{-1}). Furthermore,
2786 Fig. 5.7c shows that the maximum growth rate on the carbon source sets the
2787 saturation point for ammonium.

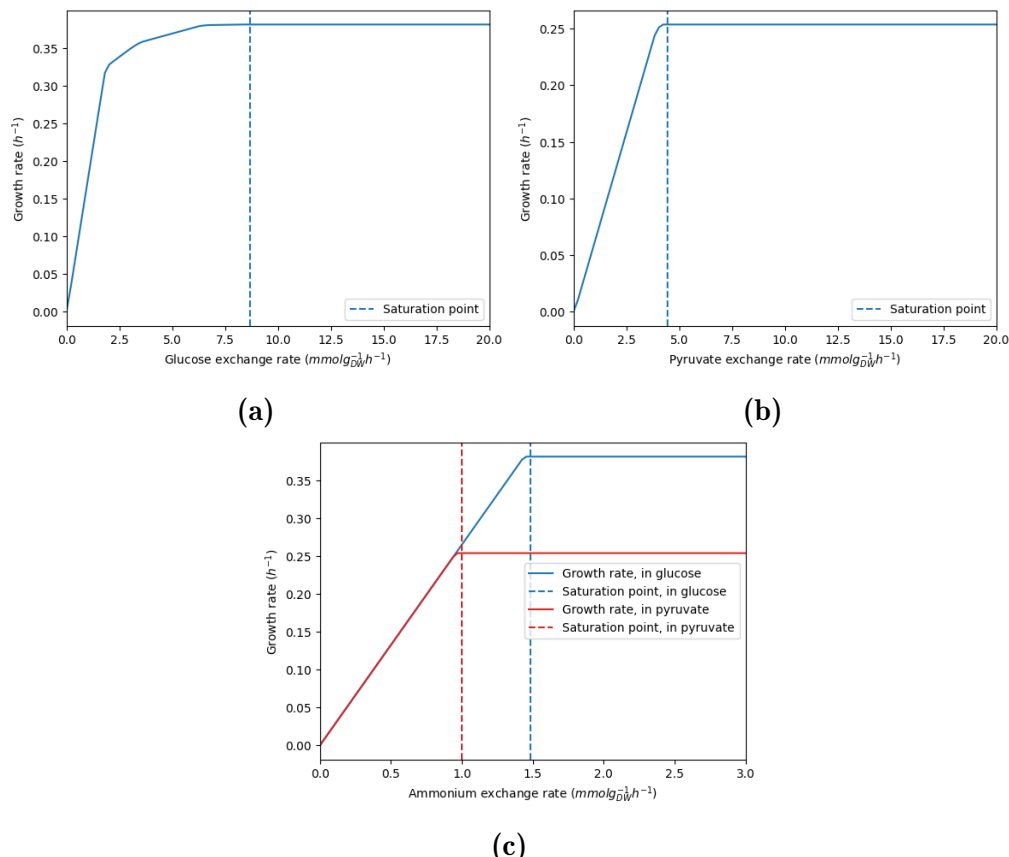


Figure 5.7: Effect of glucose (5.7a), pyruvate (5.7b), and ammonium (5.7c) exchange reactions on growth rate. The saturation point of exchange reactions is defined as the flux of an exchange reaction above which the objective function reaches its maximum.

2788 These growth saturation curves agree with similar studies. Specifically, the growth
2789 saturation curve for glucose (Fig. 5.7a) is similar to that simulated by Elsemman
2790 et al. (2022) using another derivative of the Yeast8 model. The maximum growth
2791 rate on glucose agrees with Domenzain et al. (2022), which used GECKO 2 to
2792 create the ecYeast7 model to predict maximum growth rates on various carbon
2793 sources. Domenzain et al. (2022) did not simulate growth on pyruvate, but a
2794 lower maximum growth rate on pyruvate is consistent with my experimental
2795 observations.

2796 **5.7.2 Effect of carbon and nitrogen sources on biomass synthesis**

2797 **strategies**

2798 **Glucose and ammonium**

2799 To assess the effect of glucose and ammonium concentration on biomass synthesis
2800 strategies, I ablated components in the biomass reaction in different nutrient
2801 conditions set by glucose and ammonium exchange fluxes to obtain $\tau_{\text{seq/par}}$, λ_0 ,
2802 $t_{\text{seq,carbohydrate}}$, and $t_{\text{seq,protein}}$ (Fig. 5.8). Additionally, to determine whether the
2803 carbon or nitrogen source is limiting for each of these quantities, I defined the
2804 sensitivity at each nutrient condition ($R_{\text{glc}}, R_{\text{amm}}$), with respect to each axis i as:

$$s_i(R_{\text{glc}}, R_{\text{amm}}) = \frac{R_i}{y(R_{\text{glc}}, R_{\text{amm}})} \cdot \frac{\partial y(R_{\text{glc}}, R_{\text{amm}})}{\partial R_i} \quad (5.20)$$

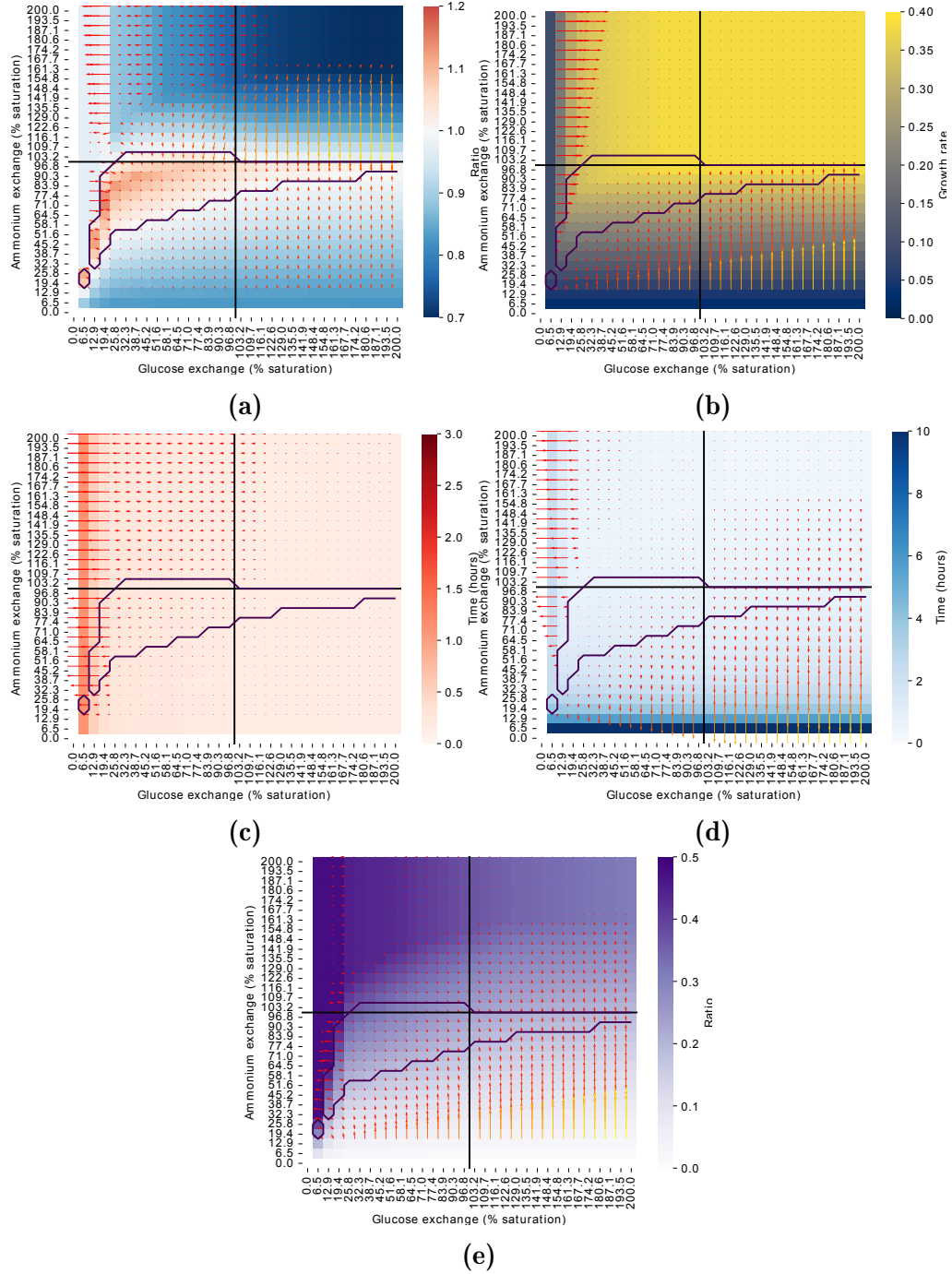


Figure 5.8: Effect of glucose and ammonium exchange rates on (5.8a) $\tau_{\text{seq/par}}$, (5.8b) growth rate based on unmodified biomass reaction, λ_0 , (5.8c) predicted carbohydrate synthesis time, $t_{\text{seq,carbohydrate}}$ (5.8d) predicted protein synthesis time, $t_{\text{seq,protein}}$, and (5.8e) ratio of carbohydrate synthesis time to protein synthesis time, $t_{\text{seq,carbohydrate}}/t_{\text{seq,protein}}$. Exchange rates are expressed in percentages of growth saturation from Fig. 5.7, with black straight lines indicate 100% of saturation. Contours show regions in which $\tau_{\text{seq/par}} > 1$. Arrows overlaid on heatmaps indicate sensitivity of the quantity as a vector ($s_{\text{glc}}, s_{\text{amm}}$) (Eq. 5.20).

where i indicates glucose (glc) or ammonium (amm), R_i indicates the exchange rate, glucose (R_{glc}) or ammonium (R_{amm}), an $(R_{\text{glc}}, R_{\text{amm}})$ pair defines a nutrient condition, and $y(R_{\text{glc}}, R_{\text{amm}})$ represents the quantity of interest at each nutrient condition. For a specific nutrient condition $(R_{\text{glc}}, R_{\text{amm}})$, if $s_{\text{glc}}(R_{\text{glc}}, R_{\text{amm}}) > s_{\text{amm}}(R_{\text{glc}}, R_{\text{amm}})$ for a quantity of interest y , then the quantity is more sensitive to glucose exchange in this condition. Conversely, if $s_{\text{glc}}(R_{\text{glc}}, R_{\text{amm}}) < s_{\text{amm}}(R_{\text{glc}}, R_{\text{amm}})$, the quantity is more sensitive to ammonium exchange.

Fig. 5.8b divides the nutrient conditions into three regions according to nutrient limitation: a glucose-limiting region, an ammonium-limiting region, and a region where neither glucose nor ammonium is limiting. These regions are determined by $(s_{\text{glc}}, s_{\text{amm}})$ vectors. Fig. 5.8a shows that parallel biosynthesis was advantageous ($\tau_{\text{seq/par}} > 1$) in two circumstances: when both glucose and ammonium limited the growth rate, and when ammonium exchange was at saturation while glucose exchange is greater than saturation. In contrast, when the growth rate was near its maximum, where neither glucose nor ammonium was limiting, when glucose or ammonium exchange increased, sequential biosynthesis became more advantageous ($\tau_{\text{seq/par}} < 1$).

To determine whether changes in the synthesis time of biomass components are responsible for switching of scheduling strategies between sequential and parallel biosynthesis, I investigated how R_{glc} and R_{amm} affected $\frac{t_{\text{seq,carbohydrate}}}{t_{\text{seq,protein}}}$. Synthesis times $t_{\text{seq},i}$ were computed to assess whether the ratio between the synthesis times differed in different conditions. The ratio $\frac{t_{\text{seq,carbohydrate}}}{t_{\text{seq,protein}}}$ serves as the principal measure to quantify how $t_{\text{seq},i}$ values change as nutrient conditions change. This ratio is informative because:

- 2829 1. Of all biomass components, predicted synthesis times of these biomass
2830 components varied the most as the glucose and ammonium exchange rates
2831 were varied.
- 2832 2. Each accounts for a large proportion of biomass: protein accounts for 52.5%
2833 and carbohydrate accounts for 36.4% (Table B.3).
- 2834 3. Carbohydrate synthesis has a clear biochemical relationship with the level
2835 of a carbon source. Additionally, protein synthesis has a clear biochemical
2836 relationship with the level of ammonium as amino acids contain amino
2837 groups.

2838 Although there is no obvious relationship between $\frac{t_{\text{seq,carbohydrate}}}{t_{\text{seq,protein}}}$ and $\tau_{\text{seq/par}}$ values
2839 (Fig. 5.8e), the effect of R_{glc} and R_{pyr} on $t_{\text{seq,carbohydrate}}$ and $t_{\text{seq,protein}}$ explains
2840 the behaviour of $\frac{t_{\text{seq,carbohydrate}}}{t_{\text{seq,protein}}}$. Fig. 5.8e shows that in the glucose-limiting region,
2841 $\frac{t_{\text{seq,carbohydrate}}}{t_{\text{seq,protein}}}$ was at a constant high value because, as R_{glc} increased in this region,
2842 both $t_{\text{seq,carbohydrate}}$ and $t_{\text{seq,protein}}$ decreased. However, in the ammonium-limited
2843 region, $\frac{t_{\text{seq,carbohydrate}}}{t_{\text{seq,protein}}}$ increased as R_{amm} increased because $t_{\text{seq,protein}}$ decreased while
2844 $t_{\text{seq,carbohydrate}}$ remained constant.

2845 Consider the trajectory of $(R_{\text{glc}}, R_{\text{amm}})$ values from $(0, 0)$ to $(R_{\text{glc,sat}}, R_{\text{amm,sat}})$
2846 through conditions with high $\tau_{\text{seq/par}}$ values (Fig. 5.8a), where $R_{\text{glc,sat}}$ and $R_{\text{amm,sat}}$
2847 are saturation values of glucose and ammonium values, respectively. This trajec-
2848 tory includes conditions in which both glucose and ammonium are limiting, and as
2849 the trajectory is followed, both $t_{\text{seq,carbohydrate}}$ and $t_{\text{seq,protein}}$ decreased, explaining
2850 why $\frac{t_{\text{seq,carbohydrate}}}{t_{\text{seq,protein}}}$ remained roughly at the same value along this trajectory.

2851 The different effects of the exchange rates on $t_{\text{seq,carbohydrate}}$ and on $t_{\text{seq,protein}}$ has a
2852 biological relevance. Fig. 5.8c shows that glucose exchange limited carbohydrate
2853 synthesis time in all nutrient conditions, and this observation can be explained by
2854 glucose being the sole carbon source for the cell. In contrast, Fig. 5.8d shows that

bit hard
to read

2855 ammonium exchange limited protein synthesis time for most nutrient conditions,
2856 except for conditions in which glucose exchange was very low. This observation
2857 can be explained by the fact that both carbon and nitrogen sources contribute
2858 to protein biosynthesis. In sum, the relationships between carbon and nitrogen
2859 source uptake and the synthesis of carbohydrates and proteins determine how
2860 scheduling strategies change according to nutrient conditions.

2861 **Pyruvate and ammonium**

2862 To investigate the effect of a non-fermentable carbon source on biomass synthesis
2863 strategies, I repeated the investigation using pyruvate as the carbon source.

2864 Results show that the saturation curve of pyruvate controlled the effect of ex-
2865 change rates on scheduling strategies. Fig. 5.9 shows that when pyruvate was
2866 the carbon source, the region of carbon source limitation was larger than when
2867 glucose was the carbon source. This observation reflected the different shapes of
2868 the pyruvate and glucose saturation curves (Fig. 5.7): on glucose, the growth rate
2869 reached half of its maximum value when glucose exchange was well below half
2870 saturation, while on pyruvate the growth rate reached half of its maximum value
2871 when pyruvate exchange was half saturation.

2872 Fig. 5.9 shows that the relationships between exchange rates and the quantities
2873 $\tau_{\text{seq/par}}$, λ_0 , $t_{\text{seq,carbohydrate}}$, and $t_{\text{seq,protein}}$ were similar to the glucose-ammonium
2874 case. In other words, when pyruvate was the carbon source, the relationship
2875 between carbon and nitrogen source uptake and the synthesis of carbohydrates
2876 and proteins still determined how scheduling strategies changed according to nu-
2877 trient conditions. Parallel biosynthesis was advantageous in two conditions: when
2878 both pyruvate and ammonium limited the growth rate, and when ammonium
2879 exchange was at saturation while pyruvate exchange was greater than saturation
2880 (Fig. 5.9a). In contrast, sequential biosynthesis was advantageous when neither

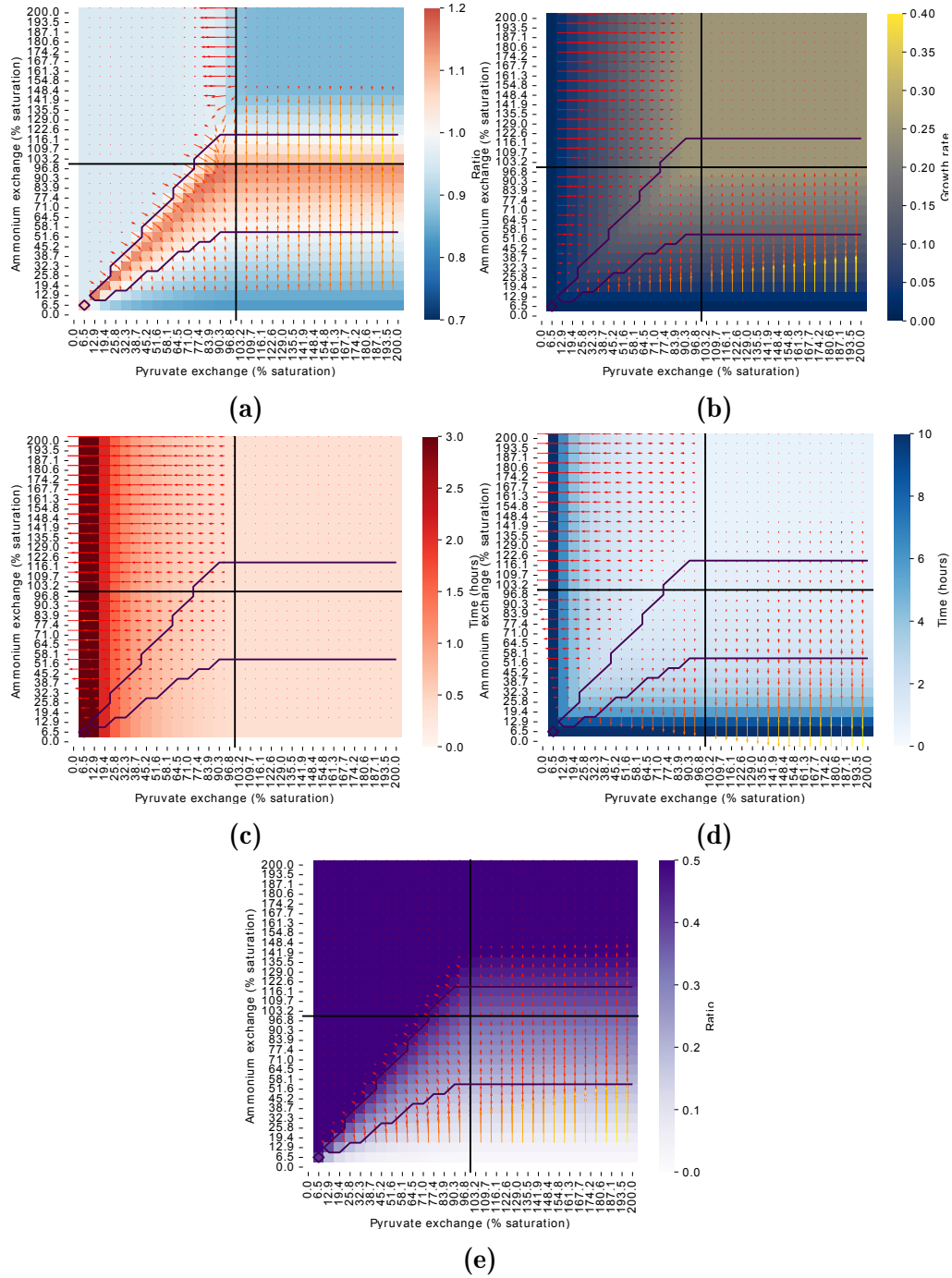


Figure 5.9: Effect of pyruvate and ammonium exchange rates on (5.9a) $\tau_{\text{seq/par}}$, (5.9b) growth rate based on unmodified biomass reaction, λ_0 , (5.9c) predicted carbohydrate synthesis time, $t_{\text{seq,carbohydrate}}$ (5.9d) predicted protein synthesis time, $t_{\text{seq,protein}}$, and (5.9e) ratio of carbohydrate synthesis time to protein synthesis time, $t_{\text{seq,carbohydrate}}/t_{\text{seq,protein}}$. Exchange rates are expressed in percentages of growth saturation from Fig. 5.7, with black straight lines indicate 100% of saturation. Contours show regions in which $\tau_{\text{seq/par}} > 1$. Arrows overlaid on heatmaps indicate sensitivity of the quantity as a vector ($s_{\text{pyr}}, s_{\text{amm}}$) (Eq. 5.20).

2881 pyruvate nor ammonium was limiting. $\frac{t_{\text{seq,carbohydrate}}}{t_{\text{seq,protein}}}$ remained at high values when
2882 pyruvate is limiting or when pyruvate and ammonium were both limiting (Fig.
2883 5.9e). Furthermore, the behaviour of $\frac{t_{\text{seq,carbohydrate}}}{t_{\text{seq,protein}}}$ as nutrient conditions varied
2884 could also be explained by pyruvate exchange limiting carbohydrate synthesis
2885 time (Fig. 5.9c) and by both pyruvate and ammonium exchange limiting protein
2886 synthesis time (Fig. 5.9d).

2887 **5.7.3 Relationship between proteome allocation and resource al-**
2888 **location strategy**

2889 **Glucose and ammonium**

2890 The investigation of the effect of carbon and nitrogen sources on scheduling
2891 strategies led to a new hypothesis: the cell favours parallel biosynthesis of biomass
2892 components when the carbon source and the nitrogen source are both limiting,
2893 especially if the associated biomass components share metabolic pathways and if
2894 the conditions dictate similar levels of enzymes. This hypothesis arose from the
2895 observation that the highest $\tau_{\text{seq/par}}$ occurred at the boundary at which both the
2896 carbon source and the nitrogen source were limiting.

2897 To evaluate this hypothesis, I compared the enzyme usage reaction flux vectors
2898 in rounds of ablation between a high $\tau_{\text{seq/par}}$ condition and a low $\tau_{\text{seq/par}}$ condition
2899 created by combinations of glucose and ammonium exchange rates. Enzyme usage
2900 reaction flux vectors show how the cell allocates its finite proteome to enzymes
2901 when each biomass component is prioritised (Section 5.5).

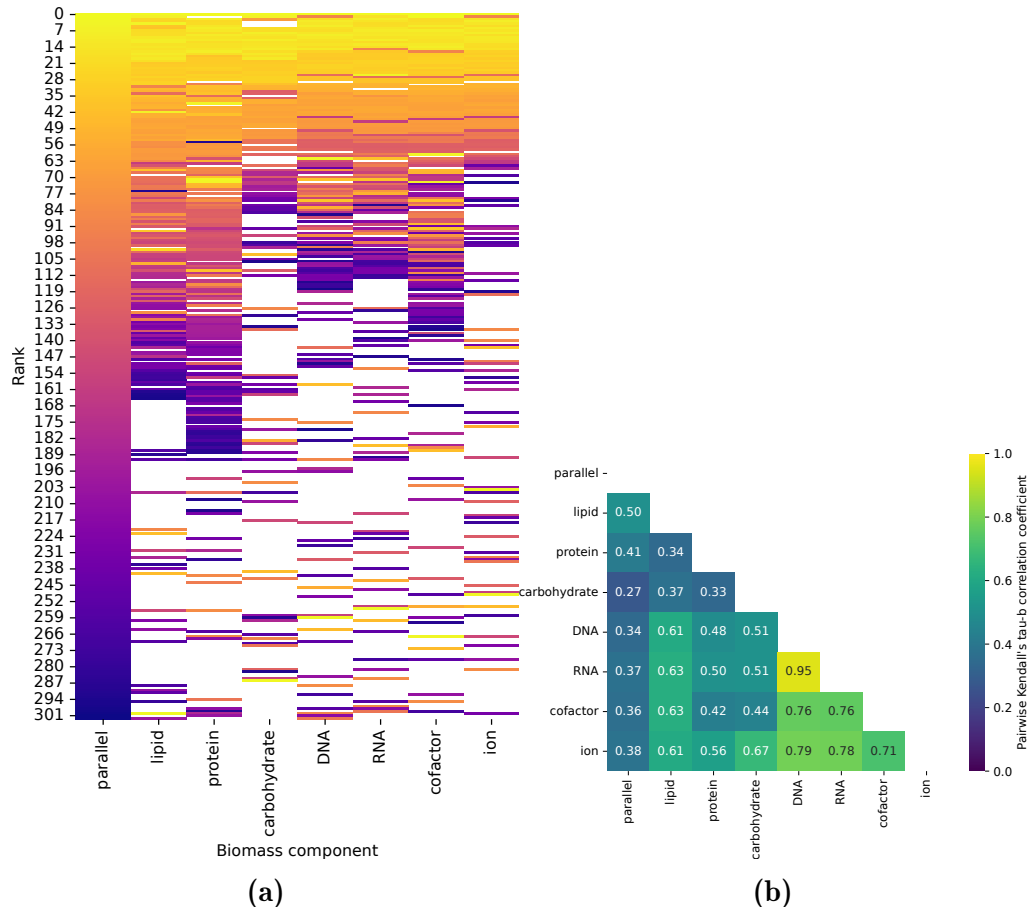


Figure 5.10: For the high $\tau_{\text{seq/par}}$ condition ($R_{\text{glc}} = 1.69 \text{ mmol g}_{\text{DW}}^{-1} \text{ h}^{-1}$, $R_{\text{amm}} = 1.05 \text{ mmol g}_{\text{DW}}^{-1} \text{ h}^{-1}$): **(5.10a)** changes in enzyme usage reaction flux in rounds of ablation. Columns show the biomass component prioritised. In each column, rows represent enzyme usage reactions, arranged in descending order of flux. Colours identify the reactions, with white indicating reactions that carry zero flux in the parallel case. **(5.10b)** Pairwise Kendall's τ -b rank correlation coefficient (KENDALL, 1945) for each pair of enzyme usage flux profiles.

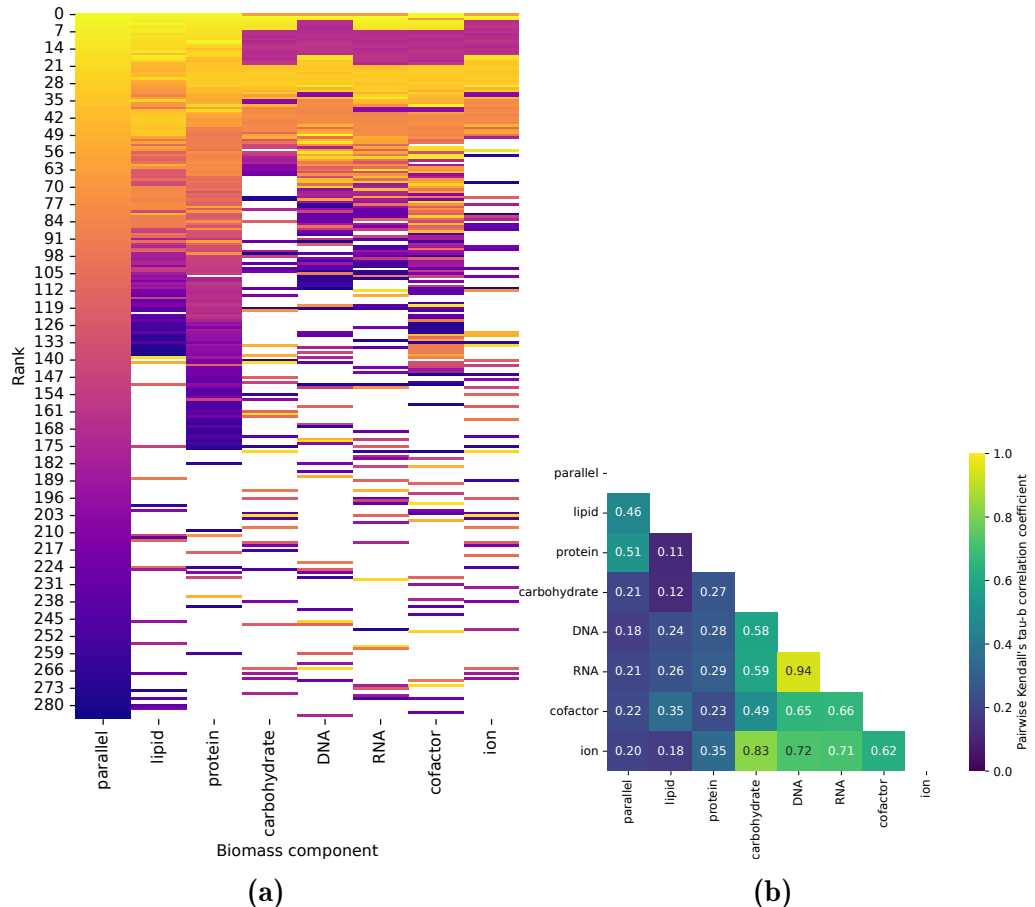


Figure 5.11: For the low $\tau_{\text{seq/par}}$ condition ($R_{\text{glc}} = 16.89 \text{ mmol g}_{\text{DW}}^{-1} \text{ h}^{-1}$): **(5.11a)** changes in enzyme usage reaction flux in rounds of ablation. Columns show the biomass component prioritised. In each column, rows represent enzyme usage reactions, arranged in descending order of flux. Colours identify the reactions, with white indicating reactions that carry zero flux in the parallel case. **(5.11b)** Pairwise Kendall's τ -b rank correlation coefficient (KENDALL, 1945) for each pair of enzyme usage flux profiles.

2902 To test whether similarities in proteome allocation to enzymes explain parallel
2903 biosynthesis, Fig. 5.10a shows that when both glucose and ammonium were limit-
2904 ing, the allocation patterns were similar across rounds of ablation, thus explaining
2905 the advantage of parallel biosynthesis of biomass components. This similarity is
2906 quantified in Fig. 5.10b, which shows that parallel biosynthesis exhibited relatively
2907 similar proteome allocation with the synthesis of individual biomass components.

2908 In contrast, Fig. 5.11a shows that when neither glucose nor ammonium limited
2909 growth, biomass components could be divided into two groups based on enzyme
2910 usage reaction flux vectors. These groups suggest an explanation for sequential
2911 biosynthesis: the cell may synthesise lipids and proteins together in one stage
2912 of its growth cycle, while synthesising carbohydrates, DNA, RNA, cofactors,
2913 and ions together in another stage. The bias towards sequential biosynthesis is
2914 further emphasised by Fig. 5.11b, which shows that parallel biosynthesis exhibited
2915 different proteome allocation compared to the synthesis of individual biomass
2916 components.

2917 Pyruvate and ammonium

2918 To evaluate, in a different carbon source, whether parallel biosynthesis is also
2919 favoured when biomass components share metabolic pathways, I extended the
2920 comparison of enzyme usage reaction flux vectors in rounds of ablation to nutrient
2921 conditions created by pyruvate and ammonium exchange rates.

2922 Similar to the glucose-ammonium investigation, in the high $\tau_{\text{seq/par}}$ condition
2923 where pyruvate and ammonium were limiting, Figs. 5.12a and 5.12b show that
2924 proteome allocation were similar across rounds of ablation, supporting parallel
2925 biosynthesis as a scheduling strategy. However, the results for the low $\tau_{\text{seq/par}}$ case
2926 suggest that grouping of biomass components explains sequential biosynthesis for
2927 only very low $\tau_{\text{seq/par}}$. Fig. 5.13a shows that when pyruvate was the carbon source,

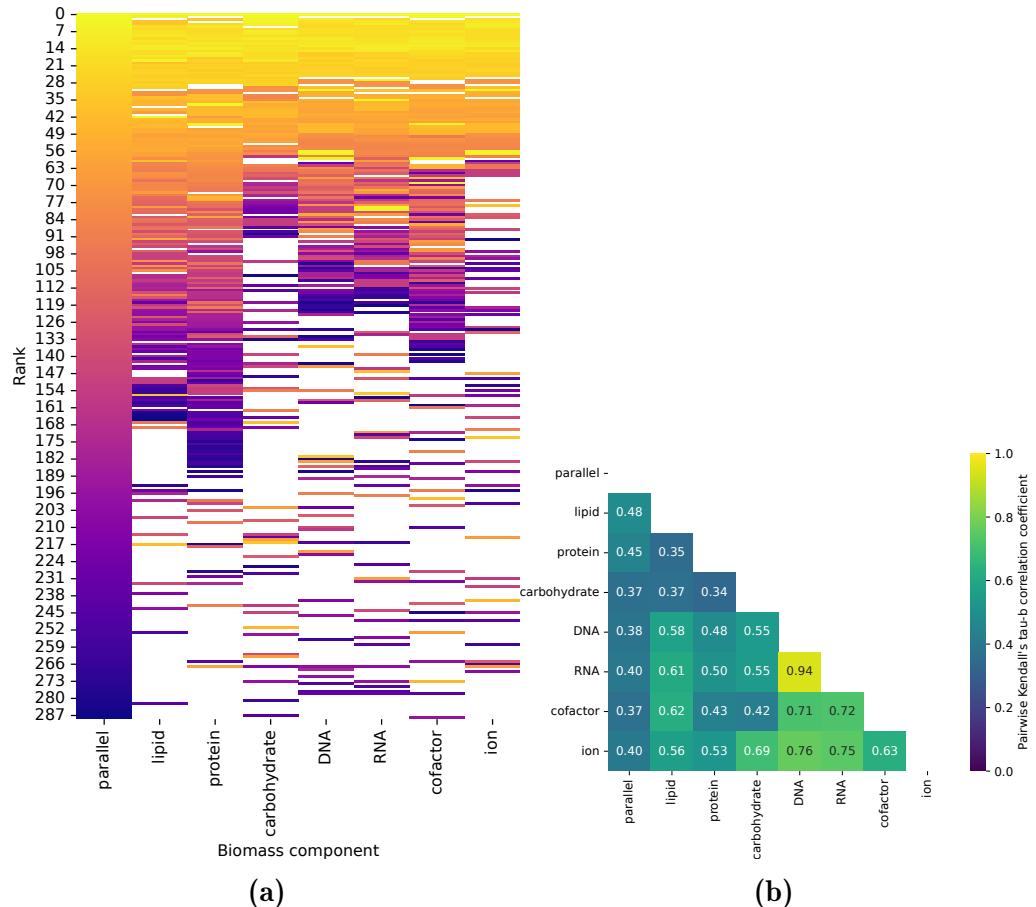


Figure 5.12: For the high $\tau_{\text{seq/par}}$ condition ($R_{\text{pyr}} = 3.73 \text{ mmol g}_{\text{DW}}^{-1} \text{ h}^{-1}$, $R_{\text{amm}} = 0.90 \text{ mmol g}_{\text{DW}}^{-1} \text{ h}^{-1}$): **(5.12a)** changes in enzyme usage reaction flux in rounds of ablation. Columns show the biomass component prioritised. In each column, rows represent enzyme usage reactions, arranged in descending order of flux. Colours identify the reactions, with white indicating reactions that carry zero flux in the parallel case. **(5.12b)** Pairwise Kendall's τ -b rank correlation coefficient (KENDALL, 1945) for each pair of enzyme usage flux profiles.

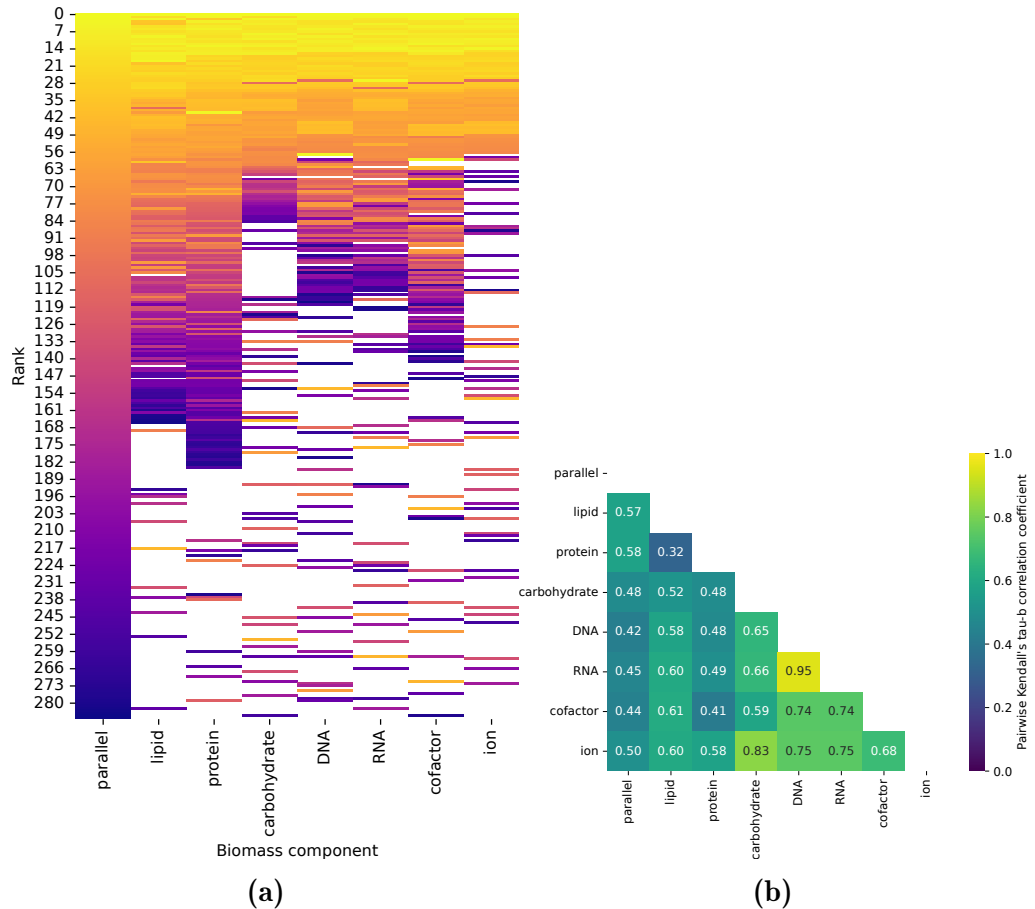


Figure 5.13: For the low $\tau_{\text{seq/par}}$ condition ($R_{\text{pyr}} = 8.89 \text{ mmol g}_{\text{DW}}^{-1} \text{ h}^{-1}$): (5.13a) changes in enzyme usage reaction flux in rounds of ablation. Columns show the biomass component prioritised. In each column, rows represent enzyme usage reactions, arranged in descending order of flux. Colours identify the reactions, with white indicating reactions that carry zero flux in the parallel case. (5.13b) Pairwise Kendall's τ -b rank correlation coefficient (KENDALL, 1945) for each pair of enzyme usage flux profiles.

2928 the contrast of proteome allocation between biomass components in the low
2929 $\tau_{\text{seq/par}}$ condition was lessened compared to when glucose was the carbon source.
2930 This may be explained by the higher $\tau_{\text{seq/par}}$ in this condition ($\tau_{\text{seq/par}} = 0.9$),
2931 compared to the $\tau_{\text{seq/par}}$ in the glucose-ammonium investigation ($\tau_{\text{seq/par}} = 0.7$).
2932 The use of enzyme usage vectors to explain biomass synthesis scheduling strategies
2933 is called into question by the multiplicity of solutions in FBA. Fig. 5.14 shows
2934 that the relationship between exchange rates and measures of similarity between
2935 enzyme usage fluxes when carbohydrate was prioritised and when protein was
2936 prioritised was not continuous. This observation is likely explained by the mul-
2937 tiplicity of solutions in FBA. Namely, while FBA finds the optimal value of the
2938 objective function, there is no guarantee that the flux vector \mathbf{v} (Eq. 5.2) is equiva-
2939 lent across linear programming solvers. In sum, although choosing representative
2940 nutrient conditions led to an attractive picture that may confirm the hypothesis
2941 of this section, the computational limitations of FBA ~~may render any conclusion~~
2942 ~~flawed.~~

may cast doubts on ...

2943 5.8 Discussion

2944 This chapter uses a genome-scale model of budding yeast and flux balance analysis
2945 to test whether sequential synthesis of biomass components reflects an adaptation
2946 to limited cellular resources.

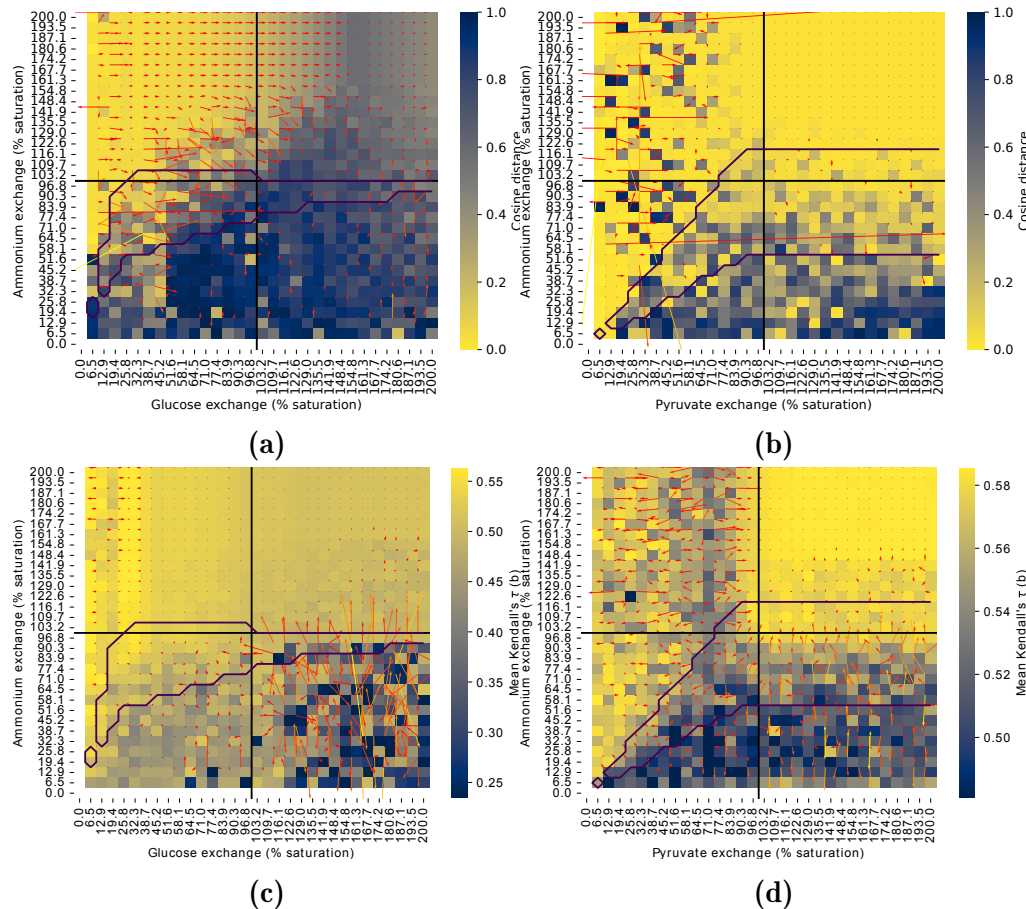


Figure 5.14: Measures of similarity between enzyme usage fluxes in different nutrient conditions. Cosine distances between the vector of enzyme usage fluxes when protein is prioritised and the equivalent vector when carbohydrate is prioritised are shown (5.14a) for glucose-ammonium conditions and (5.14b) pyruvate-ammonium conditions; smaller distances indicate a greater similarity between the two conditions. Means of the set of Kendall's τ -b rank correlation coefficients between the parallel case and each biomass-prioritised case are shown (5.14c) for glucose-ammonium conditions and (5.14d) pyruvate-ammonium conditions; larger means indicate a greater similarity between parallel biosynthesis and individual biomass component synthesis.

2947 My results suggest that ablation of components of the biomass reaction was
2948 a viable method to simulate sequential synthesis of biomass components, as
2949 evidenced by how ablation predicted biologically relevant changes in proteome
2950 allocation to enzymes. In addition, ablation lead to a way to estimate the time
2951 of synthesis of biomass components. These times suggest that sequential scheduling
2952 of biosynthesis saves time during growth and remains advantageous across
2953 deletion strains.

2954 My results further show that within realistic growth rates, a smaller proteome
2955 pool led to a greater advantage of sequential biosynthesis over parallel biosyn-
2956 thesis. However, parallel scheduling of biosynthesis becomes advantageous in
2957 some nutrient conditions, such as when both carbon and nitrogen sources are
2958 limiting. Further simulations suggest an explanation for this advantage of parallel
2959 biosynthesis: as each biomass component is synthesised, the cell allocates its
2960 proteome pool to enzymes in similar patterns.

2961 The advantage of sequential scheduling of biosynthesis over parallel scheduling of
2962 biosynthesis may explain why yeast cells exhibit metabolic cycles, in which there
2963 is a sequence of synthesising biomass components. Conversely, the advantage of
2964 parallel scheduling of biosynthesis over sequential scheduling of biosynthesis in
2965 nutrient-limiting conditions may explain the absence of metabolic cycles in ex-
2966 treme, non-permissive conditions. The metabolic cycle may thus be an adaptation
2967 to a limited proteome pool and having to carry out the metabolically expensive
2968 process of protein synthesis during cell growth (O' Neill et al., 2020). Clustering
2969 of the synthesis of lipids and proteins in one group may explain cycling of storage
2970 lipids (Campbell et al., 2020), while clustering of carbohydrate, DNA, and RNA
2971 synthesis in another group to group together processes that require oxidative
2972 phosphorylation may explain respiratory cycles in the YMC (Tu, Kudlicki et al.,
2973 2005).

2974 However, the limitations of using FBA to investigate resource allocation strategies
2975 in this chapter include multiplicity of solutions and a lack of ability to preform
2976 concentration-dependent, time-dependent, and compartment-dependent simula-
2977 tions. The multiplicity of solutions in FBA makes it challenging to draw conclu-
2978 sions about how quantities derived from flux values apart from growth. These
2979 values in the GECKO model include enzyme usage reaction fluxes, which would
2980 inform proteome allocation strategies. In addition, FBA gives a steady-state
2981 picture of metabolism. To describe changes in fluxes over time, derivatives such
2982 as dynamic FBA (Mahadevan et al., 2002) could be used. To further increase the
2983 precision of the model and thus its ability to make predictions, compartmental-
2984 isation can be considered (Elsemman et al., 2022), or resource balance analysis
2985 (Goelzer et al., 2011) can be used.

Chapter 6

Conclusions

2988 Although biological rhythms are crucial for living organisms to control their
2989 physiological processes in response to external conditions, not all biological rhythms
2990 are well-characterised. In contrast to the circadian rhythm and the cell division
2991 cycle, our knowledge of the biochemical basis of the yeast metabolic cycle is
2992 incomplete. It is unclear which mechanism drives cell division-independent cycling
2993 of biosynthesis observed in the yeast metabolic cycle, and it is also unclear what
2994 mechanism is responsible for the adaptation of the yeast metabolic cycle to chan-
2995 ging demands (Zylstra and Heinemann, 2022). Additionally, chemostat-based and
2996 single-cell experiments led to conflicting conclusions about the yeast metabolic
2997 cycle because each type of experiment creates different culture conditions and
2998 have different types of measurements.

2999 The primary goal of this thesis was thus to develop an explanation to reconcile
3000 chemostat and single-cell studies on the yeast metabolic cycle. Specifically, I
3001 developed such explanations through testing whether specific characteristics of
3002 the yeast metabolic cycle as observed in the chemostat could be recapitulated in
3003 single-cell microfluidics. In addition, this thesis aimed to show whether proteomic
3004 constraints could explain why the yeast cell temporally segregates biosynthetic
3005 events as it progresses through the yeast metabolic cycle. This secondary goal
3006 provided a coarse-grained explanation of a model of the yeast metabolic cycle as
3007 a fundamental metabolic adaptation to physiological constraints.

3008 **6.1 Microfluidics and fluorescence microscopy for cel-**
3009 **lular metabolic cycles**

3010 In Chapter 3, I used the ALCATRAS (Crane et al., 2014) single-cell microfluidics
3011 platform to physically separate budding yeast cells and fluorescence microscopy
3012 to monitor the yeast metabolic cycle and the cell division cycle. I showed that
3013 yeast cells independently generated flavin-based single-cell metabolic cycles. In
3014 addition, a specific phase of such cycles likely gated the cell division cycle, as
3015 evidenced by decoupling between the metabolic and cell division cycles during
3016 starvation. I further showed that the metabolic cycle was retained in nutrient
3017 perturbations and in deletion strains. In particular, I showed that cells generated
3018 such cycles in potassium-deficient conditions, contrary to O' Neill et al. (2020). I
3019 also showed that that *zwf1Δ* and *tsa1Δ tsa2Δ* cells generated flavin cycles whose
3020 waveforms differed from cycles of dissolved oxygen previously observed in the
3021 chemostat (Tu, Mohler et al., 2007; Causton et al., 2015).

3022 My results suggest that the yeast metabolic cycle is likely an intrinsic cycle in
3023 budding yeast that oscillates within a range of natural frequencies, but the cell
3024 is able to adjust this frequency to respond to nutrient conditions. If conditions
3025 are permissive, the metabolic cycle provides windows of opportunities for the cell
3026 division cycle to be initiated. Otherwise, if conditions are not permissive, the
3027 metabolic cycle continues while the cell division cycle is halted at a gap phase
3028 (G_1 or G_2/M).

3029 My results further suggest that the presence of sub-populations in the yeast
3030 culture could explain the discrepancy between single-cell and chemostat observa-
3031 tions. The idea of sub-populations that stagger their entry into the yeast metabolic
3032 cycle has been suggested before to explain chemostat observations (Burnetti et

3033 al., 2016), and the presence of genetically identical sub-populations that respond
3034 differently to the same nutrient perturbation has later been shown (Bagamery et
3035 al., 2020). Additionally, genetically identical sub-populations that have different
3036 levels of sensitivities to an inhibitor may also explain chemostat oscillations
3037 (Smith and P. Waltman, 1995).

3038 To provide more clarity to the role of nutrient storage in the yeast metabolic cycle,
3039 future work may include experiments with lipid synthesis-deficient strains. Ad-
3040 ditionally, a feast-and-famine experimental set-up which better emulates chemo-
3041 stat conditions could lead to a clearer explanation for previous chemostat-based
3042 studies. The glucose pulses imposed by this set-up may lead to a mathematical
3043 model of coupled oscillations that links the intrinsic yeast metabolic cycle to
3044 extrinsically-imposed oscillations.

3045 **6.2 Analysis of oscillatory time series in the yeast** 3046 **metabolic cycle**

3047 Because the ALCATRAS platform produces large datasets of time series, in
3048 Chapter 4, I developed a series of time series analysis methods. These methods
3049 clean data, visualise groups in a dataset, detect rhythmicity, estimate period-
3050 icity of signals, and detect synchrony between two types of signals. I showed
3051 that a high-pass filter offered good control over the frequency domain of time
3052 series. Subsequently, I showed that dimension-reduction (UMAP) and clustering
3053 (modularity clustering) methods agreed on a division between oscillatory and
3054 non-oscillatory time series in a dataset. Following this, I demonstrated that a
3055 statistical method based on the power spectrum and a support vector classifier
3056 offer modest performances in rhythmicity detection. Additionally, I showed that

3057 the autocorrelation function could be used to estimate periodicity and noise
3058 parameters from synthetic data. However, my current implementation of the
3059 autocorrelation function has limited ability in characterising noise parameters
3060 from real data. Finally, I showed that the cross-correlation function could be
3061 used to quantify the shift of one type of time series relative to another, across a
3062 population of paired time series

3063 Rhythmicity detection is complicated by its different definitions depending on the
3064 approach — reflected in the variety of rhythmicity detection methods compared
3065 in Chapter 4. From a signal-processing perspective, it can be defined as finding
3066 a strong signal within a range of expected frequencies (Zielinski et al., 2014).
3067 However, from a data science perspective, rhythmicity detection can be seen as
3068 identifying the values of a set of time series features that best discriminate between
3069 non-oscillatory and oscillatory time series.

3070 To improve the usefulness of the time series analysis methods, further refinement
3071 is needed. To make the clustering methods and the support vector classifier
3072 generalisable, we require a large enough dataset of signals that includes a variety
3073 of oscillation types and shapes, and hyperparameter tuning. Furthermore, to
3074 improve the ability of the autocorrelation function to infer noise properties of real
3075 data, a broader range of noise parameters should be simulated. Such simulations
3076 would provide addition information that leads to give a more precise relationship
3077 between noise parameters and the shape of the autocorrelation function. A precise
3078 way to detect of noise parameters can then be useful to compare the noise from
3079 different environmental conditions and imaging methods. With the improvements
3080 in place, the methods developed in Chapter 4 can form a powerful time series
3081 analysis pipeline for oscillatory signals from any natural phenomenon.

3082 6.3 Modelling yeast biosynthesis strategies under con-

3083 straints

Finally, in Chapter 5, I used an enzyme-constrained genome-scale model of budding yeast and flux balance analysis to address whether a limited proteome pool leads to a preference of sequential biosynthesis over parallel biosynthesis. In this chapter, I used the novel approach of ablating components of the biomass reaction to simulate temporal segregation of biosynthesis, and devised a time ratio that indicates whether sequential or parallel biosynthesis was more advantageous. I showed that sequential scheduling of biosynthesis was advantageous across deletion strains, and became more advantageous if the proteome pool was smaller. However, I also showed that parallel scheduling of biosynthesis became advantageous when both carbon and nitrogen sources were limiting. This observation may be explained by the synthesis pathways across different biomass components sharing enzymes.

The advantage of sequential biosynthesis may explain why the yeast cell sequentially schedules biosynthesis of biomass components across phases of the yeast metabolic cycle, even when such sequential scheduling is not needed to coordinate events of the cell division cycle — e.g. when the metabolic cycle proceeds without cell division during starvation. Furthermore, the advantage of parallel biosynthesis in some conditions suggests that the metabolic cycle may cease to occur if nutrient conditions are too harsh, in concordance with studies that suggest disappearance of the metabolic cycle in extreme conditions (O' Neill et al., 2020). To improve model predictability, this study could be extended by using derivations of flux balance analysis that account for compartmentalisation or temporality, such as dynamic flux balance analysis.

3107 6.4 Summary and broader context of thesis

3108 Put together, single-cell analysis of flavin-based yeast metabolic cycles and mod-
3109 elling of the metabolism of budding yeast may provide a mechanistic explanation
3110 for such an under-characterised biological rhythm. I envisege a biochemical ex-
3111 planation for the autonomous generation of the yeast metabolic cycle and for
3112 its response to nutrient conditions. The biochemistry of the yeast metabolic cycle
3113 could then be modelled using techniques such as flux balance analysis. In addition,
3114 robust time series analysis methods would be able to discover classes of oscillations
3115 within a microfluidics experiment that could correspond to sub-populations in the
3116 culture. Identification of such sub-populations could then potentially reconcile
3117 results of single-cell and chemostat experiments.

3118 Biological rhythms are an important physiological adaptation of all living organ-
3119 isms. This thesis, in sum, shows the robustness of the yeast metabolic cycle and
3120 relates it to resource allocation strategies, thus potentially shedding light on what
3121 could be a fundamental biological process.

3122 The presence of the yeast metabolic cycle leads to questions about the benefits
3123 of biological oscillations that justify their existence. The benefits of the circa-
3124 dian rhythm and the cell division cycle are clear: circadian rhythms synchronise
3125 physiological processes to the light-dark cycle, while the cell division cycle co-
3126 ordinates resource-intensive processes with the presence of nutrient stores and
3127 maintains genetic fidelity. In the yeast metabolic cycle, it has been proposed that
3128 sequential scheduling of biosynthesis optimises the use of the limited proteome
3129 for cell growth (O' Neill et al., 2020; Takhayev et al., 2023) so that biomass
3130 components are synthesised 'just-in-time' for when they are required for phase
3131 of the cell division cycle (Zylstra and Heinemann, 2022). However, the continued
3132 presence of the yeast metabolic cycle when the cell division cycle is halted implies

*unclear if you know
the explanation
or not.*

3133 that the metabolic cycle has functions other than control of the cell division cycle.
3134 Alternatively, the metabolic cycle may function as a environment-sensitive back-
3135 ground rhythm to ensure that just-in-time biosynthesis for the cell division cycle
3136 can be switched on rapidly, as supported by my observation of rapid responses of
3137 cells to restoration of glucose after starvation.

3138 Furthermore, the common control features of the yeast metabolic cycle and other
3139 biological rhythms may reflect a common evolutionary or functional origin. The
3140 yeast metabolic cycle may be mediated via post-translational modifications, as
3141 evidenced by how the proteome shows far less cyclic variation than the transcrip-
3142 tome (Feltham et al., 2020) or the metabolome (O' Neill et al., 2020). Specifically,
3143 studies have highlighted the role of peroxiredoxin oxidation cycles in the integrity
3144 of the yeast metabolic cycle in chemostats (Causton et al., 2015; Ampontsah et al.,
3145 2021), while other studies highlight the importance of chromatin remodelling in
3146 this biological rhythm (Nocetti and Whitehouse, 2016; Gowans et al., 2018).

3147 Continued peroxiredoxin oxidation cycles have also been observed in circadian
3148 rhythms of transcription-disabled *Ostreococcus tauri* cells (J. S. O'Neill, van Oo-
3149 ijen et al., 2011) and DNA-lacking human red blood cells (J. S. O'Neill and Reddy,
3150 2011). Furthermore, human red blood cells also exhibit NADH/NADPH and ATP
3151 cycles, independent of the glycolytic cycle (J. S. O'Neill and Reddy, 2011), similar
3152 to the yeast metabolic cycle (Papagiannakis et al., 2017). In addition, the gly-
3153 colytic cycle is regulated through solely biochemical means (Ghosh and Chance,
3154 1964; Higgins, 1964), so this cycle may represent a basal mechanism of regulation
3155 of biological rhythms. Such similarities, across a range of biological kingdoms,
3156 thus strongly suggest a non-genetic common origin of biological rhythms.

3157 Appendix A

3158 Time series

3159 **A.1 catch22 features**

3160 Table A.1 lists *catch22* features.

3161 **A.2 UMAP hyperparameters**

3162 UMAP (McInnes et al., 2020) is a dimension reduction method which aims to
3163 find a global manifold structure of the input observations and computes a low-
3164 dimension embedding that preserves the structure of the manifold.

3165 UMAP has several hyperparameters, of which four have major effects on the
3166 embedding:

- 3167 1. The *number of neighbours* (n) to consider when approximating the local
3168 metric controls how the method balances local and global structure in the
3169 data. With low values of this parameter, the algorithm concentrates on very
3170 local structure, potentially to the detriment of the big picture. As the value
3171 increases, the algorithm ‘glues’ more nodes together to form clusters.
- 3172 2. The *largest embedding dimension* (d) controls the number of dimensions
3173 the data is reduced to. In other words, it controls whether the resulting
3174 map is one-dimensional, two-dimensional, three-dimensional, or of higher
3175 dimensions.

Feature name	Description
DN_HistogramMode_5	Mode of z-scored distribution (5-bin histogram)
DN_HistogramMode_10	Mode of z-scored distribution (10-bin histogram)
SB_BinaryStats_mean_longstretch1	Longest period of consecutive values above the mean
DN_OutlierInclude_p_001_mdrmd	Time intervals between successive extreme events above the mean
DN_OutlierInclude_n_001_mdrmd	Time intervals between successive extreme events below the mean
first_1e_ac	First 1/e crossing of autocorrelation function
firstMin_acf	First minimum of autocorrelation function
SP_Summaries_welch_rect_area_5_1	Total power in lowest fifth of frequencies in the Fourier power spectrum
SP_Summaries_welch_rect_centroid	Centroid of the Fourier power spectrum
FC_LocalSimple_mean3_stderr	Mean error from a rolling 3-sample mean forecasting
C0_trev_1_num	Time-reversibility statistic, $\langle (x_{t+1} - x_t)^3 \rangle_t$
C0_HistogramAMI_even_2_5	Automutual information, $m = 2, \tau = 5$
IN_AutoMutualInfoStats_40_gaussian_fmmi	First minimum of the automutual information function
MD_hrv_classic_pnn40	Proportion of successive differences exceeding 0.04σ
SB_BinaryStats_diff_longstretch0	Longest period of successive incremental decreases
SB_MotifThree_quantile_hh	Shannon entropy of two successive letters in equiprobable 3-letter symbolization
FC_LocalSimple_mean1_tauresrat	Change in correlation length after iterative differencing
C0_EMBED2_Dist_tau_d_expfit_meandiff	Exponential fit to successive distances in 2-d embedding space
SC_FluctAnal_2_dfa_50_1_2_logi_prop_r1	Proportion of slower timescale fluctuations that scale with DFA (50% sampling)
SC_FluctAnal_2_rsrangefit_50_1_logi_prop_r1	Proportion of slower timescale fluctuations that scale with linearly rescaled range fits
SB_TransitionMatrix_3ac_sumdiagcov	Trace of covariance of transition matrix between symbols in 3-letter alphabet
PD_PeriodicityWang_th0_01	Periodicity measure of Wang et al. (2007)

Table A.1: *catch22* features, adapted from Lubba et al. (2019).

- 3176 3. The *minimal distance* (`min_dist`) controls the desired separation between
3177 close points in the embedding space. Specifically, this parameter controls
3178 how tightly the algorithm is allowed to pack points together. With low
3179 values, the visualisation forms ‘clumps’.
- 3180 4. The previous hyperparameters are numerical, but the *metric* hyperpara-
3181 meter instead specifies the distance metric that is used to compute distances
3182 in the ambient space of the input data. For example, this metric can be the
3183 Euclidean distance, the cosine distance, or other metrics used to compute
3184 the distances between two vectors of numerical data.

3185 A.3 Classification pipeline

3186 In machine learning, classification is defined as the process of identifying a cat-
3187 egory that a piece of input data belongs to. In this section, the classification task
3188 is identifying whether a time series (input data) is oscillatory (belongs to one
3189 category of two) or non-oscillatory (belongs to the other category of two).

3190 A typical classification pipeline can be described by the following steps:

- 3191 1. *Pre-processing of data*: Input data is cleaned or normalised. For example,
3192 to classify oscillatory time series, the input time series may be normalised
3193 to give similar dynamic ranges.
- 3194 2. *Labelling*: Each piece of input data has a label assigned to it to denote
3195 which category it belongs to. For example, to classify oscillatory time series,
3196 a human can subjective assign the label ‘0’ for non-oscillatory time series
3197 and ‘1’ for oscillatory time series, for a total of two categories.

-
- 3198 3. *Featurisation*: Input data converted to feature vectors in the process of
3199 featurisation. This process uses domain knowledge related to the type or
3200 origin of the data to define characteristics of the data that may be useful
3201 for classification.
- 3202 4. *Train-test split*: The input data set is then randomly divided into a training
3203 data set and a test data set.
- 3204 5. *Training of model*: The machine learning model is then fit on the (featurised)
3205 training data set and its labels to fit parameters in the model.
- 3206 6. *Evaluation of model on test dataset*: The model, trained on the training
3207 dataset, is used to predict the labels of data in the (featurised) test data
3208 set. The performance of the model is then evaluated on the test data set.
3209 This evaluation is based on computing quantities that express how well the
3210 model assigns labels to data, compared to the labels defined earlier.

3211 A.4 Gillespie algorithm for stochastic chemical sys- 3212 tems

3213 To define the Gillespie algorithm (Gillespie, 2007), consider such a system with
3214 M reactions $R_1, \dots, R_j, \dots, R_M$ involving N species $S_1, \dots, S_i, \dots, S_N$ in a fixed
3215 volume V at thermal equilibrium. Let $X_i(t)$ represent the number of molecules of
3216 S_i at time t , and the state vector

$$\mathbf{X}(t) = [X_1(t), \dots, X_N(t)] \quad (\text{A.1})$$

3217 thus gives the state of the system at any given time t .

3218 Each reaction R_j is described by two quantities:

3219 1. A state-change vector $\mathbf{v}_j = [v_{1,j}, \dots, v_{N,j}]$ which defines how the stoichiometry of the system changes if the reaction occurs. $v_{i,j}$ represents the change in the stoichiometry of S_i when R_j occurs.

3220
3221
3222 2. A propensity function $a_j(\mathbf{x})$, which gives the probability, that one R_j reaction occurs in the volume V within the following short time interval $[t, t+dt)$, given the state $\mathbf{X}(t) = \mathbf{x}$.

3223
3224 The definition of the propensity function $a_j(\mathbf{x})$ differs depending on the reaction.

3225 For a unimolecular reaction ($S_1 \longrightarrow P$),

$$a_j(\mathbf{x}) = k_j X_1 \quad (\text{A.2})$$

3226 For a bimolecular reaction with two different species ($S_1 + S_2 \longrightarrow P$),

$$a_j(\mathbf{x}) = \frac{k_j}{V} X_1 X_2 \quad (\text{A.3})$$

3227 And finally, for a bimolecular reaction with two molecules of the same species
3228 ($S_1 + S_1 \longrightarrow P$),

$$a_j(\mathbf{x}) = \frac{k_j}{V} X_1 (X_1 - 1) \quad (\text{A.4})$$

3229 Where, in all cases, k_j is the rate constant of reaction R_j .

3230 The Gillespie algorithm aims to predict the temporal evolution of the state vector
3231 given the initial state $\mathbf{X}(t_0) = \mathbf{x}_0$. It does so by iteratively choosing the next
3232 reaction that occurs, based on its probability, and then choosing its firing time
3233 based on a propensity function. Combining these simulations gives a trajectory
3234 of state vectors across the time course of interest. In detail, the direct Gillespie
3235 algorithm can be defined as stated in algorithm 1:

Algorithm 1: Direct method of the Gillespie algorithm

Input: Stochastic model (with species $S_1, \dots, S_i, \dots, S_N$ and reactions $R_1, \dots, R_j, \dots, R_M$, along with a state-change vector \mathbf{v}_j and a rate constant k_i for each reaction R_j); initial time t_0 ; and initial model state $\mathbf{X}(t_0) = \mathbf{x}_0$

Output: Trajectory of state vectors $\mathbf{X}(t)$, with t taking discrete values in $[t_0, t_{\max}]$

while $t < t_{\max}$ **do**

- Calculate the propensities $a_j(\mathbf{x})$ based on the current state \mathbf{x} ;
- Calculate the combined propensity $a_0(\mathbf{x}) = \sum_j a_j(\mathbf{x})$;
- Generate two random numbers r_1 and r_2 , both from the uniform distribution $U(0, 1)$;
- Choose the next reaction R_j , with j given by the smallest integer that satisfies $\sum_{j'}^j a_{j'}(\mathbf{x}) > r_1 a_0(\mathbf{x})$;
- Calculate the time to the next reaction $\tau = \frac{1}{a_0(\mathbf{x})} \ln(\frac{1}{r_2})$;
- Simulate the next reaction by updating the state vector $\mathbf{x} \leftarrow \mathbf{x} + \mathbf{v}_j$ and store the new vector in $\mathbf{X}(t)$;
- Update the time by $t \leftarrow t + \tau$ and store the new time;

end

return Trajectory of state vectors $\mathbf{X}(t)$ for a vector of times t ;

Appendix B

Flux balance analysis

3237

3238

3239 **B.1 Modifications of chemical reactions in GECKO**

3240 **for non-simple cases**

3241 GECKO modifies chemical reactions in a genome-scale model so that enzymes are
3242 expressed as metabolites that take part in reactions. Section 5.3.1 describes how
3243 this was performed for the simple case of a singular chemical reaction and one
3244 enzyme having a one-to-one association. Slightly different formalisms are applied
3245 to reversible reactions, isozymes, promiscuous enzymes, and enzyme complexes.
3246 Namely:

- 3247 • Reversible reactions are modelled as the forward and reverse reactions
3248 separately.
- 3249 • For isozymes, the original reaction is copied multiple times corresponding
3250 to the number of reactions that the isozyme catalyses. Each has an isozyme
3251 catalysing the reaction. In addition, there is an ‘arm’ reaction to act as an
3252 intermediate between the substrate and the products.
- 3253 • No actions are needed for promiscuous enzymes.
- 3254 • Enzyme complexes are modelled as one reaction that uses all subunit pro-
3255 teins that all share the same k_{cat} value.

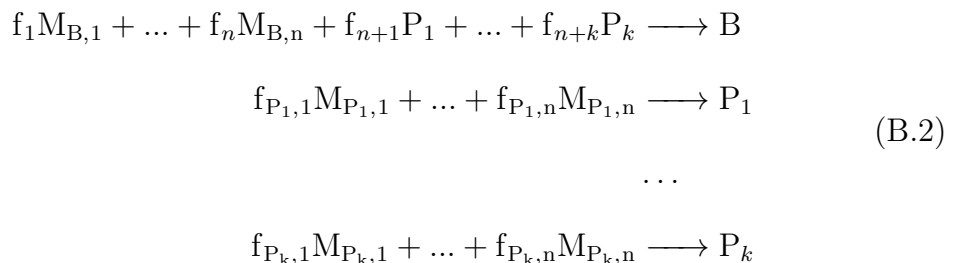
3256 B.2 Computing molecular weights of pseudometabol- 3257 ites in ecYeast8

3258 In genome-scale metabolic models, mass fractions are represented in the biomass
3259 reaction, set as the objective function, which is defined as:



3260 where $M_1 \dots M_n$ represent the chemical species that make up the cell's biomass,
3261 the stoichiometric coefficients $f_1 \dots f_n$ represent the mass fraction of each species
3262 in units of g g⁻¹_{DW}, and B represents biomass. If a chemical species M_i has a mass
3263 fraction f_i , then 1 g of cell dry weight has f_i g of chemical species M_i .

3264 In the ecYeast8 model, the mass fraction of biomass components cannot simply
3265 be obtained by taking the stoichiometric coefficients (f_i in Eq. B.1) from the
3266 objective function. This is because the objective function of Yeast8 does not
3267 conform to this format, and instead contains pseudometabolites. This formalism
3268 can be expressed as:



3269 where each M is a chemical species with a defined molecular weight, each P
3270 is a pseudometabolite, and each f is a stoichiometric coefficient. The object-
3271 ive function remains the reaction that produces B , but some chemical species
3272 $M_{B,1} \dots M_{B,n}$ are retained in the objective function, while other chemical species

3273 are replaced by pseudometabolites $P_1 \dots P_k$. The reactions that produce $P_1 \dots P_k$
 3274 are *isa* reactions. *isa* reactions define pseudometabolites by having chemical
 3275 species with known molecular weights as reactants, with their stoichiometric coef-
 3276 ficients representing abundance in mmol g⁻¹_{DW}. In Yeast8, the objective function
 3277 is defined as:

```
3278 47.5883 atp_c + 47.5883 h2o_c + lipid_c + protein_c + carbohydrate_c
  3279 + dna_c + rna_c + cofactor + ion
  3280 -> 47.5883 adp_c + biomass_c + 47.5883 h_c + 47.5883 pi_c
```

3281 Here, there are seven pseudometabolites: lipid, protein, carbohydrate, DNA, RNA,
 3282 cofactor, and ion.

3283 As the ecYeast8 model does not specify the molecular weights of these pseudo-
 3284 metabolites, in order to obtain the mass fraction of each biomass component rep-
 3285 resented by the pseudometabolites, I treated each pseudometabolite as a chemical
 3286 species and calculated its molecular weight by assuming mass balance (Chan et
 3287 al., 2017; Dinh et al., 2022; Takhayev et al., 2023). Namely, I assumed that in
 3288 reactions that produce the pseudometabolites, there is conservation of mass, and
 3289 therefore:

$$\sum_{r=j}^{n_r} m_r c_r = \sum_{p=i}^{n_p} m_p c_p \quad (\text{B.3})$$

3290 where $s = 1, \dots, n_s$ represents substrates of the reaction in question, $p = 1, \dots, n_p$
 3291 represents products. m_r represents molar mass of reactant r , m_p represents molar
 3292 mass of product p , c_r represents stoichiometric coefficient of reactant r , and c_p
 3293 represents stoichiometric coefficient of product p .

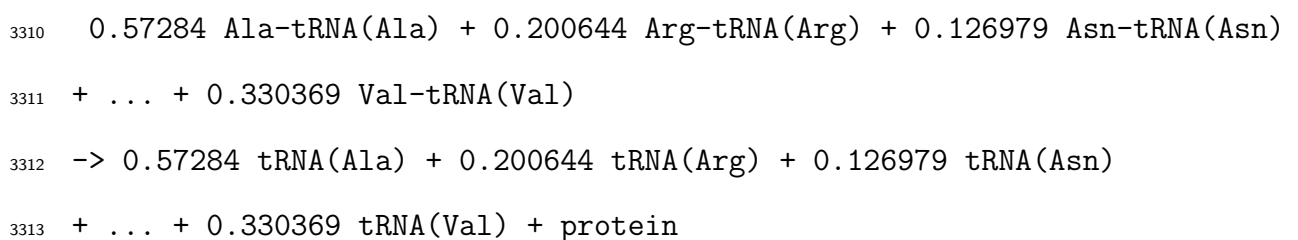
3294 The resulting molecular weight will thus represent the mass fraction of each
 3295 biomass component in units of g g⁻¹_{DW}.

3296 **B.2.1 Carbohydrate, DNA, RNA, cofactor, and ion pseudometabolites**

3298 Computing the molecular weights of the carbohydrate, DNA, RNA, cofactor, and
3299 ion pseudometabolites is straightforward. This is because the equations similarly
3300 have reactants with molecular weights specified in the model and only the pseudo-
3301 metabolite, the sole product, does not have a molecular weight specified. In such
3302 cases, Eq. B.3 can be applied directly, i.e. the molecular weight of the pseudo-
3303 metabolite is equal to $\sum_{r=j}^{n_r} m_r c_r$, where m_r values are taken directly from the
3304 molecular weights specified in the model. The results for these pseudometabolites
3305 are shown in Table B.1

3306 **B.2.2 Protein pseudometabolite**

3307 Other metabolites were less straightforward and required some judgement calls.
3308 To compute the molecular weight of the protein pseudometabolite, I inspected
3309 reaction **r_4047**:



3314 In Yeast8, aminoacyl-tRNA and tRNA species do not have molecular weights
3315 specified in the model. This is because their chemical formulas are incompletely
3316 specified in the model as the model uses R to represent the tRNA. For example,
3317 **Ala-tRNA(Ala)**, alanyl-tRNA, is represented as C3H7NOR, and **tRNA(Ala)** is rep-
3318 resented as RH. As a consequence, the molecular weights of these species cannot
3319 be directly computed from the chemical formula. Because tRNAs are unmodified

ID	Reaction	Computed molecular weight (g mol ⁻¹)
r_4048	0.684535 (1->3)-beta-D-glucan + 0.228715 (1->6)-beta-D-glucan + 0.330522 glycogen + 0.650171 mannan + 0.126456 trehalose -> carbohydrate 0.0036 dAMP + 0.0024 dCMP + 0.0024 dGMP	350.37
r_4050	+ 0.0036 dTMP -> DNA 0.0445348 AMP + 0.0432762 CMP	3.90
r_4049	+ 0.0445348 GMP + 0.0579921 UMP -> RNA 0.00019 coenzyme A + 1e-05 FAD + 0.00265 NAD + 0.00015 NADH	64.04
r_4598	+ 0.00057 NADP(+) + 0.0027 NADPH + 0.00099 riboflavin + 1.2e-06 TDP + 6.34e-05 THF + 1e-06 heme a -> cofactor 3.04e-05 iron(2+) + 0.00363 potassium + 0.00397 sodium + 0.02 sulphate	4.83
r_4599	+ 0.00129 chloride + 0.00273 Mn(2+) + 0.000748 Zn(2+) + 0.000217 Ca(2+) + 0.00124254 Mg(2+) + 0.000659 Cu(2+) -> ion	2.48

Table B.1: Straightforward cases of computing pseudometabolite molecular weights from pseudoreactions in ecYeast8

3320 during translation, R can be ignored. In other words, I treated R as a chemical
 3321 element of atomic mass 0 when computing m_r for each reactant and m_p for
 3322 each product, leaving only m_p for protein undefined. This m_p can then be
 3323 found by rearranging Eq. B.3, thus giving the molecular mass of the protein
 3324 pseudometabolite.

3325 B.2.3 Lipid pseudometabolite

3326 Finally, the lipid pseudometabolite is the least straightforward because the model
3327 does not specify the molecular weights of some of the reactants of the lipid
3328 pseudoreaction. The lipid pseudoreaction is represented in reaction r_2108:

3329 `lipid backbone + lipid chain -> lipid`

3330 And both `lipid backbone` and `lipid chain` have no molecular weight specified.

3331 Reaction r_4065 specifies a lipid chain pseudoreaction, in which `lipid chain` is
3332 generated:

3333 `0.0073947 C16:0 chain + 0.0217019 C16:1 chain + 0.0020726 C18:0 chain`
3334 `+ 0.000796243 C18:1 chain`
3335 `-> lipid chain`

3336 As all reactants have molecular weights defined in the model, the molecular weight
3337 of `lipid chain` can be computed from the mass balance of this reaction.

3338 Reaction r_4063 specifies a lipid backbone pseudoreaction, in which `lipid back-`
3339 `bone` is generated:

3340 `0.000631964 1-phosphatidyl-1D-myo-inositol backbone`
3341 `+ 0.00243107 ergosterol + 0.000622407 ergosterol ester backbone`
3342 `+ 0.000135359 fatty acid backbone + ...`
3343 `-> lipid backbone`

3344 The model specifies molecular weights for all species in the reaction that generates
3345 `lipid backbone`, except for `fatty acid backbone`. To compute the molecular
3346 weight of `fatty acid backbone`, the reactions that produce this species must be
3347 used. Because of SLIMER, four reactions in the model produce `fatty acid back-`
3348 `bone` (table B.2). The model specifies molecular weights for all species in these

ID	Reaction	Computed molecular weight (g mol ⁻¹)
	palmitate	
r_3975	-> 0.255421 fatty acid backbone 0.256429 C16:0 chain	742.54
	palmitoleate	
r_3976	-> 0.253405 fatty acid backbone 0.254413 C16:1 chain	744.56
	stearate	
r_3977	-> 0.283475 fatty acid backbone 0.284483 C18:0 chain	714.49
	oleate	
r_3978	-> 0.281459 fatty acid backbone 0.282467 C18:1 chain	716.51

Table B.2: ecYeast8 reactions that generate the **fatty acid backbone** metabolite

3349 four reactions, except for **fatty acid backbone**. Therefore, using each chemical
 3350 equation, the molecular weight of **fatty acid backbone** can be solved for by
 3351 rearranging Eq. B.3 with parameters defined to match each reaction. However,
 3352 the molecular weights computed from each equation are different. Because the
 3353 differences are slight, I took the mean of the four weights to give 729.53 g mol⁻¹.
 3354 Subsequently, the molecular weight of **lipid backbone** was computed from this
 3355 mean value and the molecular weights of other species involved in the production
 3356 of **lipid backbone**, giving 21.31 g mol⁻¹. With the molecular weights of **lipid**
 3357 **backbone** and **lipid chain** defined, the molecular weight of **lipid** is thus the
 3358 sum of the two.

3359 A summary of molecular weights can be found in Table 5.1.

3360 Subsequently, the mass fraction of each biomass component is computed by
 3361 dividing the molecular weight of the corresponding pseudometabolite by the
 3362 molecular weight of biomass:

Metabolite	f_i
Protein	0.524 53
Carbohydrate	0.364 38
RNA	0.066 60
Lipid	0.032 83
Cofactors	0.005 02
DNA	0.004 06
Ions	0.002 58

*Not sure if
this was referenced in Chapter*

Table B.3: f_i values for each biomass component.

3363

B.3 Mathematical explanation of the effect of restricting the enzyme pool

3364

3365 Let $\tau_{\text{seq/par}}$, given by Eq. 5.19, depend on x :

$$\tau_{\text{seq/par}}(x) = \left(\sum_i \frac{f_i}{\lambda_{\text{seq},i}(x)} \right) \cdot \frac{\lambda_0(x)}{f_{\text{protein}}} \quad (\text{B.4})$$

3366 where $x = e'_{\text{pool}}/e_{\text{pool}}$. The expression in Eq. B.4 takes into account how λ_0 and

3367 $\lambda_{\text{seq},i}$ values vary with x , and how f_i values are constants.

3368 We thus obtain:

$$\begin{aligned} \frac{d\tau_{\text{seq/par}}(x)}{dx} &= \frac{1}{f_{\text{protein}}} \frac{d}{dx} \left[\left(\sum_i \frac{f_i}{\lambda_{\text{seq},i}(x)} \right) \cdot \lambda_0(x) \right] \\ &= \frac{1}{f_{\text{protein}}} \left[\left(\sum_i \frac{f_i}{\lambda_{\text{seq},i}(x)} \right) \cdot \frac{d\lambda_0(x)}{dx} + \lambda_0(x) \frac{d}{dx} \left(\sum_i \frac{f_i}{\lambda_{\text{seq},i}(x)} \right) \right] \\ &= \frac{1}{f_{\text{protein}}} \left[\left(\sum_i \frac{f_i}{\lambda_{\text{seq},i}(x)} \right) \cdot \frac{d\lambda_0(x)}{dx} - \lambda_0(x) \sum_i \left(\frac{f_i}{\lambda_{\text{seq},i}(x)^2} \cdot \frac{d\lambda_{\text{seq},i}(x)}{dx} \right) \right] \end{aligned} \quad (\text{B.5})$$

3369 To explain the increase in $\tau_{\text{seq/par}}$ as e'_{pool} increases, I consider the behaviour of

3370 λ_0 and $\lambda_{\text{seq},i}$ values with respect to e'_{pool} in intervals.

With reference to Fig. 5.6, consider $0 \leq x \leq 0.5$. In this region of x , based on the observations in the figure, we model $\lambda_0 = k_0x$ and $\lambda_{\text{seq},i} = k_i x$, where constants $k_0, k_i > 0$. This models how these values initially increase linearly in Fig. 5.6. Eq.

Eq. B.5 thus becomes:

$$\begin{aligned} \frac{d\tau_{\text{seq/par}}(x)}{dx} &= \frac{1}{f_{\text{protein}}} \left[\left(\sum_i \frac{f_i}{k_i x} \right) \cdot k_0 - k_0 x \sum_i \left(\frac{f_i}{(k_i x)^2} \cdot k_i \right) \right] \\ &= \frac{1}{f_{\text{protein}}} \left[\frac{k_0}{x} \sum_i \frac{f_i}{k_i} - k_0 x \left(\sum_i \frac{f_i}{k_i x^2} \right) \right] \\ &= \frac{1}{f_{\text{protein}}} \left[\frac{k_0}{x} \sum_i \frac{f_i}{k_i} - \frac{k_0}{x} \sum_i \frac{f_i}{k_i} \right] \\ &= 0 \end{aligned} \quad (\text{B.6})$$

And this explains the constant $\tau_{\text{seq/par}}$ in this region.

Now, consider $0.5 < x \leq 9$. In this region, the trajectories of $\lambda_{\text{seq},i}$ with respect to time remain linear, but some with changes in slope. In other words, in a sub-region where the slopes of all $\lambda_{\text{seq},i}$ are constant, we can let: $\lambda_0 = k_0x$ and $\lambda_{\text{seq},i} = m_i x + c_i$, where $k_0, m_i, c_i > 0$. Eq. B.5 thus becomes:

$$\begin{aligned} \frac{d\tau_{\text{seq/par}}(x)}{dx} &= \frac{1}{f_{\text{protein}}} \left[\left(\sum_i \frac{f_i}{m_i x + c_i} \right) \cdot k_0 - k_0 x \sum_i \left(\frac{f_i}{(m_i x + c_i)^2} \cdot m_i \right) \right] \\ &= \frac{k_0}{f_{\text{protein}}} \left[\left(\sum_i \frac{f_i}{m_i x + c_i} \right) - x \left(\sum_i \frac{f_i m_i}{(m_i x + c_i)^2} \right) \right] \\ &= \frac{k_0}{f_{\text{protein}}} \sum_i \left[\frac{f_i}{m_i x + c_i} - \frac{x f_i m_i}{(m_i x + c_i)^2} \right] \\ &= \frac{k_0}{f_{\text{protein}}} \sum_i \left[\frac{f_i c_i}{(m_i x + c_i)^2} \right] \end{aligned} \quad (\text{B.7})$$

3380 As $f_i, c_i, m_i > 0$ for all biomass components i , and $k_0 > 0$, we get $\frac{d\tau_{\text{seq/par}}(x)}{dx} > 0$
 3381 regardless of the values that these constants take. Because k_0 does not change over
 3382 the region of x considered, m_i, c_i , and x values thus determine the magnitude of
 3383 $\frac{d\tau_{\text{seq/par}}(x)}{dx}$. If within a region of x , m_i and c_i values remain constant for all i , then
 3384 as x increases, $\frac{d\tau_{\text{seq/par}}(x)}{dx}$ should decrease — this is certainly the case, as can be
 3385 observed in Fig. 5.6.

3386 Lastly, consider $x > 9$. In this region, λ_0 becomes constant, thus we let $\lambda_0 = k_0$.
 3387 We keep $\lambda_{\text{seq},i} = m_i x + c_i$, and as before, $k_0, m_i, c_i > 0$. Eq. B.5 thus becomes:

$$\begin{aligned}\frac{d\tau_{\text{seq/par}}(x)}{dx} &= \frac{1}{f_{\text{protein}}} \left[0 - k_0 \sum_i \left(\frac{f_i}{(m_i x + c_i)^2} \cdot m_i \right) \right] \\ &= -\frac{k_0}{f_{\text{protein}}} \sum_i \left[\frac{f_i m_i}{(m_i x + c_i)^2} \right]\end{aligned}\quad (\text{B.8})$$

3388 This predicts decreasing $\tau_{\text{seq/par}}$ as x increases in this region. Because k_0 is
 3389 constant in this region, the rate of this decrease is thus controlled by m_i and
 3390 c_i values. As each $\lambda_{\text{seq},i}$ trajectory becomes flat as x increases, each $\frac{f_i m_i}{(m_i x + c_i)^2}$ term
 3391 becomes zero, thus shrinking the magnitude of $\frac{d\tau_{\text{seq/par}}(x)}{dx}$. Finally, as all $\lambda_{\text{seq},i}$
 3392 trajectories become flat at $x > 15$, $\frac{d\tau_{\text{seq/par}}(x)}{dx} = 0$.

Bibliography

- 3395 Adler, S. O., T. W. Spiesser, F. Uschner, U. Münzner, J. Hahn, M. Krantz and
 3396 E. Klipp (2022). “A Yeast Cell Cycle Model Integrating Stress, Signaling, and
 3397 Physiology”. In: *FEMS Yeast Research*, foac026.
- 3398 Adrover, M. À., Z. Zi, A. Duch, J. Schaber, A. González-Novo, J. Jimenez, M.
 3399 Nadal-Ribelles, J. Clotet, E. Klipp and F. Posas (2011). “Time-Dependent
 3400 Quantitative Multicomponent Control of the G1-S Network by the Stress-
 3401 Activated Protein Kinase Hog1 upon Osmostress”. In: *Science Signaling* 4.192,
 3402 ra63–ra63.
- 3403 Ahn, E., P. Kumar, D. Mukha, A. Tzur and T. Shlomi (2017). “Temporal Flux-
 3404 omics Reveals Oscillations in TCA Cycle Flux throughout the Mammalian Cell
 3405 Cycle”. In: *Molecular Systems Biology* 13.11, p. 953.
- 3406 Amponsah, P. S., G. Yahya, J. Zimmermann, M. Mai, S. Mergel, T. Mühlhaus, Z.
 3407 Storchova and B. Morgan (2021). “Peroxiredoxins Couple Metabolism and Cell
 3408 Division in an Ultradian Cycle”. In: *Nature Chemical Biology* 17.4, pp. 477–484.
- 3409 Arata, Y. and H. Takagi (2019). “Quantitative Studies for Cell-Division Cycle
 3410 Control”. In: *Frontiers in Physiology* 10.
- 3411 Ariño, J., J. Ramos and H. Sychrová (2010). “Alkali Metal Cation Transport and
 3412 Homeostasis in Yeasts”. In: *Microbiology and Molecular Biology Reviews* 74.1,
 3413 pp. 95–120.
- 3414 Aubin, J. E. (1979). “Autofluorescence of Viable Cultured Mammalian Cells.” In:
 3415 *Journal of Histochemistry & Cytochemistry* 27.1, pp. 36–43.

- 3416 Bagamery, L. E., Q. A. Justman, E. C. Garner and A. W. Murray (2020). “A
3417 Putative Bet-Hedging Strategy Buffers Budding Yeast against Environmental
3418 Instability”. In: *Current Biology*.
- 3419 Baumgartner, B. L., R. O’Laughlin, M. Jin, L. S. Tsimring, N. Hao and J. Hasty
3420 (2018). “Flavin-Based Metabolic Cycles Are Integral Features of Growth and
3421 Division in Single Yeast Cells”. In: *Scientific Reports* 8.1, pp. 1–10.
- 3422 Becker, S. A. and B. O. Palsson (2008). “Context-Specific Metabolic Networks Are
3423 Consistent with Experiments”. In: *PLOS Computational Biology* 4.5, e1000082.
- 3424 Becker-Kettern, J., N. Paczia, J.-F. Conrotte, D. P. Kay, C. Guignard, P. P. Jung
3425 and C. L. Linster (2016). “Saccharomyces Cerevisiae Forms D-2-Hydroxyglutarate
3426 and Couples Its Degradation to d-Lactate Formation via a Cytosolic Transhy-
3427 drogenase”. In: *Journal of Biological Chemistry* 291.12, pp. 6036–6058.
- 3428 Benjamini, Y. and Y. Hochberg (1995). “Controlling the False Discovery Rate:
3429 A Practical and Powerful Approach to Multiple Testing”. In: *Journal of the
3430 Royal Statistical Society. Series B (Methodological)* 57.1, pp. 289–300. JSTOR:
3431 2346101.
- 3432 Beuse, M., R. Bartling, A. Kopmann, H. Diekmann and M. Thoma (1998). “Effect
3433 of the Dilution Rate on the Mode of Oscillation in Continuous Cultures of
3434 Saccharomyces Cerevisiae”. In: *Journal of Biotechnology* 61.1, pp. 15–31.
- 3435 Blondel, V. D., J.-L. Guillaume, R. Lambiotte and E. Lefebvre (2008). “Fast
3436 Unfolding of Communities in Large Networks”. In: *Journal of Statistical Mech-
3437 anics: Theory and Experiment* 2008.10, P10008.
- 3438 Bonamore, A. and A. Boffi (2008). “Flavohemoglobin: Structure and Reactivity”.
3439 In: *IUBMB Life* 60.1, pp. 19–28.

- 3440 Boxall, S. F., L. V. Dever, J. Kneřová, P. D. Gould and J. Hartwell (2017).
3441 “Phosphorylation of Phosphoenolpyruvate Carboxylase Is Essential for Max-
3442 imal and Sustained Dark CO₂ Fixation and Core Circadian Clock Operation in
3443 the Obligate Crassulacean Acid Metabolism Species *Kalanchoë Fedtschenkoi*”.
3444 In: *The Plant Cell* 29.10, pp. 2519–2536.
- 3445 Brachmann, C. B., A. Davies, G. J. Cost, E. Caputo, J. Li, P. Hieter and J. D.
3446 Boeke (1998). “Designer Deletion Strains Derived from *Saccharomyces Cerevisiae*
3447 S288C: A Useful Set of Strains and Plasmids for PCR-mediated Gene Disrup-
3448 tion and Other Applications”. In: *Yeast* 14.2, pp. 115–132.
- 3449 Burnett, A. J., M. Aydin and N. E. Buchler (2016). “Cell Cycle Start Is Coupled
3450 to Entry into the Yeast Metabolic Cycle across Diverse Strains and Growth
3451 Rates”. In: *Molecular Biology of the Cell* 27.1, pp. 64–74.
- 3452 Calabrese, G., E. Peker, P. S. Ampontah, M. N. Hoehne, T. Riemer, M. Mai,
3453 G. P. Bienert, M. Deponte, B. Morgan and J. Riemer (2019). “Hyperoxidation
3454 of Mitochondrial Peroxiredoxin Limits H₂O₂-induced Cell Death in Yeast”. In:
3455 *The EMBO Journal* 38.18, e101552.
- 3456 Campbell, K., J. Westholm, S. Kasvandik, F. D. Bartolomeo, M. Mormino and
3457 J. Nielsen (2020). “Building Blocks Are Synthesized on Demand during the
3458 Yeast Cell Cycle”. In: *Proceedings of the National Academy of Sciences* 117.14,
3459 pp. 7575–7583.
- 3460 Canelas, A. B., C. Ras, A. ten Pierick, W. M. van Gulik and J. J. Heijnen (2011).
3461 “An in Vivo Data-Driven Framework for Classification and Quantification of
3462 Enzyme Kinetics and Determination of Apparent Thermodynamic Data”. In:
3463 *Metabolic Engineering* 13.3, pp. 294–306.

- 3464 Casey, E., N. S. Mosier, J. Adamec, Z. Stockdale, N. Ho and M. Sedlak (2013).
3465 “Effect of Salts on the Co-fermentation of Glucose and Xylose by a Genetically
3466 Engineered Strain of *Saccharomyces Cerevisiae*”. In: *Biotechnology for Biofuels*
3467 6.1, p. 83.
- 3468 Causton, H. C. (2018). “Metabolic Rhythms: A Framework for Coordinating
3469 Cellular Function”. In: *The European Journal of Neuroscience*.
- 3470 Causton, H. C., K. A. Feeney, C. A. Ziegler and J. S. O’Neill (2015). “Metabolic
3471 Cycles in Yeast Share Features Conserved among Circadian Rhythms”. In:
3472 *Current Biology* 25.8, pp. 1056–1062.
- 3473 Cesur, M. F., T. Çakır and P. Pir (2022). “Genome-Wide Analysis of Yeast
3474 Metabolic Cycle through Metabolic Network Models Reveals Superiority of
3475 Integrated ATAC-seq Data over RNA-seq Data”. In: *mSystems* 0.0 (), e01347–
3476 21.
- 3477 Chan, S. H. J., J. Cai, L. Wang, M. N. Simons-Senftle and C. D. Maranas (2017).
3478 “Standardizing Biomass Reactions and Ensuring Complete Mass Balance in
3479 Genome-Scale Metabolic Models”. In: *Bioinformatics* 33.22, pp. 3603–3609.
- 3480 Chang, A., L. Jeske, S. Ulbrich, J. Hofmann, J. Koblitz, I. Schomburg, M. Neumann-
3481 Schaal, D. Jahn and D. Schomburg (2021). “BRENDA, the ELIXIR Core Data
3482 Resource in 2021: New Developments and Updates”. In: *Nucleic Acids Research*
3483 49.D1, pp. D498–D508.
- 3484 Charvin, G., F. R. Cross and E. D. Siggia (2009). “Forced Periodic Expression of
3485 G1 Cyclins Phase-Locks the Budding Yeast Cell Cycle”. In: *Proceedings of the
3486 National Academy of Sciences* 106.16, pp. 6632–6637.
- 3487 Chen, K. C., L. Calzone, A. Csikasz-Nagy, F. R. Cross, B. Novak and J. J.
3488 Tyson (2004). “Integrative Analysis of Cell Cycle Control in Budding Yeast”.
3489 In: *Molecular Biology of the Cell* 15.8, pp. 3841–3862.

- 3490 Crane, M. M., I. B. N. Clark, E. Bakker, S. Smith and P. S. Swain (2014). “A
3491 Microfluidic System for Studying Ageing and Dynamic Single-Cell Responses
3492 in Budding Yeast”. In: *PLOS ONE* 9.6, e100042.
- 3493 Cuny, A. P., K. Tanuj Sapra, D. Martinez-Martin, G. Fläschner, J. D. Adams, S.
3494 Martin, C. Gerber, F. Rudolf and D. J. Müller (2022). “High-Resolution Mass
3495 Measurements of Single Budding Yeast Reveal Linear Growth Segments”. In:
3496 *Nature Communications* 13.1, p. 3483.
- 3497 Decroly, O. and A. Goldbeter (1982). “Birhythmicity, Chaos, and Other Patterns
3498 of Temporal Self-Organization in a Multiply Regulated Biochemical System.”
3499 In: *Proceedings of the National Academy of Sciences* 79.22, pp. 6917–6921.
- 3500 Dinh, H. V., D. Sarkar and C. D. Maranas (2022). “Quantifying the Propagation of
3501 Parametric Uncertainty on Flux Balance Analysis”. In: *Metabolic Engineering*
3502 69, pp. 26–39.
- 3503 Dodd, A. N., N. Salathia, A. Hall, E. Kévei, R. Tóth, F. Nagy, J. M. Hibberd,
3504 A. J. Millar and A. A. R. Webb (2005). “Plant Circadian Clocks Increase
3505 Photosynthesis, Growth, Survival, and Competitive Advantage”. In: *Science*
3506 309.5734, pp. 630–633.
- 3507 Dodd, B. J. T. and J. M. Kralj (2017). “Live Cell Imaging Reveals pH Oscilla-
3508 tions in *Saccharomyces Cerevisiae* During Metabolic Transitions”. In: *Scientific
3509 Reports* 7.1, p. 13922.
- 3510 Domenzain, I., B. Sánchez, M. Anton, E. J. Kerkhoven, A. Millán-Oropeza, C.
3511 Henry, V. Siewers, J. P. Morrissey, N. Sonnenschein and J. Nielsen (2022). “Re-
3512 construction of a Catalogue of Genome-Scale Metabolic Models with Enzymatic
3513 Constraints Using GECKO 2.0”. In: *Nature Communications* 13.1, p. 3766.
- 3514 Droin, C., E. R. Paquet and F. Naef (2019). “Low-Dimensional Dynamics of Two
3515 Coupled Biological Oscillators”. In: *Nature Physics* 15.10, pp. 1086–1094.

- 3516 Dunlop, M. J., R. S. Cox, J. H. Levine, R. M. Murray and M. B. Elowitz (2008).
3517 “Regulatory Activity Revealed by Dynamic Correlations in Gene Expression
3518 Noise”. In: *Nature Genetics* 40.12, pp. 1493–1498.
- 3519 Edgar, R. S., E. W. Green, Y. Zhao, G. van Ooijen, M. Olmedo, X. Qin, Y. Xu,
3520 M. Pan, U. K. Valekunja, K. A. Feeney, E. S. Maywood, M. H. Hastings, N. S.
3521 Baliga, M. Merrow, A. J. Millar, C. H. Johnson, C. P. Kyriacou, J. S. O’Neill
3522 and A. B. Reddy (2012). “Peroxiredoxins Are Conserved Markers of Circadian
3523 Rhythms”. In: *Nature* 485.7399, pp. 459–464.
- 3524 Elowitz, M. B. and S. Leibler (2000). “A Synthetic Oscillatory Network of Tran-
3525 scriptional Regulators”. In: *Nature* 403.6767, pp. 335–338.
- 3526 Elsemman, I. E., A. Rodriguez Prado, P. Grigaitis, M. Garcia Albornoz, V.
3527 Harman, S. W. Holman, J. van Heerden, F. J. Bruggeman, M. M. M. Bisschops,
3528 N. Sonnenschein, S. Hubbard, R. Beynon, P. Daran-Lapujade, J. Nielsen and
3529 B. Teusink (2022). “Whole-Cell Modeling in Yeast Predicts Compartment-
3530 Specific Proteome Constraints That Drive Metabolic Strategies”. In: *Nature
3531 Communications* 13.1, p. 801.
- 3532 Ewald, J. C. (2018). “How Yeast Coordinates Metabolism, Growth and Division”.
3533 In: *Current Opinion in Microbiology*. Antimicrobials * Microbial Systems Bio-
3534 logy 45, pp. 1–7.
- 3535 Ewald, J. C., A. Kuehne, N. Zamboni and J. M. Skotheim (2016). “The Yeast
3536 Cyclin-Dependent Kinase Routes Carbon Fluxes to Fuel Cell Cycle Progres-
3537 sion”. In: *Molecular Cell* 62.4, pp. 532–545.
- 3538 Famili, I., J. Förster, J. Nielsen and B. O. Palsson (2003). “Saccharomyces Cerevisiae
3539 Phenotypes Can Be Predicted by Using Constraint-Based Analysis of a Genome-
3540 Scale Reconstructed Metabolic Network”. In: *Proceedings of the National Academy
3541 of Sciences* 100.23, pp. 13134–13139.

- 3542 Feltham, J. E., S. Xi, S. C. Murray, M. Wouters, J. Urdiain-Arraiza, R. Heilig,
3543 C. George, A. F. Townley, E. Roberts, B. M. Kessler, S. Liberatori, P. D.
3544 Charles, A. Angel, R. Fischer and J. Mellor (2020). *Transcriptional Changes*
3545 *Are Regulated by Metabolic Pathway Dynamics but Decoupled from Protein*
3546 *Levels.*
- 3547 FitzHugh, R. (1961). "Impulses and Physiological States in Theoretical Models
3548 of Nerve Membrane". In: *Biophysical Journal* 1.6, pp. 445–466.
- 3549 Fortunato, S. and M. Barthélemy (2007). "Resolution Limit in Community De-
3550 tection". In: *Proceedings of the National Academy of Sciences* 104.1, pp. 36–41.
- 3551 Fulcher, B. D. and N. S. Jones (2017). "HctsA: A Computational Framework for
3552 Automated Time-Series Phenotyping Using Massive Feature Extraction". In:
3553 *Cell Systems* 5.5, 527–531.e3.
- 3554 Gaisne, M., A.-M. Bécam, J. Verdière and C. J. Herbert (1999). "A 'Natural'
3555 Mutation in *Saccharomyces Cerevisiae* Strains Derived from S288c Affects the
3556 Complex Regulatory Gene HAP1 (CYP1)". In: *Current Genetics* 36.4, pp. 195–
3557 200.
- 3558 Garmendia-Torres, C., O. Tassy, A. Matifas, N. Molina and G. Charvin (2018).
3559 "Multiple Inputs Ensure Yeast Cell Size Homeostasis during Cell Cycle Pro-
3560 gression". In: *eLife* 7. Ed. by A. Musacchio, e34025.
- 3561 Gérard, C. and A. Goldbeter (2012). "Entrainment of the Mammalian Cell Cycle
3562 by the Circadian Clock: Modeling Two Coupled Cellular Rhythms". In: *PLOS*
3563 *Computational Biology* 8.5, e1002516.
- 3564 Ghosh, A. and B. Chance (1964). "Oscillations of Glycolytic Intermediates in
3565 Yeast Cells". In: *Biochemical and Biophysical Research Communications* 16.2,
3566 pp. 174–181.
- 3567 Gillespie, D. T. (1977). "Exact Stochastic Simulation of Coupled Chemical Reac-
3568 tions". In: *The Journal of Physical Chemistry* 81.25, pp. 2340–2361.

- 3569 Gillespie, D. T. (2007). "Stochastic Simulation of Chemical Kinetics". In: *Annual*
3570 *Review of Physical Chemistry* 58.1, pp. 35–55.
- 3571 Glynn, E. F., J. Chen and A. R. Mushegian (2006). "Detecting Periodic Pat-
3572 terns in Unevenly Spaced Gene Expression Time Series Using Lomb–Scargle
3573 Periodograms". In: *Bioinformatics* 22.3, pp. 310–316.
- 3574 Goelzer, A., V. Fromion and G. Scorletti (2011). "Cell Design in Bacteria as
3575 a Convex Optimization Problem". In: *Automatica*. Special Issue on Systems
3576 Biology 47.6, pp. 1210–1218.
- 3577 Goldbeter, A. (1991). "A Minimal Cascade Model for the Mitotic Oscillator
3578 Involving Cyclin and Cdc2 Kinase." In: *Proceedings of the National Academy*
3579 *of Sciences* 88.20, pp. 9107–9111.
- 3580 Goldbeter, A. and R. Lefever (1972). "Dissipative Structures for an Allosteric
3581 Model". In: *Biophysical Journal* 12.10, pp. 1302–1315.
- 3582 Goldbeter, A. and J. Yan (2022). "Multi-Synchronization and Other Patterns of
3583 Multi-Rhythmicity in Oscillatory Biological Systems". In: *Interface Focus* 12.3
3584 (), p. 20210089.
- 3585 Goodwin, B. C. (1965). "Oscillatory Behavior in Enzymatic Control Processes".
3586 In: *Advances in Enzyme Regulation* 3, pp. 425–437.
- 3587 Gowans, G. J., A. N. Schep, K. M. Wong, D. A. King, W. J. Greenleaf and
3588 A. J. Morrison (2018). "INO80 Chromatin Remodeling Coordinates Metabolic
3589 Homeostasis with Cell Division". In: *Cell Reports* 22.3, pp. 611–623.
- 3590 Granados, A. A., M. M. Crane, L. F. Montano-Gutierrez, R. J. Tanaka, M. Voli-
3591 otis and P. S. Swain (2017). "Distributing Tasks via Multiple Input Pathways
3592 Increases Cellular Survival in Stress". In: *eLife* 6. Ed. by N. Barkai, e21415.
- 3593 Griffith, J. S. (1968). "Mathematics of Cellular Control Processes I. Negative
3594 Feedback to One Gene". In: *Journal of Theoretical Biology* 20.2, pp. 202–208.

- 3595 Gudipati, V., K. Koch, W.-D. Lienhart and P. Macheroux (2014). "The Flavo-
3596 proteome of the Yeast *Saccharomyces Cerevisiae*". In: *Biochimica et Biophysica
3597 Acta (BBA) - Proteins and Proteomics* 1844.3, pp. 535–544.
- 3598 Hamnett, R., P. Crosby, J. E. Chesham and M. H. Hastings (2019). "Vasoactive
3599 Intestinal Peptide Controls the Suprachiasmatic Circadian Clock Network via
3600 ERK1/2 and DUSP4 Signalling". In: *Nature Communications* 10.1, p. 542.
- 3601 Heavner, B. D., K. Smallbone, B. Barker, P. Mendes and L. P. Walker (2012).
3602 "Yeast 5 – an Expanded Reconstruction of the *Saccharomyces Cerevisiae* Meta-
3603 bolic Network". In: *BMC Systems Biology* 6.1, p. 55.
- 3604 Heltberg, M. L., S. Krishna, L. P. Kadanoff and M. H. Jensen (2021). "A Tale of
3605 Two Rhythms: Locked Clocks and Chaos in Biology". In: *Cell Systems* 12.4,
3606 pp. 291–303.
- 3607 Herskowitz, I. (1988). "Life Cycle of the Budding Yeast *Saccharomyces Cerevisiae*".
3608 In: *Microbiological Reviews* 52.4, pp. 536–553.
- 3609 Higgins, J. (1964). "A Chemical Mechanism for Oscillation of Glycolytic Interme-
3610 diates in Yeast Cells*". In: *Proceedings of the National Academy of Sciences*
3611 51.6, pp. 989–994.
- 3612 Ho, B., A. Baryshnikova and G. W. Brown (2018). "Unification of Protein Abund-
3613 ance Datasets Yields a Quantitative *Saccharomyces Cerevisiae* Proteome". In:
3614 *Cell Systems* 6.2, 192–205.e3.
- 3615 Huang, D., H. Friesen and B. Andrews (2007). "Pho85, a Multifunctional Cyclin-
3616 Dependent Protein Kinase in Budding Yeast". In: *Molecular Microbiology* 66.2,
3617 pp. 303–314.
- 3618 Hughes, M. E., J. B. Hogenesch and K. Kornacker (2010). "JTK_CYCLE: An
3619 Efficient Nonparametric Algorithm for Detecting Rhythmic Components in
3620 Genome-Scale Data Sets". In: *Journal of Biological Rhythms* 25.5, pp. 372–380.

- 3621 Hutchison, A. L., M. Maienschein-Cline, A. H. Chiang, S. M. A. Tabei, H. Gud-
3622 jonson, N. Bahroos, R. Allada and A. R. Dinner (2015). “Improved Statistical
3623 Methods Enable Greater Sensitivity in Rhythm Detection for Genome-Wide
3624 Data”. In: *PLOS Computational Biology* 11.3, e1004094.
- 3625 Jia, C. and R. Grima (2020). “Frequency Domain Analysis of Fluctuations of
3626 mRNA and Protein Copy Numbers within a Cell Lineage: Theory and Experi-
3627 mental Validation”. In: *bioRxiv*, p. 2020.09.23.309724.
- 3628 Jones, K. D. and D. S. Kompala (1999). “Cybernetic Model of the Growth Dynam-
3629 ics of *Saccharomyces Cerevisiae* in Batch and Continuous Cultures”. In: *Journal*
3630 *of Biotechnology. Modelling in Biochemical Engineering* 71.1, pp. 105–131.
- 3631 Kanehisa, M., M. Furumichi, Y. Sato, M. Kawashima and M. Ishiguro-Watanabe
3632 (2023). “KEGG for Taxonomy-Based Analysis of Pathways and Genomes”. In:
3633 *Nucleic Acids Research* 51.D1, pp. D587–D592.
- 3634 Kaspar von Meyenburg, H. (1969). “Energetics of the Budding Cycle of *Sacchar-*
3635 *omyces Cerevisiae* during Glucose Limited Aerobic Growth”. In: *Archiv für*
3636 *Mikrobiologie* 66.4, pp. 289–303.
- 3637 KENDALL, M. G. (1945). “THE TREATMENT OF TIES IN RANKING PROB-
3638 *LEMS*”. In: *Biometrika* 33.3, pp. 239–251.
- 3639 Kiviet, D. J., P. Nghe, N. Walker, S. Boulineau, V. Sunderlikova and S. J. Tans
3640 (2014). “Stochasticity of Metabolism and Growth at the Single-Cell Level”. In:
3641 *Nature* 514.7522, pp. 376–379.
- 3642 Koch, K., A. Hromic, M. Sorokina, E. Strandback, M. Reisinger, K. Gruber and
3643 P. Macheroux (2017). “Structure, Biochemical and Kinetic Properties of Recom-
3644 binant Pst2p from *Saccharomyces Cerevisiae*, a FMN-dependent NAD(P)H:Quinone
3645 Oxidoreductase”. In: *Biochimica et Biophysica Acta (BBA) - Proteins and*
3646 *Proteomics* 1865.8, pp. 1046–1056.

- 3647 Krishna, S. and S. Laxman (2018). “A Minimal “Push–Pull” Bistability Model
3648 Explains Oscillations between Quiescent and Proliferative Cell States”. In:
3649 *Molecular Biology of the Cell* 29.19, pp. 2243–2258.
- 3650 Kuang, Z., S. Pinglay, H. Ji and J. D. Boeke (2017). “Msn2/4 Regulate Expression
3651 of Glycolytic Enzymes and Control Transition from Quiescence to Growth”. In:
3652 *eLife* 6. Ed. by N. Barkai, e29938.
- 3653 Kumpula, J. M., J. Saramäki, K. Kaski and J. Kertész (2007). “Limited Resolution
3654 in Complex Network Community Detection with Potts Model Approach”. In:
3655 *The European Physical Journal B* 56.1, pp. 41–45.
- 3656 Kurat, C. F., H. Wolinski, J. Petschnigg, S. Kaluarachchi, B. Andrews, K. Natter
3657 and S. D. Kohlwein (2009). “Cdk1/Cdc28-Dependent Activation of the Major
3658 Triacylglycerol Lipase Tgl4 in Yeast Links Lipolysis to Cell-Cycle Progression”.
3659 In: *Molecular Cell* 33.1, pp. 53–63.
- 3660 Lambert, T. J. (2023). “Using FPbase: The Fluorescent Protein Database”. In:
3661 *Fluorescent Proteins: Methods and Protocols*. Ed. by M. Sharma. Methods in
3662 Molecular Biology. New York, NY: Springer US, pp. 1–45.
- 3663 Laxman, S., B. M. Sutter and B. P. Tu (2010). “Behavior of a Metabolic Cyc-
3664 ling Population at the Single Cell Level as Visualized by Fluorescent Gene
3665 Expression Reporters”. In: *PLOS ONE* 5.9, e12595.
- 3666 Li, C. M. and R. R. Klevecz (2006). “A Rapid Genome-Scale Response of the
3667 Transcriptional Oscillator to Perturbation Reveals a Period-Doubling Path to
3668 Phenotypic Change”. In: *Proceedings of the National Academy of Sciences*
3669 103.44, pp. 16254–16259.
- 3670 Lloyd, D. (2019). “Saccharomyces Cerevisiae: Oscillatory Orchestration of Growth”.
3671 In: *Advancing Frontiers in Mycology & Mycotechnology: Basic and Applied
3672 Aspects of Fungi*. Ed. by T. Satyanarayana, S. K. Deshmukh and M. V. Desh-
3673 pande. Singapore: Springer Singapore, pp. 181–214.

- 3674 Lloyd, D. and D. B. Murray (2005). “Ultradian Metronome: Timekeeper for
3675 Orchestration of Cellular Coherence”. In: *Trends in Biochemical Sciences* 30.7,
3676 pp. 373–377.
- 3677 – (2006). “The Temporal Architecture of Eukaryotic Growth”. In: *FEBS Letters*
3678 580.12, pp. 2830–2835.
- 3679 – (2007). “Redox Rhythmicity: Clocks at the Core of Temporal Coherence”. In:
3680 *BioEssays* 29.5, pp. 465–473.
- 3681 Lomb, N. R. (1976). “Least-Squares Frequency Analysis of Unequally Spaced
3682 Data”. In: *Astrophysics and Space Science* 39.2, pp. 447–462.
- 3683 Lu, H., F. Li, B. J. Sánchez, Z. Zhu, G. Li, I. Domenzain, S. Marciauskas, P. M.
3684 Anton, D. Lappa, C. Lieven, M. E. Beber, N. Sonnenschein, E. J. Kerkhoven
3685 and J. Nielsen (2019). “A Consensus *S. Cerevisiae* Metabolic Model Yeast8 and
3686 Its Ecosystem for Comprehensively Probing Cellular Metabolism”. In: *Nature
3687 Communications* 10.1, p. 3586.
- 3688 Lu, Y. and F. R. Cross (2010). “Periodic Cyclin-Cdk Activity Entrains an Autonom-
3689 ous Cdc14 Release Oscillator”. In: *Cell* 141.2, pp. 268–279.
- 3690 Lubba, C. H., S. S. Sethi, P. Knaute, S. R. Schultz, B. D. Fulcher and N. S. Jones
3691 (2019). “Catch22: CAnonical Time-series CCharacteristics”. In: *Data Mining and
3692 Knowledge Discovery* 33.6, pp. 1821–1852.
- 3693 Machado, A. K., B. A. Morgan and G. F. Merrill (1997). “Thioredoxin Reductase-
3694 dependent Inhibition of MCB Cell Cycle Box Activity in *Saccharomyces Cerevisiae*”.
3695 In: *Journal of Biological Chemistry* 272.27, pp. 17045–17054.
- 3696 Machné, R. and D. B. Murray (2012). “The Yin and Yang of Yeast Transcription:
3697 Elements of a Global Feedback System between Metabolism and Chromatin”.
3698 In: *PLOS ONE* 7.6, e37906.

- 3699 Mahadevan, R., J. S. Edwards and F. J. Doyle (2002). "Dynamic Flux Balance
3700 Analysis of Diauxic Growth in Escherichia Coli". In: *Biophysical Journal* 83.3,
3701 pp. 1331–1340.
- 3702 Malumbres, M., E. Harlow, T. Hunt, T. Hunter, J. M. Lahti, G. Manning, D. O.
3703 Morgan, L.-H. Tsai and D. J. Wolgemuth (2009). "Cyclin-Dependent Kinases:
3704 A Family Portrait". In: *Nature Cell Biology* 11.11, pp. 1275–1276.
- 3705 Maslanka, R., M. Kwolek-Mirek and R. Zadrag-Tecza (2018). "Autofluorescence of
3706 Yeast *Saccharomyces Cerevisiae* Cells Caused by Glucose Metabolism Products
3707 and Its Methodological Implications". In: *Journal of Microbiological Methods*
3708 146, pp. 55–60.
- 3709 Masters, B. R. (1994). "Confocal Redox Imaging of Cells". In: *Advances in Mo-
3710 lecular and Cell Biology*. Ed. by E. E. Bittar and L. Bo Chen. Vol. 8. Organelles
3711 in Vivo. Elsevier, pp. 1–19.
- 3712 McInnes, L., J. Healy and J. Melville (2020). "UMAP: Uniform Manifold Ap-
3713 proximation and Projection for Dimension Reduction". In: *arXiv:1802.03426*
3714 [cs, stat]. arXiv: 1802.03426 [cs, stat].
- 3715 Mellor, J. (2016). "The Molecular Basis of Metabolic Cycles and Their Relation-
3716 ship to Circadian Rhythms". In: *Nature Structural & Molecular Biology* 23.12,
3717 pp. 1035–1044.
- 3718 Mewies, M., W. S. McIntire and N. S. Scrutton (1998). "Covalent Attachment
3719 of Flavin Adenine Dinucleotide (FAD) and Flavin Mononucleotide (FMN) to
3720 Enzymes: The Current State of Affairs". In: *Protein Science* 7.1, pp. 7–20.
- 3721 Millar, A. J. (2004). "Input Signals to the Plant Circadian Clock". In: *Journal of
3722 Experimental Botany* 55.395, pp. 277–283.
- 3723 Minard, K. I. and L. McAlister-Henn (2005). "Sources of NADPH in Yeast Vary
3724 with Carbon Source*". In: *Journal of Biological Chemistry* 280.48, pp. 39890–
3725 39896.

- 3726 Mochan, E. and E. K. Pye (1973). "Respiratory Oscillations in Adapting Yeast
3727 Cultures". In: *Nature New Biology* 242.119, pp. 177–179.
- 3728 Morán, F. and A. Goldbeter (1984). "Onset of Birhythmicity in a Regulated
3729 Biochemical System". In: *Biophysical Chemistry* 20.1, pp. 149–156.
- 3730 Morrison, H. (2021). "Chapter 14 - Dihydrolipoamide Dehydrogenase". In: *En-*
3731 *zyme Active Sites and Their Reaction Mechanisms*. Ed. by H. Morrison. Aca-
3732 demic Press, pp. 71–77.
- 3733 Muñoz González, A. F. (2023). "Phenotyping Single Cells of *Saccharomyces Cerevisiae*
3734 Using an End-to-End Analysis of High-Content Time-Lapse Microscopy". PhD
3735 thesis. University of Edinburgh.
- 3736 Murray, A. W. (2004). "Recycling the Cell Cycle: Cyclins Revisited". In: *Cell*
3737 116.2, pp. 221–234.
- 3738 Murray, D. B., K. Haynes and M. Tomita (2011). "Redox Regulation in Respiring
3739 *Saccharomyces Cerevisiae*". In: *Biochimica et Biophysica Acta (BBA) - General*
3740 *Subjects. Systems Biology of Microorganisms* 1810.10, pp. 945–958.
- 3741 Newman, M. E. J. (2006). "Modularity and Community Structure in Networks".
3742 In: *Proceedings of the National Academy of Sciences of the United States of*
3743 *America* 103.23, pp. 8577–8582.
- 3744 Nijkamp, J. F., M. van den Broek, E. Datema, S. de Kok, L. Bosman, M. A.
3745 Luttik, P. Daran-Lapujade, W. Vongsangnak, J. Nielsen, W. H. Heijne, P.
3746 Klaassen, C. J. Padden, D. Platt, P. Kötter, R. C. van Ham, M. J. Reinders,
3747 J. T. Pronk, D. de Ridder and J.-M. Daran (2012). "De Novo Sequencing,
3748 Assembly and Analysis of the Genome of the Laboratory Strain *Saccharomyces*
3749 *Cerevisiae* CEN.PK113-7D, a Model for Modern Industrial Biotechnology". In:
3750 *Microbial Cell Factories* 11.1, p. 36.
- 3751 Nilsson, A. and J. Nielsen (2016). "Metabolic Trade-offs in Yeast Are Caused by
3752 F1F0-ATP Synthase". In: *Scientific Reports* 6.1, p. 22264.

- 3753 Nissen, T. L., U. Schulze, J. Nielsen and J. Villadsen (1997). “Flux Distributions in Anaerobic, Glucose-Limited Continuous Cultures of *Saccharomyces cerevisiae*”. In: *Microbiology* 143.1, pp. 203–218.
- 3756 Nocetti, N. and I. Whitehouse (2016). “Nucleosome Repositioning Underlies Dynamic Gene Expression”. In: *Genes & Development* 30.6, pp. 660–672.
- 3758 Nogae, I. and M. Johnston (1990). “Isolation and Characterization of the ZWF1 Gene of *Saccharomyces cerevisiae*, Encoding Glucose-6-Phosphate Dehydrogenase”. In: *Gene* 96.2, pp. 161–169.
- 3761 Norsigian, C. J., N. Pusarla, J. L. McConn, J. T. Yurkovich, A. Dräger, B. O. Palsson and Z. King (2020). “BiGG Models 2020: Multi-Strain Genome-Scale Models and Expansion across the Phylogenetic Tree”. In: *Nucleic Acids Research* 48.D1, pp. D402–D406.
- 3765 Nosoh, Y. and A. Takamiya (1962). “SYNCHRONIZATION OF BUDDING CYCLE IN YEAST CELLS, AND EFFECT OF CARBON MONOXIDE AND NITROGEN-DEFICIENCY ON THE SYNCHRONY”. In: *Plant and Cell Physiology* 3.1, pp. 53–66.
- 3769 Novak, B. and J. J. Tyson (2022). “Mitotic Kinase Oscillation Governs the Latching of Cell Cycle Switches”. In: *Current Biology*.
- 3771 O’Neill, J. S., N. P. Hoyle, J. B. Robertson, R. S. Edgar, A. D. Beale, S. Y. Peak-Chew, J. Day, A. S. H. Costa, C. Frezza and H. C. Causton (2020). “Eukaryotic Cell Biology Is Temporally Coordinated to Support the Energetic Demands of Protein Homeostasis”. In: *Nature Communications* 11.1, p. 4706.
- 3775 O’Neill, E. M., A. Kaffman, E. R. Jolly and E. K. O’Shea (1996). “Regulation of PHO4 Nuclear Localization by the PHO80-PHO85 Cyclin-CDK Complex”. In: *Science* 271.5246, pp. 209–212.
- 3778 O’Neill, J. S. and A. B. Reddy (2011). “Circadian Clocks in Human Red Blood Cells”. In: *Nature* 469.7331, pp. 498–503.

- 3780 O'Neill, J. S., G. van Ooijen, L. E. Dixon, C. Troein, F. Corellou, F.-Y. Bouget,
3781 A. B. Reddy and A. J. Millar (2011). “Circadian Rhythms Persist without
3782 Transcription in a Eukaryote”. In: *Nature* 469.7331, pp. 554–558.
- 3783 Odat, O., S. Matta, H. Khalil, S. C. Kampranis, R. Pfau, P. N. Tsichlis and
3784 A. M. Makris (2007). “Old Yellow Enzymes, Highly Homologous FMN Ox-
3785 idoreductases with Modulating Roles in Oxidative Stress and Programmed Cell
3786 Death in Yeast *”. In: *Journal of Biological Chemistry* 282.49, pp. 36010–36023.
- 3787 Olsen, L. F., A. Z. Andersen, A. Lunding, J. C. Brasen and A. K. Poulsen (2009).
3788 “Regulation of Glycolytic Oscillations by Mitochondrial and Plasma Membrane
3789 H+-ATPases”. In: *Biophysical Journal* 96.9, pp. 3850–3861.
- 3790 Olsen, L. F. and A. Lunding (2021). “Oscillations in Yeast Glycolysis”. In: *Physics
3791 of Biological Oscillators: New Insights into Non-Equilibrium and Non-Autonomous
3792 Systems*. Ed. by A. Stefanovska and P. V. E. McClintock. Understanding
3793 Complex Systems. Cham: Springer International Publishing, pp. 211–224.
- 3794 Orlando, D. A., C. Y. Lin, A. Bernard, J. Y. Wang, J. E. S. Socolar, E. S.
3795 Iversen, A. J. Hartemink and S. B. Haase (2008). “Global Control of Cell-Cycle
3796 Transcription by Coupled CDK and Network Oscillators”. In: *Nature* 453.7197,
3797 pp. 944–947.
- 3798 Orth, J. D., I. Thiele and B. Ø. Palsson (2010). “What Is Flux Balance Analysis?”
3799 In: *Nature Biotechnology* 28.3, pp. 245–248.
- 3800 Özsezen, S., A. Papagiannakis, H. Chen, B. Niebel, A. Milius-Argeitis and M.
3801 Heinemann (2019). “Inference of the High-Level Interaction Topology between
3802 the Metabolic and Cell-Cycle Oscillators from Single-Cell Dynamics”. In: *Cell
3803 Systems*.
- 3804 Palsson, B. Ø. (2015). *Systems Biology: Constraint-based Reconstruction and
3805 Analysis*. Cambridge: Cambridge University Press.

- 3806 Pang, S. S., R. G. Duggleby and L. W. Guddat (2002). “Crystal Structure of
3807 Yeast Acetohydroxyacid Synthase: A Target for Herbicidal inhibitors11Edited
3808 by R. Huber”. In: *Journal of Molecular Biology* 317.2, pp. 249–262.
- 3809 Papagiannakis, A., B. Niebel, E. C. Wit and M. Heinemann (2017). “Autonomous
3810 Metabolic Oscillations Robustly Gate the Early and Late Cell Cycle”. In:
3811 *Molecular Cell* 65.2, pp. 285–295.
- 3812 “Flavin-Containing Oxidative Biocatalysts” (2006). In: *Biocatalysis in the Phar-*
3813 *maceutical and Biotechnology Industries*. Ed. by R. N. Patel. CRC Press.
- 3814 Pietsch, J. M., A. F. Munoz, D.-Y. A. Adjavon, I. Farquhar, I. B. Clark and
3815 P. S. Swain (2023). “Determining Growth Rates from Bright-Field Images of
3816 Budding Cells through Identifying Overlaps”. In: *eLife* 12. Ed. by A. M. Moses,
3817 e79812.
- 3818 Platt, J. (1999). “Probabilistic Outputs for Support Vector Machines and Com-
3819 parisons to Regularized Likelihood Methods”. In: *Advances in large margin*
3820 *classifiers* 10.3, pp. 61–74.
- 3821 Potvin-Trottier, L., N. D. Lord, G. Vinnicombe and J. Paulsson (2016). “Syn-
3822 chronous Long-Term Oscillations in a Synthetic Gene Circuit”. In: *Nature*
3823 538.7626, pp. 514–517.
- 3824 Pronk, J. T. (2002). “Auxotrophic Yeast Strains in Fundamental and Applied
3825 Research”. In: *Applied and Environmental Microbiology* 68.5, pp. 2095–2100.
- 3826 Reichardt, J. and S. Bornholdt (2004). “Detecting Fuzzy Community Structures
3827 in Complex Networks with a Potts Model”. In: *Physical Review Letters* 93.21,
3828 p. 218701.
- 3829 Reimers, A.-M., H. Knoop, A. Bockmayr and R. Steuer (2017). “Cellular Trade-
3830 Offs and Optimal Resource Allocation during Cyanobacterial Diurnal Growth”.
3831 In: *Proceedings of the National Academy of Sciences* 114.31, E6457–E6465.

- 3832 Salazar-Roa, M. and M. Malumbres (2017). "Fueling the Cell Division Cycle". In:
3833 *Trends in Cell Biology*. Special Issue: Cell Cycle 27.1, pp. 69–81.
- 3834 Sánchez, B. J., C. Zhang, A. Nilsson, P.-J. Lahtvee, E. J. Kerkhoven and J.
3835 Nielsen (2017). "Improving the Phenotype Predictions of a Yeast Genome-
3836 Scale Metabolic Model by Incorporating Enzymatic Constraints". In: *Molecular
3837 Systems Biology* 13.8, p. 935.
- 3838 Sánchez, B. J., F. Li, E. J. Kerkhoven and J. Nielsen (2019). "SLIMER: Probing
3839 Flexibility of Lipid Metabolism in Yeast with an Improved Constraint-Based
3840 Modeling Framework". In: *BMC Systems Biology* 13.1, p. 4.
- 3841 Sasidharan, K., M. Tomita, M. Aon, D. Lloyd and D. B. Murray (2012). "Time-
3842 Structure of the Yeast Metabolism In Vivo". In: *Advances in Systems Biology*.
3843 Ed. by I. I. Goryanin and A. B. Goryachev. Advances in Experimental Medicine
3844 and Biology. New York, NY: Springer, pp. 359–379.
- 3845 Satoh, T., M. Horie, H. Watanabe, Y. Tsuchiya and T. Kamei (1993). "Enzymatic
3846 Properties of Squalene Epoxidase from *Saccharomyces Cerevisiae*". In: *Biolo-
3847 gical & Pharmaceutical Bulletin* 16.4, pp. 349–352.
- 3848 Satroutdinov, A. D., H. Kuriyama and H. Kobayashi (1992). "Oscillatory Meta-
3849 bolism of *Saccharomyces Cerevisiae* in Continuous Culture". In: *FEMS Micro-
3850 biology Letters* 98.1-3, pp. 261–267.
- 3851 Scargle, J. D. (1982). "Studies in Astronomical Time Series Analysis. II - Stat-
3852 istical Aspects of Spectral Analysis of Unevenly Spaced Data". In: *The Astro-
3853 physical Journal* 263, pp. 835–853.
- 3854 Sherman, F. (2002). "Getting Started with Yeast". In: *Methods in Enzymology*.
3855 Ed. by C. Guthrie and G. R. Fink. Vol. 350. Guide to Yeast Genetics and
3856 Molecular and Cell Biology - Part B. Academic Press, pp. 3–41.

- 3857 Siano, S. A. and R. Mutharasan (1989). "NADH and Flavin Fluorescence Re-
3858 sponses of Starved Yeast Cultures to Substrate Additions". In: *Biotechnology*
3859 and *Bioengineering* 34.5, pp. 660–670.
- 3860 Silverman, S. J., A. A. Petti, N. Slavov, L. Parsons, R. Briehof, S. Y. Thibierge,
3861 D. Zenklusen, S. J. Gandhi, D. R. Larson, R. H. Singer and D. Botstein (2010).
3862 "Metabolic Cycling in Single Yeast Cells from Un同步ized Steady-State
3863 Populations Limited on Glucose or Phosphate". In: *Proceedings of the National
3864 Academy of Sciences* 107.15, pp. 6946–6951.
- 3865 Singh, K., B. Graf, A. Linden, V. Sautner, H. Urlaub, K. Tittmann, H. Stark and
3866 A. Chari (2020). "Discovery of a Regulatory Subunit of the Yeast Fatty Acid
3867 Synthase". In: *Cell* 180.6, 1130–1143.e20.
- 3868 Slavov, N. and D. Botstein (2011). "Coupling among Growth Rate Response,
3869 Metabolic Cycle, and Cell Division Cycle in Yeast". In: *Molecular Biology of
3870 the Cell* 22.12, pp. 1997–2009.
- 3871 Slavov, N., J. Macinskas, A. Caudy and D. Botstein (2011). "Metabolic Cycling
3872 without Cell Division Cycling in Respiring Yeast". In: *Proceedings of the Na-
3873 tional Academy of Sciences* 108.47, pp. 19090–19095.
- 3874 Smith, H. L. and P. Waltman (1995). *The Theory of the Chemostat: Dynamics
3875 of Microbial Competition*. Cambridge Studies in Mathematical Biology. Cam-
3876 bridge: Cambridge University Press.
- 3877 Takhayev, V., S. Özsezen, E. N. Smith, A. Zylstra, M. L. Chaillet, H. Chen,
3878 A. Papagiannakis, A. Milias-Argeitis and M. Heinemann (2023). "Temporal
3879 Segregation of Biosynthetic Processes Is Responsible for Metabolic Oscillations
3880 during the Budding Yeast Cell Cycle". In: *Nature Metabolism* 5.2, pp. 294–313.
- 3881 Termonia, Y. and J. Ross (1981). "Oscillations and Control Features in Glycolysis:
3882 Numerical Analysis of a Comprehensive Model." In: *Proceedings of the National
3883 Academy of Sciences* 78.5, pp. 2952–2956.

- 3884 The UniProt Consortium (2023). “UniProt: The Universal Protein Knowledgebase
3885 in 2023”. In: *Nucleic Acids Research* 51.D1, pp. D523–D531.
- 3886 Thiele, I. and B. Ø. Palsson (2010). “A Protocol for Generating a High-Quality
3887 Genome-Scale Metabolic Reconstruction”. In: *Nature Protocols* 5.1, pp. 93–121.
- 3888 Thoke, H. S., L. F. Olsen, L. Duelund, R. P. Stock, T. Heimburg and L. A.
3889 Bagatolli (2018). “Is a Constant Low-Entropy Process at the Root of Glycolytic
3890 Oscillations?” In: *Journal of Biological Physics* 44.3, pp. 419–431.
- 3891 Traag, V. A., P. Van Dooren and Y. Nesterov (2011). “Narrow Scope for Resolution-
3892 Limit-Free Community Detection”. In: *Physical Review E* 84.1, p. 016114.
- 3893 Traag, V. A., L. Waltman and N. J. van Eck (2019). “From Louvain to Leiden:
3894 Guaranteeing Well-Connected Communities”. In: *Scientific Reports* 9.1, p. 5233.
- 3895 Tsuge, H., K. Ozeki, K. Sen-maru and K. Ohashi (1979). “Purification and Prop-
3896 erties of Pyridoxamine (Pyridoxine) 5'-Phosphate Oxidase from Baker's Yeast”.
3897 In: *Agricultural and Biological Chemistry* 43.9, pp. 1801–1807.
- 3898 Tu, B. P., A. Kudlicki, M. Rowicka and S. L. McKnight (2005). “Logic of the
3899 Yeast Metabolic Cycle: Temporal Compartmentalization of Cellular Processes”.
3900 In: *Science* 310.5751, pp. 1152–1158.
- 3901 Tu, B. P., R. E. Mohler, J. C. Liu, K. M. Dombek, E. T. Young, R. E. Synovec
3902 and S. L. McKnight (2007). “Cyclic Changes in Metabolic State during the Life
3903 of a Yeast Cell”. In: *Proceedings of the National Academy of Sciences* 104.43,
3904 pp. 16886–16891.
- 3905 VanderPlas, J. T. (2018). “Understanding the Lomb-Scargle Periodogram”. In:
3906 *The Astrophysical Journal Supplement Series* 236.1, p. 16. arXiv: 1703.09824.
- 3907 Verduyn, C., E. Postma, W. A. Scheffers and J. P. V. Dijken (1992). “Effect
3908 of Benzoic Acid on Metabolic Fluxes in Yeasts: A Continuous-Culture Study
3909 on the Regulation of Respiration and Alcoholic Fermentation”. In: *Yeast* 8.7,
3910 pp. 501–517.

- 3911 Wagnieres, G. A., W. M. Star and B. C. Wilson (1998). "In Vivo Fluorescence
3912 Spectroscopy and Imaging for Oncological Applications". In: *Photochemistry*
3913 and *Photobiology* 68.5, pp. 603–632.
- 3914 Wang, X., A. Wirth and L. Wang (2007). "Structure-Based Statistical Features
3915 and Multivariate Time Series Clustering". In: *Seventh IEEE International Con-*
3916 *ference on Data Mining (ICDM 2007)*, pp. 351–360.
- 3917 Watcharawipas, A., D. Watanabe and H. Takagi (2018). "Sodium Acetate Re-
3918 spondes in *Saccharomyces Cerevisiae* and the Ubiquitin Ligase Rsp5". In: *Fron-*
3919 *tiers in Microbiology* 9.
- 3920 Weiße, A. Y., D. A. Oyarzún, V. Danos and P. S. Swain (2015). "Mechanistic Links
3921 between Cellular Trade-Offs, Gene Expression, and Growth". In: *Proceedings*
3922 *of the National Academy of Sciences* 112.9, E1038–E1047.
- 3923 Wilson, W. A., A. M. Mahrenholz and P. J. Roach (1999). "Substrate Targeting
3924 of the Yeast Cyclin-Dependent Kinase Pho85p by the Cyclin Pcl10p". In:
3925 *Molecular and Cellular Biology* 19.10, pp. 7020–7030.
- 3926 Winston, F., C. Dollard and S. L. Ricupero-Hovasse (1995). "Construction of a Set
3927 of Convenient *Saccharomyces Cerevisiae* Strains That Are Isogenic to S288C".
3928 In: *Yeast* 11.1, pp. 53–55.
- 3929 Wong, C.-M., Y. Zhou, R. W. M. Ng, H.-f. Kung and D.-Y. Jin (2002). "Cooper-
3930 ation of Yeast Peroxiredoxins Tsa1p and Tsa2p in the Cellular Defense against
3931 Oxidative and Nitrosative Stress *". In: *Journal of Biological Chemistry* 277.7,
3932 pp. 5385–5394.
- 3933 Zameitat, E., A. J. Pierik, K. Zocher and M. Löffler (2007). "Dihydroorotate De-
3934 hydrogenase from *Saccharomyces Cerevisiae*: Spectroscopic Investigations with
3935 the Recombinant Enzyme Throw Light on Catalytic Properties and Metabolism
3936 of Fumarate Analogues". In: *FEMS Yeast Research* 7.6, pp. 897–904.

- ³⁹³⁷ Zhang, Z., A. Milius-Argeitis and M. Heinemann (2018). “Dynamic Single-Cell
³⁹³⁸ NAD(P)H Measurement Reveals Oscillatory Metabolism throughout the E.
³⁹³⁹ Coli Cell Division Cycle”. In: *Scientific Reports* 8.1, pp. 1–10.
- ³⁹⁴⁰ Zhu, B. (2022). “Logic of the Temporal Compartmentalization of the Hepatic
³⁹⁴¹ Metabolic Cycle”. In: *Physiology*.
- ³⁹⁴² Zielinski, T., A. M. Moore, E. Troup, K. J. Halliday and A. J. Millar (2014).
³⁹⁴³ “Strengths and Limitations of Period Estimation Methods for Circadian Data”.
³⁹⁴⁴ In: *PLOS ONE* 9.5, e96462.
- ³⁹⁴⁵ Zieliński, T., J. Hay and A. J. Millar (2022). “Period Estimation and Rhythm
³⁹⁴⁶ Detection in Timeseries Data Using BioDare2, the Free, Online, Community
³⁹⁴⁷ Resource”. In: *Plant Circadian Networks: Methods and Protocols*. Ed. by D.
³⁹⁴⁸ Staiger, S. Davis and A. M. Davis. Methods in Molecular Biology. New York,
³⁹⁴⁹ NY: Springer US, pp. 15–32.
- ³⁹⁵⁰ Zylstra, A. and M. Heinemann (2022). “Metabolic Dynamics during the Cell
³⁹⁵¹ Cycle”. In: *Current Opinion in Systems Biology*, p. 100415.